Induced Decoherence by Spins Environment: Relaxation and Quantum Synchronization

Lic. Axel Damián Dente

FaMAF

UNC

Tesis presentada para obtener el grado de

Doctor en Fisica

28 Marzo de 2012

Director: Horacio M. Pastawski

Resumen Corto

El control de los sistemas cuántico representa uno de los principales desafíos en la actualidad. Los efectos de relajación y decoherencia inducidos por el entorno cuántico son el principal Obstaculo. A lo largo de esta tesis usaremos tecnicas analiticas y numericas para estudiar los procesos de decaimiento y decoherencia tanto en la dinámica de sistemas de espines como en modelos de enlaces fuertes (tight binding por su nombre en Ingles), ambos en presencia de distintos tipos de entornos cuánticos. Además, mostraremos que los resultados obtenidos pueden ser aplicados tanto en el análisis de la disociación molecular, como en el estudio de la sincronización de plasmones en nanoparticulas.

Clasificación:

03.65.Yz, 73.20.Hb, 31.10.+z

Palabras Claves:

Cuántica, No-Markovianos, Espines, Decoherencia, Enlaces Fuertes (Tight Binding), Relajación

Abstract

The control of quantum systems represents one of the main challenges nowadays. The technological revolution, jointly with the Quantum Information Theory, enable the control of small systems and the manipulation of few quantum states [Bennett & DiVincenzo, 2000]. In particular, by the use of Nuclear Magnetic Resonance, it was possible manipulate nuclear spins [Zhang *et al.*, 2011] and create ad-hoc Hamiltonians (average Hamiltonian theory) [Mádi *et al.*, 1997, Cappellaro *et al.*, 2007].

The main obstacles in the control of the quantum states are the relaxation and decoherence process. In this thesis we analyze the dynamics of spin systems and the decay of the quantum evolution in tight binding models in the presence of several types of environments.

By the use of numerical and analytical tools we will show how the presence of the environment could induce phase transitions in the quantum dynamics [Dente *et al.*, 2008]. Moreover, the technics developed in this thesis let us study the molecular dissociation process as quantum phase transition, and, in the other hand, the synchronization of plasmonic excitations in nanoparticle arrays.

Additionally we use mappings between spin systems and fermionic systems to analyze the decay rate in the presence of single and multiple connections to different types of environments [Dente *et al.*, 2011]. In this sense, we characterize the corrections to the Fermi Golden Rule and correlate them with the Local Density of States of the structured environments.

Following in the same line, we will analyze the decoherence process in the presence of many-body interactions. With this purpose we compare two decoherence quantifiers: the "Loschmidt Echo " and the "Mesoscopic Echo". The first one is based on time reversal procedures and the last one use

the Mesoscopic echoes of the system [Dente *et al.*, 2011]. With these, we study the dynamical behavior of decoherence in spin systems by considering different kind of interactions (flip-flop, Ising, Heisenberg). Finally, we will analyze the decoherence rate obtained from Non-markovian systems, and compare with Fermi Golden Rule evaluations.

To Julio, Alan and Griselda

Acknowledgements

Quiero agradecer a muchas personas que hicieron posible que esta tesis llegara a su conclusión. Primero a mi director, Horacio Pastawski, de quien tuve el gusto de poder aprender física tanto desde el punto de vista teórico como intuitivo.

También quisiera agradecer a todos los organismos que de una forma u otra colaboraron en la producción de la tesis: CONICET, SECyT, ANPCyT.

A toda la facultad en general, al personal docente y no-docente, y en particular a la secretaría de postgrado, quienes, con muy buena predisposición, siempre me ayudaron a solucionar los problemas burocráticos que aparecían.

A todas las personas que integran e integraron el LANAIS con los cuales he disfrutado charlar y trabajar. En particular agradezco a Patricia Levstein, Rodolfo Acosta y Emilia Silletta, quienes me ayudaron de diversas formas.

A los miembros de la oficina 324, con quienes se hizo más ameno el día a día, y con quienes he compartido innumerable cantidad de charlas y cafes. Por demás agradecido estoy con Felix Rojo quien me ayudo con problemas de toda índole y con Pablo Zangara, con quien he disfrutado trabajar a la par.

A las personas con las que tuve la oportunidad de colaborar: Raúl Bustos-Marún, Andres Ruderman, Carlos Bederian y Nicolas Wolovick.

A mis amigos del colegio, de la facultad, de salsa y de la vida, que siempre han estado para apoyarme y compartir buenos y malos momentos a lo largo de estos años.

Por último quería agradecer enormemente a mi familia, Julio, Griselda y Alan, quienes siempre me apoyaron en todo, especialmente en el tramo final y crítico de mi tesis. Y también a Melina que me ayudó y acompaño en la culminación la tesis.

Muchas Gracias a todos!!!!

Contents

List of Figures

LIST OF FIGURES

LIST OF FIGURES

Chapter 1

INTRODUCTION

1.1 The Quantum World

For various centuries Newton's and Maxwell's fundamental laws of mechanics and electromagnetism, supplemented with Einstein's relativity principle and Boltzmann's statistical thermodynamics, have been used to successfully describe the behavior of natural world immediately around us and much beyond, at the scale of the known universe. However, we also have a description of the microscopic world and down under, from nanoscopic electronic devices and chemical reactions to elementary particles in high energy colliders. This description started to emerge at the end of XIX century when Planck introduced the empirical constant h, representing a quantum of frequency, as a necessary tool to describe the radiation spectrum of a heated body. A few years later, Albert Einstein who was studying the photoelectric effect, [Einstein, 1905] gave further reality to Planck's quantization of the energy of light waves as photons, particles that collide with the metal electrons pushing them away. Soon it became clear that the Newtonian mechanics was not a complete description this atomic level and a Quantum Mechanics started to emerge from a collective effort of which participated Bohr, DeBroglie, Schrödinger, Heisenberg, Dirac, Pauli and many others.

1.2 Waves and Interferencies

The essential analytical tool of quantum mechanics is the *Schrödinger Equation* (SE), which describes the *evolution* of a complex function ψ whose square modulus is iden-

tified with the probability of finding the object it describes in a given state or configuration:

$$\mathrm{i}\hbar\frac{\partial}{\partial t}\psi(t) = \hat{H}\psi(t). \tag{1.1}$$

Here $\hat{H}$ stands for the "energy" or Hamiltonian operator that defines the problem. It also introduces the Planck constant $\hbar$ as the fundamental scale relating energy scale and time scales. From its formal solution, one sees that for a given initial state $\psi(0)$, the evolved state $\psi(t) = e^{-\mathrm{i}\hat{H}[t-0]/\hbar}\psi(0)$ has the property of time reversibility, i.e. it is identical to the state obtained by propagation backwards in times $\psi(-t) = e^{-\mathrm{i}\hat{H}[0-(-t)]/\hbar}\psi(0)$. Thus, this description does not seem to contain in an obvious way the irreversibility observed in Nature at the macroscopic scale. Even more, an effective backwards evolution can obtained if one is able to change the Hamiltonian sign. This feature will play an important role in our work.

For a particle with mass m moving along the coordinate x in presence of the potential $U(x)$ one has a wave function $\psi(x)$ and the Hamiltonian is

$$\hat{H} = \frac{\hat{p}^2}{2m} + U(x) = -\frac{\hbar^2}{2m}\frac{\partial^2}{\partial x^2} + U(x)$$

Thus, in a homogenous space ($U(x) \equiv 0$), the SE is just the diffusion equation with an "imaginary coefficient" $D = \mathrm{i}\frac{\hbar}{2m}$. It is precisely the imaginary coefficient the one which introduces the wave-like behavior in an equation which has as only a first order in time derivative. Indeed, its solution has particle-wave duality already build in. The linearity of the wave equation one immediately understand the possibility of build superpositions of any given state. This is responsible of the uncertainties between the precision one has in defining the position Δx and the momentum Δp of a given particle. It also implies the possibility of classically forbidding tunneling. These phenomena are foreign to classical mechanics and constitute part of the conceptual challenges introduced by quantum mechanics.

With the recent technological advances, it has become possible to observe the wave behavior of the matter in innumerable situations. From all the possible examples we chose to discuss the "quantum corrals". They consists of a number of Fe atoms placed contiguously to form a closed shape over a Cu surface. The metal electrons are described by a multielectron wave function that depends on the coordinate of each one

of the electrons $\Psi(\mathbf{r}_1, \mathbf{r}_2, \mathbf{r}_{3,\cdots})$. However, electrons as indistinguishable and when they are observed by the scanning tunneling microscope (STM), they manifests a particle density $\rho(\mathbf{r})$ showing specific interferences produced as the "density wave" collides at the corral boundaries. These ripples have a close resemblance to those of water waves in a swimming pool (see Fig. 1.1). With some effort we also can appreciate a granularity in the density associated with the atomic scale of the underlying crystalline surface.

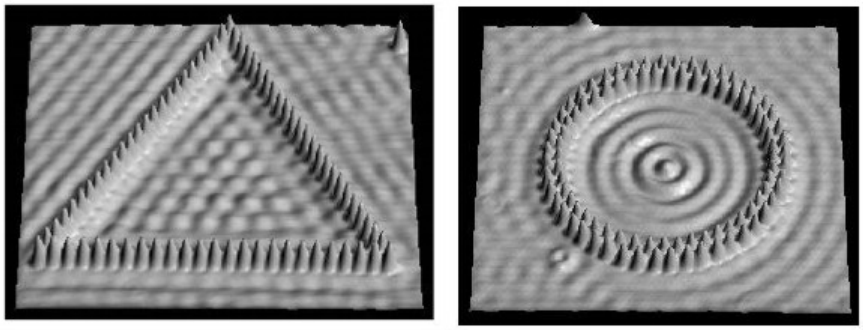

Figure 1.1: A set of 48 atoms in a circular shaped corral, made from STM-microscopy. By the combination of several atoms it is possible to observe the quantum interferences in the center of the corral. Figure Extracted From: http://www.almaden.ibm.com/vis/stm/

1.3 Dynamical Interferences

Every Physicist is familiar with interference phenomena in the steady state, however dynamical interferences are mostly absent from traditional textbooks. This is because only in recent years it has become more frequent the observation of quantum dynamical effects in various contexts. To fix ideas, we can consider the dynamics of a particle placed close to one edge of a one dimensional box of length L. We show this initial density distribution $\rho(x) = |\psi(x)|^2$ with breath Δx_0 and solve the SE to evaluate the survival probability as function of time as:

$$P_{0,0}(t) = \left| \int_0^L \psi^*(x,t)\psi(x,0)\mathrm{d}x \right|^2 ,$$

.i.e. the probability to find the particle in the initial state after a free evolution for a time t. In Fig. 1.2 we observe how the wave nature of quantum mechanics, the presence of different momentum in the range $\Delta p_0 \simeq \hbar/\Delta x_0$ makes the wave packet

to spread dispersively but there is also a component that "reflects" at the edges of the box producing a slight revival of the initial state in a time scale of the order of $mL/\Delta p_0$. This phenomenon, is a form of quantum interference, thus absent from a diffusion equation, associated the finite nature of the system and has been dubbed Mesoscopic Echo by Altshuler and collaborators [Prigodin *et al.*, 1994]. They proposed its observation in disordered electronic systems but it has not yet been observed in this case. However, we will see that in discrete systems this dynamical behavior is easily observed.

Until this moment we have spoken about the wave behavior in a continuous spatial coordinate. Indeed, in the above practical computation (see Fig. 1.2) we defined the wave function in a grid of unit a and wrote a difference equation

$$\left[-\frac{\hbar^2}{2m}\frac{\partial^2}{\partial x^2} + U(x)\right]\psi(x) \Longrightarrow -Vu_{n-1} + E_n u_n - Vu_{n+1}$$

where $\psi(na) = u_n$ is discrete wave function and $\frac{\hbar^2}{2ma^2} = V$ is the kinetic term that tends to delocalize any local excitation among different sites in the lattice. The local energy term $E_n = -2V + U(na)$ identifies the "site" energy of a particle at a given potential profile referred to the kinetic energy scale. This is the *tight-binding* representation, which is very useful to describe a wave function at an atomic scale, where it is called Linear Combination of Atomic Orbitals. There, the u_n can be interpreted as the amplitude of an atomic eigenfuntion at atom nth. Reciprocally, the continuous SE can be seen as an long wavelength approximation of a discrete equation. In this regime we used to interpret the electron density waves in the quantum corral.

1.4 Quantum Dynamics in Spin Systems

In quantum mechanics there appears a new variable: the spin. For nuclei of some elements this is a binary property assimilable to magnetic moments oriented along ($\uparrow$) or against ($\downarrow$) a given direction. Since these moments interact among them, e.g through dipole-dipole interaction, they have a dynamics which is also described by the SE. For example, the interaction J is responsible for the exchange between $\uparrow_A\downarrow_B$ and $\downarrow_A\uparrow_B$which is quite analogous to a single particle tunneling among two potential wells (see Fig. 1.3). Starting from one initial state, they would exchange as an periodic function of time yielding the Rabi oscillations with frequency $\omega_0 = 2\pi J/\hbar$. These are

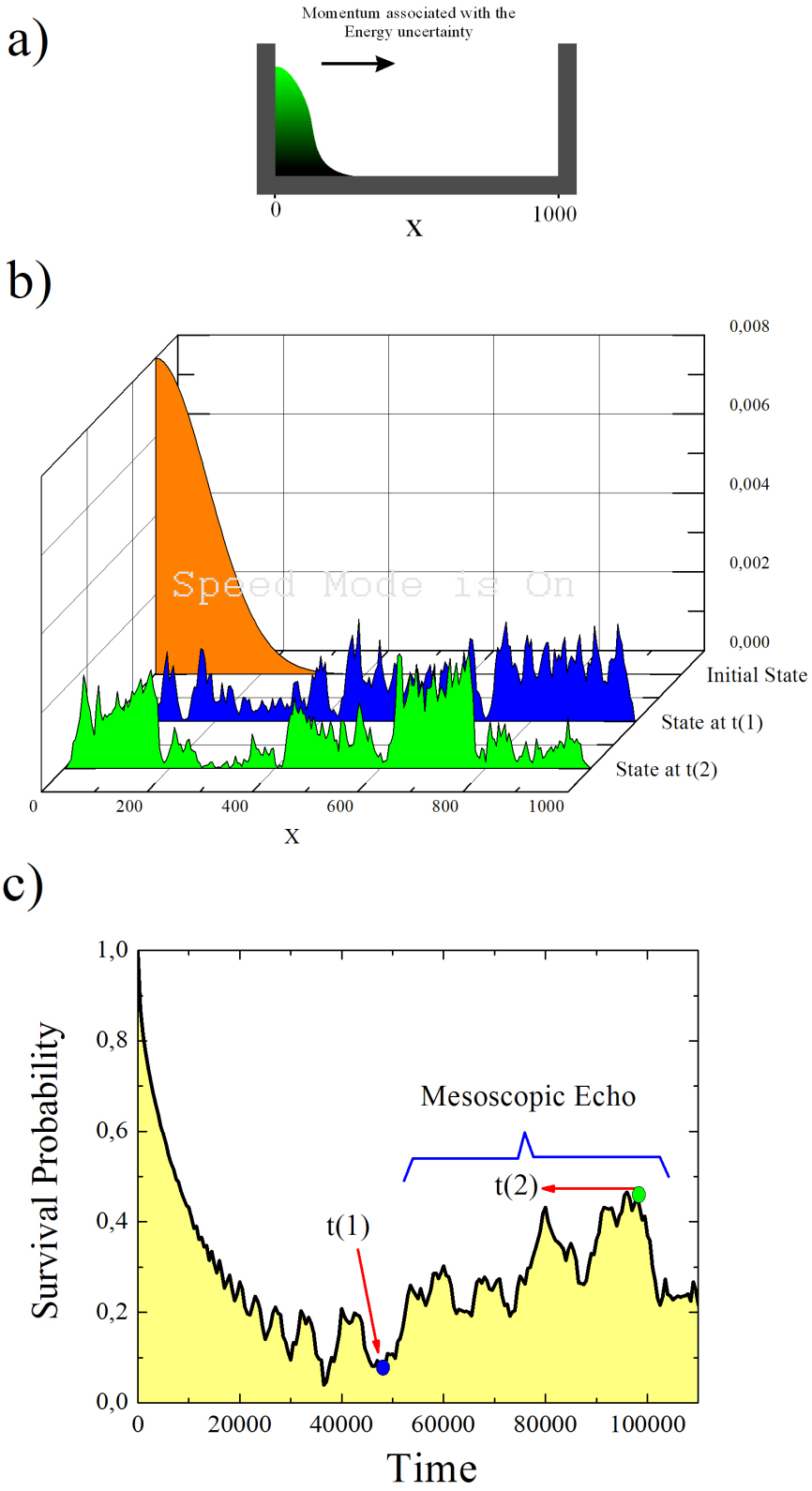

Figure 1.2: Evolution of a wave packet in a $1D$ box. The behavior shows how the superposition of waves moves through the box and is reflected in the edges.

the simplest form of the mesoscopic echo discussed above. Notice that exchange or flip-flop interaction J plays the same role in delocalizing the spin excitation as the hopping amplitude V does in delocalizing a charge excitation in the tight-binding version of the SE.

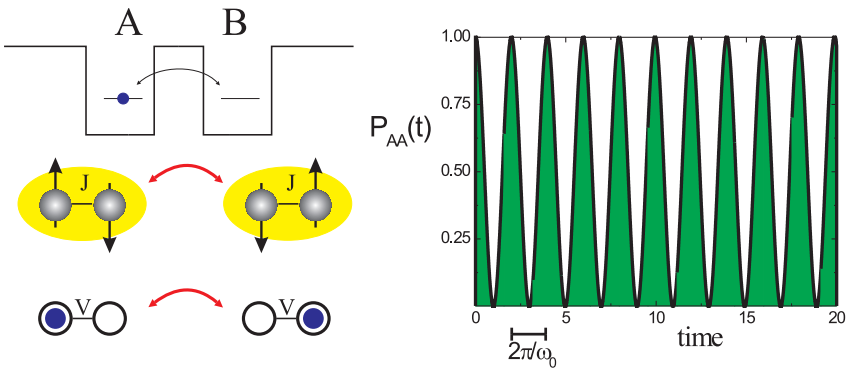

Figure 1.3: Schematic representation of the Rabi Oscillations between the state $A = |\uparrow,\downarrow\rangle$ and $B = |\downarrow,\uparrow\rangle$. These states could represent a pair of spins with opposite orientation, or a double wells potential where a particle is putted in one of the sites. The left panel shows the probability of measuring the A states being that it was in the same site at $t = 0$.

With the advance of Nuclear Magnetic Resonance (NMR) is became possible to create, manipulate and observe the polarization generated in an ensemble of interacting nuclear spins. Today, the manipulation of spins of atoms in different chemical configurations, can also be made with a combination of specific radio frequency pulses (see representation on Fig. 1.4).

For many years it was a discussion if NMR techniques could be used to measure the wave behavior of the spin. In 1997, following a suggestion by Pastawski and Levstein, the group of Ernst [Mádi *et al.*, 1997] was able to observe this behavior by making NMR experiments on lysine molecules (see Fig. 1.5). There, the propagation of a local excitation behaves as a particle in a box discussed above. Evidently, the reflection is still not perfect and we should help to understand and control the mechanisms responsible from this imperfection.

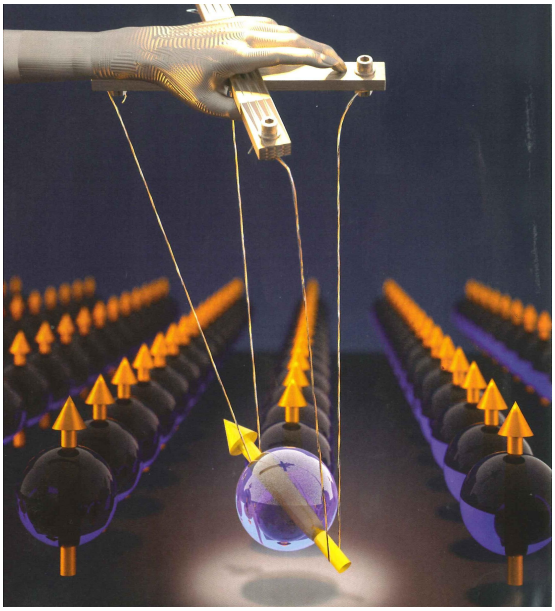

Figure 1.4: Artist representation of the quantum state controllability of single electron spins. Figure Extracted From: http://tnw.tudelft.nl/

1.5 Environment and Decoherence

The progressive development of technology capable of creating ad-hoc states and the design of specific Hamiltonians in different fields (NMR, cold atoms, superconducting circuits, quantum dots, etc.) opened the expectation to manipulate quantum systems at will. The expectation is that it would allow to exploit the potential of superposition states to generate a form of "parallel processing". In this sense, the recent implementation of devices performing quantum logical gates represents one of the main subjects of investigation in the last years in the field now defined as Quantum Information [DiVincenzo, 1995]. In this context, one is compelled to handle questions that were overlooked in **textbooks**. For example: *What are the requirements for an efficient quantum manipulation?* Its response is not generally obvious. First, we need to have the full knowledge about the object we want to control. At this point it is necessary to make our first definition: *the system*. For us, it is an idealized representation of the portion of the natural world that we are able to manipulate in an experiment. Indeed, the first step to perform a theoretical analysis is to suppose that the system is isolated. Then their solutions will allow to get the behavior of the free evolution. This method

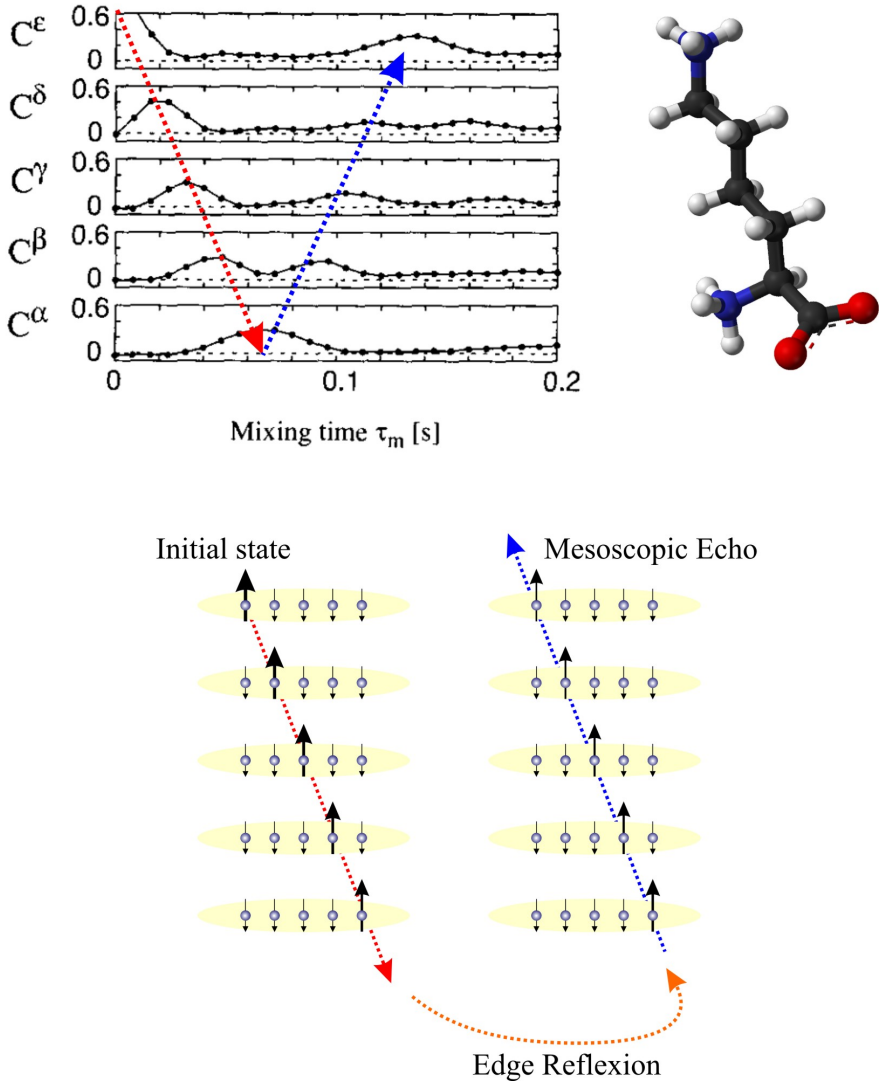

Figure 1.5: Experiment on lysine made by the group of Ernst [Mádi *et al.*, 1997]. The spin polarization behaves as wave which jumps between the Carbon sites. In the lower part it is represented the behavior of the polarization as a function of time.

is like the "*frictionless spherical horse*" solution of the system [Gamow, 1971]. In this sense, the controllability is implicit. However, there are always the uncontrolled interactions within the system and in the surrounding world, all of which we denote as: *the environment*. The environments represent one of the biggest limitation for the theoretician and certainly for the experimentalist, because it can not be solved or controlled. The environmental effects can be reduced, but never eliminated. Then, all the efforts are aimed at avoiding or compensating the effects of the environment. In this sense, the reduction of the interaction between the system and the environment represents a main goal in quantum information.

The first step is to think that the environment behaves perturbatively as a "*reservoir*" (a bath with an infinite number of degree of freedom), where it smoothly modify the dynamics of the system and damping out the interference effects (see Fig. 1.6). This is the situation is observed in the Ernst experiment shown in Fig. 1.5, where the uncontrolled interaction and degrees of freedom produce the attenuation of the expected mesoscopic echoes beyond the ideal spin wave description, i.e. our spherical horse solution. The environment subtracts probability to the idealized "spin wave" solution which is complemented with a probability representing a featureless background. In other words, the environment does not seem to maintain any memory from its previous state. We may attempt to describe this attenuation of the expected interferences as *environmentally induced "decoherence"*.

The "spherical horse" description for an environment is describing it through the Fermi Golden Rule (FGR) [Facchi & Pascazio, 1999]. The FGR allows to evaluate the transition rate, $1/\tau$, from a system eigenstate into the environment. The simplest form of this approach results as a second order approximation in a perturbation theory in presence of a continuum spectrum which appears as consequence of the thermodynamic limit. This limit considers that the number of degrees of freedom of the environment is infinite before any dynamics is evaluated. If we weakly connect our two spin system to an infinite spin chain, the spin excitation is seen to decay as shown in Fig 1.6.

The decay rate can also be evaluated from the imaginary part, $\Gamma = \hbar/2\tau$, of the response function of open systems, i.e. a problem in which the infinite chain constituting the environment is implicitly represented by open boundary conditions on the system. In thermodynamics this concept is equivalent to require that the environment behaves as a reservoir which is maintained at a constant temperature. In other words, every

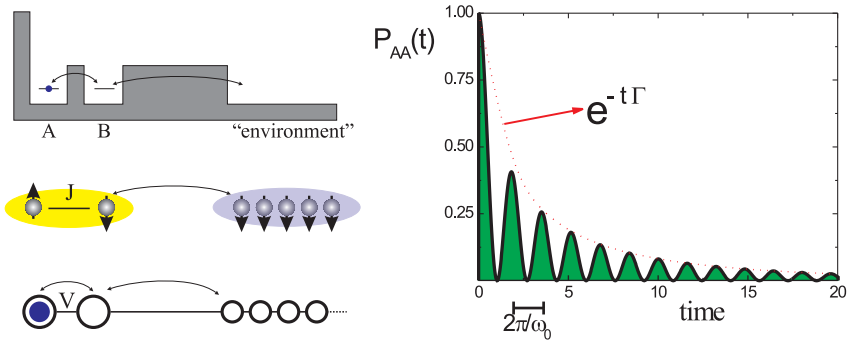

Figure 1.6: Equivalent plot to that presented in Fig. 1.3, but in this case we have considered an infinite environment.

amount of energy that enters in the reservoir is fastly dispersed away, so the local temperature does not change at all.

1.6 Leaving the Spherical Horse Aside: The Many-body Problem

In this work we decided to move away from the "spherical horse" descriptions introduced above. The strategy is to consider small systems where the analytical solution is feasible and jointly with the numerical simulations we could extract the physical properties. In our models we will try to keep our descriptions realistic enough to be close to the experimental situations. However, the experimental system have a many-body nature. This property complicate every theoretical approach. Despite of this, there are specific types of many-body dynamics that could be treated in terms of a number of independent one-body like problems which are easy to solve. An important example of this, is the dynamics of the polarization excess in a $1D$ spin system with flip-flop (or XY) interactions. Then, with the use of Wigner-Jordan transformations [Lieb *et al.*, 1961], the spins chain can be mapped into non-interacting electrons propagating in a $1D$ tight-binding chain evolution of this polarization. In that case the polarization dynamics is the same as the dynamics of the single particle density in the linear chain. This type of mapping is of particular interest for us, because it allows the comparison between particle evolutions in tight-binding system with the polarization evolution in spin arrays.

As mention before it could be our "*spherical horse*" solution for the $1D$ spin arrays. This allows us to start increasing the complexity of the problem by adding other types of interactions (for example the Ising coupling) or changing the topology of the arrays by including for example a lateral chain.

1.7 Non Trivial Role of the Environment

1.7.1 Decoherence and the Loschmidt Echo

The most important issue that affects the dynamics of the system, is the environmentally induced decoherence. One form of measuring these effects, is by evaluating the attenuation of the mesoscopic echoes. If we were able to vary the coupling value between the system and the "environment" in the Ernst experiment (see Fig. 1.5), we might be able to observe and quantify the attenuation of the mesoscopic echoes [Álvarez *et al.*, 2010a]. Another form to evaluate the decoherence experimentally is by the use of a time reversal of the evolution, produced by the effective Hamiltonian H_1 for period t_1, of an initially localized polarization excitation. The procedure, called Loschmidt Echo (LE), consist in the sign inversion of the system's effective Hamiltonian for a period t_2 (i.e. $H_2 \simeq -H_1$). Since in an ideally isolated system, the change in the sign is equivalent to the reversion of arrow of time (see Eq. 1.1). Thus, the "backwards" evolution proceeds for a time t_2 and at $\mathrm{t}_2 = t_1$ a revival or Loschmidt echo occurs. The Loschmidt echo quantifies the reversibility of the system and consequently the coherence loss of the system.

In the terms used above, the initial local polarization amplitude can be identified with the wave packet $\psi(x,0)$, and the observed local polarization (see Fig. 1.7) is essentially:

$$M(t_2,t_1) = \left| \int \psi^*(x,0) e^{\mathrm{i}\hat{H}_2 t_2/\hbar} e^{-\mathrm{i}\hat{H}_1 t_1/\hbar} \psi(x,0) \mathrm{d}x \right|^2 \leq 1.$$

When reversion is perfect the echo reach its maximum value at $t_2 = t_1 \equiv t$. The imperfect reversal $M(t) < 1$ can arrise either from limitation to precisely invert the system's Hamiltonian or from the fact that there is a uncontrolled environment. In both cases,

$$\hat{\Sigma} = \hat{H}_2 - \hat{H}_1,$$

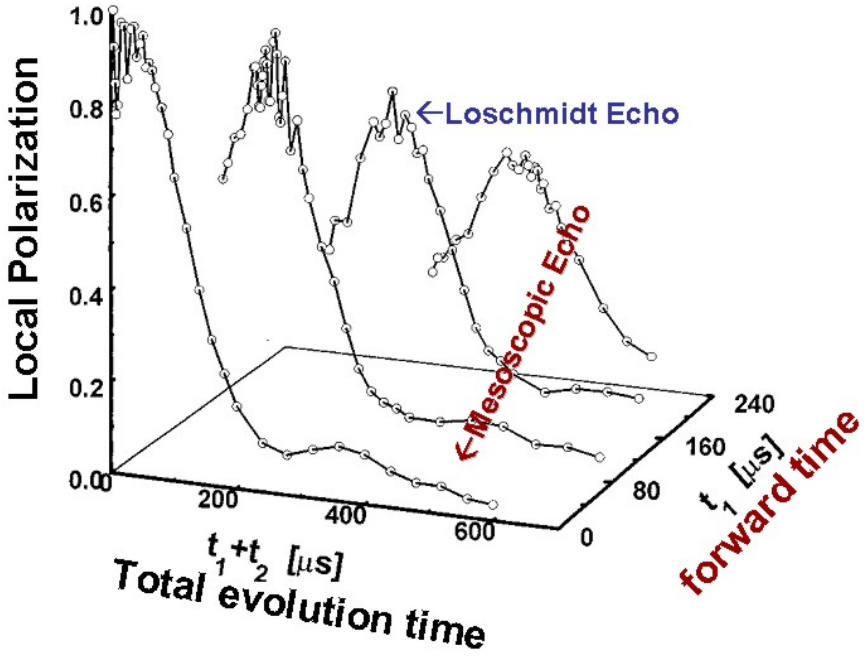

Figure 1.7: Local polarization measurements in NMR. Ferrocene experimental data as function of $t_1 + t_2$. In each curve represent different t_1 revertion times. The maximun of local polarization it is observed when $t_2 = t_1$.

by introducing fluctuations in the quantum phase can be seen as a decoherent process. Thus, the LE constitutes a natural quantifier for decoherent processes.

The biggest experimental puzzle left by the experiments is that even in cases where the effective Hamiltonian is extremely well controlled, $M(t)$ decay quite rapidly and it does in a timescale which is an intrinsic characteristic of the inverted Hamiltonian and does not depend on the (weak) interaction with the environment. This is what has been called *intrinsic decoherence or perturbation independent decay.*

The experimentalist suggest the this is a manifestation of a sort of intrinsic instability of the many body systems. Thus it is an objective of this work to present the first steps to account for decoherence as one moves continuously from one body dynamics to actual many-body systems.

1.7.2 Quantum Dynamical Phase transition and Synchronization

In the previous paragraphs (see Sec. 1.5) we discussed how the environment could be treated as a reservoir, and that it smoothly modifies the dynamics of the system. There are cases where the environment is still considered in the Markovian approximation, but where their interaction produces drastic changes in the dynamical behavior of the system. Our group was able to report on of such *Quantum Dynamical Phase Transition* (QDPT), in this case, this is observed in the Swapping dynamics between spins of ^{13}C and ^{1}H (see Fig. 1.8). This transition appears when the interaction time scale between the system and the environment is of the order of the internal coupling J_s. As we will show in the next chapter, the simple Markovian environments could produce non-analytic changes (non-perturbatives) in the dynamics of Rabi oscillators. Even more, this non-analytic behavior could only be reached if the environmental spins are considered in the thermodynamic limit, otherwise the non-analytic discontinuity that identifies the phase transition does not occurs [Sachdev, 2011].

The first report of a phase transition in the a systems dynamics is connected to classical mechanics. C. Huygens in the XVII century, by observing the motion of two pendulum clocks (which could have different natural oscillation frequencies), realized that they become synchronized if they are imbedded in the same wooden beam [Huygens, 1673]. In this case the wood beam acted as an infinite reservoir that is capable of steal energy from one of the oscillations modes. Thus, the other mode is the

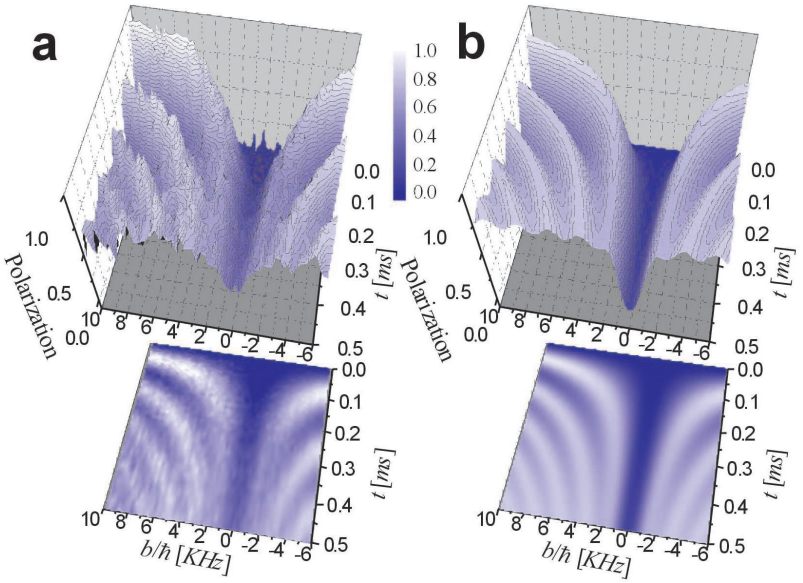

Figure 1.8: Swapping dynamics between ^{13}C and ^{1}H. a) Experimental ^{13}C polarization in $Fe(C_5H_5)_2$ as a function of the contact time t and spin-spin coupling b. b) Numerical simulations of the ^{13}C polarization. Projection plots in the b-t plane show a canyon where the oscillation period diverges indicating a quantum dynamical phase transition. Figure extracted from Ref. [Álvarez *et al.*, 2006].

surviving and defines the phase of synchronization. Depending on the value of the difference between both natural frequencies, the oscillations could become synchronized or not.

Another interesting case in the classical mechanics is the *Coupled Motion of Piano Strings [Weinreich, 1979].* In this case with the use of some approximations it is possible to analytically describe the synchronization induced by the wood bridge which couples the piano strings. Here the wood bridge also plays the role of the environment in the quantum systems as it is capable of absorbs energy mainly from oscillation modes corresponding to the symmetrically coupled strings while it lets the antisymmetric oscillation mode to survive. In Fig. 1.9 it is plotted the "complex frequencies" solutions of a pair of strings. There, the real part corresponds to the "observable frequency" and the imaginary part is associated with the decay rate of each mode of oscillation. In this simplest case, it is observed that one of the those solutions have bigger decay rate than the other. Thus if we analyze the evolution of each piano string for long times, we see that they become synchronized with a fixed relative phase defined by the mode which has the lower decay rate. The transition between the synchronized and the non-synchronized dynamics is then defined by a non-analytical critical point in the real frequencies. There, as we observe in Fig. 1.9, the synchronization only occurs if the mistuning between the strings is sufficiently small. It is important to remark that the presence of the infinite number of degrees of freedom in the environment is responsible for the non-analytical behavior of the solutions. For example, if the environment is finite, the solutions becomes reals and the collapse of frequencies is avoided (see the outer curves in the upper part of Fig. 1.9)

This last example has a direct connection with the propagation of plasmonic excitation in metallic nanoparticles, where each particle sustains an specific plasmonic oscillation which is coupled with that of its neighboring particles. The fast damping of these modes will require an energy restoration processes in analogy to the mainspring in the Huygens' clocks. Although these examples are drawn from the realm of classical mechanics, we will observe that the phase transition in the quantum dynamics of Fig. 1.8 is equivalent to that presented here. It is induced by the "infinite" environment which selectively steal energy from some of the oscillation modes.

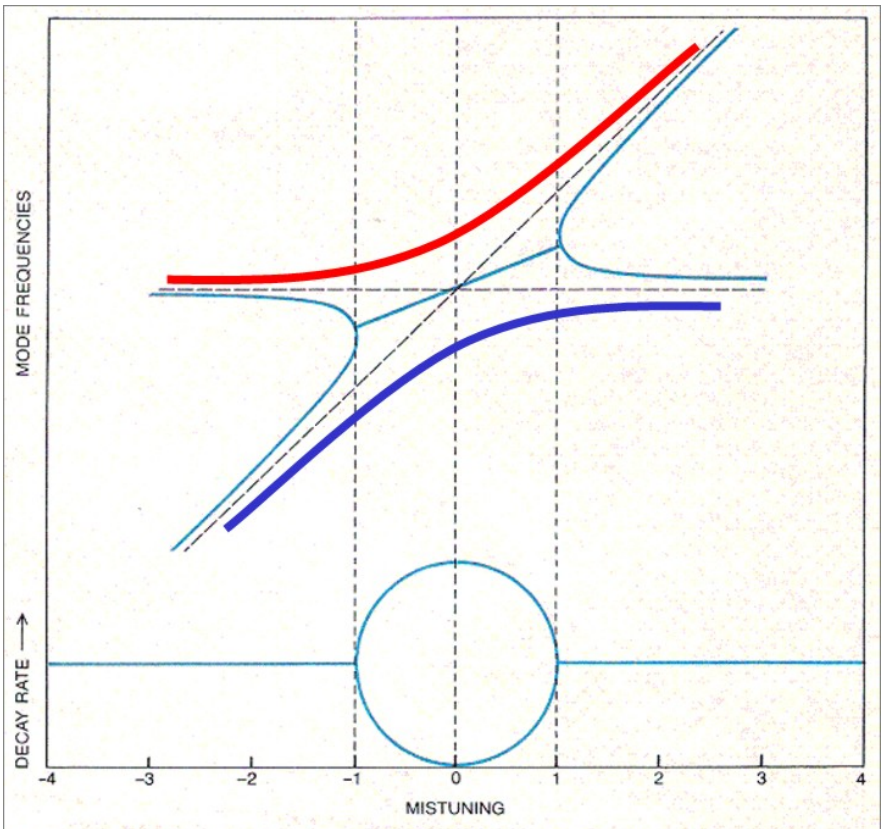

FREQUENCIES OF A PAIR OF STRINGS lock together when the motions of the strings are coupled through a purely resistive support. The mistuning, or difference between the uncoupled frequencies, is given in "natural units," which are related to the single-string damping rate. For a typical pair of strings in the middle of the keyboard, one natural unit is about a third of a vibration per second. The broken lines in the top graph indicate the frequencies in the absence of coupling. The point where the broken lines cross each other is where the two strings have exactly the same frequency. In a piano the presence of a purely resistive support causes frequencies with a mistuning of either $+1$ or -1 natural unit to come together and lock at a common frequency. For smaller mistunings the frequencies stay locked but the decay rate, which equals the single-string rate for larger mistunings, splits for the two strings (*bottom*).

Figure 1.9: Figure with the caption extracted from Ref. [Weinreich, 1979]. We added two new curves over the real part of the frequencies that represent a typical avoided crossing of the solutions.

1.7.3 Non Markovian Effects

If we now move away from the usual Markovian approximations we will find new types of behavior. All this dynamical effects are denoted as *Non-Markovian Dynamical evolutions*. In Fig. 1.10 we show a simple example of these effects. The first difference that we observe from the previous cases, is the appearance of deep and sudden depletion in the survival probability: the survival collapse. It appear when the return probability amplitude interferes destructively with survival amplitude. This is followed for a diffusive regime. Here, the decay is governed by a power law where the exponent depends on the spectral structure of the environment. This diffusive regime is observed if the environment is "slow", i.e. the structure of the environment is not capable of spread energy as rapidly as it steals it from the system.

The survival collapse and diffusive evolution may appear as if the environment is finite or infinite. If the system is finite, we also expect the formation of mesoscopic echoes where probability returns after a reflection in edges of the environment (see Fig. 1.10-b).

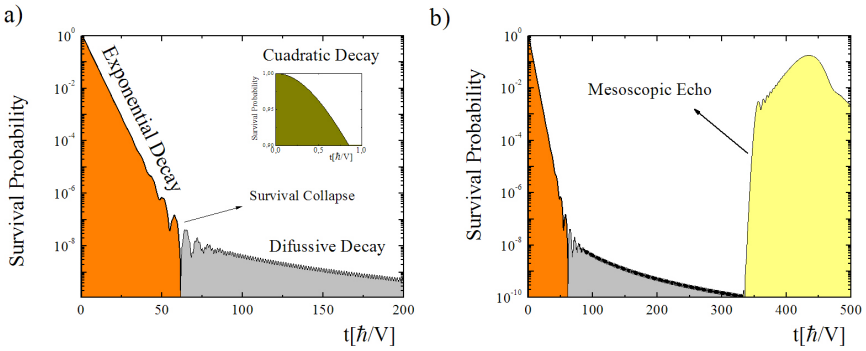

Figure 1.10: Non-Markovian effects in linear tight binding systems. The survival probability for a model of one site couple to a semi-infinite chain, as a function of time. a) The cuadratic, exponendial and the difussive decay. b) The Mesoscopic Echo appear for longer times if the environment is finite. For more details see Ref. [Rufeil-Fiori & Pastawski, 2006].

1.8 Organization of this Thesis

Along this work we explored several model Hamiltonians in which we incorporate specific structures in the environment that allow to analyze the Non-Markovian effects on

the system dynamics. We will show that the "environment" (in its more general form) is capable of produce phase transitions in the quantum dynamics, molecular dissociations, plasmonic synchronization, and corrections to the usual forms of evaluate decoherence. The combination of analytical tools with the numerical solutions, will allow us to make deep analysis of each problem and obtain numerous physical interpretations.

The first chapter (Chap. 2) introduces the *"leitmotiv"* of this work. There, we present the simplest form of a Rabi oscillator and couple it to a structured environment. We start analyzing the Rabi oscillations in spin systems, but then we quickly move to the one-body dynamics in tight binding systems. In this scenario we study the evolution of a single particle jumping among two potential wells where the variation of the tunneling amplitude and the coupling with the a specifically structured environment, leads to several phase transitions in the quantum dynamical behavior.

In this context we will show the collapse of eigen-frequencies in the complex plane assimilable to the *exchange narrowing* introduced by P.W. Anderson [Anderson, 1954] as well as a appreciable dynamical effects resulting from the appearance of "*Virtual States*", which corresponds to the unphysical pole of the response function. We will analyze how their properties differ from those of the typical resonant or localized states. From the models presented in Chap. 2 we will observe that the evolution of the survival probability can be separated in three kind of decays: quadratic, exponential (as the envelope of the internal dynamics) and polynomial (diffusive). They will result equivalent to those presented in Fig. 1.10. The quadratic decay, which appears in shorter times, is related to the weak interaction limit, where the environment is weakly coupled to system. The next time scale, is defined by the exponential decay of the dynamics. The decay rates of this exponential behavior can be evaluated from the Fermi Golden Rule (FGR) if the environment is considered in the Wide Band Approximation (WBA).

In this first chapter we also include most of the analytical and numerical tools that we will use in nexts chapters. In particular, the analysis of the Green function poles represent one of the central strategies used along this work. Their relation with the Local Density of States (LDoS) and the dynamics, this last evaluated from diagonalization procedures and Trotter-Suzuki algorithms, let us make a complete study of each one of the considered systems.

The understanding of the physical properties involved on the quantum dynamical phase transitions (i.e. phase transition in the quantum dynamics) gave us the tools

to analyze other related problems like the *molecular dissociation in catalytic reactions* in Chap. 3 and *plasmonic synchronization in nanoparticle arrays* in Chap. 4. In the first case the analytical properties of the Green function theory and its relation with the Local Density of States (LDoS) are used to explain the Molecular Bond Breaking observed in catalytic processes. There, we will show that the abrupt molecular dissociation, which occurs in the proximity of a transition metal, is generated by the presence of phase transitions in the quantum dynamics previously analyzed in Chap. 2.

In the other case, with the knowledge of the QDPT and the dynamical behavior of the Rabi oscillations in presence of a common environment, we will analyze how the surface plasmons in nano-parcicle arrays could become synchronized. We will apply the Green function formalism to shed light about the dynamical behavior of the plasmonic systems. The use of several types of dynamical simulations allows us to confirm our results and conserve realistic parameters for the nano particle arrays. Additionally the study of these plasmonic systems helped us to increase our experience on how the systems behaves in the presence of different types of environments.

In the second half of this thesis (Chapters 5, 6 and 7) we will focus on the analysis of the quantum coherence degradation in presence of several types of $\mathcal{S}$-$\mathcal{E}$ interactions. In these chapters we will use the "Loschmidt Echo" as a decoherence quantifier to measure the degradation of the interferences produced by the coupling with different environments. In Chap. 5 we used a one-body version of the LE to evaluate the decoherence in one-body like spin systems. There, we also use the Green's Function formalism to compare the decoherence rate with its usual evaluation from the Fermi golden rule.

In chapters 6 and 7 we add another ingredient to the interaction between the system and the environment: the Ising Coupling. The consideration of this coupling converts the one-body solvable problem into a complex problem with not analytical solutions. The numerical simulation of the spin dynamics, was our first approach to the problem. We begin by considering a spin ladder in which we take one of the chains as the *system* and the other as the *environment*. From those simulations we will be able to compare results with previous measurements of the decoherence rate by the evaluation of the Mesoscopic echoes attenuation (see Chap. 6).

In Chap. 7 we will analyze the dynamical effects of including environments with small number of spins. In that cases we will study how the decoherence rates depart

from the WBA approximation in the presence of small environments. With the use the Keldysh formalism we will be able to interpret each of the decoherence rates and connect them with the cases analyzed in the previous chapters.

The organization of the thesis is presented in Fig. 1.11.

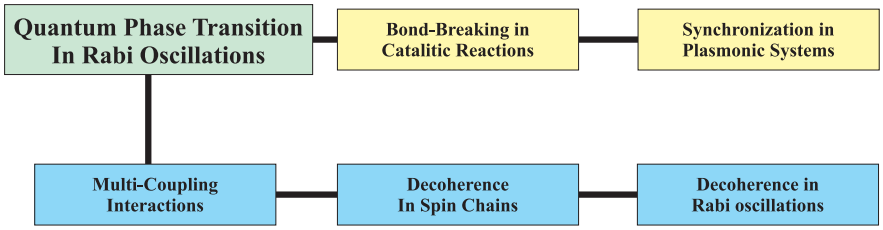

Figure 1.11: Diagram of the chapters.

Chapter 2

Phase Transitions in the Quantum Dynamics

2.1 Introduction

It is well known that processing information using quantum mechanics makes possible communication procedures and computational tasks that could outperform classical devices in terms of security or speed [Bennett & DiVincenzo, 2000]. There are extensive experimental efforts to realize implementations of the necessary building blocks for Quantum Information Processing (QIP).

The Swap gate is one important building block in QIP, where a "particle" jumps between two degenerated states, A and B, when a the coupling V_{AB} between them is turned on. In cases where a initial state is put in A, then the return probability oscillates with the Rabi frequency given by the inter coupling: $\omega_0 = 2V_{AB}/\hbar$.

As we mentioned in the introduction, the isolation of any real system can not be made completely reached. In the practice, the interactions with an environment [Zurek, 2003, Zurek *et al.*, 2007, Myatt *et al.*, 2000] perturb the evolution, smoothly degrading the quantum interferences and producing a "decoherence" rate $1/\tau_\phi$. This rate is usually identified with the system-environment (SE) interaction rate $1/\tau_{\mathrm{SE}}$, typically evaluated from the Fermi Golden Rule (FGR).

In spin systems, it is possible to represent A and B with the $\uparrow\downarrow$ and $\downarrow\uparrow$ spin configurations respectively. In this kind of system it is expected that for weak interactions ($1/\tau_{\mathrm{SE}} \ll 2\omega_0$), the environment produce a slightly degradation of the oscillation,

which decays at the rate $1/\tau_\phi = 1/(2\tau_{\rm SE})$. There are experimental conditions, however, where the observed frequency shows a dynamical transition on its dependence of the SE interaction [Álvarez *et al.*, 2006]. In fact, the swapping frequency results to be a *non-analytic* function of the interaction rate. At a critical strength $1/\tau^c_{\rm SE} = 2\omega_0$, the oscillation freezes indicating a *transition* to a new *dynamical regime*. The initial state now decays to equilibrium at a slower rate $1/\tau_\phi \propto \omega_0^2\ \tau_{\rm SE}$, which vanishes for strong SE interactions.

This last regime can also be seen as a Quantum Zeno regime, where the internal dynamics is inhibited by the frequent "observations" [Misra & Sudarshan, 1977] of the environment. Such quantum freeze can arise as a pure dynamical process, governed by strictly unitary evolutions (see Ref. [Pascazio & Namiki, 1994], [Pastawski & Usaj, 1998]). Indeed, some of the phenomenology of that transition was not foreign to spectroscopists. The collapse of the independent resonance lines leads to the exchange and motional narrowing addressed by Van Vleck [Van Vleck, 1948] and Bloembergen, Purcell and Pound [Bloembergen *et al.*, 1948] in the 40's and synthesized in the analytic properties of a phenomenological classical probabilistic model, by P. W. Anderson [Anderson, 1954].

The quantum description of the phase transition [Álvarez *et al.*, 2006] required a self-consistent calculation of the oscillation in presence of the SE interaction. There, the environment was described in the "fast fluctuations"approximation where it has no memory of its previous state [Álvarez *et al.*, 2007].

In this chapter we present a simple and exactly solvable quantum model that presents the dynamical transitions. Although we describe the coherent part of a spin SWAP dynamics [Danieli *et al.*, 2005], we will show that essence of the dynamics is maintained when the incoherent part is taken into account.

A complementary vision for the dynamics under the action of a given Hamiltonian is, of course, the spectral representation which can be studied as function of the SE interaction strength. However, the energy representation hides much useful dynamical information in subtle spectral properties, such us resonances that collapse at the "Exceptional Points" (EP) [Müller *et al.*, 1995, Rotter, 2009, Rotter, 2010] in the complex plane. Other unusual properties involve resonances that shrink and jump into the non-physical Riemann sheet to become virtual states. Ultimately, these resonances can transform themselves into isolated singularities on the real axis, accounting for localized states.

In our model all of these transitions appear naturally through the variation of a *single* control parameter. There are a number of physical systems that show some of these delicate spectral properties: The EP or collapse of resonances has been observed in crystals of light [Oberthaler *et al.*, 1996], electronic circuits [Stehmann *et al.*, 2004], propagation of light in dissipative media [Shuvalov & Scott, 2000, Berry & Dennis, 2003], vacuum Rabi splitting in semiconductors cavities [Khitrova *et al.*, 2006], in microwave billiards [Dembowski *et al.*, 2001], [Dembowski *et al.*, 2004], [Dembowski *et al.*, 2003], [Dietz *et al.*, 2007], and there are a number of examples drawn from electron-paramagnetic resonance [Napolitano *et al.*, 2008, Costa-Filho *et al.*, 1999, Calvo, 2007], and solid state NMR [Álvarez *et al.*, 2006]. It also appears in many theoretical models: e.g., describing the decay of superdeformed nuclei [Stafford & Barrett, 1999], phase transitions and avoided level crossings [Heiss & Sannino, 1991, Keck *et al.*, 2003, Heiss, 2000], geomagnetic polarity reversal [Stefani & Gerbeth, 2005], tunneling between quantum dots [Cardamone *et al.*, 2002, Danieli *et al.*, 2007], optical microcavity [Longhi, 2006a], vibrational surface modes [Calvo & Pastawski, 2006], and in the context of the crossing of two Coulomb blockade resonances [Weidenmüller, 2003]. On the other hand, the Virtual-Localized transition has been addressed in the context of the $n-p$ singlet system [Taylor, 2006], models of stabilization of quantum mechanical binding by potential barriers [Hogreve, 1995], Feshbach resonances [Marcelis *et al.*, 2004, Pupasov *et al.*, 2008], stability of atomic and molecular states [Serra *et al.*, 2001, Yamashita *et al.*, 2002] and also in virtual bound states in photonic crystals [Inoue & Ohtaka, 2004].

In section 2.3 the model is presented and with the use of the Green's function formalism [Pastawski & Medina, 2001], the solution is obtained in section 2.4. In section 2.5 we analize the parametric regions and associate them with the analytic properties of the local density of states and the different dynamical regimens:

- Region I) **collapsed resonances** $\mapsto$ *Overdamped*
- Region II) **resolved resonances** $\mapsto$ *damped oscillations*
- Region III) **out of band resonances** $\mapsto$ *environment controlled quantum diffusion*
- Region IV) **virtual states** $\mapsto$ *anomalous diffusion*
- Region V) **pure point spectrum** $\mapsto$ *localized dynamics.*

2.2 The Spin-Fermion Mapping

In this section we will introduce the spin-fermion mapping which let us solve analytically the spin polarization dynamics (details can be found in Appendix A). This map, also called as the Jordan-Wigner transformation (JWT) [Lieb *et al.*, 1961], has been extensively addressed in the literature [Mádi *et al.*, 1997, Pastawski *et al.*, 1995, Danieli *et al.*, 2004, Danieli *et al.*, 2005, Álvarez *et al.*, 2007, Álvarez *et al.*, 2010a] in the context of dynamical properties of spin systems. This JWT establish that the relation between spin and fermions operators at a given site n is given by:

$$\hat{S}_n^+ = \hat{c}_n^\dagger \exp\left\{ \mathrm{i}\pi \sum_{m=1}^{n-1} \hat{c}_m^\dagger \hat{c}_m \right\}, \tag{2.1}$$

where $\hat{c}_n^\dagger$ and $\hat{c}_n$ are the common creation and annihilation fermionic operators, and $\hat{S}_n^\pm$ the spin rising and lowering operators.

With the purpose of applied this transformation to our model, let us first define an arbitrary linear model. Then, the spin system is ruled by,

$$\hat{H}_{spin} = \sum_{n=1}^{\infty} J_n (\hat{S}_{n+1}^x \hat{S}_n^x + \hat{S}_{n+1}^y \hat{S}_n^y), \tag{2.2}$$

$$\hat{H}_{spin} = \sum_{n=1}^{\infty} \frac{J_n}{2} (\hat{S}_{n+1}^+ \hat{S}_n^- + \hat{S}_{n+1}^- \hat{S}_n^+), \tag{2.3}$$

$$\tag{2.4}$$

This system represents a linear spin chain couple through XY interactions. Then, if we applied the JWT, we obtain:

$$\hat{H}_{spin} \longrightarrow \hat{H}_{fermionic} = \sum_{n=1}^{\infty} V_n (\hat{c}_n^\dagger \hat{c}_{n+1} + \hat{c}_{n+1}^\dagger \hat{c}_n). \tag{2.5}$$

where $V_n = J_n/2$ is related to the Rabi frequency $\omega_0 = 2V_n/\hbar$ between the sites n and $n+1$. Eventually, one can include appropriate energies E_n for the local states n, but it is not relevant for the present analysis.

It is important to note that in this model we let outside the Ising interactions. This kind of interactions, jointly with the interactions beyond the $1D$ systems, give rise to

many-body interactions in the fermionic picture. In our first approach we neglect this kind of interactions, but we will discuss about them in the Chapters 6 and 7.

In summary, we are now interested in an electron jumping between tight binding sites arranged as a linear chain. The specific selection of the V_n couplings will give us the opportunity of study different dynamical properties.

2.3 The Model

Our first model is the two-spin system couple to an semi-infinite linear chain of spins. As we mention before, we can map this problem into a tight-binding scheme, and obtain what we observe in Fig. 2.1. Then, the Hamiltonian for this problem can be arranged in three parts: The system, the environment and the interaction between them,

$$H = H_S + H_E + V_{SE}, \tag{2.6}$$

where,

$$H_S = -V_{AB} \left(|A\rangle \langle B| + |B\rangle \langle A| \right) \tag{2.7}$$

$$H_E = -V \sum_{n=1}^{\infty} \left(|n\rangle \langle n+1| + |n+1\rangle \langle n| \right) \tag{2.8}$$

$$V_{SE} = -V_0 \left(|B\rangle \langle 1| + |1\rangle \langle B| \right), \tag{2.9}$$

and $|n\rangle$, with $n \geq 1$, is the state localized at the n-th site of the chain. V_{AB}, V_0 and V are the positive hopping amplitudes between two contiguous sites. The first two sites, linked by V_{AB}, are what we denote as *the System*. The rest of the chain is what we take as *the environment*.

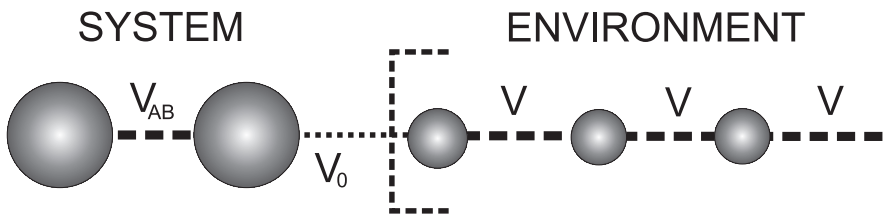

Figure 2.1: Representation of the system and the environment. The first two sites are connected through V_{AB}, while in the environment the hopping is V. The interaction between the system and the environment will be defined by the parameter V_0.

At this point it is necessary to remark that the local excitations in spin chains with XY interaction can be transformed into single fermions moving in a tight binding chain (in the high temperature limit) [Mádi *et al.*, 1997]. Thus, if put a local polarization in a spin system in the high temperature limit, and then we map it, we will see that the evolutions is dominated by the coherent term, i.e. the evolution of only one particle in the tight binding systems. The rest of the particles (or the up spins) will contribute to the incoherent contribution.

Let us show how the presence of these incoherent contributions do not change the essential behavior that we want to present. To do this, we will compare the dynamics of the coherent and incoherent part for one specific case. In Fig. 2.2 we show the dynamical behavior for an spin system and its mapped fermionic system. Later on we will enter in the details on how we evaluate those dynamics, but for the moment, we want to focus on their physical solutions.

In the spin case, we considered the evolution of the initial state $\uparrow_A\downarrow_B$connected to a "thermal state" for the rest of the spins. This notation represents that the A spin is in the up ($\uparrow$) configuration and B in down ($\downarrow$) state. The "Thermal state" for the next $N = 18$ spin means that all these spins are in the infinite temperature limit, where each one has the same probability of been $\uparrow$ or $\downarrow$.

On the other hand, we have decomposed the fermionic evolution into two contributions: the coherent and the incoherent part. The first one is the survival probability of seen one particle in the site A given that it was there at $t = 0$. However, the incoherent part represents the "Thermal state" contribution, which involves the sum over the dynamics of all the environmental spins which contributes to the A site at time t. The presence of the ensemble, introduces an extra weight of $1/2$ which has to be considered in the sum. This factor appears because the infinite temperature limit makes that each spin has $1/2$ of probability of been in the $\uparrow$ state. This incoherent sum can be summarized as follows:

$$P_{incoh}(t) = \sum_{n=1}^{N} \frac{1}{2} P_{An}(t), \tag{2.10}$$

where $P_{An}(t)$ is the probability of observing a particle in A at time t, given that it was in the site n at $t = 0$.

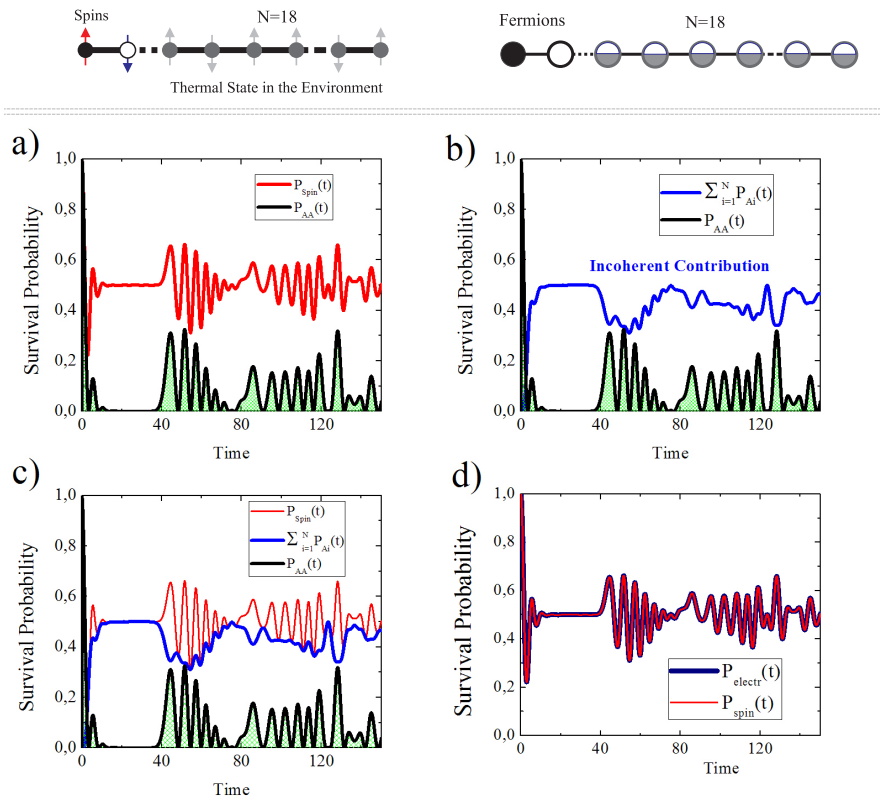

Figure 2.2: Comparison between the Spin and the Fermion evolutions of a $2 + 18$ spin system. a) Survival probability $P_{AA}(t)$ (black) for the fermion system and $P_{spin}(t)$ for spin an system with initial condition $\uparrow_A\downarrow_B \leftrightsquigarrow (ThermalState)$. b) $P_{AA}(t)$ and the incoherent contribution in the fermionic model. c) the superposition of a) and b). d) $P_{spin}(t)$ and the coherent+incoherent part in the fermionic model.

Taking into account these definitions, we can observe from Fig. 2.2-d that the sum of the coherent and incoherent part, evaluated from fermonic evolutions, is just the exact spin dynamics. Additionally from Figs. 2.2-a,b and c, it is possible to infer that the incoherent part only makes that the sum tends to the final state of 1/2, but no modify the structure of the dynamics. In this way, with the analysis of the coherent part we can obtain the main dynamical properties without having to evaluate all the incoherent dynamics.

One last question that may arise in this context is why, if we have put N particles (with half probability), sum is lower than 1 in the site A in the evaluation of $P_{incoh}(t)$? This apparent inconsistency is solved once we think on what happens when we applied an unitary evolution into two orthogonal vectors. In Fig. 2.3 we can observe that the sum of each component of the vectors over each axe is never greater than 1. In our model, the initial condition of one "half" particle on each site defines N orthogonal initial states. Then, the sum of all those initial states over any site will be always lower than 1, because the mesure over each site is equivalent to evalu the contribution over each axes of Fig. 2.3. This fact ensures the conservation of the number of particles over all the system.

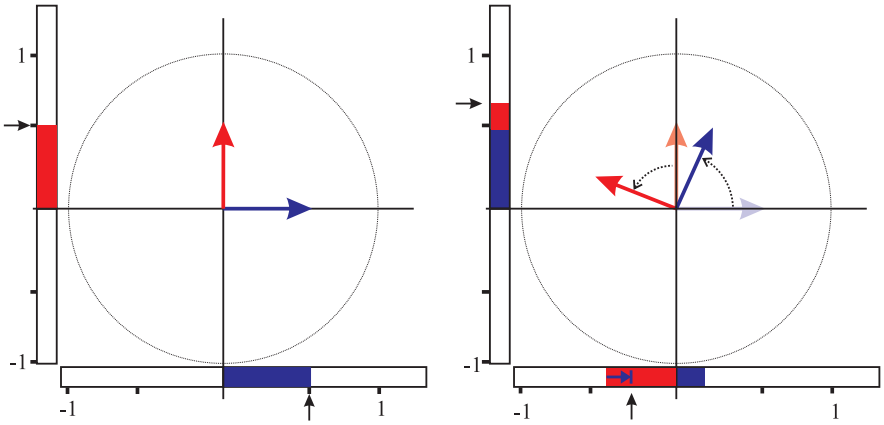

Figure 2.3: Schematic representation of orthogonal vectors under unitary evolutions. Here it is possible to observe that the sum on each component is never greater than 1.

2.4 Analytic Solution.

Let's start solving the Hamiltonian presented in Eq. 2.6. The solutions for this problem and for almost all the cases presented in this thesis will be obtained within the Green's Function (GF) formalism [Economou, 2006]. For the case of an isolated system H_S, we can define the GF matrix as follows, $\mathbb{G}$,

$$\mathbb{G}^{(0)}(\varepsilon) = (\mathbb{H}_S - \varepsilon\mathbb{I})^{-1}. \tag{2.11}$$

From this equation it is shown that the poles of the GF represent the eigen energies of the system. Thus, the search for this poles will give us information about the energy spectrum of the system and also the decay rate in cases where the system have resonances.

In order to make a fully consistent definition of $G_{n,m}(\varepsilon)$ as the Fourier transform of the retarded propagator, $G_{n,m}(t)$, we assume that each site n has an intrinsic decay process $E_n \to E_n - \mathrm{i}\eta_n$. This solves the Gutzwiller objection on this aspect [Giannoni *et al.*, 1991]. However, since these imaginary parts are considered infinitesimal, they are not written explicitly in what follows.

The first diagonal component of $\mathbb{G}(\varepsilon)$ gives us information about the system dynamics. This component becomes,

$$G^{(0)}_{AA}(\varepsilon) = \frac{1}{\varepsilon - \frac{V_{AB}^2}{\varepsilon}}. \tag{2.12}$$

Here, we can see that the poles of $G^{(0)}_{AA}(\varepsilon)$ are $\widetilde{E}_{A,B} = \pm V_{AB}$, just the system energies as we say before. If we consider an isolated system of two sites, and excite the first one; the system evolves oscillating between the states $|10\rangle$ and $|01\rangle$ with a characteristic Rabi frequency $\omega_0 = \frac{2V_{AB}}{\hbar}$. This oscillation is used to generate the SWAP gate by letting the Hamiltonian act during a time $t_{\text{swap}} = \frac{5\pi}{2}\frac{1}{\omega_0}$.

When we take into account the environment, the first diagonal component of the GF becomes,

$$G_{AA}(\varepsilon) = \frac{1}{\varepsilon - \frac{V_{AB}^2}{\varepsilon - \frac{V_0^2}{V^2}\Sigma(\varepsilon)}}. \tag{2.13}$$

Typically the Self Energy $\Sigma \simeq \Delta - \mathrm{i}\Gamma$ is evaluated within a Fermi Golden Rule approximation [Facchi & Pascazio, 1999] as an ε independent complex number. Since

this would imply neglecting all dynamics and memory effects of the environment, such procedure could miss some subtle behaviors [Khalfin, 1958, Fonda *et al.*, 1978, García-Calderón *et al.*, 1995]. Our model enables the evaluation of the exact self-energy of an environment represented by the Semi-Infinite Chain, and hence accounts precisely for these "memory effects". According to the continued fractions solution [Pastawski & Medina, 2001] of the Renormalized Perturbation Expansion [Economou, 2006],

$$\Sigma(\varepsilon) = \cfrac{V^2}{\varepsilon - \cfrac{V^2}{\varepsilon - \cfrac{V^2}{\varepsilon - \ddots}}} \tag{2.14}$$

$$= \frac{V^2}{\varepsilon - \Sigma(\varepsilon)}. \tag{2.15}$$

which sums up to the form:

$$\Sigma(\varepsilon) = \Delta(\varepsilon) - \mathrm{i}\Gamma(\varepsilon), \tag{2.16}$$

with

$$\Delta(\varepsilon) = \begin{cases} \frac{\varepsilon}{2} - \sqrt{\left(\frac{\varepsilon}{2}\right)^2 - V^2} & \varepsilon > 2V \\ \frac{\varepsilon}{2} & |\varepsilon| \leq 2V \\ \frac{\varepsilon}{2} + \sqrt{\left(\frac{\varepsilon}{2}\right)^2 - V^2} & \varepsilon < -2V, \end{cases} \tag{2.17}$$

and

$$\Gamma(\varepsilon) = \begin{cases} 0 & \varepsilon > 2V \\ \sqrt{V^2 - \left(\frac{\varepsilon}{2}\right)^2} & |\varepsilon| \leq 2V \\ 0 & \varepsilon < -2V. \end{cases} \tag{2.18}$$

At this point, a brief commentary on the complex self-energies, i.e. the non-Hermitian terms, is necessary. Its appearance, either in a FGR calculation or in the exact solution of Eq. 2.15, relays on the fact that the new eigenstates are completely orthogonal to the unperturbed ones. In our case they are extended states enabled by taking the thermodynamic limit of an infinite number of states before η reach 0 [Pastawski, 2007]. As discussed above, adding this small imaginary part means putting the system in contact with an additional environment. In this situation, Eq. 2.15 produces a self-energy containing a square root function of the energy instead of a ratio among polynomials that results when Eq. 2.14 is applied to a finite system. The sign in front of the square root in Eqs. 2.17 and 2.18 is chosen to ensure the physical (i.e.

decaying) behavior when $\eta < 0$. As discussed in Ref. [Pastawski, 2007] the presence of non-Hermitian terms is fundamental in allowing a dynamical phase transition. In the general context of non-Hermitian quantum mechanics a similar conclusion holds [Narevicius *et al.*, 2003].

In summary, the poles of Eq. 2.13, control the dynamics of the system and can be obtained analytically as,

$$\varepsilon_r^2 = \frac{V_{AB}^2\left(2V^2 - V_0^2\right) - V_0^4 \pm V_0^2\sqrt{\left(V_{AB}^2 + V_0^2\right)^2 - 4V_{AB}^2V^2}}{2\left(V^2 - V_0^2\right)}. \tag{2.19}$$

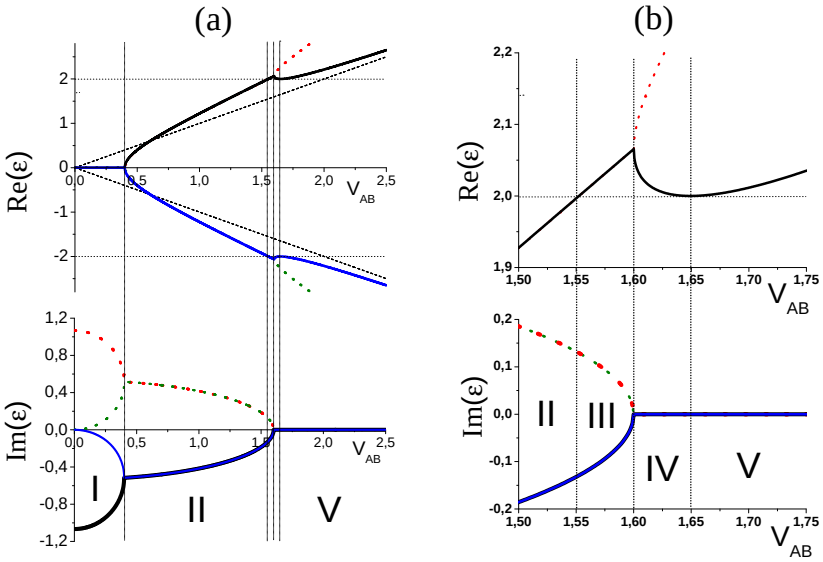

Figure 2.4: a) Real and imaginary part of the Green function poles vs. V_{AB} for $V_0 = 0.8$. All energies are in V units. The dashed line represent the poles for an isolated system. Different colors identify the poles. The non-physical ones are represented with dotted lines. The vertical dotted lines divide the dynamical regions. b)Zoom of a) in the limit of regions III and IV.

Equation 2.19 has four solutions which are plotted in Fig. 2.4. When they have an imaginary part, only the negative one represents a decaying response to an initial condition. This imaginary part is precisely the exponential decay rate in the Self-Consistent Fermi Golden Rule [Rufeil-Fiori & Pastawski, 2006]. When the four poles are real, the physical ones approach to the isolated system poles shown with dashed lines. In Figure 2.4, the real and imaginary part are shown as a function of the system

hopping V_{AB} for fixed values of $V_0 = 0.8V$. The solutions not satisfying the above conditions are indicated with dotted lines. Hereafter, we will refer as "the Poles" of the GF only those indicated by the continuous line.

The Local Density of States (LDoS) describes the number of states per interval of energy at each energy level in the local state we are measuring it. This LDOS, which defines the dynamical properties of the system, can be evaluated as

$$N_A(\varepsilon) = -\frac{1}{\pi} \lim_{\eta \to 0^+} \operatorname{Im} G_{AA}\left(\{E_n - \mathrm{i}\eta_n\}_{\forall n}, \varepsilon\right). \tag{2.20}$$

This definition is equivalent to the standard one, $-\frac{1}{\pi}\lim_{\eta\to 0^+} \operatorname{Im} G_{AA}(\varepsilon + \mathrm{i}\eta)$, for most practical purposes.

An advantageous feature of the present model is that LDoS for $|\varepsilon| \leq 2V$ can be factorized as

$$N_A(\varepsilon) = N_1(\varepsilon) \times L_1(\varepsilon) \times L_2(\varepsilon). \tag{2.21}$$

Here, L_1 and L_2, are Lorentzian Functions (LFs), and N_1,is the *density of directly connected states* (i.e. the LDoS of the first site of the semi infinite-chain).

$$N_1(\varepsilon) = \frac{1}{\pi V^2}\sqrt{V^2 - \frac{\varepsilon^2}{4}}. \tag{2.22}$$

The LFs $L_1(\varepsilon)$ and $L_2(\varepsilon)$ are related with the real and the imaginary part of the GF's poles. Their centers move with the real part of the poles, and their widths are determined by the imaginary part.

In Fig. 2.4 it is observed that there are regions with different analytical behaviors, some of them separated by abrupt changes that are consequence of the non-analytical points of the GF poles.

The difference between real parts of the physical poles is $\widetilde{\omega} = |\operatorname{Re}(\varepsilon_{r1}) - \operatorname{Re}(\varepsilon_{r2})| = 2\,|\operatorname{Re}(\varepsilon_{r1})|$, which represents an effective Rabi oscillation frequency. The imaginary part is associated with the decay rate toward the environment. Hereafter we will focus on the study of $\widetilde{\omega}$ behavior, as the parameter that characterizes the dynamics.

The relation between GF's analytic properties and the dynamics is clarified by writing the survival probability in the energy-time representation:

$$P_{AA}(t) = \int_{-\infty}^{\infty} \mathrm{d}\varepsilon \int_{-\infty}^{\infty} \frac{\mathrm{d}\omega}{2\pi} G_{AA}(\varepsilon + \tfrac{1}{2}\hbar\omega) G^{*}_{AA}(\varepsilon - \tfrac{1}{2}\hbar\omega) \exp(-\mathrm{i}\omega t) \tag{2.23}$$

$$= \left| \int_{-\infty}^{\infty} \mathrm{d}\varepsilon N_A(\varepsilon) \exp(-\mathrm{i}\varepsilon t/\hbar) \right|^2 . \tag{2.24}$$

This function measures the probability to find a particle in the site A at time t, provided that the system has had a particle at the same site at time $t = 0$. When the system is isolated, $P_{AA}(t)$ oscillates with frequency ω_0, which coincides with $\widetilde{\omega}$. When the environment is taken into account $P_{AA}(t)$ evolves in a more complex way. However, in spite of this complexity, the evolution at short times can be described by an exponentially decaying oscillation with frequency $\widetilde{\omega}$.

In the next section we will present a deeper analysis of all spectral regions and their main dynamical characteristics.

2.5 Parametric Regions

By analyzing the qualitative features of the Local Density of States (LDoS) as function of the control parameter V_{AB} we find five parametric regions separated by well defined critical values. We enumerate them from I to V as they are appearing by increasing the value of V_{AB} and we name them according to the main features in the LDoS and the behavior of the GF's poles in the complex plane.

The most common situation occurs when the two states of the isolated system are mixed with the environment continuous and hence acquire a finite mean-life. This is Region II) of **Resolved Resonances**, a regime typically described by the FGR. When the interaction with the environment becomes strong enough, at the exceptional point appears the non trivial transition to Region I) of **Collapsed Resonances**. This is the regime where the exchange narrowing occurs [Anderson, 1954]. In the other extreme, we may consider that the internal interaction of the system is much stronger than the bandwidth of the environment's continuous spectrum. Hence, the system's bonding and anti-bonding states are pushed away from the band according to perturbation theory and they will remain localized. This is Region V) **Pure Point States**. Region III) **Out-of-Band Resonant States** and Region IV) **Virtual States**, would go almost

unnoticed unless the internal and external interactions are very similar (see Fig. 2.5). In these cases the separation between system and environment becomes very delicate.

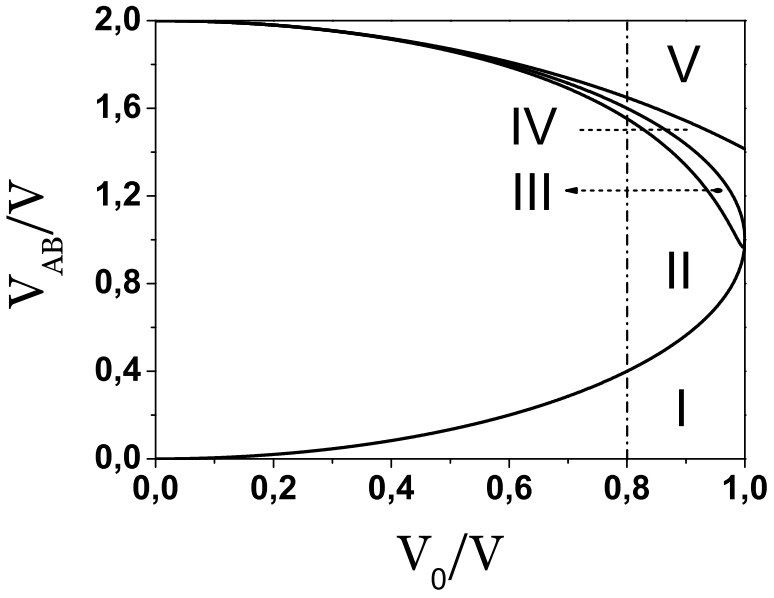

Figure 2.5: Phase diagram of the different regimes as a function of V_{AB}/V and V_0/V. The vertical dash-dotted line represents the condition used in Figs. 2.4, 2.7, 2.6 and 2.8.

The main features of these regions can be identified if we follows the behavior of the GF's poles into the complex plane as represented in Figs. 2.4-a and zoomed in Fig. 2.4-b. We notice that poles in Region III and IV have a real part extending outside the band edges (indicated with an horizontal dotted line). However, as they enter region IV they loose their imaginary part. At this point the poles jump up to the second Riemann sheet, as represented in Fig. 2.7, and they become virtual states [Hogreve, 1995]. This is manifested because they are poles of Eq. 2.13 using the unphysical branch of the self-energy, i.e. which opposite sign in imaginary part of Eq. 2.16. Hence, they do not show up as peaks or deltas in the local density of states as it was expected if there were localized states. Indeed, the LDoS given by Eq. 2.21 integrates to 1 within the band support. Only when the poles reach the band edge again, see Fig. 2.7, they return to the first Riemann sheet and become localized states.

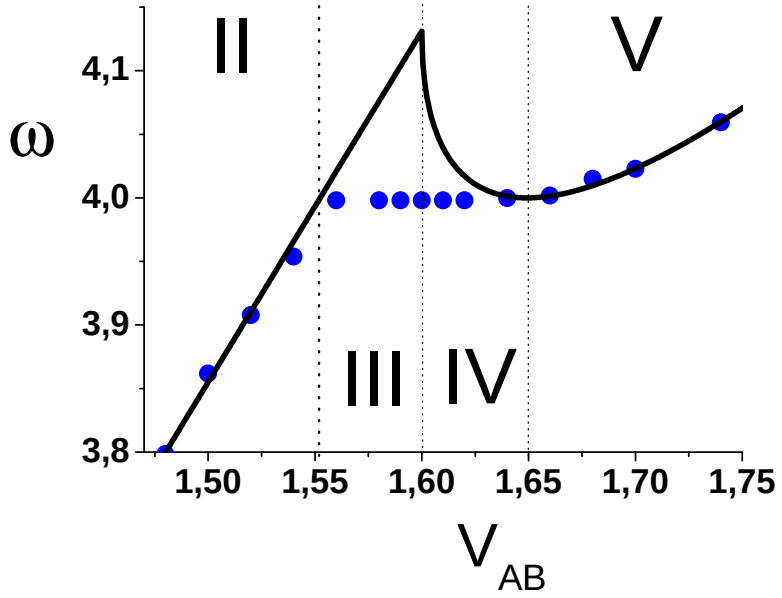

Figure 2.6: *Solid line*: frequency $\widetilde{\omega}$ evaluated from the poles distance (in units of $V/\hbar$) vs. V_{AB} (in units of V). *Blue dots*: frequency fitted from the dynamics. The value for V_0 is the same as in Fig.2.4.

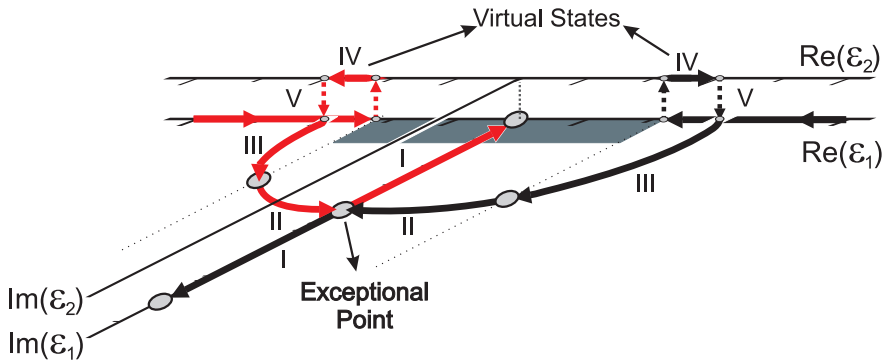

Figure 2.7: Paths of the two poles (Black and Red) of the GF as V_{AB} decreases. They go from the localized bonding and antibonding states into respective resonances that eventually collapse at the exceptional point. The bottom Riemann sheet contains the physical poles, while the upper sheet has the non-physical poles. The broader horizontal line in the center represents the continuous band of environment states. Notice that localized states transform into virtual states and out-of-band resonances before becoming well defined resonances.

Notice that if in Fig. 2.5 we move along the parameter space with a horizontal line, which means to keep V_{AB} constant, we are not going to past through all the regions. At least one region would escape the analysis. From the experimental point of view this implies that it is preferable to vary the system frequency instead of the system environment interaction, in order to find all the regimes by controlling only one parameter. For that reason, hereafter in the plots we only vary the parameter V_{AB} while keeping V_0 and V constant at 0.8 and 1 respectively.

In order to ensure consistency, we also studied the behavior of $P_{AA}(t)$ by evaluating the dynamics through the exact diagonalization of the Hamiltonian of a finite system. In this case the environment size is taken large enough so the mesoscopic echoes (interferences due to the finiteness of the system) do not show up at times of interest [Rufeil-Fiori & Pastawski, 2006]. Then, the evaluation of $P_{AA}(t)$ allows us to univocally identify the localized states and the different decay laws of the whole regimes. In next sub-sections we will show details about the system dynamics in each region.

2.5.1 Region I: Collapsed resonances (overdamped decay)

This region is found for:

$$|V_{AB}| < \left| V - \left(V^2 - V_0^2 \right)^{1/2} \right| . \tag{2.25}$$

Under this condition, $P_{AA}(t)$ decays exponentially and without oscillations until the survival collapse time [Rufeil-Fiori & Pastawski, 2006]. At this moment the return amplitude from the environment starts to be comparable with the survival amplitude (see Fig. 2.8(I-b)). If we set $V_0 = V$ we arrive to the case already treated in Ref. [Rufeil-Fiori & Pastawski, 2006] where it is analyzed the decay of a surface spin excitation when it interacts with a spin chain.

The *real part* of both poles of the GF *coincide* with the site energy, which means that the effective frequency is zero. However, their respective *imaginary parts differ* substantially (see Fig. 2.7). One of them moves away from the real axis as the SE interaction increases while the other approaches the real axis. This means that one states is captured by the environment while the other becomes isolated by cause the Quantum Zeno Effect[Álvarez *et al.*, 2006].

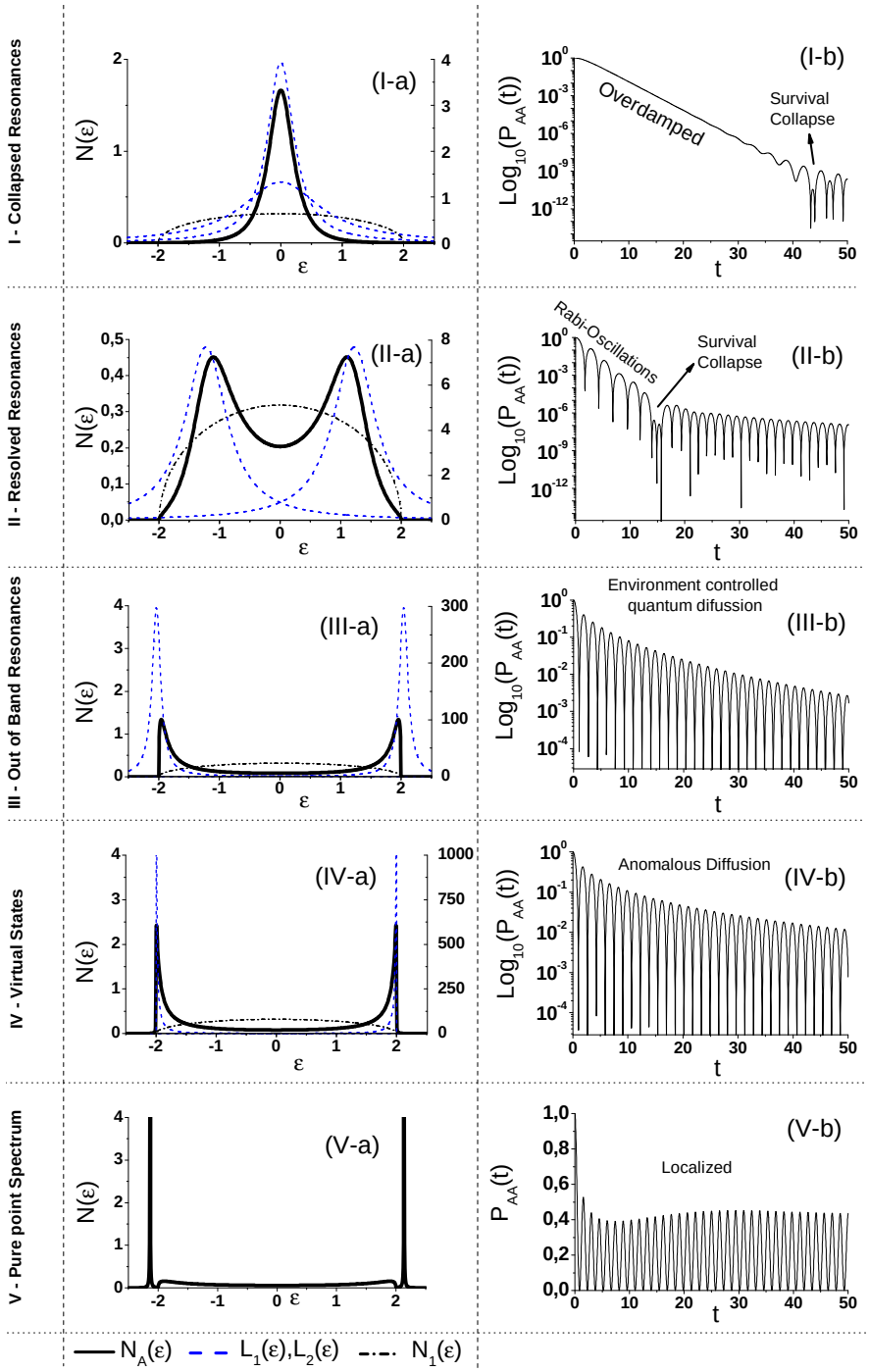

Figure 2.8: (a)-Left side panels: *Black solid line:* LDoS for the different regions [V_{AB} = 0.35 (I), 1.0(II), 1.58 (III), 1.62 (IV) and 1.9 (V)]. *Blue dotted line:* $L_1(\varepsilon)$ and $L_2(\varepsilon)$. *Black Dash-Dotted line:* $N_1(\varepsilon)$. The right side scale corresponds to the L_1 and L_2 plots.**(b)-Right side panels:** Survival probability $P_{AA}(t)$ in logarithmic scale except for (V-b), which is in normal scale.

In this region L_1 and L_2 are two LF centered at 0, but with different widths,

$$L_{1,2}(\varepsilon) = C\frac{2\Gamma_{1,2}}{\varepsilon^2 + \Gamma_{1,2}^2}, \tag{2.26}$$

where,

$$C^2 = \frac{V_0^2 V_{AB}^2}{4\Gamma_1\Gamma_2} \tag{2.27}$$

$$\Gamma_{1,2}^2 = \frac{V_0^4 - V_{AB}^2\left(2V^2 - V_0^2\right)}{2\left(V^2 - V_0^2\right)} \mp \frac{\sqrt{\left(V_0^4 - V_{AB}^2\left(2V^2 - V_0^2\right)\right)^2 - 4V^2V_{AB}^4\left(V^2 - V_0^2\right)}}{2\left(V^2 - V_0^2\right)}. \tag{2.28}$$

Fig. 2.8(I-a) shows the behavior of N_A, N_1 and the Lorentzians functions: L_1 and L_2. The centers and the linewidth of $L_1(\varepsilon)$ and $L_2(\varepsilon)$ are exactly equal to the real and imaginary part of the poles of the GF respectively.

When V_{AB} reaches zero, Γ_1 vanishes, which is consistent with the fact that the first site becomes completely isolated and the second site behaves exactly as the case treated in Ref. [Rufeil-Fiori & Pastawski, 2006], where only one site remain interacting with the environment. On the other hand at the value $V_{AB} = \left|V - \left(V^2 - V_0^2\right)^{1/2}\right|$ the system presents an EP. In this point both Lorentzians are equal and beyond this point $\widetilde{\omega}$ starts to grow up (see Fig. 2.4). This kind of behavior was observed previously for different physical systems [Álvarez *et al.*, 2006], [Oberthaler *et al.*, 1996], [Stehmann *et al.*, 2004], [Shuvalov & Scott, 2000], [Dietz *et al.*, 2007], [Müller *et al.*, 1995], [Dembowski *et al.*, 2001], [Dembowski *et al.*, 2004], [Dembowski *et al.*, 2003], [Berry & Dennis, 2003, Khitrova *et al.*, 2006]. In our case, we can interpret this as a change of model from one with two sites interacting with an environment, to other with only one surface site coupled to a semi-infinite chain.

Before moving to the next region let us make a briefly comment about the relation of the region the the Synchronization phenomena observed in the Introduction of this thesis. If we compare Fig. 1.9 and Fig. 2.4 we can observe that the behavior in both cases is equivalent, but remember that in one case we were working with couple strings and in the other with fermionic systems. Along this year we analyze these tight binding models as a possible case for quantum synchronization. However, there were an ingredient that fermionic systems do not have: the self-sustained evolution of each site.

Along this years we searched this type of self-sustained evolution in quantum systems but we did not found how to introduce it in a simple way.

Despite this, if we only consider the transient period, we can observe that there is one state that decay faster than the other. Thus the dynamical evolution will show that only one normal mode survives for long times, inducing a fixing of the relative phases. Indeed it is possible to observe that the model presented in Fig. 2.9-a can be mapped (through a change of basis in the system) to the model presented in this chapter (see Fig. 2.9-b). Therefore, the long living mode is equivalent to the survival of the anti-symmetric mode of 2.9-a. Hence, this case can be connected with the synchronization showed with the pendulums of Huygen [Huygens, 1673].

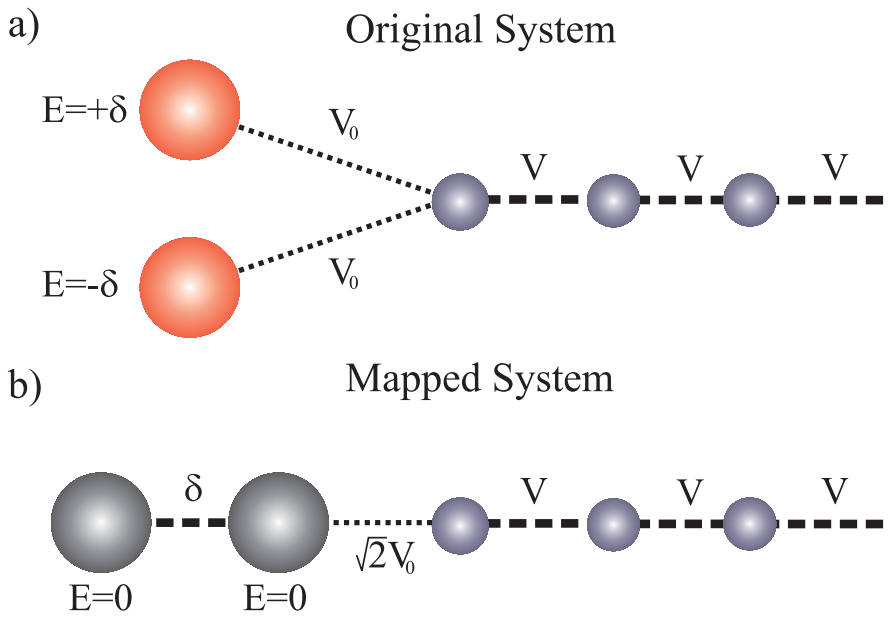

Figure 2.9: a) A tight binding system in which is possible to observe the "synchronization" in fermionic system. b) the mapped problem which is equivalent to that presented in Fig. 2.1. The energy shift δ is the control parameter that moves the problem from a non-synchronized state (region II) to the synchronized one (region I).

This type of links and the more "realistic"connections between the tight binding system and the evolution of coupled plasmon oscillators, led us study the how the surface plasmon in nano-particles could become synchronized. Their results will be presented in Chap. 4.

2.5.2 Region II: Resolved Resonances (damped oscillations)

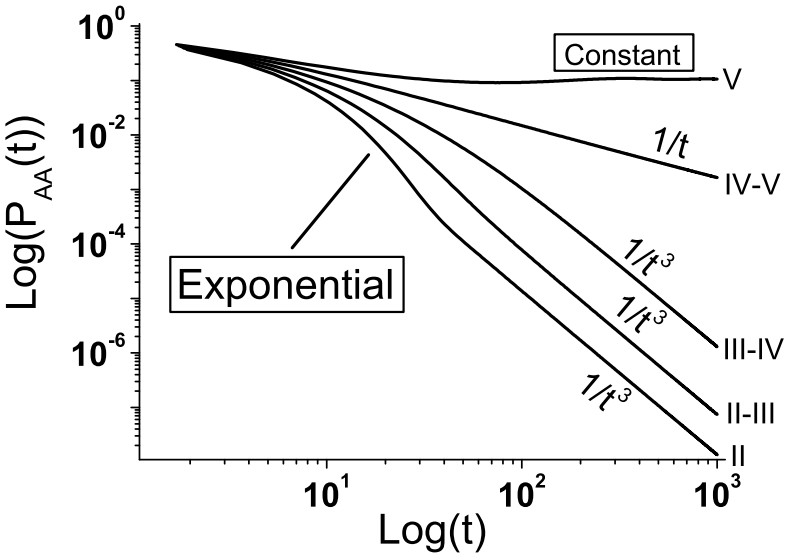

Figure 2.10: Local dynamics in Log-Log scale for different regimes. The curve II and V represent evolutions inside the region II and V respectively. Curves II-III, III-IV and IV-V represent the survival probability at the transitions between regimes.

This regime occurs for values of V_{AB} satisfying:

$$\left|V - \left(V^2 - V_0^2\right)^{1/2}\right| < |V_{AB}|\,, \tag{2.29}$$

and

$$|V_{AB}| < \left|\sqrt{\left(1 + 16\frac{V^2}{V_0^4}\left(V^2 - V_0^2\right)\right)\left(\left(2V^2 - V_0^2\right) - 2\sqrt{V^2\left(V^2 - V_0^2\right)}\right)}\right|. \tag{2.30}$$

This parametric region is characterized by the oscillatory-exponential decay of $P_{AA}(t)$ at short times, Figs. 2.8(II-b), followed by a quantum diffusive regime (t^{-3}) that is better appreciated in Fig. 2.10. The power law decay is consequence of the environment memory effects and corresponds to quantum diffusion from a $1-d$ edge. This is verified by making a Fourier Transform of a LDoS of the form $N_1(\varepsilon) \propto \varepsilon^{\nu}\theta[\varepsilon]$ which leads to a survival probability of the asymptotic form $P(t) \backsim t^{-(2\nu+2)}$. In a *bulk* of d dimensions $\nu = d_{\text{eff.}}/2 - 1$ with $d_{\text{eff.}} = d$. Notably, our case corresponds to a

survival probability of a state in a *surface* or *edge*. This one decays as being in a higher effective dimension, $d_{\text{eff.}} = d + 2n$ with $n \leq d$ the order of the surface. In our case $n = d = 1$.

The poles in this region have both real and imaginary parts. At shorts times, the real part controls the oscillatory behavior ($\widetilde{\omega} = 2\text{Re}(\varepsilon)$) and the imaginary part determines the rate of the exponential decay. On the other hand, at long times the excitation decays with a t^{-3} law and oscillates with a frequency determined by the environment band width $4V$.

Here, the critical time t_c is the time scale at which the quantum pathways returning from the environment starts to be comparable to the pure survival amplitude. Hence, t_c, which decreases with V_{AB}, divides the exponential decay from the diffusive decay.

The LDoS can be expressed in the same way as Eq. 2.21, but in this regime the LF are centered at symmetric points and have the same width (see Fig. 2.8(II-a)),

$$L_{1,2}(\varepsilon) = C\frac{2\Gamma}{(\varepsilon \mp \varepsilon_r)^2 + \Gamma^2}, \tag{2.31}$$

with,

$$C^2 = \frac{V_0^2 V_{AB}^2}{4\Gamma^2} \tag{2.32}$$

$$\Gamma^2 = \frac{V_0^4 - V_{AB}^2\left(2V^2 - V_0^2\right)}{4\left(V^2 - V_0^2\right)} + \sqrt{\frac{V^2 V_{AB}^4}{4\left(V^2 - V_0^2\right)}} \tag{2.33}$$

$$\varepsilon_r^2 = \frac{V_{AB}^2\left(2V^2 - V_0^2\right) - V_0^4}{2\left(V^2 - V_0^2\right)} + \Gamma^2. \tag{2.34}$$

It is interesting to notice that the Rabi frequency could either be slower than the unperturbed one, when $V_{AB} \ll V$, or faster, when $V_{AB} \gtrsim V$. The precise cross over results from Eq.2.34 when $\varepsilon_r = V_{AB}$.

2.5.3 Region III: Out-of-Band Resonances (environment controlled quantum diffusion).

This region is found for V_{AB} satisfying:

$$\left|\sqrt{\left(1 + 16\frac{V^2}{V_0^4}\left(V^2 - V_0^2\right)\right)\left(\left(2V^2 - V_0^2\right) - 2\sqrt{V^2\left(V^2 - V_0^2\right)}\right)}\right| < |V_{AB}|, \tag{2.35}$$

and

$$|V_{AB}| < \left| V + \left(V^2 - V_0^2 \right)^{1/2} \right|. \tag{2.36}$$

If we only take into account the poles of the GF the system resembles the Resolved Resonances regime. However, if we compare their LDoS and $P_{AA}(t)$, we conclude that this is a new regime.

In this region, it is no longer possible to distinguish an exponential decay in $P_{AA}(t)$ (see Fig. 2.8(III-b)). This is because the time t_c is too short. This implies that the oscillations are a direct consequence of the environment. In Fig. 2.6 it is observed that the frequency obtained directly from the numerical solutions remains constant at $4V$ while $\widetilde{\omega}$ (poles effective frequency) continues growing, confirming our analysis.

The expression for the LDoS presented in Eq. 2.21 is still valid, but the LF are centered outside the band edges (see Fig. 2.8(III-a)). If we analyze the dynamics in term of the LDoS, we see that the tails of the LF decay as ε^{-2}, which means that the LDoS will have a Van Hove singularity as $\varepsilon^{1/2} \times \varepsilon^{-2}$,which implies that the local excitation will decay as t^{-3} at long times (see Figs. 2.8(III-b) and 2.10).

2.5.4 Region IV: Virtual States (anomalous diffusion)

This region corresponds to the range,

$$\left| V + \left(V^2 - V_0^2 \right)^{1/2} \right| < |V_{AB}| < \sqrt{2\left(2V^2 - V_0^2 \right)}. \tag{2.37}$$

The poles in this region do not have imaginary part. For this reason it might be expected that poles were localized states[Economou, 2006]. However, both the LDoS of Fig. 2.8(IV-a) and the dynamics shown in Fig. 2.8(IV-b) and Fig. 2.10 probes that this is not the case. The reason is that the poles had moved to a second Riemann sheet [Hogreve, 1995, Marcelis *et al.*, 2004] (see Fig. 2.7). In such case only the use of the unphysical sign of the self-energy could provide poles. The dynamics in this regime presents a striking transition between a t^{-3} decay (at $V_{AB} = \left| V + \left(V^2 - V_0^2 \right)^{1/2} \right|$) to a t^{-1} behavior (at $V_{AB} = \sqrt{2\left(2V^2 - V_0^2 \right)}$). This is shown in Fig. 2.10.

Once again, we can express the LDoS as in Eq. 2.21, however its interpretation is different. In this region ε_r is still outside the band edges and yet the value of Γ becomes imaginary. The fact that Γ is transformed into an imaginary number implies that L_1 and L_2 are no longer LF. If we now analyze the tails of these functions, we observe

that they decay as ε^{-1}. This leads to a LDoS with a Van Hove singularity of the form $\varepsilon^{1/2} \times \varepsilon^{-1}$.Therefore, we can achieve a t^{-1} behavior of P_{AA} at long times. This fact is indeed confirmed by the observed dynamics (see Fig. 2.10). As in the previously analyzed section, $\widetilde{\omega}$ do not follows the observed oscillation frequency (see Fig. 2.6 and 2.8(IV-a)). Instead, it is fixed by the environment band width $4V$.

When V_{AB} reaches the value $\sqrt{2\left(2V^2 - V_0^2\right)}$, there is a change in the nature of the Van Hove singularities from $\varepsilon^{\frac{1}{2}}$ to $\varepsilon^{-\frac{1}{2}}$. Consequently, $P_{AA}(t)$ decays exactly as a t^{-1}(see Fig. 2.10). From this point on, the states become localized.

It is interesting to note that while the presence of the virtual states is not clearly distinguishable in the observable LDoS, the anomalous diffusion, where $P_{AA}(t)$ moves gradually between $t^{-3}$and t^{-1}, should enable its experimental identification.

2.5.5 Region V: Pure Point States (localized)

Finally, the last region appears when,

$$|V_{AB}| > \sqrt{2\left(2V^2 - V_0^2\right)}. \tag{2.38}$$

Two localized states emerge from the band edges as shown in Fig. 2.8(V-a). The poles are real. Fig. 2.6 shows that $\widetilde{\omega}$ recovers it interpretation as the effective system frequency. In this region the environment renormalization is almost negligible and its only effect is to slightly correct the value of the effective frequency. If V_{AB} becomes large enough $\widetilde{\omega}$ reaches ω_0.

The dynamics in this region, Fig. 2.8(V-b) is characterized by an oscillatory $P_{AA}(t)$ that only decays at very short times, after which the amplitude of the oscillation remains constant.

2.6 Concluding Remarks of the chapter

By considering an exactly solvable model for two spin system (SWAP gate) in presence of an environment of spins, we discussed how the bath's memory affects the dynamics when treated beyond the Fermi Golden Rule. The unperturbed Rabi frequency sweep through different dynamical and analytic regimes when moving continuously a single parameter.

2. PHASE TRANSITIONS IN THE QUANTUM DYNAMICS

We have shown that depending on the value of the internal time scales of the system, the environment can induce multiple phase transitions in the system dynamics. Our model shows uncommon regimes as the exchange narrowing starting at the Exceptional Point and the Virtual States by moving a single parameter. The fact that all the dynamical phases appear in the same system, offered the opportunity to study the transitions between them and hence to determine the precise points where the transition occurs. Through the dynamics, we have characterized the difference between collapsed resonances, resolved resonances, out-of-band resonances, virtual states and the pure point states. In particular, we have shown that in the virtual state regime there is an anomalous quantum diffusive law, which at long times is observed as a change in the decay law from t^{-3} to t^{-1}. From the observation of this anomalous diffusion, Butos-Marún et al. in Ref. [Bustos-Marún *et al.*, 2010], deduced that the highest plasmonic excitation transfer does not occur when the system has a well defined extended resonant state but just at the virtual-localized transition, where the main plasmonic modes have eigenfrequencies at the passband edge. Thus the detailed analysis of these regions helped to understand the underlining physics.

In this sense, we have also found an expression for the LDoS which explicit the presence of the resonances. This LDoS results factorized in three terms. A density of directly connected states (i.e. the LDoS at the environment's surface) and two Lorentzian Functions, whose widths, become imaginary in the virtual state regime. The edges of the LDoS determine the behavior at long times. It is then clear that the anomalous diffusion is related to the fact that the Van Hove singularities at these edges are modified. This change occurs when the Lorentzian widths become imaginary.

Note that the complexity of the dynamics for this relatively simple system, emerges as a consequence of the explicit way in which the environment is modeled. Details like Out-of-band Resonant States and Virtual States could not have been observed in simpler representations of the environment as the usual broad-band or the self-consistent Born approximations. The results of our model system shows that a zero imaginary part of the poles is not enough as a localization criteria [Economou, 2006]. In particular, virtual states have zero imaginary part, but any local excitation in this parametric regime shows a complete decay to the environment.

Another parameter that characterizes the dynamics, is the oscillation frequency. First, in the Region I (collapsed resonances), before the system reaches the EP, there

is an overdamped decay as expected [Rotter, 2009]. When the unperturbed Rabi frequency ω_0 exceeds the critical value, at the EP, the resonances become resolved (Region II). $P_{AA}(t)$ show an exponentially attenuated oscillation with a frequency $\tilde{\omega}$ given by the poles difference. This frequency, $\tilde{\omega}$, goes from 0, at the EP, to a value higher than ω_0. In the region III (out-of-band resonances) and IV (virtual states) the observed frequency is fully determined by the environment bandwidth and not by the GF poles, while the decay follows different power laws. These are particularly stable regimes for a swap gate since the effective Rabi frequency does not depend on the internal parameter. Further increase of ω_0 leads to Region V of localized states where the observed frequency is always higher than ω_0 but tends to it as $V_{AB} \to \infty$.

An interesting message that we can extract from the phase diagram of Fig. 2.5 is that by changing V_{AB}/V one can always move between all five regimes. However, for small values of the interaction with the environment (V_0/V) the transition to localized states occurs within a very small range of V_{AB}/V and hence most chances are that it goes unobserved. Within this parametric setup it its possible to describe the system evolution as an smoothly decoherent dynamics mediated by the environment.

The diagram of Fig. 2.5 also indicates that a clear numerical or experimental observation of the full dynamical wealth would only be possible for $V_0/V \lesssim 1$.

As a final remark, we again mention that because of its simplicity, our model can be arranged to describe various physical systems such as spin chains [Álvarez *et al.*, 2006], microwave devices [Luke A. Sweatlock & Atwater, 2003], arrays of tunneling coupled optical waveguides [Longhi, 2006b], periodic elastic arrays [Gutiérrez *et al.*, 2006], or acoustic time reversal cavities [Calvo *et al.*, 2007]. Reciprocally, most of them should present the variate dynamical phenomena discussed here, provided that one focuses in the proper parameter range. These examples also suggest possible experimental setups where the parameters found in this work can be used as a knob enabling to store and exchange energy.

Chapter 3

Molecular Dissociation as an Environmental QDPT

3.1 Introduction

When are two individual atoms no longer interacting units and must be considered a new entity, a molecule...? This question is very relevant for chemistry and its applications, and it seems to involve the sort of elements we have developed in the previous Chap. 2 (quantum phase transitions). There, we been able to describe analytically the infinite portion of the quantum system that constitutes "the environment". Thus, the finite portion that constitutes "the system", can have a discontinuous or non-analytic behavior, i.e. we have been able to describe a phenomenom the is not readily obtainable from finite size numerical calculation. Those phenomena are ubiquitous in Nature, and one might wonder whether the atom/molecule discontinuity might be one of them. Thus, in this chapter we will attempt to use the analytical tools we developed, to describe the molecule formation/dissociation. We will study the bond-breaking or molecule forming reactions observed when a diatomic molecules get close to certain metallic surfaces. By the end of this chapter we will be able to describe this bond breaking reaction as an quantum phase transition.

The work developed in this chapter was made in collaboration with Andrés Ruderman and Elizabeth Santos, who had an interest on this problem because its implications for heterogeneous electrocatalysis. Some details of the calculations presented in this thesis can be found in the Licenciado degree thesis of A. Ruderman (see Ref.

[Ruderman, 2011]).

Let us first introduce a few concepts about electrochemical reactions and how this topics are related to our field. The understanding of electrocatalytic reactions is one of the big challenges for theoretical electrochemistry. It traditionally has constituted a cornerstone for petrochemistry and nowadays it is crucial for the development of fuel cells and artificial photosynthetic systems. There are two different approaches to study this kind of problems. One approach emphasizes on the conceptual framework and extends the theory of electron transfer to catalytic processes, the other approach is mainly computational and relies on a density-functional theory (DFT) to describe electrochemical reactions. The theoretical line started with the pioneering works of Marcus [Marcus, 1956] and Hush [Hush, 1958], makes use of the symmetry considerations introduced by Roald Hoffmann [Hoffmann, 1988] and was then taken up by the Soviet school [Levich, 1970], to which Alexander Kuznetsov made so many important contributions [Kuznetsov, 1995]. In this case many of the analysis are based on the qualitative features of the Local Density of States at the relevant atoms. The other approach relies on computational experiments seeks to reach conclusions from a first principle calculation with as few approximations as possible, e.g. DFT calculation complemented with molecular dynamics. In recent years, both schools focused on bond-breaking or forming reactions.

Our effort lines up with the first alternative, and in order to get more motivation let's refresh a paragraph of P. W. Anderson written in Ref. [Anderson, 1978],

"*One of my strongest stylistic prejudices in science is that many of the facts Nature confronts us with are so implausible, given the simplicities of nonrelativistic quantum mechanics and statistical mechanics, that the mere demonstration of a reasonable mechanism leaves no doubt of the correct explanation. . . . Very often such a simplified model throws more light on the real workings of nature than any number of ab initio calculations of individual situations, which even where correct, often contain so much detail as to conceal rather than reveal reality. It can be a disadvantage rather than an advantage to be able to compute or to measure too accurately, since often what one measures or computes is irrelevant in terms of mechanism. After all, the perfect computation simply reproduces Nature, it does not explain her.*"

In this quotation Anderson emphasizes how the "realistic" calculations, focus too much in specific details and parameters and often miss the generality of physical phe-

nomena. Thus, a simplified model tends to be better as long as it does not become so complex to prevent analytical solutions.

Previous theoretical works made by Anderson and Newns [Anderson, 1978], [Newns, 1969] initiated the investigation of hydrogen chemisorption at metal surfaces. Recently, the work from the group of Schmickler extended this theory to include the solvent role and combined it with DFT in order to investigate electrochemical reactions. Thus, the Santos-Schmickler group, together with M. Koper, proposed a simple model Hamiltonian that, being a variant of the Anderson-Newns model, could describe bond-breaking reactions [Santos *et al.*, 2008, Santos *et al.*, 2006], which served as a basis to explain the general principles of electrocatalysis [Santos & Schmickler, 2007a].

In order to apply this work to the hydrogen evolution reaction, the group of E. Santos used DFT calculations to obtain the system parameters [Santos & Schmickler, 2007b, Santos *et al.*, 2009] and also analyzed the Hamiltonian for bond-breaking in symmetric cases [Santos *et al.*, 2008, Santos *et al.*, 2006] and systems made of heteronuclear molecules [Santos *et al.*, 2011]. A good example for the latter process is the Heyrowsky reaction, in which initially one hydrogen atom is absorbed on the surface while the other approaches in the form of a solvated proton, then the two combine to form a hydrogen molecule that leaves the surface.

We will show examples of how the hydrogen molecule formation can be interpreted as an a *phase transition in the quantum dynamics*. Generally, we will work from the opposite case, where a molecule approaches to the surface of a transition metal crystal, and then it breaks forming two separated systems: the isolated atom and the surface plus an added atom.

Through this chapter we will study two particular molecular approaching cases: The parallel and the perpendicular configurations (see. Fig. 3.1).

The model Hamiltonian proposed by Santos et al. [Santos *et al.*, 2006] represents our starting point to begin the analysis.

3.2 Electrocatalysis and the quantum model

Electrocatalysis is any one of the mechanisms which produce a speeding up of reactions at electrode surfaces. Thus, a basic description of this process involves a set of atoms (or molecules), a metallic surface and the surrounding solvent. In particular we considered

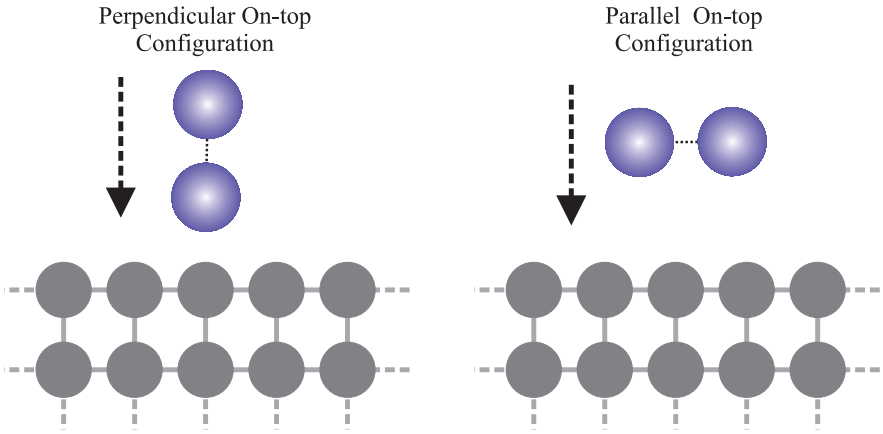

Figure 3.1: Parallel and Perpendicular on-top configurations for Molecular Bond-Breaking problem.

transition metals whose d band constitutes an electron reservoir responsible for its useful properties. As we mention before, we consider a diatomic molecule which approaches to the metal. On each atom, we keep with only one valence orbital explicitly, and describe the bonding in a tight-binding or extended Hückel scheme.

We introduce the indices A and B for the valence orbitals of each of the two atoms, and denote by E_A and E_B their corresponding energies. The Hückel coupling constant V_{AB} can be taken as real, and the model Hamiltonian for the isolated molecule can then be written in the form:

$$\mathbf{H}_S = E_A \left|A\right\rangle \left\langle A\right| + E_B \left|B\right\rangle \left\langle B\right| + V_{AB} \left(\left|A\right\rangle \left\langle B\right| + \left|B\right\rangle \left\langle A\right|\right), \tag{3.1}$$

where V_{AB} is the coupling between the atoms in the molecule. The site energies E_A and E_B are the electronic energies corresponding to the valence orbital of the atoms. The solutions for $\mathbf{H}_S$ are the well known bonding and anti-bonding states with energies

$$E_{\pm} = \frac{E_A + E_B}{2} \pm \sqrt{\left(\frac{E_A - E_B}{2}\right)^2 + V_{AB}^2}$$

.

If we set the energies $E_{A,B} \equiv 0$ and consider that the fermi energy is $E_f = 0$, then the bonding solution E_- is always below E_f and it seems that the molecule would never break. However, if we consider the presence of the transition metal, the dissociation

of the molecule can occurs. In order to explore this possibility, we have to evaluate different topologies and the transition metal structure by itself.

The metal can be represented by two different electronic configurations: the sp-band and the d-band. In Fig. 3.2 is schematized the typical interaction between one atom (a localized state) and the metal through the sp and d bands. There, it is possible to observe that the sp-band is wider than the d-band, and in the region of interest (approximately $|\varepsilon - E_f| \leq 5$) the sp-band behaves almost constant. Thus as we saw in the Chap. 2, this only adds a small component in the lifetime, but the renormalized energies are essentially similar than before the interaction with the sp-band. Therefore neglecting the sp-band interaction is a good approximation for treat this problem. For details on this argument one can follows the work made by D. Newns in ref. [Newns, 1969], where he has showed that relevant contribution to the catalysis process comes from the neighboring metal d orbitals. Hence, for the rest of this chapter we will work only with the d-band interaction.

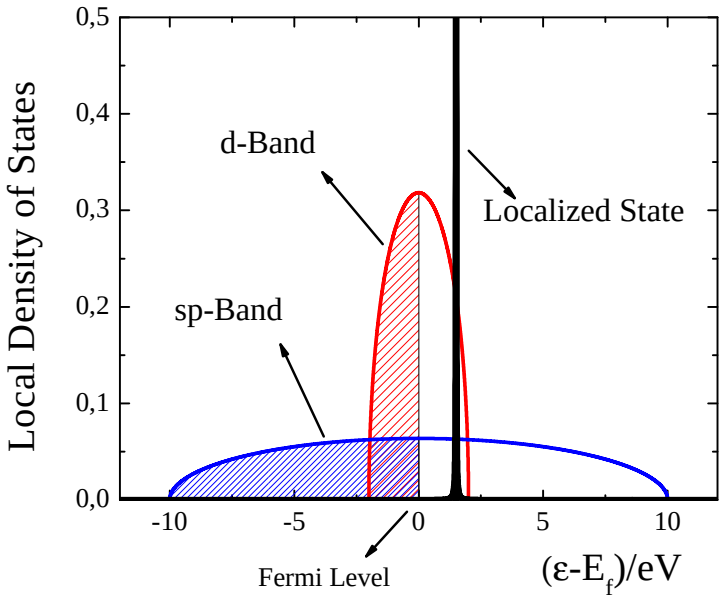

Figure 3.2: Schematic representation of one localized states interacting with the sp and d bands. The energies are refered to the Fermi energy E_f. In the region of interest, $|\varepsilon - E_f| \leq 5$, the sp-Band is almost constant. Thus it can be neglected.

Let us now focus on the d-band. In the previous chapter (Chap. 2) we have seen that

the semi-infinite linear chain has the following Local Density of states in the surface:

$$N_d(\varepsilon) = \frac{1}{\pi V^2}\sqrt{V^2 - \frac{\varepsilon^2}{4}}. \tag{3.2}$$

This is just the local density of states corresponding to the d-band at the surface of the metal. The question that arises is how to get the linear chain from the 3d metral? The solution comes with the Lanczo's method [Haydock *et al.*, 1972, Lanczos, 1950]. This is a recipe that provides a reduction transformation of a $2D$ metal into a $1D$ is presented in Fig. 3.3. The $3d$ metal is reduced with the same tridiagonalization procedure. To understand how this method works on this problem, we will use the labeling presented in Fig. 3.3. From the left picture, we observe that the first neighbor interactions define successive layers of interaction represented with the numbers **1**, **2** , **3**, etc. to be connected only with the next nearest diagonals. Thus the net interactions between the capital letters becomes: **1** $\leftrightarrow$ **2**, **2** $\leftrightarrow$ **3**, **3** $\leftrightarrow$ **4**, etc. By construction there are no other types of interactions. Therefore, if we apply the decimation procedure shown in the central picture of Fig. 3.3, we obtain the expected $1D$ linear chain. It is important to notice that the site **1** will be the one that will interact with the molecule.

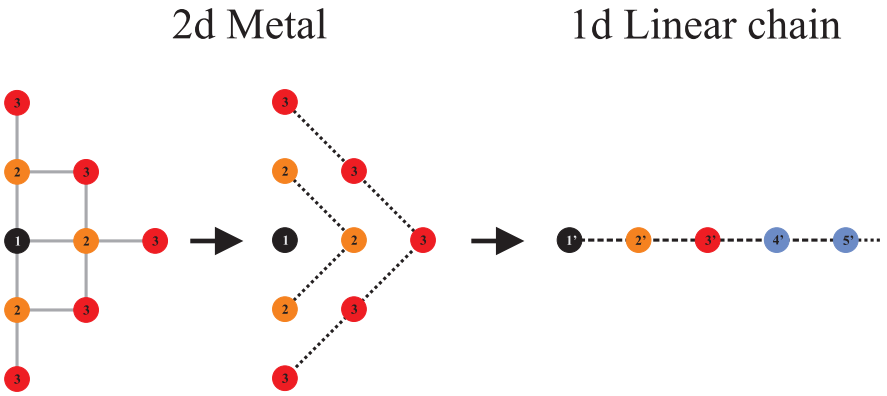

Figure 3.3: Lanczo's method. Decimation from the $2d$ system of first neighbors interactions, to the $1d$ linear chain. The same procedure can be applied to the $3d$ metal.

With the reduction of the $3D$ problem to the $1D$ problem we now can start studying the bond-breaking in electron transfer from a metal to diatomic molecule. Remember that in equation 3.1 we have already presented the 2-atoms system (the molecule). By adding the interaction with the metal we complete the whole problem. Thus the

Hamiltonian becomes,

$$\mathbf{H} = \mathbf{H}_S + \mathbf{V}_{SM} + \mathbf{H}_M, \tag{3.3}$$

where

$$\mathbf{V}_{SM} = V_0 \left(|B\rangle \langle 1| + |1\rangle \langle B| \right), \tag{3.4}$$

and

$$\mathbf{H}_M = \sum_{n=1}^{\infty} E_n |n\rangle \langle n| + \sum_{n=1}^{\infty} V_n \left(|n\rangle \langle n+1| + |n+1\rangle \langle n| \right). \tag{3.5}$$

The interaction between the metal and molecule is controlled by V_0. The hoppings inside the tight binding chain are V_n, connecting the effective sites n with the contiguous $n+1$. The kets $|n\rangle$ are the localized states at the effective nth site of the metallic chain. In order to simplify the problem we will set $V_n = V \ \forall n \geq 3$. The values for V_1 and V_2 have to account the fact that in the surface of the metal, the coupling between atoms is weaker than in the bulk. Thus we will assume $V_1 < V_2 < V$.

3.3 Perpendicular Molecule on-top of the metal

The perpendicular on-top configuration is conformed by a molecule of two atoms which approach to the metal in a perpendicular on-top position respect to the metal surface (see Fig. 3.1). This model shows two different schemes depending on the distance to the metal surface. If the atoms are far away, the electrons occupy the bonding level and form the molecular bond. In the other extreme, when the molecule is close enough to the surface, it is expected that the molecule dissociates, producing an isolated atom plus an atom absorbed by the metal. In this situation the electrons stay in a bonding state between one of the atoms and the metal surface. In Fig. 3.4 the inverse behavior evaluated from DFT calculations made by the group of E. Santos.

The tight binding model Hamiltonian for this problem is represented in Fig. 3.5-a.

With the purpose to define an optimum configuration for the molecular dissociation we use will base our model in the Marcus-Hush theory and assume $E_A = E_B = E_n = 0$. This setup put the Fermi energy level (E_f) in the center of the d-band and produce a symmetric splitting around the center of the band. Additionally, we will set the coupling elements $V_1/V = 0.8$, $V_2/V = 0.9$, and $V_{AB}/V = -2.5eV$ to work with a

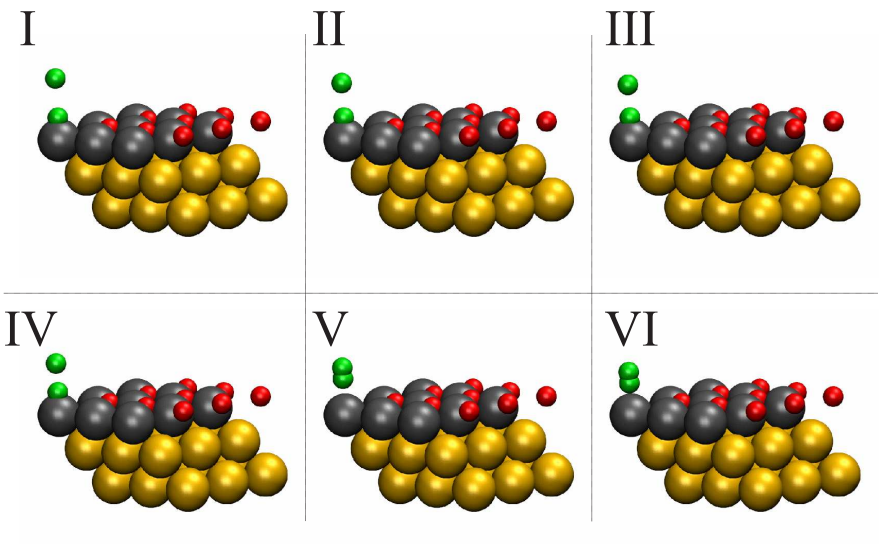

Figure 3.4: DFT calculations of the perpendicular approach to the metal surface. In V) it is observed the abrupt transition from two separated atoms to the molecular formation. (Frames extracted from a Video belonging to E. Santos).

useful case. The V_0 coupling accounts for distance between the molecule and the metal surface.

At this point it is necessary to list some of the approximations hidden in the the model:

■ The fixed value of V_{AB} neglects the variation of the distance between the molecules (A) and (B). Despite that this restriction do not allows the rupture of the molecular binding, we still define the bond-breaking point by thinking that the dissociation occurs in two steps. First, the molecule moves close enough to the surface and the electrons occupied the lower energy level. Then, we free the coupling V_{AB}, and allow the dissociation.

■ The atoms in the metal are also consider fixed in the whole the problem. In this approach we do not allow the surface to be modified by the interaction with the molecule.

■ By assuming a null coupling between the site A (the furthest) and the metal surface neglects an exponentially small interaction between the distant atom and the catalyst.

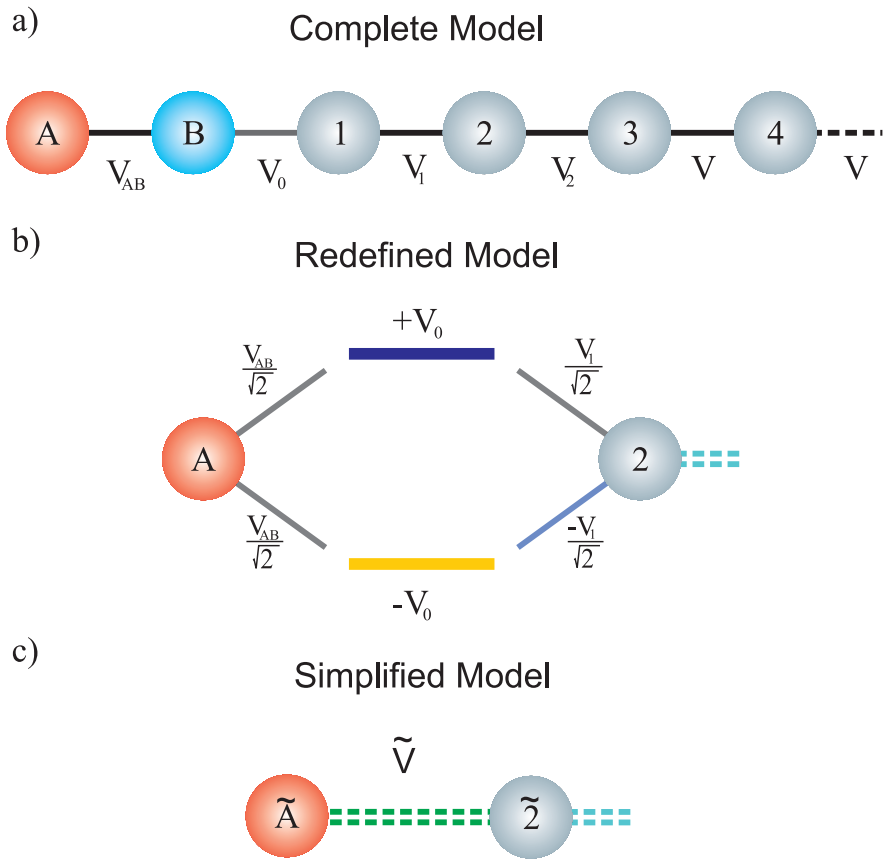

Figure 3.5: Perpendicular On-top configuration. a) Tight binding model for the system and the metal. b) New representation through the symmetric and anti-symmetric basis change. c) Simplified model with the decimation procedure.

3.3.1 An effective model: a very useful approximation

In order to proceed with our analysis and obtain information about the system properties we use again the matrix form of the Green's function,

$$\mathbf{G} = (\varepsilon \mathbf{I} - \mathbf{H})^{-1}. \tag{3.6}$$

The complete solution for the problem involve the analysis of several number of poles and their interpretations could become cumbersome. Instead of attack the original system, we first prefer to explore an effective model which will show the approximate behavior of the poles and then we proceed to explore the full problem.

The first step to reach the effective model, consist in a unitary transformation that change the basis of the sites (B) and (1). This kind of transformation will be useful along the whole thesis, so we decide to denote it as the *Symmetric Transformation* between the sites (B) and (1):

$$|\pm\rangle = \frac{1}{\sqrt{2}} \left(|B\rangle \pm |1\rangle \right) \tag{3.7}$$

The original Hamiltonian in the site basis was,

$$\hat{H} = \begin{array}{c} \\ \langle A| \\ \langle B| \\ \langle 1| \\ \langle 2| \\ \langle 3| \\ \vdots \\ \vdots \end{array} \begin{array}{c} \begin{array}{ccccccc} |A\rangle & |B\rangle & |1\rangle & |2\rangle & |3\rangle & \cdots & \end{array} \\ \begin{pmatrix} E_A & V_{AB} & & & & & \\ V_{AB} & E_B & V_0 & & & & \\ & V_0 & E_d & V_1 & & & \\ & & V_1 & E_d & V_2 & & \\ & & & V_2 & E_d & V_d & \\ & & & & V_d & E_d & \ddots \\ & & & & & \ddots & \ddots \end{pmatrix} \end{array} \tag{3.8}$$

After the transformation it becomes,

$$\hat{H} = \begin{array}{c} \\ |A\rangle \\ |+\rangle \\ |-\rangle \\ |2\rangle \\ |3\rangle \\ |4\rangle \\ \vdots \end{array} \begin{array}{c} \begin{array}{ccccccc} |A\rangle & |+\rangle & |-\rangle & |2\rangle & |3\rangle & |4\rangle & \cdots \end{array} \\ \begin{pmatrix} 0 & V_{AB}/\sqrt{2} & V_{AB}/\sqrt{2} & 0 & 0 & 0 & \cdots \\ V_{AB}/\sqrt{2} & V_0 & 0 & V_1/\sqrt{2} & 0 & 0 & \\ V_{AB}/\sqrt{2} & 0 & -V_0 & -V_1/\sqrt{2} & 0 & 0 & \\ 0 & V_1/\sqrt{2} & -V_1/\sqrt{2} & 0 & V_2 & 0 & \\ 0 & 0 & 0 & V_2 & 0 & V & \\ 0 & 0 & 0 & 0 & V & 0 & \ddots \\ \vdots & & & & & \ddots & \ddots \end{pmatrix} \end{array} \tag{3.9}$$

In figure 3.5-b it is represented this basis change.

The next step is to perform a decimation process over the sites $|+\rangle$ and $|-\rangle$. This method, explained in Ref. [Pastawski & Medina, 2001], rewrite the Hamiltonian in a new version where properties of the sites $|\pm\rangle$ are introduced in the energies of $|A\rangle$ and $|2\rangle$,

$$\Delta_A(\varepsilon) = \frac{|V_{AB}|^2}{2}\left(\frac{1}{\varepsilon - V_0} + \frac{1}{\varepsilon + V_0}\right), \tag{3.10}$$

$$\Delta_2(\varepsilon) = \frac{|V_1|^2}{2}\left(\frac{1}{\varepsilon - V_0} + \frac{1}{\varepsilon + V_0}\right), \tag{3.11}$$

and the new coupling between the sites $|A\rangle$ and $|2\rangle$,

$$V_{eff}(\varepsilon) = \frac{V_{AB}V_1}{2}\left(\frac{1}{\varepsilon + V_0} - \frac{1}{\varepsilon - V_0}\right), \tag{3.12}$$

In Fig. 3.5-c it is possible to observe the form of the hamiltonian after the last transformation. Until this point, all the performed transformations were exacts. The approximation emerge once we evaluate Eqs. 3.10, 3.11 and 3.12 at $\varepsilon = (E_A + E_2)/2 = 0$ (remember that $E_A = E_2 = 0$), which give us

$$\Delta_B(E_B) = 0, \tag{3.13}$$

$$\Delta_2(E_2) = 0, \tag{3.14}$$

$$V_{eff}\left(\frac{E_B+E_2}{2}\right)=\frac{V_{AB}V_1}{V_0}. \tag{3.15}$$

This approximación behaves better as it gets larger V_0 [Pastawski & Medina, 2001]. After all the steps, the effective system becomes

$$\mathbf{H}_{eff}=V_{eff}\left(|A\rangle\langle 2|+|2\rangle\langle A|\right)+V_2\left(|2\rangle\langle 3|+|3\rangle\langle 2|\right)+\sum_{n=3}^{\infty}V\left(|n\rangle\langle n+1|+|n+1\rangle\langle n|\right). \tag{3.16}$$

This Hamiltonian is equivalent to that treated in the Chap. 2. This fact allows us to use the results derived there and applied all the knowledge about the poles behavior. For completeness we show again the first diagonal element of the Green function:

$$G_{AA}=\frac{1}{\varepsilon-\dfrac{V_{eff}^2}{\varepsilon-\left(V_2/V\right)^2\left[\Delta\left(\varepsilon\right)-\mathrm{i}\Gamma\left(\varepsilon\right)\right]}}. \tag{3.17}$$

By comparing and replacing the variables in Eq. 2.19 we obtain the next four solutions (only two of them are physicals),

$$\varepsilon_r^2=\frac{V_{eff}^2\left(2V^2-V_2^2\right)-V_2^4\pm V_2^2\sqrt{\left(V_{eff}^2+V_2^2\right)^2-4V_{eff}^2V^2}}{2\left(V^2-V_2^2\right)}. \tag{3.18}$$

If we again reproduce the analysis developed in the previous chapter, we found that the final solutions to Eq. 3.18 are those plotted in Fig. 3.6. There, we can observe that in the value of

$$V_0^c=\frac{V_{AB}V_1}{V_2^2}\left[V+\sqrt{V^2-V_2^2}\right], \tag{3.19}$$

we found a critical point which represent the first evidence of the presence of a quantum face transition. By using the parameters applied in Fig. 3.6, we obtain $V_0^c\simeq 3.545$. If $V_0<V_0^c$ the model shows up a bifurcation of the resonances in the form of bonding and anti-bonding states. In the other case ($V_0>V_0^c$) the energy levels are superposed in the real part, but bifurcated in the imaginary part. This means that the one atom will be absorbed by the metal (red curve in 3.6-b), while the other becomes isolated. This is the first clue about the bond-breaking transition.

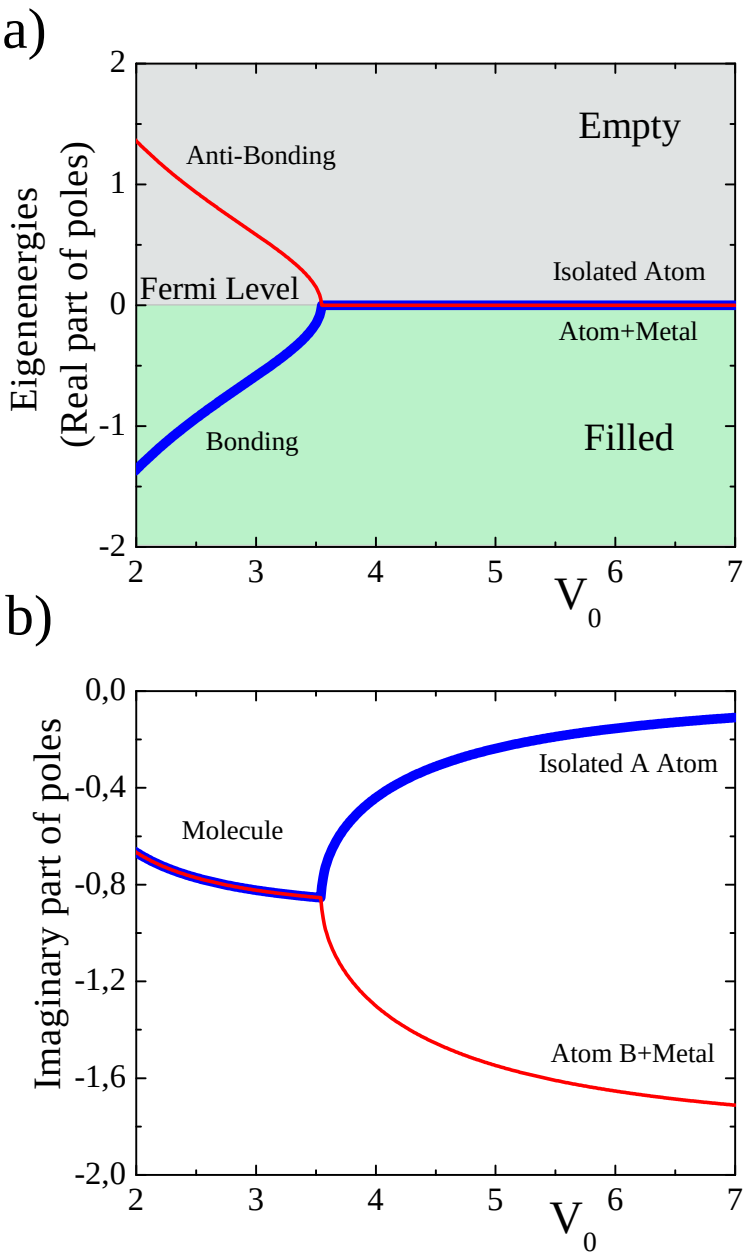

Figure 3.6: Poles from the perpendicular approach: a) The real part of the poles versus the V_0 hopping which is related to the inverse of the distance between the molecule and the metallic surface. The d-band goes from -2 to 2. b) The Imaginary part of each pole. The Quantum phase transition can be observed at $V_0 \simeq 3.545$.

The bonding and anti-bonding states observed for $V_0 < V_0^c$ can be understand by applying again the Symmetric Transformation between (A) and (2), and evaluating the LDoS for the $|\pm\rangle_{A,2}$ states. In Fig. 3.7 the results shows that the bonding and anti-bonding resonance energies correspond to the anti-symmetric and symmetric state between (A) and (2) respectively. We will denote them as: $b(A-2)$ for the bonding case and $a(A-2)$ for the anti-bonding. This interaction is generated by the effective coupling V_{eff} between (A) and (2).

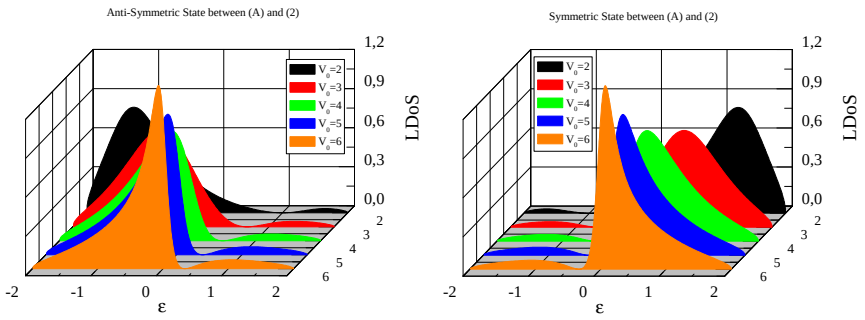

Figure 3.7: Local Density of States of the Symmetric and Anti-Symmetric states between the sites (A) and (2). This LDoS indicates that the bonding and anti-bonding resonances correspond to the anti-Symmetric and Symmetric states respectively.

3.3.1.1 Complete solution to the perpendicular topology

The approximation used above help us to get an intuition about the emergency of the molecular bond-breaking. Now we want to analyze the full solution, which gives the exact value of V_0^c and completes the whole scheme.

This particular problem has eight 8 solutions (in the square form), thus the analytic solution could not be easily found. Thus, to perform the evaluation of the poles, we appealed to numerical tools (Maple and Fortran), and once we obtain the solutions, we choose the physical ones. With this purpose we first drop those which have a positive imaginary part and later on, we re-evaluate the rest of the solutions in the Green Function, verifying which of them are real poles. This method for selecting the poles will be repeated several times in this chapter.

In Fig. 3.8 we show the complete set of solutions. There we observe the emergence of two new states respect to the approximated case (see Fig. 3.6). These new energies are localized states outside the d-band. When the molecule is far away from the metal,

it is known that the atoms form two localized states with values $\pm V_{AB} = \pm 2, 5$. This is just shown in Fig. 3.8 when $V_0 = 0$. Insofar as V_0 increases, the states suffer a smooth change. For example, when $V_0 = 6$, the outside band energies becomes into bonding and anti-bonding states between (B) and (1). This can be proof by looking the LDoS in the sites $|\pm\rangle_{B,1}$ (with the exact model). In the Fig. 3.9 is the results of such an evaluation, and there we can see that for $V_0 > V_0^c$ the LDoS of the $|+\rangle_{B,1}$ has a higher weight over the bonding state while the $|-\rangle_{B,1}$ has over the anti-bonding.

3.4 Parallel Molecule on-top of the metal.

Let now start the analysis of the parallel configuration (see Fig. 3.1). The solutions to this model will have different properties compared with the previous case. This model will show up new types of quantum phases transitions.

The model Hamiltonian for this problem is defined in the site basis as follows,

$$\mathbf{H} = \begin{pmatrix} & |A\rangle & |B\rangle & |1 + Metal\rangle \\ |A\rangle & 0 & V_{ab} & V_0 \\ |B\rangle & V_{ab} & 0 & \pm V_0 \\ |1 + Metal\rangle & V_0 & \pm V_0 & \Sigma(\varepsilon) \end{pmatrix}. \tag{3.20}$$

where the ket $|1 + Metal\rangle$ represent the first site of the metal plus the rest of the metal bulk (through a decimation procedure). The interaction with only one surface atom implies that the molecule has a strong coupling with the first site of the metal, but the it is weak with the nearest d orbital. Despite of this, in this model we introduced the minus-plus sign ($\pm$) to explore different types of topologies: the symmetric and anti-symmetric configurations. The choice of this sign correspond to the kind of electronic state presented in the surface of the metal (see Fig. 3.10). For example, if it is an "d" state in the z direction, the interaction will be symmetric, i.e. $\mathbf{H}_{A,1} = \mathbf{H}_{B,1} = V_0$ (see Fig. 3.10-b). In the other hand, if the surface has a "d" quadrupolar state, it will interact anti-symmetrically with A and B, i.e. $\mathbf{H}_{A,1} = V_0 = -\mathbf{H}_{B,1}$ (see Fig. 3.10-b).

These symmetries properties in the connections, naturally induce the symmetric

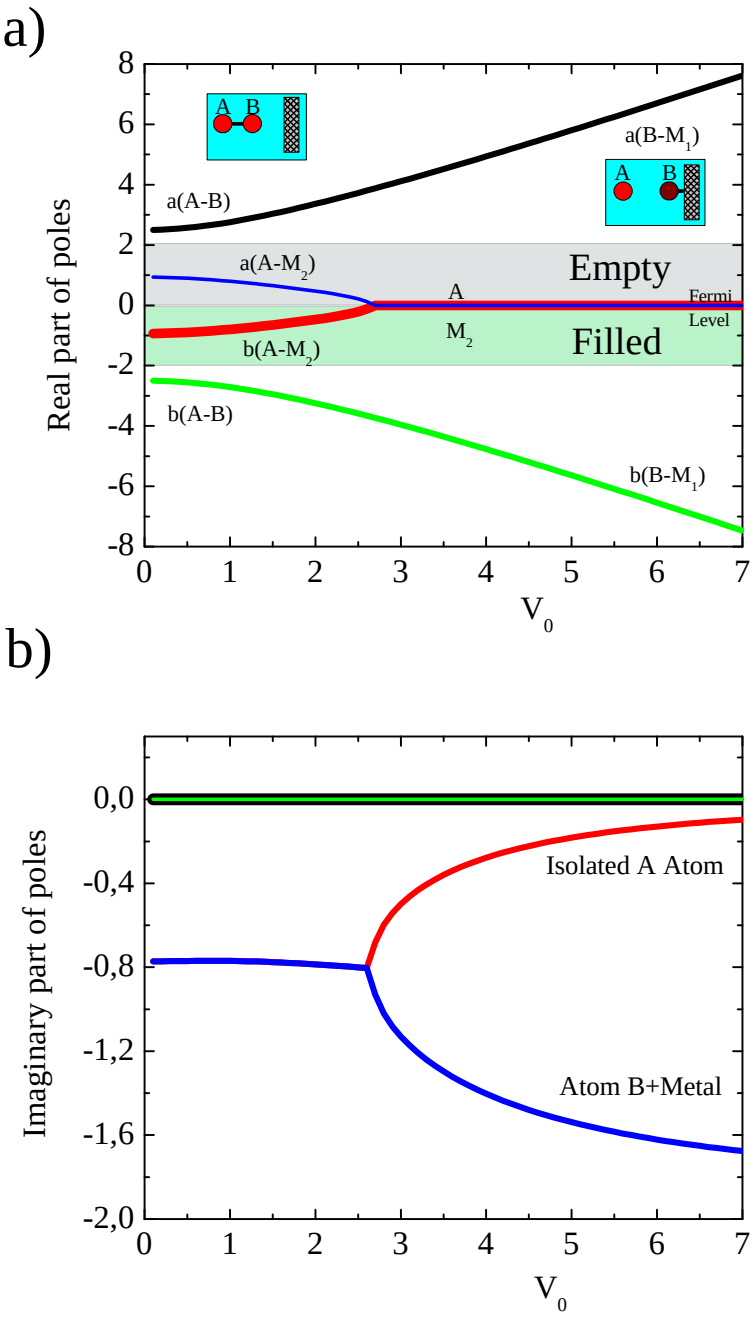

Figure 3.8: Poles of complete solution for the Perpendicular topology. a) The real part of the poles versus the V_0 hopping. The gray area represents the d-band, which goes from -2 to 2. b) The Imaginary part of each pole. In the critical value $V_0 \simeq 2,6$ appears the Quantum phase transition that represent the dissociation transition.

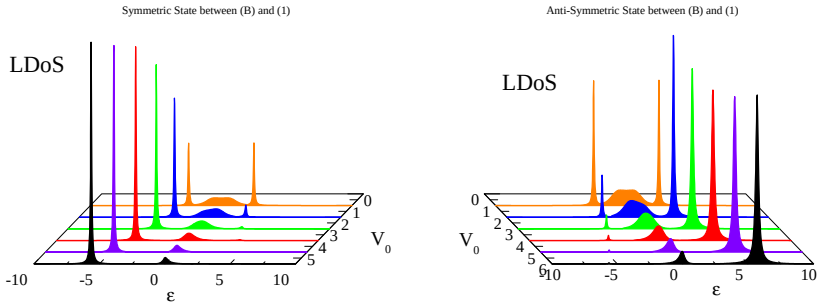

Figure 3.9: Local Density of States for the symmetric and anti-symmetric states between the sites (B) and (1). Here it is observed that the symmetric state correspond to the bonding energy observed in Fig. 3.8.

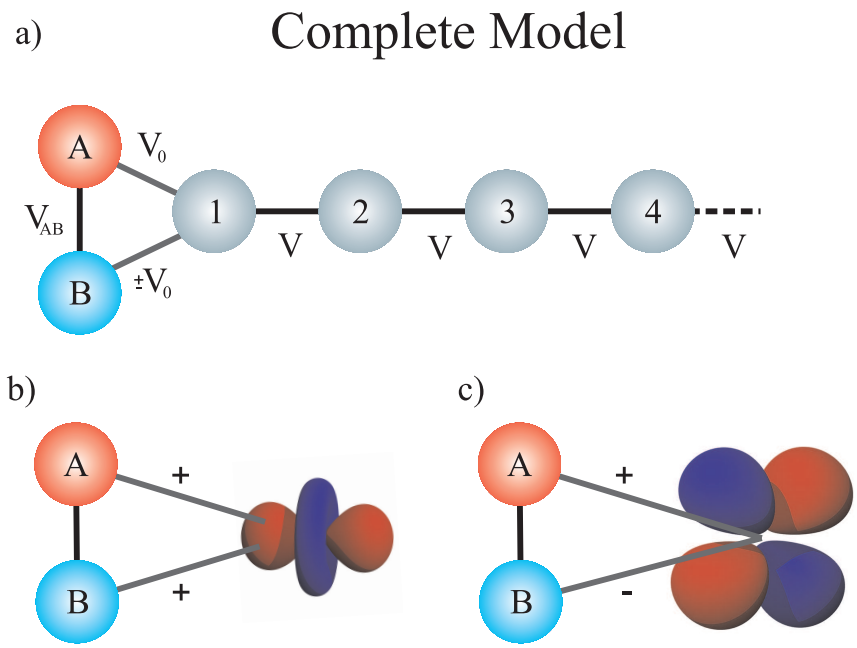

Figure 3.10: Parallel interaction of two atoms with one of the metal surface. a) Tight binding model for the system and the metal. b) and c) are the possible types of interaction with the metal surface. If the surface has a d_z state we obtain the b) configuration. On the other hand, if a quadrupolar state is in the surface the interaction is like the c) form.

transformation between sites (A) and (B),

$$\mathbf{H_{trans}} = \begin{pmatrix} & |+\rangle & |-\rangle & |1+Metal\rangle \\ |+\rangle & +V_{AB} & 0 & \frac{(1\pm1)}{\sqrt{2}}V_0 \\ |-\rangle & & -V_{AB} & \frac{(1\mp1)}{\sqrt{2}}V_0 \\ |3+Metal\rangle & \frac{(1\pm1)}{\sqrt{2}}V_0 & \frac{(1\mp1)}{\sqrt{2}}V_0 & \Sigma(\varepsilon) \end{pmatrix}. \tag{3.21}$$

In Fig. 3.11 it is schematized the the transformation for this system. As we can observe, for the symmetric case, the $(-)$ site becomes isolated while the $(+)$ is absorbed by the chain with a coupling constant of $\sqrt{2}V_0$. The opposite situation occurs when the coupling to the metal is anti-symmetric (see Fig. 3.11-b).

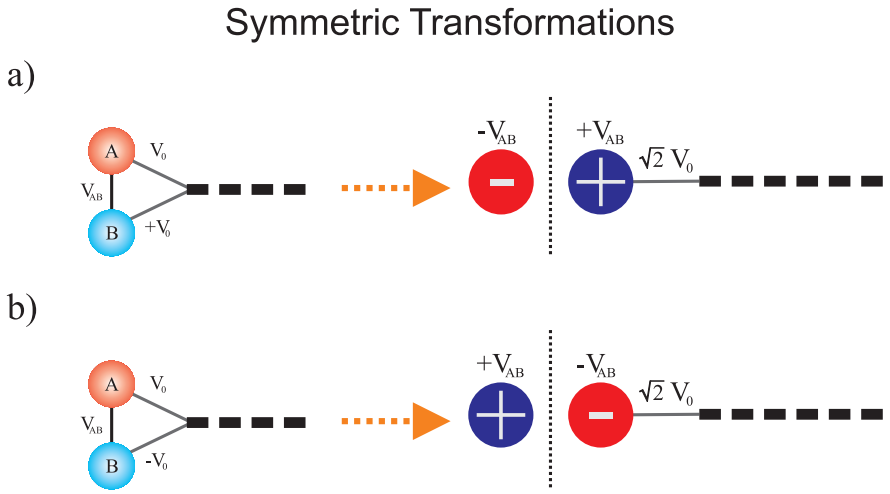

Figure 3.11: Symmetric Transformation applied to the parallel topologies. Here it is possible to observe how one of the state, in each case, remains isolated, while the other is absorbed by the metal.

The absorbed-atom model obtained from the transformation results equivalent to that treated in Ref. [Rufeil-Fiori & Pastawski, 2006]. Thus, we use the solutions from that paper to obtain the behavior of the poles. The result is the following,

$$\varepsilon_{poles=1,2} = \frac{(\pm V_{AB})(2V^2 - 2V_0^2)}{2\left(V^2 - 2V_0^2\right)} \pm \frac{V_0^2}{\left(V^2 - 2V_0^2\right)} \sqrt{(\pm V_{AB})^2 - 4\left(V^2 - 2V_0^2\right)}. \tag{3.22}$$

$$\varepsilon_{poles=3} = (\mp V_{AB}) \tag{3.23}$$

In Fig. 3.12 we plotted the behavior of the poles as a function of V_0. For both cases it is possible to observe the presence of virtual states (red dotted lines). Remember that this kind of states are solution of the non-physical Green function.

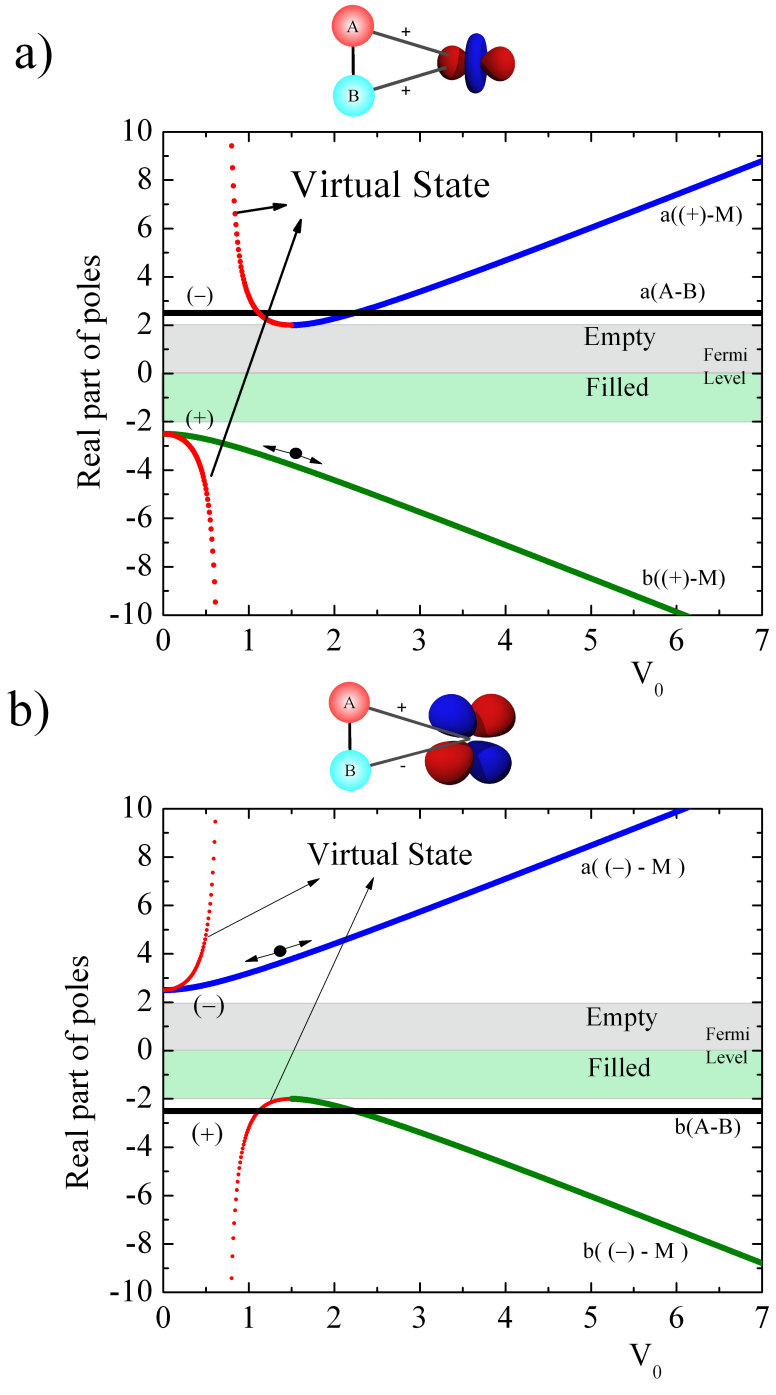

Figure 3.12: Poles of the Parallel Configuration. a) Real part of the poles for the case of symmetric connection to the metal. All the poles have null imaginary part. b) Same as a) but for the anti-symmetric interaction case.

For the symmetric case (see Fig. 3.12-a) appears two localized states at low values of V_0 (at $\approx \pm V_{AB}$). One correspond to the bonding between (A) and (B), and the other to the anti-bonding. Due to the topology of the interaction one of the states remains constant for every value of V_0, while the other becomes absorbed by the metal as far as V_0 increases. At the value of $V_0 \approx 1.5$ appears the quantum phase transition which mixture the $(+)$ state with the metal, thus forming two new states: $b((+)\text{-}M)$ and $a((+)\text{-}M)$. For this system we will denote this transition as the one on which the system is absorbed by the metal. However this phase transition do not induce any molecular dissociation. This is because the energy of this new localized state is above the Fermi level.

In the anti-symmetric topology this transition is more clearly, because the new energy level appears below the fermi energy. It emerge as a bonding state between the $(-)$ and the Metal: $b((-)\text{-}M)$, at the same critical point as before ($V_0 \approx 1.5$). In the other side of the band, the $(+)$ site transforms smoothly into the $a((-)\text{-}M)$ state as far V_0 crosses the critical value.

3.5 Conclusions

In this chapter we analyzed the Heterogeneous Catalysis process from a quantum point of view. We could associate the dissociation phenomena to the quantum dynamical phase transitions previously studied in the Chap. 2. Through the analysis of several geometrical forms of approaching a molecule to the metal surface, we have found that the mechanism of dissociation differs depending on the type of topology considered.

In the first part of this chapter we focus our analysis on the perpendicular on-top problem. We founded that the dissociation occurs through the collapse of resonances in the center of the d-band. Each of them is formed from the bonding and antibonding interaction between the furthest atom and the second layer of the metal broadened by the rest of the metal.The inclusion of the V_1 and V_2 (different from V) in the metal surface is crucial to facilitate this interpretation. We have seen there is an abrupt transition at the center of the band into a "isolated" atomic state and an collective state centered in the second layer. We also observe a smooth change in the localized out of the band states from a molecular bonding state into the bonding combination

between the closes atom an its host metal orbital. This analysis is corroborated with the use of the Local Density of States.

In the second part of this chapter we analyzed two parallel on-top topologies, with symmetric or anti-symmetric interactions. There we found that the transition is different from the previous one. Now there is one virtual state that comes from high energy and transforms into a localized state at some critical value of V_0 (studied in Chap. 2). This local state corresponds to a bonding combination between the antibonding molecular state and metal orbital. This lead to the occupation of the antibonding molecular state with consequent molecule breaking.

As a final remark in this chapter, we have to mention that the use of the symmetric transformation between pair of sites helped us to understand the results obtained along this work. This technique which represents a useful tool to analyze this kind of tight binding models and will be applied in the following chapters to explore the synchronization process of surface plasmon in Nano-particles arrays.

Chapter 4

Seeking the Synchronization of Plasmonic Oscillators in Nano-Particle Arrays

4.1 INTRODUCTION

In this chapter we will explore the synchronization phenomenon in Nanoparticles (NP) arrays in terms of the quantum phase transition developed in Chap 2. We will analyze this type systems by combining the analytical tools developed in the chapters 2 and 3. The work performed along this chapter was made in collaboration with Raúl. Bustos-Marún, which is interested in the dynamical behavior of nanoparticles arrays.

By using the specific design of plasmonic systems we will able, at the end of this chapter, to control the Localized Surface Plasmons (LSP) and make them evolve synchronously. Depending on the NP material and their lengths, the system will end oscillating in phase or in anti-phase.

The definitions of Synchronization (see Ref. [Pikovsky *et al.*, 2003]) requires that the sub-systems (in our case, the NP) has to evolve with a fixed relative phase and additionally they have to oscillated self-sustained. If one evolve the LSP, one can see that they can not maintain oscillating by them self. Thus, in principle the self-sustained condition is not a property of the NPs systems. However the presence of active mediums around the nanoparticles injects the enough amount of energy in such a way that the NP keep oscillating with the same amplitude. Then, the use of active medias plus the

specific designs of the NP produce the desired synchronization.

In this chapter we will work with the synchronization phenomena without looking for a non-analytic point which separates the non-synchronized region from the synchronized one. Due to the use of realistic values for the parameters, this phase transition could not been seen as a non-analytical point, however we still can observe if the system is synchronized or not.

Before starting with the work, let us made a brief introduction about nanoparticles system. In the past decades, the advances in fabrication and characterization of nanometric devices have given rise to a revolution in many field of science fueled by the intriguing new properties of matter in this nanometric scale. Among the new fields that rapidly became central, emerged plasmonics with its promises that go from ultra sensitive nano-sensors to plasmonic circuitry [Maier, 2007, Novotny & Hecht, 2006, Coronado *et al.*, 2011, Halas *et al.*, 2011, Ebbesen *et al.*, 2008]. Currently new ideas are emerging in this field by combining plasmonic devices with active media that compensate in part or totally their losses. [Kottos, 2010, Krasavin *et al.*, 2011, Li & Xia, 2010, Citrin, 2006, Wuestner *et al.*, 2010, Noginov *et al.*, 2009, Bergman & Stockman, 2003, Stockman, 2008, Stockman, 2009, Stockman, 2010] Active media are created by dye molecules or semiconductors where the population inversion is optically or electrically produced. The concept of spaser (surface plasmon amplification by stimulated emission of radiation) is an example of that and it is basically a source of electromagnetic fields, containing both propagating and evanescent waves, formed by the interaction of surface plasmons with an active media that fully compensate the losses of the plasmonics system [Bergman & Stockman, 2003], [Stockman, 2009], [Stockman, 2010]. This work is another example of the new effects that arise form combining plasmonic devices with active media. In particular, we studied plasmonic systems consisting of metallic nanoparticle arrays where losses are partially or fully compensated by an active medium. We not only found that localized surface plasmons of individual NPs keep oscillating with a fixed amplitude and relative phase, becoming a new example of synchronization, but we also understood the mechanism behind it and propose a way of controlling the relative phases of the LSP.

The phenomenon of synchronization, defined as the adjustment of rhythms of self-sustained oscillating objects because of their mutual interaction, has been observed in many physical and biological systems [Pikovsky *et al.*, 2003],

[Stein *et al.*, 2011, Goldstein *et al.*, 2011, Lai *et al.*, 2011, Mertens & Weaver, 2011], [Wójcik *et al.*, 2011, Huygens, 1673, Stein *et al.*, 2011, Goldstein *et al.*, 2011, Buck, 1938] from coupled pendulums clocks first described by Christian Huygens[Huygens, 1673] to the chemical [Stein *et al.*, 2011, Goldstein *et al.*, 2011] or biological examples, such as fireflies that flash in unison [Buck, 1938]. However, up to our knowledge, this is the first time that synchronization is described in the context of plasmonics.

The aim of this chapter is on one hand, to increase the menu of available tools to design new nano-metric devices and on the other hand, to bring the phenomenon of synchronization to the nano-world by presenting a feasible example and contributing to its general understanding.

4.2 COUPLED DIPOLE APPROXIMATION FOR ELLIPSOIDS WITH RADIATION DAMPING.

The systems studied are basically different arrays of metallic NPs which are modeled through the well known coupled dipole approximation [Bustos-Marún *et al.*, 2010, Hernández *et al.*, 2005, Park & Stroud, 2004, Zou & Schatz, 2004, García de Abajo, 2007, Markel & Sarychev, 2007, Malyshev *et al.*, 2008, Citrin, 2004, Brongersma *et al.*, 2000]. In this model, each i^{th}-NP is described by a dipole P_i induced by the electric field produced by the others dipoles, $E_{j,i}$, and the external source, $E_i^{(\text{ext})}$. We assume a generic ellipsoidal shape for the NPs whose polarizabilities α are described in a quasi-static approximation, [Jones, 1945, Kelly *et al.*, 2003] $\alpha = \frac{\epsilon_0 V(\epsilon-\epsilon_m)}{[\epsilon_m+L(\epsilon-\epsilon_m)]}$, where V is the volume, ϵ_0 is the free space permittivity, ϵ_m is the dielectric constant of the host medium, and L is a geometric factor that depends on the shape of the ellipsoidal NP. The dielectric constant of the NP, ϵ, is described by a Drude-Sommerfeld model $\epsilon = \epsilon_\infty - \frac{\omega_{\text{P}}^2}{(\omega^2+i\omega\eta)}$, where ϵ_∞ is a material dependent constant and take into account the contribution of the bound electrons to the polarizability, ω_{P} is the plasmon frequency, and η the electronic damping factor. We assume for simplicity a near field approximation, $E_{i,j} = \frac{-\gamma^{T,L} P_j}{4\pi\epsilon_0\epsilon_m d^3}$, where d the distance between NPs, and γ is a constant that depends on the orientation of NPs relative to the direction of E, $\gamma^T = 1$ if they are perpendicular and $\gamma^L = -2$ if they are parallel. Taking into account all these consideration, P_i and $E_i^{(\text{ext})}$ can be

arranged as vectors **P** and **E** resulting in:[Bustos-Marún *et al.*, 2010]

$$\mathbf{P} = \left(\mathbb{I}\omega^2 - \mathbb{M}\right)^{-1} \mathbb{R}\mathbf{E} = \chi\mathbf{E}, \tag{4.1}$$

where χ is the response function, $\mathbb{M}$ is the dynamical matrix and $\mathbb{R}$ is a diagonal matrix that rescales the external applied field according to local properties:

$$R_{i,i} = -\epsilon_0 V_i \omega_{\mathrm{P}i}^2 \; f, \tag{4.2}$$

with $f = \frac{\left[1-(\epsilon_\infty - \epsilon_{m,i})\left(\omega^2 + i\omega\eta_i\right)/\omega_{\mathrm{P}i}^2\right]}{[\epsilon_{m,i} + L_i(\epsilon_\infty - \epsilon_{m,i})]}$.

Let us make a little parenthesis to observe the connection with the previous chapters. If we have no electrical field, we can re-arrange Equation 4.1 as follows,

$$\left(\mathbb{I}\omega^2 - \mathbb{M}\right)\mathbf{P} = \mathbf{0}. \tag{4.3}$$

This last equation is equivalent to the time independent Schrödinger equation, where ω^2 is associated with the eingenvalues, $\mathbb{M}$ with the Hamiltonian, and **P** with the eigenvectors. Moreover, the problem can be framed within the general problem of couple oscillators, where we can interpret the electric field as the external force which acts over each oscillator. Within this associations it is possible to observe that the Green function formalism can be used to solve the dynamical evolution of the LSP. Thus, we exploit all the techniques learned in the chapters 2 and 3 to perform the full analysis of the synchronization problem.

Returning to the system of Nanoparticles, we observe that the cubic dependence of E on d, makes small contributions beyond nearest neighbors, thus we neglect this terms [Bustos-Marún *et al.*, 2010, Brongersma *et al.*, 2000]. The coupling constants, $M_{i,j} = \omega_{\mathrm{X}i,j}^2$, and the LSP complex square frequencies, $M_{i,i} = \omega_{\mathrm{SP}i}^2 - \mathrm{i}\Gamma_i(\omega)$, are given by:[Bustos-Marún *et al.*, 2010]

$$\omega_{\mathrm{X}i,j}^2 = \frac{\gamma^{T,L} V_i \omega_{\mathrm{P}i}^2}{4\pi\epsilon_m d_{i,j}^3} f, \tag{4.4}$$

$$\omega_{\mathrm{SP}i}^2 = \frac{\omega_{\mathrm{P}i}^2 L_i}{[\epsilon_{m,i} + L_i(\epsilon_\infty - \epsilon_{m,i})]}, \tag{4.5}$$

and

$$\Gamma(\omega) = \eta\omega + \eta_R\omega^3. \tag{4.6}$$

where η is the electronic damping and η_R the radiation damping. The electronic damping η can be evaluated from the Fermi velocity v_f, the bulk mean free path l_{bulk}, the volume V, and the surface S of the NP by using the Matthiessen's rule $\eta = v_f(1/l_{bulk} - C/l_{eff})$, with $C \approx 1$ and the Coronado-Schatz formula $l_{eff} = 4V/S$ [Coronado & Schatz, 2003].

On the other hand, the radiation damping η_R can be calculated from the ellipsoid's radius a, b, and c, $\eta_R = 2/9(abc/v^3)\omega_P^2\ f$, where v is the speed of light in the host medium. This extra damping term appears when the polarizability α is corrected by using the modified long-wavelength approximation, $\alpha'^3\alpha^{-1}$[Kelly *et al.*, 2003]. In the examples analyzed here, dynamic depolarization is negligible and thus not included in the equations for simplicity.

4.2.1 Temporal Evolution.

The temporal evolution of dipolar moments of individual NPs can be evaluated in two different ways: First, by using the Fourier transform, and second by directly solving the set of coupled differential equations. In the first case, one should transform the response function $\chi(\omega)$ into $\chi(t)$ and then evaluate the contributions to the i site due to the presence of the external field and the whole system. Additionally, as in any dynamical problem, it is necessary consider the contributions from the initial time $t = 0$. Thus the final equation for the polarization evolution becomes,

$$P_i(t) = \sum_j \int_0^t \chi_{i,j}(t-\tau)E_j^{(ext)}(\tau)d\tau. \tag{4.7}$$

In this work, we used the fast Fourier transform algorithm to obtain the functions $\chi(t)_{i,j}$ from $\chi(\omega)_{i,j}$. In the case of using active medias, one must be careful in not to get so close to the "loss compensation condition", because the solution could not be square integrable.

Another alternative is to directly solve the set of differential equations associated with each $P_i(t)$. They can be deduced from Eqs. 4.1-4.6 by using $P_i(t) = P_i(\omega)e^{-i\omega t}$.

In the present work, a simple version of these equations were used in section "Gain-Loss Compensation" just to show an illustrative example. The simplification comes through the f factor of Eqs. 4.2 and 4.4. There we used the wide-band approximation which assumes that ω is constant in the whole range of interest. Thus we set $f(\omega) \approx f(\omega_{SP})$, and obtain the following equations:

$$\begin{aligned} \ddot{P}_i(t) + \omega_{\mathrm{SP}i}^2 P_i(t) + \eta \dot{P}_i(t) - \eta_R \dddot{P}_i(t) \\ = R_{i,i} E_i^{(ext)}(t) - \sum_{j \neq i} \omega_{\mathrm{X}i,j}^2 P_j(t), \end{aligned} \tag{4.8}$$

The resulting equations are the equivalent to those used for the chain of Hertzian dipoles (see Ref. [Brongersma *et al.*, 2000, Hernández *et al.*, 2005]). Due to the complexity of the equation we decided to solve them by using numerical algorithms like the 4th order Runge-Kutta method [Press, 1992].

4.3 RESULTS.

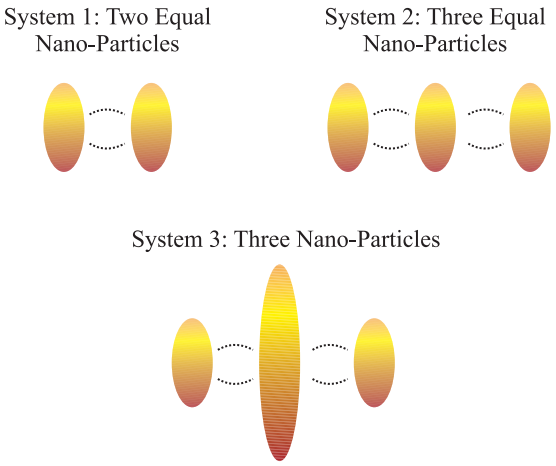

Figure 4.1: The three examples of Nano-particles arrays used in this chapter. The first two are formed by equivalent NPs. The last one has a bigger NP in the middle of the array. Remembering that the size is related to the damping factor, one obtain a bigger radiation damping for the central nanoparticle.

In the present chapter we developed a systematic way of constructing synchronized system at the nanoscale by carefully designing losses and gains of plasmonic structures.

In order to understand the proposed strategy we will first analyze three simply examples of linear arrays of metallic NPs in order to understand the meaning of their solutions. These systems are represented in Fig. 4.1. The first one consist of two equivalent nanoparticles, in the second case, are three, and the last one are three NP but the middle one is bigger than the others two. The fact that the nano particles are equivalent, means that their frequencies are exactly equals. In our problems we will assume that the NP could have little fabrication defects and thus they have a $\delta = \omega^2_{\text{SP1}} - \omega^2_{\text{SP3}}$ shift between their frequencies. This δ parameter will let us to explore the solution of these systems.

We will start the analysis by studying the isolated problem, i.e. when the electrical field is not acting. For this problem, we need to obtain the square eigenvalues of $\mathbb{M}$ (we will denote as ω^2_{eig}) as function of the square frequency difference, $\delta = \omega^2_{\text{SP1}} - \omega^2_{\text{SP3}}$, between the NPs of the ends.

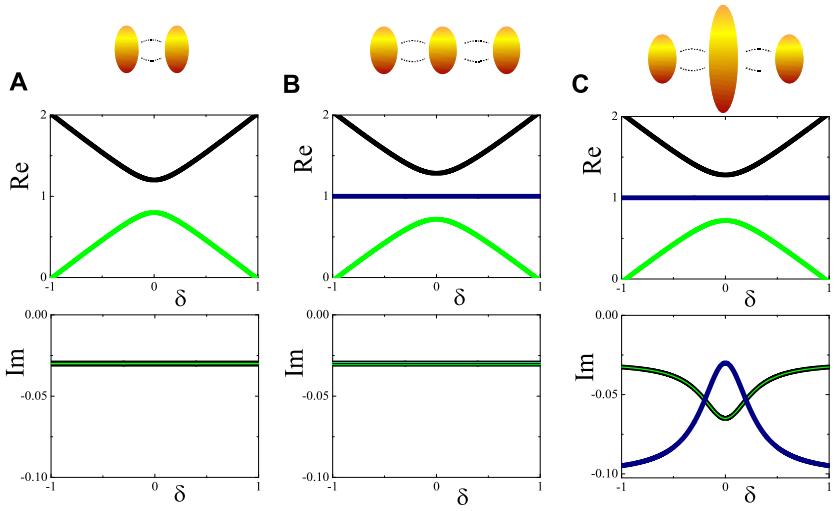

Figure 4.2: Real and imaginary part of the square eigenvalues of $\mathbb{M}$ corresponding to each system plotted in the upper part (and in Fig. 4.1), as function of the frequency shift δ between the first and the last NPs. Only nearest neighbors couplings is considered. $\omega^2_X = 0.2/\omega^2_{SP}$ and $\Gamma = 0.03/\omega^2_{SP}$ for all NPs except for case C where Γ of the middle NP is 0.1. All the frequencies are referenced to the unperturbed frequency ω^2_{SP}.

In this case the interaction frequency ω^2_{X} and the intrinsic decaying rate Γ were taken in a wide band approximation for simplicity and all the frequencies referenced to ω^2_{SP}, see caption of Fig 4.2 for more details. Fig 4.2-**A** corresponds to two NPs with

the same Γ, 4.2-**B** to a system of three NPs with the same Γ, and 4.2-**C** to systems of three NPs with the middle one having a bigger value of Γ. In the **A** case, the results indicate the presence of an avoided crossing for the real part of ω^2_{eig} and a constant (and equal) imaginary part for both eigenmodes. Evaluating ω_{eig} instead of ω^2_{eig}, just adds some distortion to the above plots, and put small differences to the imaginary parts of the two normal modes splitting them. Here, it is important to remember that the imaginary part of the poles is associated with the decay rates of the normal modes. The avoided crossing is the region where the interaction between the nanoparticles tend to repel the crossing of the two eigenfrequencies. However the imaginary part of the solutions are equal in the ω^2 plot and little different in a ω plot.

This implies that both solutions will decay almost with the same rate. For this case, the two solutions correspond with normal mode of oscillation for a two site system: the Symmetric and Anti-symmetric modes. Thus, the fact that both of them decay with the same rate, implies that if one put any initial state, the evolution for long times will be a mixture of modes with no fixed phase. Hence, this system will tend not to be synchronized. However, as we will see later, the small difference on the imaginary part, still make them to synchronize at very long times. In this case, the longest living mode is the antisymmetric. Therefore any evolution will tend to evolve in anti-phase for enough long times.

A similar situation is found for the second example (see Fig. 4.2-**B)**. The difference on this case is that we are only concerned in the two nanoparticles of the ends. Between those two NP, we can still define the Symmetric and Anti-symmetric modes and associate their decays with the imaginary parts observed in Fig. 4.2-**B**.

For the third case, where the middle site has a greater decay component, we observe that the imaginary parts are different even for the ω^2 plot. For this case we observe that the Anti-symmetric mode of oscillation, which correspond to the central energy in Fig. 4.2-**C**, is the state that has the lower value in the imaginary part. Thus, as we will further check with the simulations, the Anti-symmetric mode is the longest living mode.

At this point it is important to mention that our first intention was to find a phase transition where the synchronization drastically disappear with the variation of one parameter. This behavior for example is observed in Fig. 4.3 where the higher value for the damping Γ, in the central nanoparticle, enables the collapse of the frequencies

just like the case studied by Weinreich in Ref. [Weinreich, 1979]. However, this set of values, is not experimentally accessible. Thus, to keep our analysis within realistic parameters, we relax the search for a non-analytical transition and only observe the phase-synchronization within experimental values.

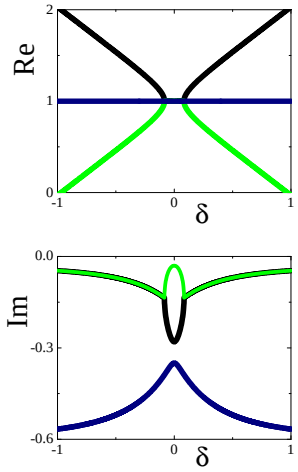

Figure 4.3: Equivalent to Fig. 4.2, but for with 3-particle system where the damping Γ for the central nanoparticle is high enough.

After these three examples we have seen how the number and the form of the nanoparticles allows us to obtain synchronization with different types of fixed phases. It is important to note that the essential key in all this model is the intrinsic decay suported by each nano-particle. The NP material and the form of each one, determines the decaying rate of the polarization. This enables the survival of only one mode of oscillation for long times. However, the amplitude of the oscillations of the LSPs decays so fast that it would be impossible to measure this phenomenon in experimental setups. Therefore, two thing are desirable in order to use it for concrete applications. First, it should be possible to control how the LSP will remain oscillating at long time and second, the amplitude of the oscillation should be kept constant over time. This last subject will be solve in the next sections by the introduction of active medias which inject energy to the system in such a form that it not force the system to oscillate in a specific mode.

4.3.1 Phase Synchronization

The key to fixing the relative phase is a careful designing of the damping factors of the NPs in such a way that it leaves one normal mode with zero weight over the sites with the largest damping factors. In the problem of Fig. 4.2-**C**, it has been shown that the middle NP has a larger damping factor. There, the three normal mode are the following:

$$\begin{aligned} \text{Mode-1 (totally Symmetric):}\ & (P_1 + \sqrt{2}P_2 + P_3)/4, \\ \text{Mode-2 (Anti-Symmetric):}\ & (P_1 + 0 \times P_2 - P_3)/2, \\ \text{Mode-3 (partially Symmetric):}\ & (P_1 - \sqrt{2}P_2 + P_3)/4. \end{aligned}$$

The only mode which has zero weight over the nanostructrure is second one (Anti-Symmetric). For $\delta = 0$, this state will have a smaller decay rate compared with the other two which have finite weights over the highly dispersive nanostructrure, the 2nd NP in this example. In this respect it should be mentioned that there are several ways of increase the damping factor of a NP. One is to change the shape or material of the NP but there are other alternatives like connecting the NP to a waveguide [Bustos-Marún *et al.*, 2010]. After the analysis of several models, we decided, in this chapter, to use the shape of the NPs to control the damping factors, being the radiation damping term the dominant one for the highly dispersive NPs, and the electronic damping term the dominant one for the other NPs.

In order to complete the analysis of what we explained, we calculate the temporal evolution of $P_i(t)$ by using Eq. 4.7. In the three concrete examples of Fig. 4.1 we show how changing the shape of a NP can be used to control phase fixation. In Fig. 4.4 it is shown the dynamical evolution for those examples. It is important to note that here we consider the full dependence of ω_{x}^2 and Γ with the frequency (ω). Also, we use realistic values for the constant by taking into account explicitly the material used (Ag: Silver) and shape of NPs (Ellipsoidal NP: between 8 and 90 nm of diameter).

In the lower inset of each plot in Fig. 4.4 it is shown the amplitude of the normal modes. There we observe that, for the first two cases, the symmetric and the anti-symmetric mode have little differences, but at the end only one survives. On the other hand, for the third case, the anti-symmetric mode has the shortest decay rate, and its

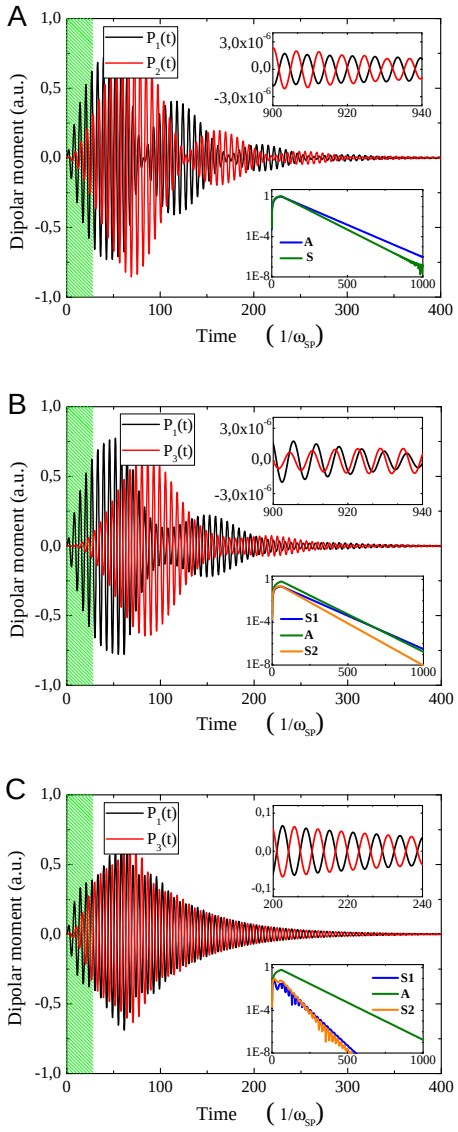

Figure 4.4: **A**: Dipolar moment in arbitrary units vs time in units of ω_{SP}^{-1} for two NPs (1 and 2) of Ag of 30x30x8 nm, separated $32nm$ in water, $\epsilon_m = 1.77$. Between $t = 0$ and 62 an external field of frequency $\omega = \omega_{SP}$ is applied locally at NP 1. **B**: The same but for three NPs (1, 2, and 3) with the middle one, NP 2, having a different size and shape 90x90x8 nm. **Upper insets**: Detail of the main figure. **Bottom insets**: Detail of the decay rate of different modes of oscillation. Mode S is $(P_1 + P_2)/2$, mode $S1$ is $(P_1 + \sqrt{2}P_2 + P_3)/4$, mode A is $(P_1 - P_3)/2$, and mode $S2$ is $(P_1 - \sqrt{2}P_2 + P_3)/4$. In all the cases, we exited the system with an external field during the period of $t_{exitation} = 2Pi * 10$. After that, we let the system evol without any electrical field.

evolution separates very much from the others modes. Thus, for long times, the upper inset of Fig. 4.4, shows a clear anti-phase synchronization between the first and the last site of the system 3.

Another important aspect to analyze is the effect of δ, the difference in frequency of the NPs, on phase synchronization. A non zero δ has two consequences, the first one is that in general it changes the imaginary part of the eigenvalues of $\mathbb{M}$ and thus the relative decay rates, see Fig. 4.2-**C** for example. The other one is that it also changes the eigenfrequencies of the system (the real part of the poles). Then, if the objective were to make NPs of the ends to oscillate in anti-phase as in the case shown in 4.4-**C**, a δ different form 0 will allow a transfer the excitation from the mode A, to modes *S1 (totally symmetric)* and *S2 (partially symmetric)* of the inset. However, if δ is not so large ($\delta \lesssim 0.1$ in the third case), the only appreciable effect is a small fluctuation in the relative amplitude of P_1, P_2 and P_3 which no affects the overall behavior.

4.3.2 Active Media.

As mentioned above, there is a problem with the synchronization phenomenon. The SP dynamics occurs extremely fast, making it very difficult to measure and limiting its possible applications. Note that the time scales are in units of the unpertubed frequency ω_{SP}, which for the used NPs, is around 0.2 fs. This imply that all the process start and finish in less than 0.1 ps approximately. At present there is no capable devide of measure such faster dynamics. Hence, it is mandatory to keep the system oscillating for longer periods of time in order to have a chance of measuring the synchronization phenomena. The first idea that ones has in mind, is to put a permanent external field, but this is no longer synchronization. It would be more like the forced coupled oscillator, where the eigen-frequencies, are equal to the external frequency.

One experimental feasible option to maintain the amplitude, was embedding the system in an optically active medium. If the gain of the active medium is below the loss compensation threshold, its effect can be modeled phenomenologically on the basis of classical electrodynamic without taking into account explicitly the quantum dynamics of the chromophores. This is done by considering the *active medium* as a dielectric material with a *negative imaginary part* in the refraction index n, $n = n_0 - i\kappa$ [Kottos, 2010, Krasavin *et al.*, 2011, Citrin, 2006, Wuestner *et al.*, 2010, Noginov *et al.*, 2009, Stockman, 2008, Li & Xia, 2010, Stockman, 2009]. *A priori* it is

not obvious how it will affect the synchronization mechanism depicted in Fig. 4.4, because the evaluation of the dielectric constant $\epsilon_m = n^2$ enters not linearly in all the equations (see Eqs. 4.1 and 4.6).

In order to explore the effects of incorporate the active media, we proceeded to numerically evaluate (with the fourier transform of Eq. 4.7) the full dynamics for the three systems of Fig. 4.1. In Fig. 4.5 we show that such incorporation of optical gain mediums do not change what we have seen in Fig. 4.4. In the evaluation of the dynamics we have used a value for κ that almost completely compensate the losses produced by the NP damping. Thus, at least for these cases, the incorporation of the active medion do not change synchronization of the SP neither the final relative phase. The only difference, apart of keeping the system oscillating for longer periods of times, is that active media increase even further the differences in the decaying rates, making the fixing of the phases to occurs even earlier.

As the system remains oscillating for longer periods of time, it is easier to see the final relative phase and how it is affected by tailoring the damping factors. For the system 1, the NPs end oscillating in anti-phase, in case 2 the NPs of the ends finish oscillating in phase, while, if we increase the damping factor of the middle NP as in case 3, the NPs oscillate in anti-phase for longer times. As mentioned before the reason of that is simply that the anti-phase oscillation of the NPs of the ends interfere destructively over the NP of the middle, which has the largest damping factor. The other two normal modes due to their weight over the middle NP, have a faster decay rate.

4.3.3 Gain-Loss Compensation.

At this points it is important to bring light into the limiting value of κ, i.e. the value of κ_{lim} for which all the losses are compensated. The value of κ_{lim} can be evaluated from the poles of Eq. 4.1 by looking for pole with have the smallest imaginary part. Thus, κ_{lim} is the value of κ for which the imaginary part of this pole reach zero. It is important to remark that the imaginary part is associated with the decay rate, therefore its zero value implies that the state will survive forever. In some cases, it can be easy to analytically obtain the value of κ_{lim}, but in other cases one must resort to numerical evaluations.

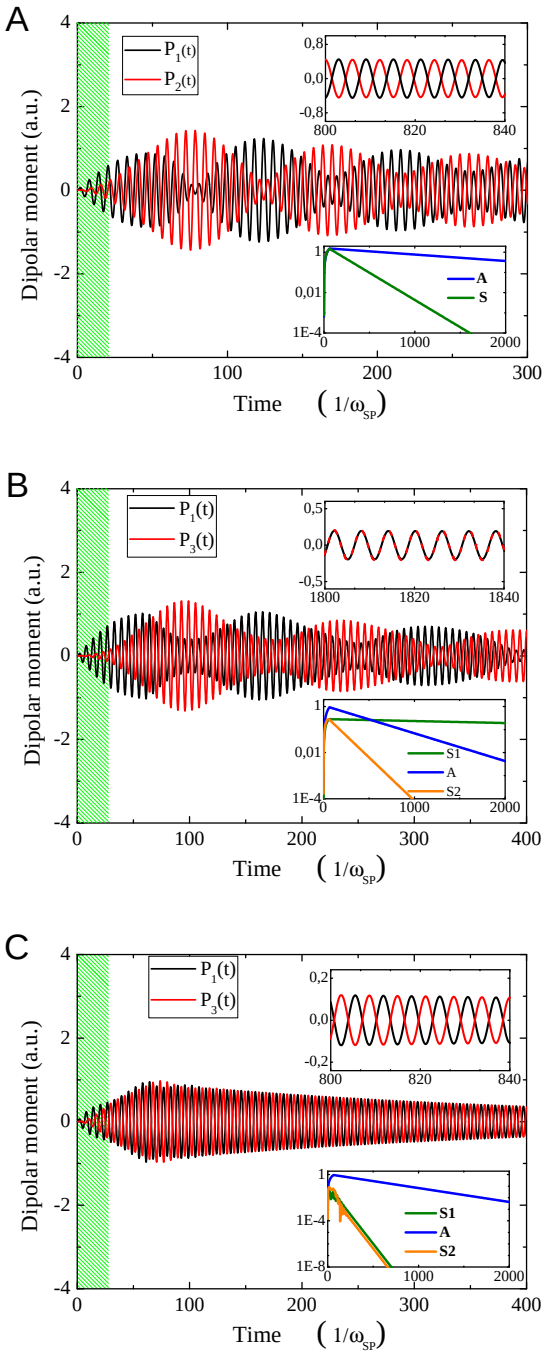

Figure 4.5: Same than Fig. 4.4 but considering an optically active medium with $\kappa = 0.1$.

In the third example (see the **C** plots of Figs. 4.2 and 4.5), the eigenvalue of the Anti-symmetric eigenmode $\omega^2_{\mathrm{eig-A}}$, can be obtained by assuming $\delta \approx 0$, and using the wide band approximation:

$$\omega^2_{\mathrm{eig-A}} \approx \omega^2_{\mathrm{SP}} - \mathrm{i}\Gamma. \tag{4.9}$$

By remembering that ω^2_{SP} is the SP resonant frequency of the unpertubed NPs of the ends, and Γ is its damping factor, we can obtain the value of κ_{lim} by using: Eq. 4.5, $\epsilon_m = n^2$, and assuming a small value of κ. The result is the following:

$$\kappa_{\mathrm{lim}} \approx \frac{\Gamma[n_0^2 + L(\epsilon_\infty - n_0^2)]}{2n_0\omega^2_{\mathrm{SP}}(1-L)} \tag{4.10}$$

For the first two examples of Fig. 4.1, the equations become more complex, due to the presence of ω^2_{X} (which depends of κ) in the whole calculation. Despite of this, they can be evaluated by numerical method and the results are,

$$\begin{aligned} &\text{System 1: } \kappa_{\mathrm{lim}} = 0.113, \\ &\text{System 2: } \kappa_{\mathrm{lim}} = 0.112, \\ &\text{System 3: } \kappa_{\mathrm{lim}} = 0.117. \end{aligned} \tag{4.11}$$

This values, obtained for κ_{lim}, should be accessible experimentally based on Refs. [Pisignano *et al.*, 2002, Noginov *et al.*, 2009], [Carre're *et al.*, 2006, Seidel *et al.*, 2005, Noginov *et al.*, 2008].

The value of κ, related with the amplification coefficient $g = 4\pi\kappa/\lambda$, is a phenomenological coefficient that represent the property of some media of coherently amplify electromagnetic fields. Gain media in plasmonics are made of chromophores that overlap spatially and spectrally with the surface plasmon modes of the nanostructure. This chromophores may be semiconductors nanocrystals, dye molecules, rare-earth ions, or electron-hole excitations of a bulk semiconductor [Bergman & Stockman, 2003, Stockman, 2009, Stockman, 2010]. In general, the gain coefficient depends on the stimulated emission cross section σ_e and the concentration of electron-holes pairs N, or the concentration and the inversion population of the dye molecules, $g = N\sigma_e$ [Li & Xia, 2010].

This leads to another important aspect: what happens when $\kappa > \kappa_{\text{lim}}$? If we follows the above reasoning, we found that $P(t)$ should grow exponentially *at infinitum*, which is not realistic. At some point the pumping mechanism that keeps the inversion population must be overcome by the decay rate of the molecules in the excited state toward their fundamental state. The realistic situation is that the amplitude of the surface plasmon oscillations should stabilize at some point, and this is the reason of why it is difficult to build plasmonic amplifiers based on active media [Stockman, 2009, Stockman, 2010]. A complete treatment would require to solve the quantum mechanics dynamics of each chromophore under the influence of the electromagnetic field corresponding to its position and the coupled equation of motion of the surface plasmon dynamics. This was done by Stockman (in Ref. [Stockman, 2009]) in the context of spasers and the important result, for our work, is that the system evolved in a complex way until a stationary regime is reached. This stationary regime corresponds to the situation in which all the dampings are just compensed by the amplification of the active medium [Stockman, 2009, Stockman, 2010], a condition expressed in our case by Eq. 4.11.

Essentially, the convergence towards a stationary regime where losses are compensated, implies the fixing of the amplitude. The evaluation of the final value for the amplitude could be difficult to evaluate, however the important thing is that it exist and it is non zero for $\kappa_{\text{initial}} > \kappa_{\text{lim}}$.

The other important issue is that once the stationary state is reached, the inversion population freezes at the value of $\kappa = \kappa_{\text{lim}}$. Then, independently of the value of κ_{initial}, the evolution should have the same behavior at long time as for the case of $\kappa_{\text{initial}} = \kappa_{\text{lim}}$.

Just as an illustrative example, lets assume that the dynamics of the population inversion is much faster than the dynamic of the surface plasmons, i.e population inversion adapts instantaneously to a given value of the dipolar moments P_i. Under this assumption we can think in the existence of a function $\kappa(|P|)$ which governs the evolution of κ as a function of the instantaneous modulus of the dipolar moment P. This function should be maximum for $|P| = 0$, $\kappa(P) = \kappa_0$, because at this point the system should have the maximum gain of the media, however, when $|P|$ increases, the have to decrease somehow in order to cross the κ_{lim} value.

Which the purpose of observe the effect of this dependence of the active media, we will use some hypothetical model for $\kappa(P)$ and then numerically evaluate $P(t)$ by means of Eq. 4.8. We have tried several ad-hoc models for $\kappa(P)$ and obtain similar results for

all the cases. Fig. 4.6 just shows one example of that for $\kappa(P) = \kappa_0\ exp\{-(|P|/P_0)^2/2\}$ with $\kappa_0 = 0.2$ and $P_0 = 0.75$ applied over the system 3 of Fig. 4.1. The results show that after a transient regime, that of course depends on the particular model of $\kappa(P)$, the evolution reaches a stationary state characterized by a fixed amplitudes different from zero. It is also observed that the phases remains fixed as in Fig. 4.5 and they are still determined by the slowest decaying normal mode.

The behavior observed in all the evolutions of the hypothetical models is that independently of the initial conditions or the particular model of $\kappa(P)$, the value of κ always evolves until it asymptotically reaches the same and fixed value of κ_{lim}, given by Eq. 4.11. After that point, the dynamics of P corresponds to that governed by the fixed value of κ_{lim}.

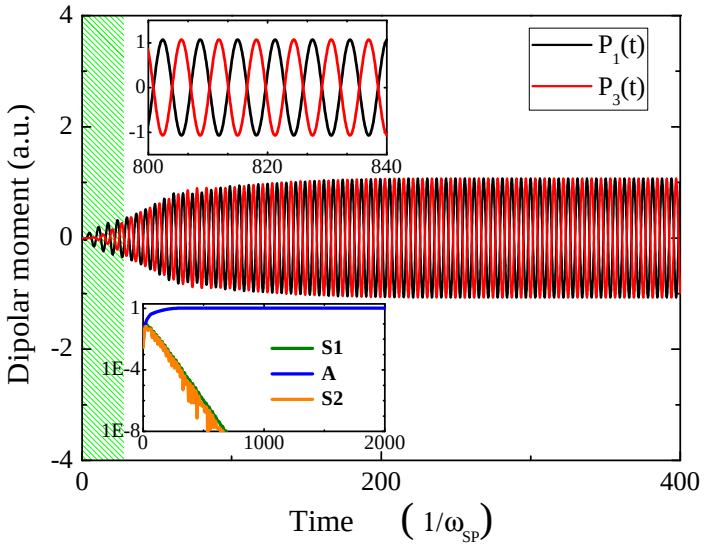

Figure 4.6: Same than Fig. 4.5-C but considering an explicit dependence of $\kappa(P)$. It is observed that the evolution reach and stationary amplitude value, while the oscillations still correspond with the Anti-symmetric mode.

4.3.4 Generalization to More Complex Structures.

The proposed synchronization mechanism can be easily extended to more complex nano-structures. The key ingredient is that all normal modes except one, must have some weight on the highly dispersive NPs, for example the middle Nanoparticles in

Fig. 4.5-**C**. Then, if the damping factor of the highly dispersive NP is large enough, the slowest decaying normal mode which will control the longtime relative phases of the LSP, is that which has zero weight over these NPs.

In Fig. 4.7 we present a set of possible examples in the nearest neighbor approximation, of how to extend our proposal to more complex nanostructures. The light blue NPs represent equal NPs with large damping factors while the golden ones represent equal NPs with small damping factors. In this cases, there is always one eigenvalue of $\mathbb{M}$ that has zero weight over the light blue NPs. This normal mode corresponds to the one where the LSP of the golden NPs oscillates in anti-phase with respect to their nearest golden NPs neighbors. Then, this mode will have the slowest decay rate, and thus controlling the phase fixation at long time, for a sufficiently large damping factor of the light blue NPs. Furthermore, as mentioned in the previous section, amplitude fixation should be achievable by embedding the system in an optical active medium. Therefore, the system will be a source, of arbitrary nano-metric size, of evanescent electromagnetic fields with a predetermined interference pattern.

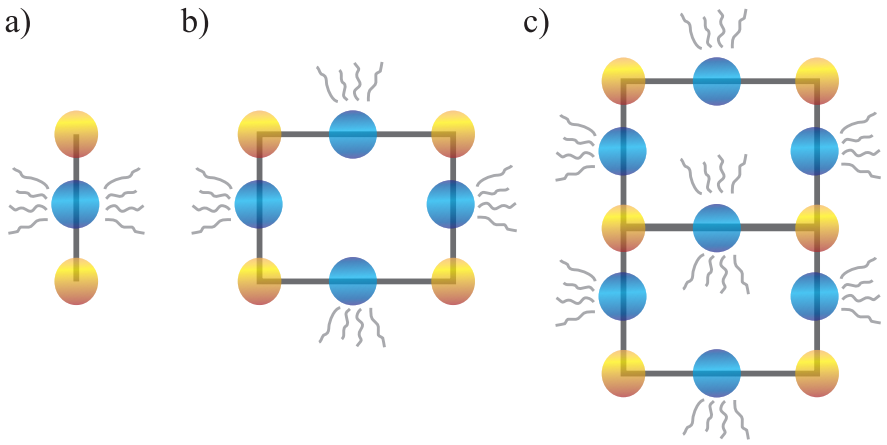

Figure 4.7: Scheme showing how to generalize that shown in Figs. 4.1 to arbitrary large nano-structures with nearest neighbors interactions. The blue Nanoparticles have the largest damping factors. The oscillation mode which have zero weight over this sites, is the one that most will survive.

4.4 CONCLUSIONS.

In this chapter we have shown a way of controlling the phase final relative phases of the localized surface plasmons of different NPs in a array. The specific tailoring of the damping factors allows us to control the phase of the synchronization. Furthermore, we have shown that is should be possible to keep the system oscillating with constant amplitude by including an optically active media properly tuned. We interpret that this as a new example of synchronization as we are in presence of self sustained oscillating objects, clearly separable, that present the fixing of the phases as consequence of their mutual interaction and also maintain their amplitude for long times. The ability of controlling the asymptotic state of these NP arrays, allows the designing of interference patterns in the subwavelength scale which could have applications in optoelectronic, nanoscale lithography and probing microscopy.

4. SEEKING THE SYNCHRONIZATION OF PLASMONIC OSCILLATORS IN NANO-PARTICLE ARRAYS

Chapter 5

Simple Models for Non-Markovian Structured Environments

5.1 INTRODUCTION

In this chapter, we recover the analysis of decoherence processes in spin system previously introduced in Chap. 2 and start analyzing the effects of multiple connection between the system and the surrounding spins (the environment). By the moment we will continue working within the fermionic models, in order to get a full understand of the XY dynamics, but in the following chapters, this analysis, will help us to get a deep understanding on the full many-body spin dynamics.

The work developed in this and the following two chapters was made in collaboration with Pablo R. Zangara, who is also studying decoherence process in spin systems.

Let us start remembering that the interaction rate $1/\tau_{\mathcal{S}-\mathcal{E}}$ between a quantum system $\mathcal{S}$ and its environment $\mathcal{E}$ is typically evaluated from a Fermi Golden Rule (FGR), which assumes that the environment has a Markovian nature. Thus, it neglects any trace of memory becoming from the environmet. However, as we have seen in Chap. 2, the interplay between the system time scales (e.g. $1/\omega_0$) and that of the interaction ($\tau_{\mathcal{S}-\mathcal{E}}$) could result in striking effects. While weak interactions ($1/\tau_{\mathcal{S}-\mathcal{E}} \ll 2\omega_0$) simply degrade dynamical interferences at a rate $1/\tau_\phi \propto 1/\tau_{\mathcal{S}-\mathcal{E}}$, stronger ones may change the system's response radically, leading to a quantum dynamical phase transi-

tion in its dependence on $1/\tau_{\mathcal{S}-\mathcal{E}}$ [Álvarez *et al.*, 2006]. Indeed, the possibility of a non-analytic behavior appears because the system's effective Hamiltonian is non-Hermitian [Rotter, 2009, Pastawski, 2007]. This, in turn, can be traced back to the fact that the environment has a number of degrees of freedom $\mathtt{N}$ which can be considered infinite. As P.W. Anderson put forth: "more is different", and new physical phenomena may appear when this thermodynamic limit ($\mathtt{N} \longrightarrow \infty$) is properly taken [Anderson, 1972]. Indeed, there are several models of both non-Markovian and Markovian environments [Chakravarty & Leggett, 1984, Danieli *et al.*, 2007, Álvarez *et al.*, 2007, Pastawski, 2007] which show that the frequency spectrum is a non-analytic function of the interaction strength [Anderson, 1954].

While the Markovian approximation is sufficient for most traditional applications, it leaves aside important memory effects and interferences in the time domain. These result from the coherent interaction between $\mathcal{S}$ and $\mathcal{E}$, and are becoming a topic of increasing interest [Taylor *et al.*, 2003]. The system-environment dynamics may go through different temporal regimes, passing from a quadratic short time decay to the usual exponential FGR decay and then to an inverse power law behavior that appears for very long times (see Chap. 2 and Ref. [Rufeil-Fiori & Pastawski, 2006]). Here, we will focus on the more relevant exponential (or intermediate) regime, treated with a Self-Consistent (SC) FGR, which gives rates different from the standard FGR due to the bath memory effects. Once again, a deep understanding of the environment dynamics is central to identify the different regimes and to foresee possible dynamical transitions.

A natural way to quantify the decoherence time τ_ϕ is through the degradation of specific interferences, e.g. Rabi oscillations [Müller *et al.*, 1974, Danieli *et al.*, 2005] or mesoscopic echoes [Mádi *et al.*, 1997, Álvarez *et al.*, 2010a, Pastawski *et al.*, 1995, Pastawski *et al.*, 1996]. Alternatively, the implementation of a time reversal procedure, the Loschmidt Echo (LE) [Jalabert & Pastawski, 2001], allows the evaluation of the decoherence time by measuring the reversibility of the system's dynamics in presence of an uncontrolled environment. The LE can be accessed experimentally in spin systems [Pastawski *et al.*, 2000, Levstein *et al.*, 1998], confined atoms [Andersen *et al.*, 2006], microwave excitations [Schäfer *et al.*, 2005], etc., and has become a powerful tool for quantifying decoherence, stability and complexity in dynamical processes in several physical situations [Gorin *et al.*, 2006, Jacquod & Petitjean, 2009].

In this chapter we consider again the evolution of two coupled spins in the $\uparrow\downarrow$ and $\downarrow\uparrow$ configurations (as was made in Chap. 2) in the presence of different spin environments with a fully characterized coherent dynamics [Dente *et al.*, 2008]. It is important to remember that the Rabi oscillations presented in that system [Cohen-Tannoudji *et al.*, 1998] can act as a SWAP gate, and after appropriate mappings, this boils down to an excitation that jumps between two degenerate states A and B according to a coupling V_{AB}, which can be switched at will. Starting on state A, the return probability oscillates with $\omega_0 = 2V_{AB}/\hbar$, the Rabi frequency. In order to understand the incidence of environmental memory effects in the rate $1/\tau_\phi$, two different issues are considered. First, the *relation between the system's time scale* (typically ruled by $\hbar/V_{AB}$) *and the bath's inner excitation spreading time scale* as determined by the density of directly connected states (Local Density of States, LDoS) $\hbar N_1$. Second, and closely related to the first one, *the specific form in which the system couples to the bath* (see Fig. 5.1):

Each site coupled to a different environment: *Private bath*, or
Both sites coupled to the same environment: *Public bath*.

This allows a quantitative comparison between rates and a qualitative interpretation in terms of the bath's spectral structure. The comparison of the effects of public and private $\mathcal{S}-\mathcal{E}$ interaction should deepen our understanding about how the involved correlations modify the degradation rate $1/\tau_\phi$. Indeed, if the system's and the bath's time scales are similar, then the problem cannot be treated within the Markovian paradigm of a "slow variable interacting with a fast equilibrating background". It requires to be carefully addressed beyond the FGR. Memory effects arising not only from the structured environment but also from collective $\mathcal{S}-\mathcal{E}$ interaction are expected. This last mechanism of correlated coupling (public) has been previously pointed in the literature of open quantum systems, particularly in terms of the spin-boson models [Palma *et al.*, 1996, Breuer & Petruccione, 2007]. It can be shown [Breuer & Petruccione, 2007], at least for a simple model of a $\mathtt{N}-$qubit register, that the decoherence increases linearly with $\mathtt{N}$ for independent reservoirs, while it grows with the square $\mathtt{N}^2$ for a collective environment. This example suggest that such a public interaction may lead to a strong amplification of decoherence. On the other hand, it has been pointed in the literature of error correction protocols that symmetric (public) $\mathcal{S}-\mathcal{E}$ coupling can be exploited to design states that are hardly corrupted by such a coherent environmental noise [Zanardi & Rasetti, 1997]. Finally, in recent

years it has been explored the role of a common environment in the correlations (entanglement) within a system [Buchleitner *et al.*, 2007, Paz & Roncaglia, 2009], and the possibility of creating and manipulating those correlations by environment-mediated interactions [Hor-Meyll *et al.*, 2009]. Notice that spectral correlations in the bath would be quite cumbersome in attempts to describe them in statistical terms. However, realistic Hamiltonian models of the bath should allow a simple and natural description of such correlations.

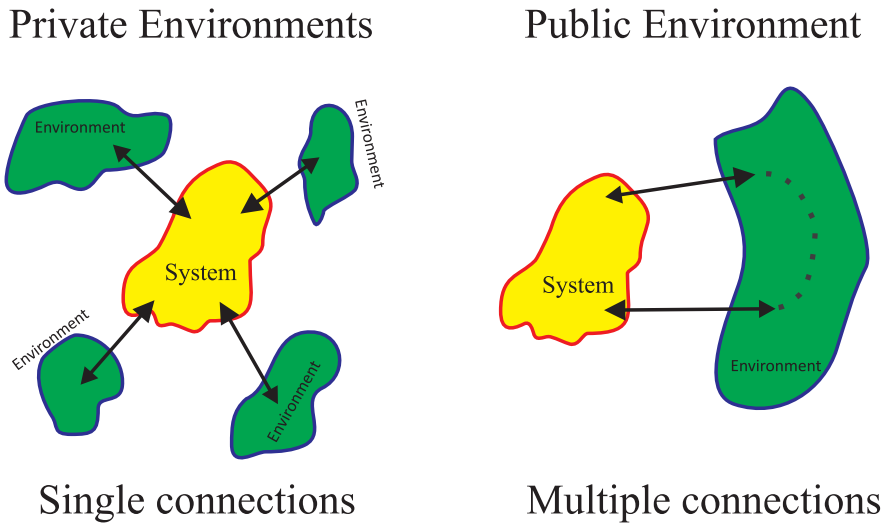

Figure 5.1: Representation of the public and private environments. In the left picture it is observed the single connections to individual environments, while in the other side, we shows the multiple connections to the single environment with the correlations inside the bath.

The cases we analyze can be casted directly to 1-D spin systems interacting by means of a planar (XY or flip-flop) as well as double-quantum (flip-flip / flop-flop) effective Hamiltonians. Indeed, the spin-fermion mapping provided by the Jordan-Wigner Transformation (JWT) [Lieb *et al.*, 1961] has been successfully exploited to predict spin polarization dynamics in linear chains and rings [Pastawski *et al.*, 1995] and results in full agreement with the experiments [Pastawski *et al.*, 1996, Mádi *et al.*, 1997]. It further allowed to address polarization dynamics in homogenous chains [Danieli *et al.*, 2004, Danieli *et al.*, 2005, Rufeil-Fiori & Pastawski, 2006] and multiple spin coherence dynamics [Fel'dman & Lacelle, 1997, Rufeil-Fiori *et al.*, 2009, Cappellaro *et al.*, 2007], [Doronin *et al.*, 2000] by mapping them to fermionic excitations. In both cases, the

local excitation is identified with a single fermion propagating in a tight-binding linear chain, and one can assume that the environment is described by an identical chain. Another interesting application of the tight-binding model, is that their results can be mapped, sometimes quite straightforwardly, to describe the propagation of excitations in several scenarios, like classical and quantum coupled oscillators [Economou, 2006], plasmonics [Bustos-Marún *et al.*, 2010], sound propagation [Calvo & Pastawski, 2010], spin-boson interactions and other models used for decoherence in quantum information [Hu *et al.*, 1992, Bartels, 2011].

Another important issue about the integrability of the chosen model is that it enables an analytical expression valid in the thermodynamic limit of an infinite number of spins. Thus, we are certain when ruling out a phase transition. In fact, an analytically tractable bath means the capability to sum up an otherwise divergent perturbation series into a complex self-energy through the Dyson Equation, which is considered in the FGR approach. Additionally, having a smooth LDoS, which arises from a continuous spectrum ($\mathtt{N} \longrightarrow \infty$), avoids spurious resonances that might appear in finite systems. Besides, we will see that a defined curvature of the LDoS will be central to modify the FGR.

This chapter is organized as follows. In Sec. 5.2 we present the $\mathcal{S} - \mathcal{E}$ tight-binding models that yields a fully solvable quantum dynamics (the underlying spin-fermion mapping is summarized in the Appendix A). In Sec. 5.3, the notions of Survival Probability and local Loschmidt Echo are presented on the face of their numerical implementation. We deal analytically with every case by a Green's Function approach. Further details related to the Green's function poles are discussed in Appendix B. In Sec. 5.4, the analytical decay rates obtained with the FGR and the SC-FGR are presented for each case under consideration. These rates are compared with those computed by numerical solution, contrasting the results of the Survival Probability (SP) and the Loschmidt Echo (LE) of the local excitation. All these magnitudes are analyzed taking into account that the environmental memory effects are provided by its spectral structure (LDoS). In the last section, further discussions and conclusions are presented to argue how the public bath is more effective to depart the decay process away from the usual Fermi Golden Rule (energy independent rate).

5.2 TIGHT BINDING MODEL FOR EXCITATION DYNAMICS

As pointed above, while our motivation relies mainly on spin dynamics under flip-flop interactions, we use the spin-fermion mapping to cast it in terms of tight-binding models that apply to a wide variety of systems. Thus, we leave to Appendix A a brief outline of how this mapping is achieved. Here, we present the models and analyze them in terms of straightforward single particle physics. These are basically variations of tight-binding infinite linear chains where the bath's memory can be fully characterized. Of course, the cases where the interactions network topology has branching points or loops would preclude the simple back transformation into spin systems. However, even in these situations some of the physics of the memory would remain. The general situations are sketched in Fig.5.2.

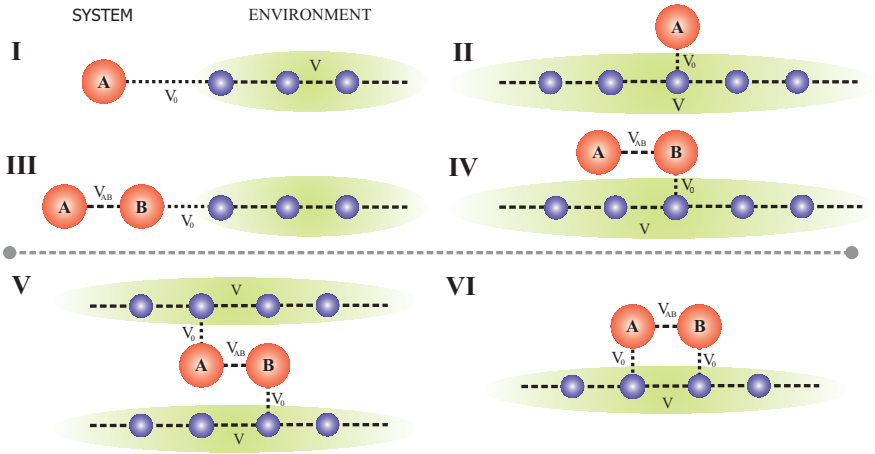

Figure 5.2: Non interacting fermion modelization. **I**) A single site state connected to a semi infinite chain. **II)** One site coupled to an infinite chain. Since $V_0 \ll V$, both cases can be treated by a simple decay process, given by the FGR. **III**) Two sites; the initial configuration is given by a particle in the site **A**. The sites are coupled to a semi infinite chain by only one of them. **IV)** Same as **III**), but with an infinite linear chain standing for the bath.**V)** Two sites coupled both to different infinite chains (private environments). **VI)** Two sites coupled to the same infinite chain (public environment).

For the cases considered in this chapter, the whole Hamiltonian can be written as:

$$\hat{H} = \hat{H}_{\mathcal{S}} + \hat{H}_{\mathcal{E}} + \hat{H}_{\mathcal{S}-\mathcal{E}}, \tag{5.1}$$

where:

$$\hat{H}_{\mathcal{S}} = E_A \hat{c}_A^\dagger \hat{c}_A + E_B \hat{c}_B^\dagger \hat{c}_B - V_{AB}(\hat{c}_A^\dagger \hat{c}_B + \hat{c}_B^\dagger \hat{c}_A), \tag{5.2}$$

with $\hat{c}_s^\dagger$ and $\hat{c}_s$ ($s \in \{A, B\}$), the creation and destruction operators for fermions. The hopping amplitude V_{AB} defines the isolated system dynamical time scale. The bath $\mathcal{E}_\nu$ (where ν=1,2), with a spectral bandwidth of $4V$, is described by the Hamiltonian:

$$\hat{H}_{\mathcal{E}_\nu} = \sum_{n=n_\nu}^{\infty} E_{\nu,n} \hat{c}_{\nu,n}^\dagger \hat{c}_{\nu,n} - V(\hat{c}_{\nu,n+1}^\dagger \hat{c}_{\nu,n} + \hat{c}_{\nu n}^\dagger \hat{c}_{\nu.n+1}). \tag{5.3}$$

Choosing the site energies with identical values: $E_{\nu,n} = 0$ ensures a continuum spectrum, while the election $E_A = E_B = 0$ will further simplify the analysis. Two different alternatives for the spectrum dynamics arise when $n_\nu = 1$ (semi-infinite linear chain) and $n_\nu = -\infty$ (infinite linear chain). The system-bath Hamiltonian $\hat{H}_{\mathcal{S}-\mathcal{E}}$ depends on how we couple our two-site system to the environment (linear chain), but in general it will be of the form:

$$\hat{H}_{\mathcal{S}-\mathcal{E}} = -V_0 \left(\hat{c}_A^\dagger \hat{c}_{\nu,i} + \hat{c}_{\nu,i}^\dagger \hat{c}_A + \hat{c}_B^\dagger \widehat{c}_{\mu,j} + \hat{c}_{\mu,j}^\dagger \hat{c}_B \right), \tag{5.4}$$

where ν, i and μ, j label sites i and j in the environments ν and μ respectively. Here it is important to note that the problem could have several environments. Despite of this, we decided only to work with one or two environments. This will reduce the complexity of the problems, but not the underlaying physics.

It is crucial to stress that V_{AB}, V_0 and V determine the relevant time scales of the whole problem. The first two give the rate of hoppings from site A to site B and to the environment, respectively. The third is the jumping rate between sites in the environment. An "irreversible" decay to the environment, and hence the Fermi Golden Rule, implies that the unperturbed isolated system state has zero overlap with eigenstates of $\mathcal{S} + \mathcal{E}$. For this perturbation theory break down, the interaction with each environment eigenstate, $V_0/\sqrt{\mathtt{N}}$ must be much greather than the spacing between adjacent levels, of about $V/\mathtt{N}$, i.e. the interaction time scale $\hbar/V_0$ must be greater than the environment's Heisenberg time $\hbar\mathtt{N}/V$. Imposing $V_0 \ll V_{AB}$ for all the cases we treated (weak coupling regime), we ensure the smooth degradation of the system's coherent evolution. When $V \approx V_{AB}$ the memory effects characterizing a *non-Markovian*

situation lead to a very rich dynamical behavior. In the opposite limit, if $V \gg V_{AB}$ then the validity of the FGR (*Markovian* situation) is expected to be recovered. Typically, this last situation will be represented in this work by a hopping $V = 5V_{AB}$.

5.3 NUMERICAL AND ANALYTICAL TOOLS

5.3.1 SURVIVAL PROBABILITY AND LOSCHMIDT ECHO

Two kind of measures for dynamical degradation are employed in this work: the Survival Probability (SP) $P_{AA}(t)$ and the local Loschmidt Echo. The SP which has been previous defined in Chap. 2, is:

$$P_{A,A}(t) = \left| \langle A| \exp\left[-\mathrm{i}\hat{H}t/\hbar\right] |A\rangle \, \Theta(t) \right|^2, \tag{5.5}$$

where $\Theta(t)$ is the Heaviside step function, and the Hamiltonian $\hat{H}$ is defined by Eq. 5.1. It is important to remember that it measures the probability of finding a particle in site A at time t, provided that the system has had a particle in the same site at time $t = 0$. In spin systems, this is a spin autocorrelation function (see Eq. A.3 and A.6 in Appendix A). The whole evolution of the system as reflected in the SP, is affected by a decay process, which is not trivial to separate from the intrinsic dynamics. Thus, to quantify decoherence, one relies on the observation of specific features as natural recurrences (Rabi oscillations or mesoscopic echoes) that appear at specific times. This limits the used time windows and limits the detailed assessment of $\mathcal{S} - \mathcal{E}$ dynamics. Although it is not the perfect tool to quantify the effects of the environment, the SP behaves as a probe that reflects the overall dynamical process.

With the purpose of get a continuous access to the $\mathcal{S} - \mathcal{E}$ dynamics that better reflects the environmental memory effects, we focus our attention over the LE. This type of measure has been used in the last years in different physical scenarios (both experimental [Levstein *et al.*, 1998, Pastawski *et al.*, 2000, Schäfer *et al.*, 2005, Andersen *et al.*, 2006] and theoretical [Cucchietti *et al.*, 2003, Gorin *et al.*, 2006], [Jalabert & Pastawski, 2001]) in order to explain the behavior of the decoherence characteristic time. In general, the LE provides a direct measure of the decoherence process due to the environment, and even though it depends on the nature of the system's intrinsic dynamics, it does not depend much on its details. Its usual dynamical behavior

presents an exponential decay regime [1], which will be used to characterize the destruction of the system's coherent dynamics.

The LE relies on the time reversal of the system's evolution and, in the present scenario, it has a direct physical interpretation. The LE can be understood as the measure of the amount of polarization returned to *local* site where it started. The controlled quantum dynamics is separated in two stages. First, the initial local excitation (particle in site A) evolves during a time t_1, and then a time reversal procedure is applied during a period time $(T - t_1)$ which reverses the system's dynamics ($\hat{H}_{\mathcal{S}} \to -\hat{H}_{\mathcal{S}}$). It is important to note that the bath's dynamics and the $\mathcal{S} - \mathcal{E}$ interactions ($\hat{H}_{\mathcal{E}}$ and $\hat{H}_{\mathcal{S}-\mathcal{E}}$ respectively) remain unreversed during the backward evolution. This partial control results in a non-reversed perturbation $\hat{\Sigma} = (\hat{H}_{\mathcal{E}} + \hat{H}_{\mathcal{S}-\mathcal{E}})$ acting in both periods. Finally, the probability of finding the particle in site A forms the Loschmidt echo provided that $t_1 = T/2$:

$$M_{LE}(T) = \left| \langle A | \exp\left[-\mathrm{i}(-\hat{H}_{\mathcal{S}} + \hat{\Sigma})(T - t_1)/\hbar\right] \exp\left[-\mathrm{i}(\hat{H}_{\mathcal{S}} + \hat{\Sigma})t_1/\hbar\right] |A\rangle \right|^2 . \qquad (5.6)$$

Clearly, in the case where the system is isolated, the local LE will have a steady value of 1. This means that the system is fully reversible. On the other hand, if the system is coupled to the infinite and continuous environment's spectrum, both the forward and backward effective Hamiltonians, $\hat{H}_{\mathcal{S}} + \hat{\Sigma}$ and $-\hat{H}_{\mathcal{S}} + \hat{\Sigma}$ respectively, become non-Hermitian. Thus, the LE decays with a characteristic rate, i.e., our reversal procedure has not been able to recover the excitation spread to the environment. The net decay of the norm of the state simply means the decay of the coherent part and then describes the non-trivial part of the Loschmidt Echo.

For the evaluation of both survival probability and Loschmidt Echo, we diagonalize the Hamiltonian and obtain the evolution for every time. We use sufficiently large chains to approximate the nature of infinite ones (just like we do in Chap. 2 and in Ref. [Dente *et al.*, 2008]). Indeed, the evolution times considered in this work are short enough to ensure that the presence dynamical finite-size effects (e.g. mesoscopic echoes appearing at the environment's Heisenberg time) do not build up. A typical system is presented in Fig. 5.3-**a**.

[1] Notice that the systems we are considering do not have enough complexity to warrant a perturbation independent (i.e. Lyapunov) decoherence rate.

In all the cases, we are interested in studying the rates as a function of the $\mathcal{S}-\mathcal{E}$ coupling parameter (V_0). In order to obtain those rates for the local LE, we fit the dynamics by a exponential decay function, which for the case plotted in Fig. 5.3-**b**, it turns to be the envelope of the SP Rabi oscillations and has the advantage of having a monotonous behavior. This mach between the LE and the envelope of the SP is not always true, one should be aware that for an arbitrary system, the characteristic rates obtained by te LE and the SP could be different.

Remembering that every obtained rate is related to a particular choice of V_0, we have ploted the decay rates as a function of $V_0^2/\hbar V$ (Fig. 5.3-**c**). This was made with the objective of verify the validity of a FGR regime:

$$\frac{1}{\tau_\phi} \simeq \frac{2\pi}{\hbar}\left(\hat{H}_{\mathcal{S}-\mathcal{E}}\right)^2 N_1, \tag{5.7}$$

where $\left(\hat{H}_{\mathcal{S}-\mathcal{E}}\right)^2$ is a characteristic second moment of the $\mathcal{S}-\mathcal{E}$ interaction and N_1 represents an appropriate density of directly connected states. It is interesting to comment that because of the linear chain topology the second moment coincides with V_0^2, and N_1 can be identified with a local density of state at the first site of the chain. In a general environment this correspondence can be assigned through a Lanczos transformation [Lanczos, 1950, Rufeil-Fiori & Pastawski, 2006].

5.3.2 ENVIRONMENT'S EFFECT IN A SELF-CONSISTENT FERMI GOLDEN RULE

For the study of the analytical solutions we use the Green's Function (GF) formalism introduced in the Chap. 2. In this framework it is possible to obtain the overall dynamics of the system by looking at the behavior of the GF poles [Rufeil-Fiori & Pastawski, 2006, Dente *et al.*, 2008]. Any element of the retarded GF results a Fourier transform of the full propagator:

$$\begin{aligned} G^R_{AA}(\varepsilon) &= \lim_{\eta\to 0}\int_{-\infty}^{\infty} \langle A|\exp\left[-\mathrm{i}\ \left(\hat{H}-\mathrm{i}\eta\hat{I}\right)\ t/\hbar\right]|A\rangle\,\Theta(t)\exp\left[+\mathrm{i}\varepsilon t/\hbar\right]\mathrm{d}t \\ &= \frac{1}{\varepsilon - E_A - \Sigma(\varepsilon)} = \frac{1}{\varepsilon - E_A - (\Delta(\varepsilon)-\mathrm{i}\Gamma(\varepsilon))}, \end{aligned} \tag{5.8}$$

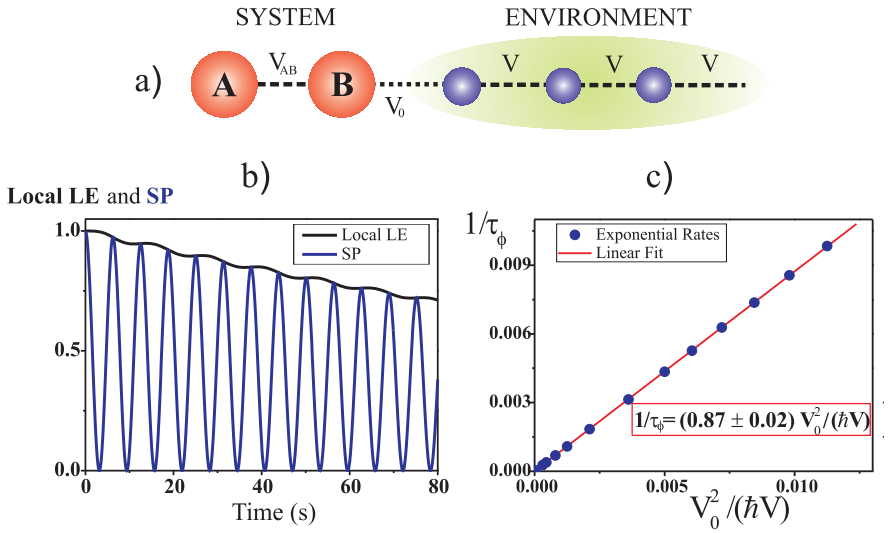

Figure 5.3: Non interacting fermion modelization. **I**) A single site state connected to a semi infinite chain. **II)** One site coupled to an infinite chain. Since $V_0 \ll V$, both cases can be treated by a simple decay process, given by the FGR. **III**) Two sites; the initial configuration is given by a particle in the site **A**. The sites are coupled to a semi infinite chain by only one of them. **IV)** Same as **III**), but with an infinite linear chain standing for the bath.**V)** Two sites coupled both to different infinite chains (private environments). **VI)** Two sites coupled to the same infinite chain (public environment).

where $\Sigma(\varepsilon)$ is the appropriate self-energy with real and imaginary parts $\Delta(\varepsilon)$ and $-\Gamma(\varepsilon)$ respectively. The self-energy operator is diagrammatically presented in Fig. 5.4. The bath memory is contained in their dependence on ε, which arises from the bath's exact Green's Function $\overline{G}^R_{11}(\varepsilon)$ at the directly connected site. Indeed, $\Sigma(\varepsilon)$ is given by $|V_0|^2 \overline{G}^R_{11}(\varepsilon)$, see Fig. 5.4-**b**. All the environments considered in this work (see Fig. 5.2) are 1d chains, which can be reduced to the self-energy of a semi-infinite (or infinite) linear chain ($n_\nu = 1$, see Eq. 5.3), i.e.

$$\Sigma(\varepsilon) = \frac{V_0^2}{V^2}\left[\frac{\varepsilon}{2} - \mathrm{i}\sqrt{V^2 - \left(\frac{\varepsilon}{2}\right)^2}\right] \quad \text{for } |\varepsilon| \leq 2|V|\,. \tag{5.9}$$

For the infinite linear case ($n_\nu = -\infty$), the previous expressions must be multiplied by 2.

Notice that $\Sigma(\varepsilon)$ plays the role of the influence functional in the Feynman path integral formulation usually used to deal with memory effects for bosonic baths [Ingold, 2002]. However, in such cases there are many more free parameters than in our case, i.e. the bath spectral density, the coupling strength with each mode and the temperature that fixes the bath occupation. In our spin environment model however, the last is simplified by the high temperature limit, while the two first become naturally determined by specific sum rules arising from the physical Hamiltonian we select.

We have to remember that the complex GF poles are consequence of the unbounded nature of the system which prevents mesoscopic echoes [Pastawski *et al.*, 1995] and Poincare's recurrences. Also it is important to point out that in the region where we are working ($V_0 \ll V, V_{AB}$), the Hamiltonian holds a continuous spectrum where no localized modes appear.

To get a better understanding of the connection between the dynamical behavior and the poles of the GF, we expand the initial condition in the Survival Probability (see Eq. 5.5) in terms of the energy eigenstates:

$$\begin{aligned} P_{AA}(t) &= \left|\Theta(t)\sum_{k=1}^{\infty}|\langle\psi_k|A\rangle|^2 \exp\left[-\mathrm{i}\varepsilon_k t/\hbar\right]\right|^2 \\ &= \left|\Theta(t)\int_{-\infty}^{\infty}\mathrm{d}\varepsilon\left[\sum_{k=1}^{\infty}|\langle\psi_k|A\rangle|^2\,\delta(\varepsilon-\varepsilon_k)\right]\exp\left[-\mathrm{i}\varepsilon_k t/\hbar\right]\right|^2 . \end{aligned} \tag{5.10}$$

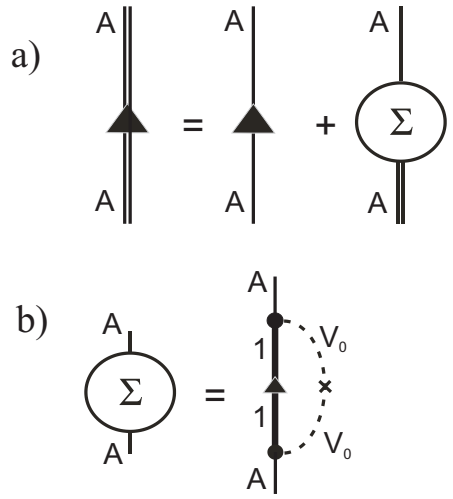

Figure 5.4: **a**) Diagrammatic representation for the retarded GF at site A, in the form of a Dyson's equation. The interaction with the environment is to infinite order in the self-energy given in (**b**) (see Eq. 5.8). Simple lines with arrows are exact GF in absence of $\mathcal{S}-\mathcal{E}$ interactions. **b**) Self-energy diagram sums all orders in the hopping to the environment. Thick line with arrows is the exact propagator at a point of the isolated bath, denoted by $\overline{G}^R_{11}$ (see text).

The term in brackets is identified as the Local Density of States (LDoS) $N_A(\varepsilon)$ at the site A:

$$\begin{aligned} N_A(\varepsilon) &= -\frac{1}{\pi}\,\mathrm{Im}\int_{-\infty}^{\infty}\mathrm{d}t G^R_{AA}(t)\exp\left[-\mathrm{i}\varepsilon t/\hbar\right] \\ &= -\frac{1}{\pi}\,\mathrm{Im}\,G^R_{AA}(\varepsilon). \end{aligned} \tag{5.11}$$

Therefore, we can identify Eq. 5.5 as the LDoS Fourier transform:

$$P_{A,A}(t) = \left|\Theta(t)\int_{-\infty}^{\infty}\frac{\mathrm{d}\varepsilon}{2\pi\hbar}N_A(\varepsilon)\exp\left[-\mathrm{i}\varepsilon t/\hbar\right]\right|^2 . \tag{5.12}$$

The last expression can be numerically and analytically computed once we know the GF in the energy representation (remember that this procedure has been made in the Chap. 4). As a matter of fact, since we have $\Sigma(\varepsilon)$, and hence $N_A(\varepsilon)$, explicitly, we can compute the dynamics from the Fourier Transform mentioned. But, we prefered to obtain the numerical evolution (by exact diagonalization, as explained in previous

section) of a finite environment. The interest in this last method arises from the fact that its use can be directly generalized to more complex systems (many-body), where an exact analytical solution is not accessible. The analytical alternative based on the evaluation of the GF poles will enable to summarize the decay rate in a simple expression, as it is shown below.

The characteristic decay of $P_{A,A}(t)$ is determined by the bath's LDoS, $N_1(\varepsilon)$. This last can be obtained from the isolated bath's exact GF at site 1 (i.e. $\overline{G}^R_{11}$),

$$N_1(\varepsilon) = -\frac{1}{\pi}\,\mathrm{Im}\,\overline{G}^R_{11}(\varepsilon)\,. \tag{5.13}$$

Hence, we recall that $N_1(\varepsilon)$ plays the most relevant role in $\mathcal{S}-\mathcal{E}$ dynamics as was quoted in Ref. [Dente *et al.*, 2008]. In some systems the LDoS can be factorized as $N_A(\varepsilon) = N_1(\varepsilon)\times L_1(\varepsilon)\times L_2(\varepsilon)$ (result obtained in Chap. 2), where $L_i(\varepsilon)$ are Lorentzian functions (LFs) related to the real and imaginary parts (denoted by Δ_0 and Γ_0 respectively) of the GF poles. Hence, the convolution theorem applied to Eq. 5.12 leads to a characteristic decay of $P_{A,A}(t)$ ruled by Γ_0. In fact, the decay parameter of the exponential regime is given by $1/\tau = 2\Gamma_0/\hbar$. This is what we call self-consistent Fermi Golden Rule (SC-FGR) [Rufeil-Fiori & Pastawski, 2006].

With the purpose of finding Γ_0, we focus on the Hamiltonian of Eq. 5.1, and follow the continued-fraction procedure described in Ref. [Pastawski & Medina, 2001]. For each type of $\mathcal{S}-\mathcal{E}$ coupling (see Fig. 5.2), it was necessary to recalculate the poles of the GF. Due to the small number of poles of the systems, it was feasible to obtain the analytical solutions for all the cases presented in this work. Also, we address the behavior of Γ_0 as a function of $V_0 \ll 1$. Indeed, we proceed to expand the solution near $V_0 \simeq 0$.

It is important to notice that in the Taylor expansion, the linear and zero order terms vanish. Therefore, the imaginary part has V_0^2 as the first non trivial term. As expected for a FGR, this is in strong agreement with Eq. 5.7, where we identify the order V_0^2 as the second moment of the $\mathcal{S}-\mathcal{E}$ interaction (in general denoted by $\left\|\hat{H}_{\mathcal{S}-\mathcal{E}}\right\|^2$). In the next section, we present the corresponding values for $1/\tau = 2\Gamma_0/\hbar$, expressed in the first non trivial order (as we said, the 2^{nd} one), for each case considered.

The usual alternative (easier and cheaper) to the presented scheme (SC-FGR) is the simple FGR, which is equivalent to evaluate the Green's function in a first pole

approximation:

$$\left[G^R_{AA}(\varepsilon)\right]^{-1} \simeq \varepsilon - E_A - \Sigma(E_A) \tag{5.14}$$

$$= \varepsilon - E_A - \Delta(E_A) + \mathrm{i}\Gamma(E_A) \tag{5.15}$$

Since this yields an ε-independent rate, it can be understood as a Wide Band Approximation (WBA) [Facchi & Pascazio, 1999]. This approximation would imply neglecting any signature of dynamics and memory effects in the environment. Also, it misses some striking dynamical behaviors appearing at long times as the survival collapse [Rufeil-Fiori & Pastawski, 2006, Dente *et al.*, 2008] and the subsequent power law decay [Khalfin, 1958, Fonda *et al.*, 1978, García-Calderón *et al.*, 1995].

As a matter of fact, the WBA is represented by the condition of $V \gg V_{AB}$. Under this assumption, the environment acquires fast dynamics and the system does not receive any return from it (Markovian limit). In general, the common FGR has the form expressed in Eq. 5.7. There, the last factor (N_1) stands for the LDoS of the directly connected states, and by the application of the WBA, it is evaluated in the middle of the band spectrum (in our case, $\varepsilon = 0$).

In this work it is important to remember that the LDoS varies from the semi-infinite chain ($n_\nu = 1$, surface state) to the infinite chain ($n_\nu = -\infty$, bulk state) as follows,

$$N_{1s}(\varepsilon) = \frac{1}{\pi V^2}\left(V^2 - \frac{\varepsilon^2}{4}\right)^{1/2} \Theta\left[2V - |\varepsilon|\right], \tag{5.16}$$

$$N_{1b}(\varepsilon) = \frac{1}{2\pi}\left(V^2 - \frac{\varepsilon^2}{4}\right)^{-1/2} \Theta\left[2V - |\varepsilon|\right]. \tag{5.17}$$

From the previous spectral structures, we stress the presence of van Hove singularities, which play an important role for long time dynamical behavior [Khalfin, 1958, Rufeil-Fiori & Pastawski, 2006, Dente *et al.*, 2008]. Indeed, the critical exponent characterizing the van Hove singularity can be related to the dimensionality of the space where the quantum excitation diffuses. Also, the two different convexities in the LDoS, near the middle of the band spectrum, will be of great relevance in the following discussions.

Table 5.1: Degradation rates for all the methods analyzed (Survival Probability and local Loschmidt Echo degradation, Wide Band Approximation, and Self Consistent FGR). The cases are described in Fig. 5.2. If the system's and bath's time scales are equal, the physical situation is strictly non-Markovian. We point to restore Markovianity in cases where both scales differ by a factor of five.

System	SP degradation rate $\left[\frac{V_0^2}{\hbar V}\right]$	Local LE degradation rate $\left[\frac{V_0^2}{\hbar V}\right]$	WBA $\left[\frac{V_0^2}{\hbar V}\right]$	SC-FGR $\left[\frac{V_0^2}{\hbar V}\right]$
I	2.04 ± 0.05	2.04 ± 0.05	2	2
II	1.00 ± 0.02	1.00 ± 0.02	1	1
III - ($V = V_{AB}$)	0.88 ± 0.05	0.88 ± 0.05	1	0.87
III - ($V = 5V_{AB}$)	1.00 ± 0.02	1.00 ± 0.02	1	0.995
IV - ($V = V_{AB}$)	0.56 ± 0.02	0.56 ± 0.02	0.5	0.577
IV - ($V = 5V_{AB}$)	0.50 ± 0.02	0.50 ± 0.02	0.5	0.502
V	1.16 ± 0.03	1.16 ± 0.03	1	1.15
VI - ($V = V_{AB}$)	1.71 ± 0.04	1.20 ± 0.04	1	1.732(*forward*) and 0.577 (*backward*)
VI - ($V = 5V_{AB}$)	1.11 ± 0.03	1.02 ± 0.03	1	1.106(*forward*) and 0.904 (*backward*)

5.4 DECAY RATES: FGR AND BEYOND

In this section we expose the main results of this chapter. They are summarized in Table 5.1, where the decay rates are presented as function of $V_0^2/\hbar V$, for every case analyzed (Fig. 5.2) and each approach employed (SP degradation, local LE degradation, WBA-FGR, and SC-FGR).

The rates predicted in the WBA column of Table 5.1, correspond to the direct evaluation of Eq. 5.7, i.e.:

$$\frac{1}{\tau_\phi} \simeq \frac{2\pi}{\hbar} V_0^2 N_{1\lambda}(\varepsilon = 0), \tag{5.18}$$

where λ stands for s (surface, for semi infinite chains) or b (bulk, in the case of infinite chains), in accordance to Eq. 5.16 and Eq. 5.17 respectively. Also, the details on the analytic calculation of the rates (SC FGR column, obtained by means of the GF poles) are presented in the Appendix B.

Systems **I** and **II** involves only one site. The difference between them is that **I** has a semi infinite chain acting as environment and **II** has an infinite one. The decay rates for these cases can be directly evaluated within the WBA, and agree exactly with the numerical solutions.

From the cases **III** to **VI**, the system acquires his own time scale ($\hbar/V_{AB}$). For these cases, we consider two time scales for the environment, as compared to the system's

time scale. The first one, in which the time scales are equal ($V = V_{AB}$) and the second in which the environment is "accelerated" by five times ($V = 5V_{AB}$).

Quite obviously, when the environment has the same time scale as the system, the WBA rate does not works at all. However, the rates computed by SP and LE degradation agree with the SC-FGR perfectly (except for the public environment, case **VI**, which will be analyzed below). This last quantity can be interpreted as the LDoS of the bath being evaluated in the exact solution for the eigen-energies of the whole ($\mathcal{S}$ and $\mathcal{E}$), and not in the middle of the band spectrum (see Fig. 5.5-**a)**. Indeed, the rate of the SC-FGR is obtained by evaluating the LDoS at the real part of the GF poles.

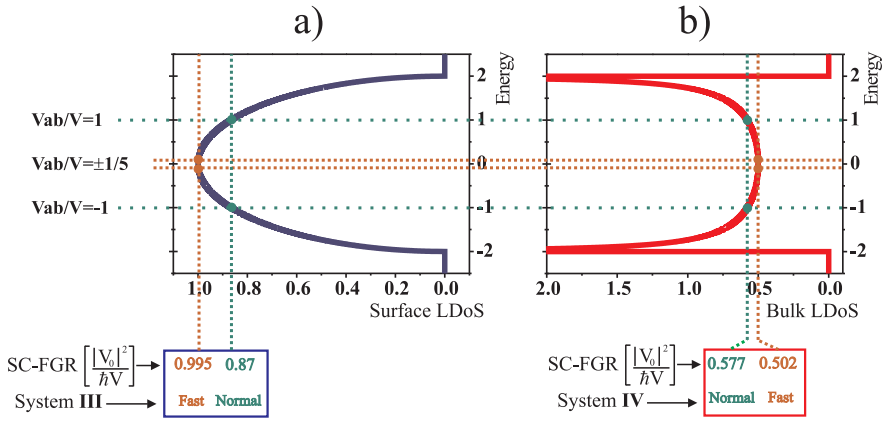

Figure 5.5: Local Density of States for: **a**) Semi-Infinite chain (Surface) and **b**) Infinite chain (Bulk). The horizontal dashed lines are the values V_{AB}/V which stand for the system energies (renormalized with V). The vertical dashed lines together with their numerical values are the LDoS for each system in the normal ($V = V_{AB}$) or the fast ($V = 5V_{AB}$) configuration.

It is important to notice that the rate obtained for the SC-FGR are *higher* or *lower* than the predicted by the WBA, depending if the bath is *infinite* or *semi-infinite respectively*. We can interpret this result by looking at Fig. 5.5. Once we evaluate the LDoS in $\mathrm{Re}\,(\varepsilon_{pole}) \simeq \pm V_{AB}/V$, we observe that the values are lower for the SC-FGR than the WBA in the semi-infinite LDoS, otherwise it is higher if the infinite LDOS is considered.

At this point, for the two level system, we are able to link the convexity of the bath's LDoS to the observed decay rate. We notice that if the LDoS is *convex*, the exact rates are *greater* than the WBA prediction (see Fig. 5.5-b), but instead if it is

concave, the rates are *smaller* (see Fig. 5.5-a). In other words, it depends on the shift away from the middle of the band spectrum, moving along the LDoS slope.

In order to point to the strictly Markovian case, where any return from $\mathcal{E}$ to $\mathcal{S}$ is suppressed, we examine accelerated environments. For these cases, all the rates converge to the same value. From Fig. 5.5-**a** we can see the convergence of the exact solutions towards the middle of the band spectrum, as long as the condition $V \gg V_{AB}$ is better fulfilled.

So far we have only considered a single and private environment, and in the following cases we address the private-public discussion. As we mentioned before, *private baths* act over each site individually, and a single *public bath* acts over two (or eventually more sites) of the same system (see Fig. 5.1). This public $\mathcal{S} - \mathcal{E}$ interaction induce new types of correlations, increasing the dynamical complexity of the physical process.

For case **V** we explore the possibility of two private baths (i.e. two infinite environments each one connected to one site). Since here both sites, instead of only one, are affected by the environment, it is expected a double rate compared to the case **IV** (this is because we have doubled the sources of decoherence). In Table 5.1 we found that the simulations agree with the analytical prediction and again, the rates are greater than the WBA value, which means that we are moving with the exact eigen-energies through a convex LDoS, away from middle of the band.

Finally we analyze a very interesting case, where the system is in presence of a public bath (**VI**). For these cases it is observed that the SP rate differs from the local LE. This behavior shows a certain asymmetry between the forward and backward evolutions. Using the SC-FGR approach it can be shown that the imaginary part of the poles depends on the relative value of V_{AB} and V (see Appendix B),

$$\frac{1}{\tau} = \frac{2}{\hbar}\Gamma_0 \simeq \frac{\sqrt{4V^2 - V_{AB}^2}}{2V - V_{AB}} \frac{V_0^2}{\hbar V}. \tag{5.19}$$

This dependence induces a different decay rate whenever the system evolves forward ($V_{AB} > 0$) or backward ($V_{AB} < 0$). Thus the SP and the local LE are not equivalent for the this case (see Table 5.1). It is worth mentioning that the asymmetry (dependence on the relative sign) in the rates for the forward and backward evolutions, can arises only when the bath is public.

The analytical prediction for the local LE rate is obtained by observing that the total evolution for the reversed dynamics is proportional to a product of two exponential evolutions (the forward and the backward),

$$M_{LE}(T=2t) \propto \exp(-\frac{t}{\tau_f}) \exp(-\frac{t}{\tau_b}) \tag{5.20}$$

$$= \exp\left[-t\left(\frac{\tau_f+\tau_b}{\tau_f\tau_b}\right)\right] = \exp\left[-T\left(\frac{\tau_f+\tau_b}{2\tau_f\tau_b}\right)\right], \tag{5.21}$$

where τ_f and τ_b correspond to the forward and backward degradation rates (see also case **VI** in Table 5.1). Eq. 5.20 shows that the mean rate for a single time-reversed evolution should agree with the LE decay ($1/\tau_{LE} = 1.20 \pm 0.04\ V_0^2/\hbar V$). In fact, this is true, since the two SC-FGR rates ($1/\tau_f$ and $1/\tau_b$) yield a mean value $1/\tau = 1.15\ V_0^2/\hbar V$. Moreover, and quite obviously, the *forward* rate agrees with the SP decay.

Let us now link the decay process to an appropriate LDoS. As it is shown in Appendix B, we can transform the original model of case **VI** to an equivalent one by performing the symmetric transformation analyzed in Chap. 3 (see Fig. 5.6). If the suitable change of basis is applied (basically turning pairs of sites into the symmetric and anti symmetric basis), then it is only necessary to analyze two semi infinite linear chains. Which just are the particular cases treated in Ref. [Rufeil-Fiori & Pastawski, 2006, Rufeil-Fiori & Pastawski, 2009]. Since the initial condition has equal weight on both effective chains, the corresponding rates for them have to be added. Further details on the symmetrization transformation are explained in Appendix B.

From the LDoS considered in Fig. 5.7 we can explain why the rate $1/\tau_f$ is always above the WBA limit, and the $1/\tau_b$ rate is always below it. Moreover, as long as the *forward* rate agrees with the SP decay, this also supports the SP rate being greater than the WBA value (see the "Forward" points in Fig. 5.7).

Once more, if we make the bath's dynamics faster, leading to a better applicability of the WBA, then the rates converge again to the traditional FGR description (middle of the band spectrum).

In order to generalize our analysis, we will make a briefly characterization of the local LE decay times for a "highly public" bath (See Fig. 5.8). This case is of interest for studying spin dynamics in ring and ladder like systems (see Ref. [Álvarez *et al.*, 2010a]). In particular, this type of systems will be studied Chap. 6.

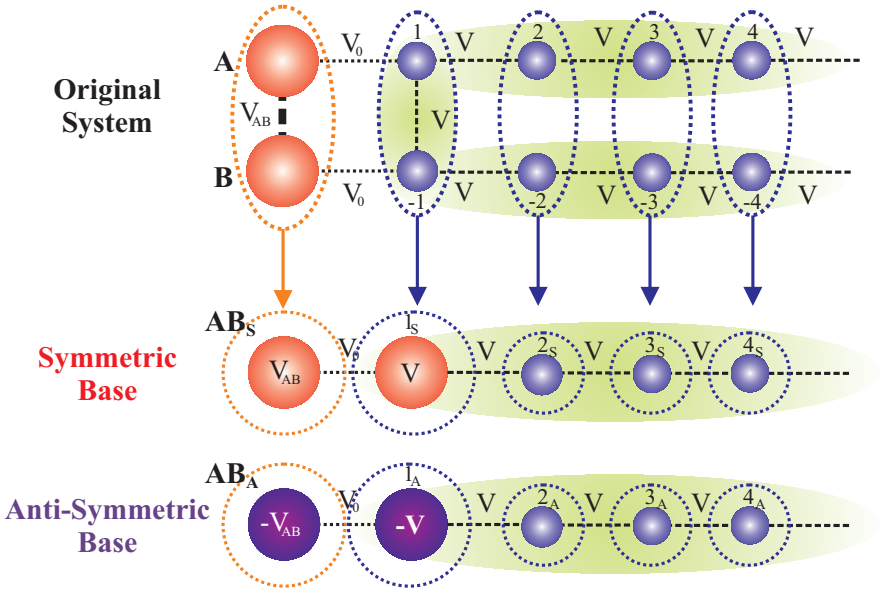

Figure 5.6: The schematic symmetrization procedure of the 2-sites system interacting with the public environment. The original problem can be casted as two independent semi infinite linear chains.

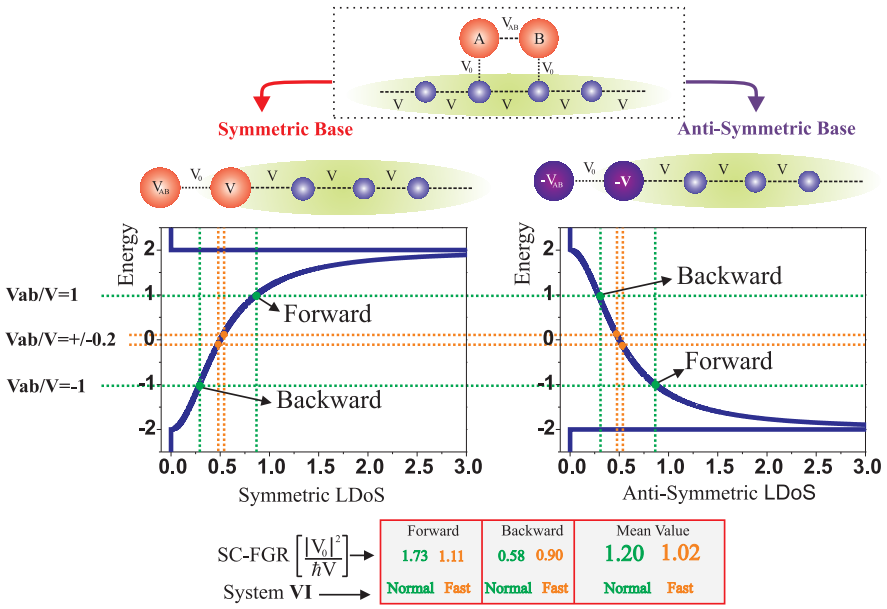

Figure 5.7: LDoS for the equivalent problem of the public case, after symmetrization transformation. Forward and backward stages of the evolution are indicated. The horizontal lines dashed lines are the values V_{AB}/V which stand for the system energies (renormalized to V). The vertical dashed lines together with their numerical values are the LDoS for the system **VI** in the normal ($V = V_{AB}$) or the fast ($V = 5V_{AB}$) configuration.

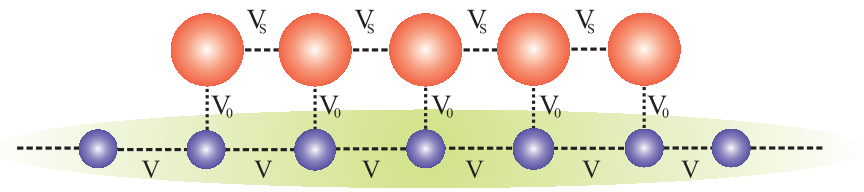

Figure 5.8: Fermion model. A five-site system laterally coupled to an infinite chain.

In this system we considere three different relations for the time scales: $V = V_s$, $V = 5V_s$ and $V = 8.75V_s$ (we also assume $V \gg V_0$). For these cases the decay rates (local LE degradation rate measured in units of $V_0^2/\hbar V$) computed by the numerical solution are (2.66 ± 0.07), (1.54 ± 0.05) and (1.16 ± 0.04), respectively. Therefore, we observe that the first two results do not match with that expected by WBA. Moreover, as we have seen before, the convexity of the bulk LDoS, induce bigger values. By setting $V = 8.75V_s$ (approximately one order of magnitude of difference) we are near the WBA validity and thus it almost reproduce the expected result: an energy independent rate, of value 1.00 $V_0^2/\hbar V$, in accordance to Eq. 5.18. We stress here that the strong sensibility on the relation between time scales, is enhanced by a highly public $\mathcal{S} - \mathcal{E}$ interaction.

5.5 FURTHER DISCUSSIONS AND CONCLUSIONS

Traditionally, the first approach to evaluate decay rates is the FGR based on an underlying WBA. We have shown several variations of a simple SWAP gate interacting with an environment (or several ones) where this scheme is not as good a one might assume. This failure, which can be understood as non-Markovianity, is build up by two contributions (which should not be considered as well separated effects).

First, if the WBA limit ($V \gg V_{AB}$) is not well fulfilled, then it is quite obvious that the energy independent rate will not be representative as it would oversimplify the decay process. When the system's time scale becomes comparable to that of the environment (i.e. $V_{AB} \simeq V$, non-Markovian situation), the decay rate departs from the usual FGR approximation evaluated at single energy level. Depending on the bath's spectral structure (LDoS) the actual rate can be greater or lower. We have shown that if the LDoS is a convex function of the energy, then any shift away from the middle of the band spectrum will produce a greater decay rate. But if the LDoS is a concave

energy function, then the rate would be lower. In general, we have seen that dynamical complexity (understood as how much the decay departs from the WBA validity) arises when the time scales of the system, the environment and the $\mathcal{S}-\mathcal{E}$ interactions, are commensurable.

Second, when the dynamics is non-Markovian due to similar time scales, the possibility of interaction through the environment becomes appreciable. In a public bath, the correlations generated by the multiple connections between different parts of the system and the bath, are more effective to depart the physical process away from the WBA validity, for a given relation of time scales. In general this leads to too subtle correlations to be treated in spectral models for the bath which here becomes quite natural through the use of specific Hamiltonian models of the environment.

In order to address the question on the private and public nature of the $\mathcal{S}-\mathcal{E}$ interaction, we confront the cases of *two independent baths* (case **V**) and *one common bath* (case **VI**).

In cases, where $\mathcal{S}-\mathcal{E}$ interaction is private there is no dependence of the rate on the relative sign of V and V_{AB}. On the other hand, if the $\mathcal{S}-\mathcal{E}$ interaction is public, the forward and backward evolution will change the decay rates and will produce a mean value for the local LE decoherence rate. It is important to stress here that we are comparing cases where $\mathcal{S}$ and $\mathcal{E}$ have similar time scales. In this condition, it is observed that decay rates for the public case are greater than for the private. In this sense we interpret (at least for this cases) that the private bath is "less harmful" than a public one. Strictly speaking, this a consequence of moving along the LDoS in the *effective* FGR (see Figs. 5.5 and 5.7). A public scenario produces an enhancement in the alteration of the FGR away from the WBA limit, as compared to the private one. As a matter of fact, private bath is less efficient for correlated memory-like returns to the system. As it has been previously stated in a general sense, and based on complete formal grounds, the feedback of information from $\mathcal{E}$ to $\mathcal{S}$ is the central issue for quantifying a non-Markovian bath [Breuer *et al.*, 2009].

On the other hand, we have shown how Markovianity is restored by changing the relation between $\mathcal{S}$ and $\mathcal{E}$ time scales. In fact, for all the cases treated in this work, we have found that once we move towards the WBA limit (represented by a bath dynamics 5 times faster than the system), the effects of a public or private bath are no longer relevant. For both cases the environment is fast enough to wash out all the

memory effects, since any inner excitation is rapidly spread. At this point the rate for both situations become equal and agree with the one predicted by the common FGR. This means that when the system's and the bath's time scales are well differentiated (specifically when the bath's is very short as compared to the system's), then the public-private reservoir discussion becomes irrelevant.

In many physical situations, when addressing 1-D and 1-D$^+$ systems (see, for example [Álvarez *et al.*, 2010a]), a coupled environment behaves with a convex LDoS. Therefore, memory effects and complexity in the structure of the $\mathcal{S}-\mathcal{E}$ interaction produce an enhancement of the coherent dynamics degradation. Additionally, we stress here the wider "spectral exploration" of the Loschmidt Echo as compared to the Survival Probability (a difference clearly shown in the public $\mathcal{S}-\mathcal{E}$ interaction case, where the global LE rate is a mean value of two non symmetric processes).

Even though we do not claim full generality for the results discussed here, there are some interesting universal issues to remark. The use of the Wide Band Approximation (simple FGR) can easily lead to quantitative and qualitative wrong results if the time scales and the physical structure of $\mathcal{S}$ and $\mathcal{E}$ are similar. Also the way they are coupled to each other (*public* or *private*), plays a fundamental role. In general, dynamical complexity grows up when those characteristic times are similar and when there is no privacy in the $\mathcal{S}-\mathcal{E}$ interaction.

Chapter 6

Loschmidt Echo Evaluation of Environmental Induce Decoherence in Spin Systems

6.1 Introduction

In this chapter we start to explore the many body problem of decoherence in spin systems. We will numerically analyze the decoherence process in spin ladder systems, where each chain has 1/2 spins with XY interaction. One of them constitutes the controlled system $\mathcal{S}$ whose dynamics is degraded by the weak coupling with the uncontrolled second chain, i.e. the environment $\mathcal{E}$. The employ of the Loschmidt Echo quantifier, i.e. the signal recovered after the reversal of an evolution, let us to identify and quantify the processes contributing to decoherence. This procedure, which has been used in the single particle fermion model of the previous chapters, is now successfully applied in this many-body system, where their excitations would sustain a one-body like propagation. The perturbative System-Environment ($\mathcal{SE}$) coupling is swept through arbitrary combinations of XY and Ising like interactions, that contain the standard Heisenberg and dipolar ones. The fact that the isolated chains have a simple internal dynamics allows the comparison with previous analytical and numerical evaluations of decoherence based on the attenuation of specific interferences described in terms of the Fermi golden rule. The contributions of the different $\mathcal{SE}$ terms to decoherence are individually evaluated and analyzed. The results will shows that the Loschmidt Echo is

a good decoherence quantifier as it yields a meaningful description of the decoherence processes at any time independently of the S internal dynamics.

One of the first questions that arises, is why the choice of the spin ladder problem? In the literature we found that, least for short distance communications, spin chains can be used to transfer information [Bose, 2003]. Several selective polarization techniques have been developed in NMR experiments to set up an initial local excitation in one edge of a spin chain and transfer it to the other edge by means of an effective XY Hamiltonian (i.e. $S_i^+ S_j^- + S_i^- S_j^+$ or polarization conserving "flip-flop" processes) [Mádi *et al.*, 1997, Cappellaro *et al.*, 2007]. Additionally, Multiple Quantum Coherence spectroscopy has allowed the study of quasi-one-dimensional spin systems under the influence of spin environments [Zhang *et al.*, 2009, Rufeil-Fiori *et al.*, 2009]. In particular, the Double Quantum (DQ) Hamiltonian (i.e. the polarization non-conserving processes $S_i^+ S_j^+ + S_i^- S_j^-$), can be mapped to an XY Hamiltonian allowing the design and control of the excitation transfer in a broader family of solid-state spin structures [Fel'dman & Lacelle, 1997, Cappellaro *et al.*, 2007, Doronin & Fel'dman, 2005], [Doronin *et al.*, 2000]. Thus, our work is intended to deepen the analysis of decoherence process in such 1-D systems. This kind of studies are crucial to improve the degree of control available for NMR-based state transfer protocols [Álvarez *et al.*, 2010b, Cappellaro *et al.*, 2011].

As we have seen in the Chap. 5, a natural way to quantify the decoherence time τ_ϕ is through the degradation of the contrast of interferences. This requires the identification of specific coherence "witnesses". Particularly useful are the excitations in the local polarization, as their reflections on the boundaries can be observed as well defined Mesoscopic Echoes (ME) [Pastawski *et al.*, 1995, Pastawski, 1996, Prigodin *et al.*, 1994]. Recently, the ME intensity has been used to quantify decoherence of spins arranged in a ladder topology [Álvarez *et al.*, 2010a]. Alternatively, the evaluation of τ_ϕ can be performed by a time reversal procedure, the Loschmidt Echo (LE) [Jalabert & Pastawski, 2001], where one evaluates the reversibility of the system's dynamics in presence of an uncontrolled environment. The LE can be accessed experimentally in many situations, such as spin systems [Pastawski *et al.*, 2000, Levstein *et al.*, 1998, Sánchez *et al.*, 2009], confined atoms [Andersen *et al.*, 2006], microwave excitations [Schäfer *et al.*, 2005], etc. Also, it has become a standard way to quantify decoherence, stability and complexity

in dynamical processes, in several physical situations involving non-interacting particles [Gorin *et al.*, 2006, Jacquod & Petitjean, 2009].

The quantitative study of the LE degradation, characterizes the decoherence due to the interplay between the system ($\mathcal{S}$) and the environment ($\mathcal{E}$). Indeed, the many-body nature of the $\mathcal{S}$-$\mathcal{E}$ interaction yields a very rich behavior in the dynamical regimes of decoherence. Additionally, the non Markovian nature of the $\mathcal{S}$-$\mathcal{E}$ interaction will be quantitatively analyzed in terms of the environment's spectral structure or local density of states (LDoS).

In the next section, we describe our system $\mathcal{S}$ as a spin chain or ring, the environment $\mathcal{E}$ as a second chain, and the perturbative interactions linking them side by side. Within this model we discuss the relevant time scales and the requirements for a Markovian behavior. In this many-body context, we introduce a local (many-body) version of the Loschmidt Echo evaluated from an experimentally accessible observable: the local polarization. We analyze its role as a decoherence quantifier. In Section 6.3, we perform a numerical study of the physically relevant parameter regimes. In Section 6.4 we analyze the obtained rates and show that these account for corrections to the Fermi golden rule (Markovian regime) arising from finite size and memory effects [Álvarez *et al.*, 2010a, Dente *et al.*, 2011]. We further argue that, for short times, certain environment fluctuations reduce the decoherence rate as measured by the LE. This is because the LE reverses the phases arising from the $\mathcal{S}$-$\mathcal{E}$ Ising interaction thus rebuilding original interferences. In the last section we conclude that the LE compares favorably with the evaluation of interference contrast (ME attenuation) as a tool for decoherence quantification.

6.2 QUANTUM DYNAMICS OF SPIN-CHAIN SYSTEMS

6.2.1 THE MODELS

The spin models analyzed in this article are schematized in Fig. 6.1. In the first one, the system $\mathcal{S}$ is an m-spin chain (Fig. 6.1-**a**), which could constitute a quantum channel, that interacts with a second chain $\mathcal{E}$. This chain, stands for the "environment" which perturbs the dynamics of $\mathcal{S}$. The second model (Fig. 6.1-**b**) is obtained from the first one by imposing a periodic boundary condition that transforms the chains into rings.

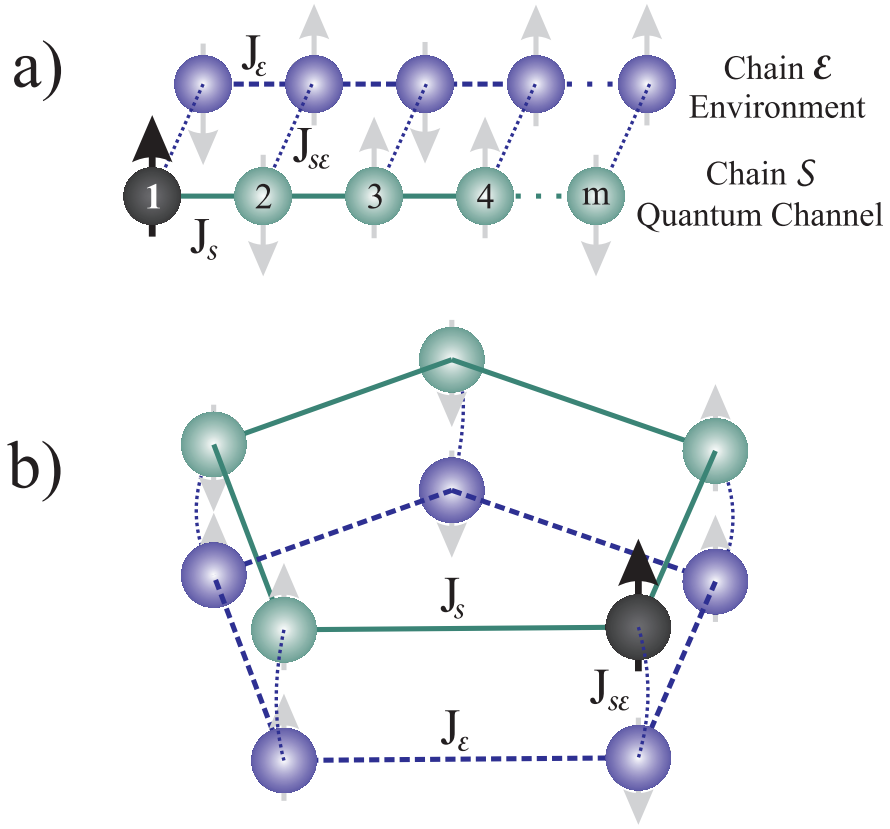

Figure 6.1: The spin system. (**a**) Open boundary conditions. (**b**) Closed boundary conditions (ring-like). Continuous (green) connections represent interactions that can be inverted to obtain the Loschmidt echo. Dash (blue) lines represent non-controllable interactions. The first spin (black circle) is initially polarized. The rest of the spins are in the high temperature regime.

For both models, the spin Hamiltonian is given by:

$$\hat{H}_{total} = \hat{H}_{\mathcal{S}} + \hat{H}_{\mathcal{E}} + \hat{V}_{\mathcal{S}\mathcal{E}}, \tag{6.1}$$

where the first and second terms represent the system and the environment respectively, and the third one is the interaction between them. In particular, for both $\nu = \mathcal{S}$ or $\mathcal{E}$, we use an effective "planar" or XY Hamiltonian [Mádi *et al.*, 1997], that describes the homogenous flip-flop interaction between first neighbor spins. In the first model, i.e. the chain:

$$\begin{aligned}\hat{H}_{\nu} &= \sum_{n=1}^{m-1} J_{\nu}(\hat{S}^{x}_{\nu,n+1}\hat{S}^{x}_{\nu,n} + \hat{S}^{y}_{\nu,n+1}\hat{S}^{y}_{\nu,n}) \\ &= \sum_{n=1}^{m-1} \frac{J_{\nu}}{2}(\hat{S}^{+}_{\nu,n+1}\hat{S}^{-}_{\nu,n} + \hat{S}^{-}_{\nu,n+1}\hat{S}^{+}_{\nu,n}).\end{aligned} \tag{6.2}$$

Here $\hat{S}^{x}_{\nu,n}$ and $\hat{S}^{y}_{\nu,n}$ are the x and y components of the spin operator in the n-th site in the ν chain respectively, while $\hat{S}^{+}_{\nu,n}$ and $\hat{S}^{-}_{\nu,n}$ are the raising and lowering operators. If one wants to consider the second model, i.e. spins in a ring, an extra XY coupling appears between the 1-st and m-th spins.

The interchain coupling is:

$$\hat{V}_{\mathcal{S}\mathcal{E}} = \sum_{n=1}^{m} J_{\mathcal{S}\mathcal{E}}[2\alpha\hat{S}^{z}_{\mathcal{S},n}\hat{S}^{z}_{\mathcal{E},n} - (\hat{S}^{x}_{\mathcal{S},n}\hat{S}^{x}_{\mathcal{E},n} + \hat{S}^{y}_{\mathcal{S},n}\hat{S}^{y}_{\mathcal{E},n})] \tag{6.3}$$

$$= \sum_{n=1}^{m} J_{\mathcal{S}\mathcal{E}}[2\alpha\hat{S}^{z}_{\mathcal{S},n}\hat{S}^{z}_{\mathcal{E},n} - \frac{1}{2}(\hat{S}^{+}_{\mathcal{S},n}\hat{S}^{-}_{\mathcal{E},n} + \hat{S}^{-}_{\mathcal{S},n}\hat{S}^{+}_{\mathcal{E},n})], \tag{6.4}$$

where the first term is an Ising interaction. The α parameter determines the nature of the coupling (see Ref. [Pastawski *et al.*, 1995]). For typical NMR scenarios: XY interaction [Mádi *et al.*, 1997] is represented by $\alpha = 0$, the standard isotropic Heisenberg interaction corresponds to $\alpha = -\frac{1}{2}$, while $\alpha = 1$ is the truncated dipolar interaction. In order to extend and systematize our analysis we also consider several other values for α. It is important to notice that for finite α the $\mathcal{S}$-$\mathcal{E}$ interaction always has an XY component. This allows a polarization exchange which, in a Fermionic representation,

can be seen as a "single-particle tunneling"[Danieli *et al.*, 2004]. In such a picture, the Ising term corresponds to a nearest neighbor Hubbard term which is a two-body interaction.

It is crucial to stress that the real constants $J_{\mathcal{S}}$, $J_{\mathcal{E}}$ and $J_{\mathcal{SE}}$ determine the relevant time scales of the whole problem. As introduced above, the first two give the homogenous XY coupling within the $\mathcal{S}$ and $\mathcal{E}$ respectively, while $J_{\mathcal{SE}}$ stands for the interchain coupling between them. With the purpose of ensuring a smooth degradation of $\mathcal{S}$'s coherent dynamics, we set $J_{\mathcal{SE}}$ in the weak coupling limit, i.e. $J_{\mathcal{SE}} \ll J_{\mathcal{S}}$, $J_{\mathcal{E}}$.

The Fermi golden rule, which involves the thermodynamic limit of infinite degrees of freedom, describes the "irreversible" decay of a pure state in $\mathcal{S}$ into collective $\mathcal{S} \otimes \mathcal{E}$ states. This implies that the unperturbed eigenstates of $\mathcal{S}$ have negligible overlap with the eigenstates of $\mathcal{S} \otimes \mathcal{E}$. For example, in a tight-binding picture of non-interacting fermions, the breakdown of the time independent perturbation theory occurs when the interaction with each environment eigenstate, $J_{\mathcal{SE}}/\sqrt{m}$, becomes of the order of the spacing between contiguous energy levels, which is about $J_{\mathcal{E}}/m$. In other words, the decay time, $\tau_{\mathcal{SE}}$, associated with the Fermi golden rule

$$1/\tau_{\mathcal{SE}} \simeq \frac{2\pi}{\hbar} \left| \frac{J_{\mathcal{SE}}}{\sqrt{m}} \right|^2 \frac{m}{J_{\mathcal{E}}}, \tag{6.5}$$

must be shorter than the bath's recurrences at the Heisenberg time $t_H \simeq \hbar m/J_{\mathcal{E}}$. Additionally, as we have seen in the Chap. 5, when both $\mathcal{S}$ and $\mathcal{E}$ have similar time scales, the coherent memory effects may produce decay rates that differ appreciably from those provided by the FGR [Dente *et al.*, 2011]. These are well described by a self-consistent Fermi golden rule (SC-FGR) [Rufeil-Fiori & Pastawski, 2006]. Thus, one should remember that $J_{\mathcal{S}} \simeq J_{\mathcal{E}}$ may lead to a *non-Markovian* scenario. On the other hand, when $J_{\mathcal{S}} \ll J_{\mathcal{E}}$ the environment fluctuations are much faster than those in the system and the Markovian approximation becomes satisfactory [Dente *et al.*, 2011].

As we will see below, the evaluation of spin dynamics and decoherence can become more complex in a many-body systems. A chain of m spins corresponds to 2^m energy levels where as many as $\binom{m}{m/2}$ of them can be coupled by an interaction conserving spin projection.

6.2.2 MEASURING DECOHERENCE IN SPIN SYSTEMS: MESOSCOPIC AND LOCAL LOSCHMIDT ECHOES

A natural question that arises for the spin models introduced above, is how to quantify decoherence of $\mathcal{S}$ in the presence of $\mathcal{E}$. The first answer relies on finding an appropriate decoherence rate $1/\tau_\phi$ through the quantification of the attenuation of system's specific interferences. As in the experiments, one can starts evaluating the evolution of an injected local polarization through the spin autocorrelation function [Danieli *et al.*, 2004, Danieli *et al.*, 2005]:

$$P_{1,1}(t) = \frac{\left\langle \Psi_{eq} \right| \hat{S}^z_{\mathcal{S},1}(t) \hat{S}^z_{\mathcal{S},1}(0) \left| \Psi_{eq} \right\rangle}{\left\langle \Psi_{eq} \right| \hat{S}^z_{\mathcal{S},1}(0) \hat{S}^z_{\mathcal{S},1}(0) \left| \Psi_{eq} \right\rangle}. \tag{6.6}$$

This function gives the local polarization at time t along the z direction in site 1 provided that at time $t = 0$ the system was in its thermal equilibrium state plus a local excitation in site 1. In fact, it is precisely the experimentally observed magnitude after the excitation is created by a special pulse sequence [Pastawski, 1996]. Here, $\hat{S}^z_{\nu,1}(t) = e^{\mathrm{i}\hat{H}_{total}t/\hbar} \hat{S}^z_{\nu,1} e^{-\mathrm{i}\hat{H}_{total}t/\hbar}$ is the spin operator in the Heisenberg representation. The many body state $\left|\Psi_{eq}\right\rangle$ corresponding to high temperature thermal equilibrium represents a mixture of all states with amplitudes satisfying the appropriate statistical weights and random phases. Then, the local excitation can be defined in the computational (Ising) basis$\{|\Psi_r\rangle\}$ as

$$\frac{\hat{S}^z_{\mathcal{S},1} \left|\Psi_{eq}\right\rangle}{\left| \left\langle \Psi_{eq} \right| \hat{S}^z_{\mathcal{S},1} \hat{S}^z_{\mathcal{S},1} \left| \Psi_{eq} \right\rangle \right|^{1/2}} = \sum_r c_r \left|\Psi_r\right\rangle, \tag{6.7}$$

In the regime of NMR spin dynamics, the thermal energy $k_B T$ is much higher than any other energy scale of the system [Ernst *et al.*, 2004, Abragam, 1986] , then all statistical weights result identical, i.e. $|c_r| = 1/\sqrt{2^{2m-1}}$. It turns out that each contribution to the locally polarized initial state can be written as :

$$|\Psi_r\rangle = |\uparrow_1\rangle \otimes |\beta_r\rangle, \tag{6.8}$$

where the basis for the remaining $2m-1$ spins is

$$|\beta_r\rangle = |s_2\rangle \otimes |s_3\rangle \otimes |s_4\rangle \otimes ... \otimes |s_{2m}\rangle \quad \text{with } |s_k\rangle \in \{|\uparrow\rangle, |\downarrow\rangle\}. \tag{6.9}$$

The computation of the time dependent observable in Eq. 6.6 requires evolving each of these pure states to evaluate the ensemble averaged observable. This is implemented

using a Trotter decomposition [Rieth & Schommers, 2006] assisted by quantum parallelism [Álvarez *et al.*, 2008] (See appendix C for further details).

Once the initial excitation is created, a first physical picture about its evolution may be obtained from the Wigner-Jordan spin-fermion mapping (see Appendix PVP-Apendice-1), i.e. we can start by thinking in models like those analyzed in Chap. 5. According to it, an m spins chain with XY interaction where N of them are up is mapped to a chain with N non-interacting fermions (See details in Chap. 2). Thus, if we only consider the isolated chain $\mathcal{S}$, a polarization excitation has the same dynamics as a single fermion in a tight-binding linear chain [Pastawski, 1996, Mádi *et al.*, 1997, Rufeil-Fiori & Pastawski, 2006]. Indeed, the observed autocorrelation function in the limit of infinite temperature is precisely described by the evolution of a single spin up in a chain of down spins:

$$\begin{aligned}\left|\Psi_1^{\mathcal{S}}\right\rangle &= |\uparrow_1\rangle \otimes |\beta_{r=1}\rangle \\ &= |\uparrow_1\rangle \otimes |\downarrow_2\rangle \otimes |\downarrow_3\rangle \otimes ... \otimes |\downarrow_m\rangle\,,\end{aligned} \tag{6.10}$$

and

$$P_{1,1}^{\mathcal{S}}(t) = \left|\left\langle \Psi_1^{\mathcal{S}}\right| \exp[-\mathrm{i}\hat{H}_{\mathcal{S}}t/\hbar] \left|\Psi_1^{\mathcal{S}}\right\rangle\right|^2, \tag{6.11}$$

where $\left|\Psi_1^{\mathcal{S}}\right\rangle$ belongs to the $\mathcal{S}$ sub-space. Thus, $\exp[-\mathrm{i}\hat{H}_{\mathcal{S}}t/\hbar]\left|\Psi_1^{\mathcal{S}}\right\rangle$, is a one-body wave function which accounts for the dynamics isolated dynamics of the system chain.

Once we add a weakly coupled second chain ($\mathcal{E}$), we can think that the dynamics of the first chain remains approximately valid. Hence, the revivals observed in by $P_{1,1}^{\mathcal{S}}(t)$ (the isolated $\mathcal{S}$ dynamics) which characterize the system finite size, should still show up. In fact, it is possible to observe this constructive interference reappearing after every Heisenberg time $t_H \sim \hbar/\Delta$, with Δ being the typical mean energy level spacing. Such polarization revival is called Mesoscopic Echo (ME) [Prigodin *et al.*, 1994, Pastawski *et al.*, 1995]. In the particular cases treated in this work (spin chains with XY interactions), one may safely use $\Delta \simeq J_{\mathcal{S}}/m$. Then, the Heisenberg time becomes: $t_H \sim \hbar m/J_{\mathcal{S}}$.

The effect of coupling the $\mathcal{E}$ bath becomes in a progressive attenuation of the ME (compared to the isolated dynamics). In a previous work (see Ref. [Álvarez *et al.*, 2010a]), this attenuation has been used to quantify the environmentally induced decoherence. It is interesting to mention that in the many-body problem analyzed in this chapter,

the FGR evaluation of decoherence time remains valid for times much longer than the isolated system's Heisenberg time t_H. This may seem paradoxical as the Heisenberg time of the isolated environment would be comparable to that of the system. Also, it is in apparent contradiction with the validity range of the Fermi golden rule stated above. However, these bounds were given for a single particle picture which is no longer valid once the $\mathcal{S}$-$\mathcal{E}$ interaction is considered. This is indicative that the whole $\mathcal{S} \otimes \mathcal{E}$ is a fully many-body system where most of the degeneracies of the decoupled finite XY chains have been broken. Thus, the situation resembles that of a single particle propagating in presence of the environment represented by a much larger tight-binding chain as considered in Fig. 7 of Ref. [Dente *et al.*, 2011] and in Chap. 5.

Let us now explain the essence of the experimental protocol that uses the Loschmidt Echo to quantify decoherence in a spin system using a $LOCAL$ spin as an observable [Levstein *et al.*, 1998]. This relies on the controllability of the chain $\mathcal{S}$, whose Hamiltonian's sign can be switched at will as is often the case in NMR. The reversibility of the dynamics within the channel is perturbed by the interaction with a non-controlled spin chain $\mathcal{E}$ (a similar scenario can be found in Ref. [Petitjean & Jacquod, 2006]). There are two stages in the evolution. First, a spin excitation is created and the chains evolve according to the Hamiltonian of Eq. 6.1, during a time t_R. At t_R the internal interactions within $\mathcal{S}$ are reversed (i.e. $\hat{H}_{\mathcal{S}}$ is replaced by $-\hat{H}_{\mathcal{S}}$ during a second period t_R). However, neither $\mathcal{S}$-$\mathcal{E}$ coupling nor interactions within chain $\mathcal{E}$ are reversed, resulting in a non-reversed perturbation,

$$\hat{\Sigma} = \hat{H}_{\mathcal{E}} + \hat{V}_{\mathcal{S}\mathcal{E}}, \tag{6.12}$$

acting in both periods. Thus, in analogy with Eq. 6.6, we define the observable Local Loschmidt echo as the local recovered polarization:

$$M_{LE}(2t_R) = \frac{\left\langle \Psi_{eq} \right| \hat{S}^z_{\mathcal{S},1}(2t_R)\hat{S}^z_{\mathcal{S},1}(0) \left| \Psi_{eq} \right\rangle}{\left\langle \Psi_{eq} \right| \hat{S}^z_{\mathcal{S},1}(0)\hat{S}^z_{\mathcal{S},1}(0) \left| \Psi_{eq} \right\rangle}. \tag{6.13}$$

The spin operators, expressed in the Heisenberg representation, are now:

$$\hat{S}^z_{\nu,1}(2t_R) = e^{\frac{\mathrm{i}}{\hbar}(\hat{H}_{\mathcal{S}}+\hat{\Sigma})t_R} e^{\frac{\mathrm{i}}{\hbar}(-\hat{H}_{\mathcal{S}}+\hat{\Sigma})t_R} \hat{S}^z_{\nu,1} e^{-\frac{\mathrm{i}}{\hbar}(-\hat{H}_{\mathcal{S}}+\hat{\Sigma})t_R} e^{-\frac{\mathrm{i}}{\hbar}(\hat{H}_{\mathcal{S}}+\hat{\Sigma})t_R}. \tag{6.14}$$

At this point it is important to remark that the Loschmidt echo introduced above is a local observable which acts over the first spin. If we compare with other definitions

of that measure in the literature (for example in Ref. [Petitjean & Jacquod, 2006]), we will found that the here we make a local proyection (i.e. we trace over the system and enviromental variables), while in other cases the proyection is made with only one global state of the whole controlled system $\mathcal{S}$.

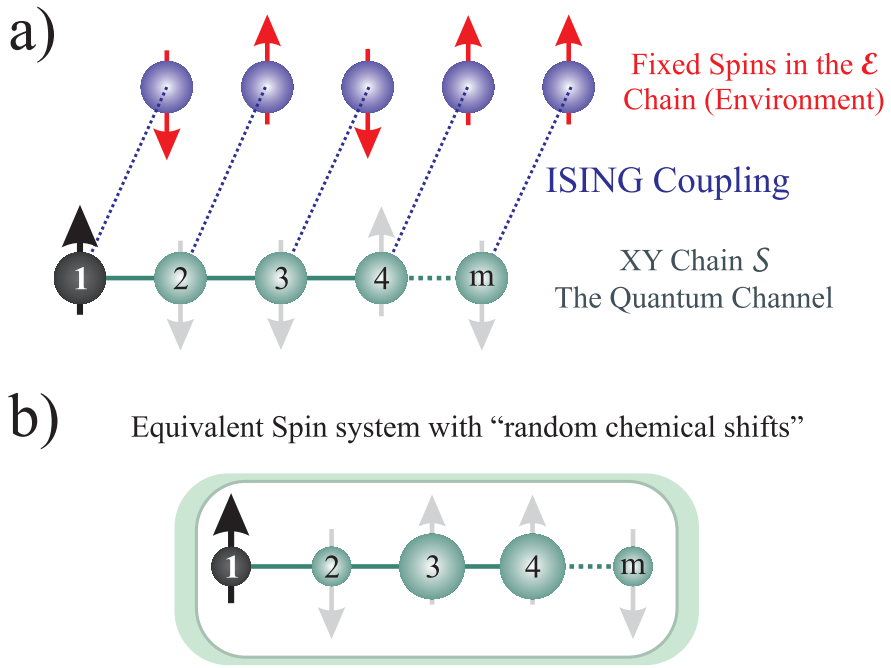

Figure 6.2: Representation of the "equivalence" between the Ising like problem and the "random chemical shift" problem. a) The particular case of $\hat{V}_{S\mathcal{E}}$ restricted to the ising form and a fixed state in the environment. b) "Equivalent" model for the a) system. Smaller and bigger circles represent the random chemical shift which depends on the instantaneous spin configuration of the system.

Continuing with the analysis, it can be useful to think in the particular case where $\hat{V}_{S\mathcal{E}}$ is restricted to an Ising interaction and $\hat{H}_{\mathcal{E}}$ has no dynamics at all but remains quenched in a random configuration. In such case, Eq. 6.13 reduces to the time-reversed dynamics of a spin in the presence of an oriented chain. There we can reduce the problem by considering only one spin chain with a set of non-reversed random chemical shifts (see Fig. 6.2). Here, we have "transformed" $\hat{\Sigma}$, a operator with acts over the full Hilbert space, into $\hat{\Sigma}_S$, a operator of random potentials with only acts over the S Hilber space. Thus if we restrict our analysis to the S system, in analogously to

Eq. 6.11, we found that the Loschmidt echo becomes:

$$M_{LE}^{\mathcal{S}}(2t_R) = \left| \left\langle \Psi_1^{\mathcal{S}} \right| \exp\{-\frac{\mathrm{i}}{\hbar}(-\hat{H}_{\mathcal{S}} + \hat{\Sigma}_{\mathcal{S}})t_R\} \exp\{-\frac{\mathrm{i}}{\hbar}(\hat{H}_{\mathcal{S}} + \hat{\Sigma}_{\mathcal{S}})t_R\} \left| \Psi_1^{\mathcal{S}} \right\rangle \right|^2 , \quad (6.15)$$

where one can recognize the LE definition as the overlap of two wave functions introduced in Ref. [Jalabert & Pastawski, 2001].

Despite of this simplification for one specific case, we still have to compute the Loschmidt Echo (presented in Eq. 6.13) to evaluate the decoherence lost in a system with a general interaction. Thus, it necessarily requires a full many-body evolution.

As we mention above the initial state of Eq. 6.7 is composed by a set of $|\Psi_r\rangle$ states belonging to the $\mathcal{S} \otimes \mathcal{E}$ space. For each of these states, the resulting wave function at time $t = 2t_R$, after the whole time-reversal procedure, is

$$|\Psi_r(2t_R)\rangle = \exp\{-\tfrac{\mathrm{i}}{\hbar}(-\hat{H}_{\mathcal{S}} + \hat{\Sigma})t_R\} \exp\{-\tfrac{\mathrm{i}}{\hbar}(\hat{H}_{\mathcal{S}} + \hat{\Sigma})t_R\} |\Psi_r\rangle . \quad (6.16)$$

In analogy with the discussion above, the probability of finding the first spin up-polarized is:

$$P_{1,1}^{[r]}(t) = \sum_j |(\langle\uparrow| \otimes \langle\beta_j|) |\Psi_r(t)\rangle|^2 , \quad (6.17)$$

where the sum runs over the 2^{2m-1} configurations of the $2m-1$ remaining spins. After the summation over all $|\Psi_r\rangle$ contributions to the initial state, and expressing the result as a local polarization [Pastawski *et al.*, 1995], we obtain the local LE:

$$M_{LE}(t) = [\sum_{r=1}^{2^{2m-1}} |c_r|^2 P_{1,1}^{[r]}(t) - \frac{1}{2}] \times 2. \quad (6.18)$$

Here again, the statistical weight $|c_r|^2$ is the inverse of 2^{2m-1}, the number of initial states in the ensemble that satisfy the "1$^{\mathrm{st}}$ *spin up polarized*" condition. Notice again that, except for the fact that the evolution operator contains a partially reversed dynamics, this quantity refers to the same physical observable as Eq. 6.6.

Clearly, in the case where $\mathcal{S}$ is isolated, the local LE will have a constant value of 1. This means that $\mathcal{S}$ is fully reversible. On the other hand, if $\mathcal{S}$ is coupled to $\mathcal{E}$, the local LE should decay, i.e. our reversal procedure fails to recover the excitation spread to the environment. Then the local LE decay rate is directly identified as the

decoherence rate $1/\tau_\phi$ [Petitjean & Jacquod, 2006]. Naturally, in the present situation this rate should be a function of the $\mathcal{S}$-$\mathcal{E}$ coupling parameter $J_{\mathcal{S}\mathcal{E}}$. Since we are interested in the regime of weak coupling with the fluctuating environment, in what follows we numerically analyze the conditions of validity of a FGR [Rufeil-Fiori & Pastawski, 2006, Jacquod *et al.*, 2001, Cucchietti *et al.*, 2006] as applied to the many-body context:

$$\frac{1}{\tau_\phi} \simeq \sum_\delta \frac{2\pi}{\hbar} \left| V^\delta_{\mathcal{S}\mathcal{E}} \right|^2 N_{0\delta}, \tag{6.19}$$

where $\left|V^\delta_{\mathcal{S}\mathcal{E}}\right|^2$ is the local second moment of the process δ (e.g. Ising or XY) contributing to the $\mathcal{S}$-$\mathcal{E}$ interaction and $N_{0\delta}$ represents the appropriate density of directly connected states or LDOS [Rufeil-Fiori & Pastawski, 2009].

6.3 DECOHERENCE EVALUATION BASED ON THE LOSCHMIDT ECHO DECAY

In this section we present the results obtained for the local LE $M_{LE}(t)$ (see Eq. 6.18) in the spin models represented in Fig. 6.1. Even though our major concern lies on the exponential decay ruled by the FGR, we can also identify other regimes, as shown in Fig. 6.3. It is noticeable that the Loschmidt echo yields results for a wide range of parameters and times scales. This feature contrasts with the study of interferences through the mesoscopic echoes whose observability restricts the quantification of decoherence, i.e. the decoherence can not be evaluated in any time. Thus, it is clear that the LE provides a privileged access to the decoherence processes.

In Fig. 6.3-**b** the short time dynamics displays the expected quadratic decay (inset), which should appear in any quantum evolution at short times. Indeed, the plot of $1 - M_{LE}$ (in log-log scale) shows that M_{LE} can be fit by a quadratic function in t:

$$M_{LE}(t) = 1 - [\frac{J_{\mathcal{S}\mathcal{E}}}{2\hbar}]^2 t^2. \tag{6.20}$$

This confirms that the short time decay is given by the local second moment of the perturbation. For very long times, the LE shows a saturation plateau (see Fig. 6.3-**a**). Such observation is consistent with the expectation that, with these parameters, the whole spin system behaves ergodically under the Loschmidt Echo dynamics, and

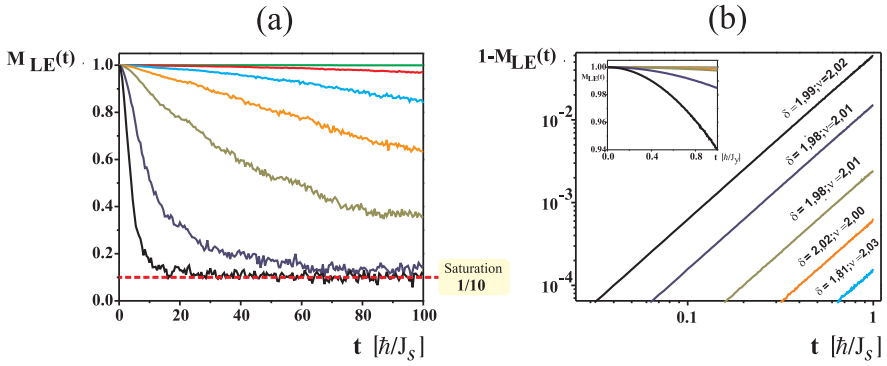

Figure 6.3: Time regimes of the local Loschmidt echo. Numerical results for a ring of 5 spins weakly coupled to an identical one, by an XY interchain interaction ($\alpha = 0$). **a**) M_{LE} as a function of the total evolution time $t = 2t_R$. Notice that the stronger the interchain coupling $J_{\mathcal{SE}}$, the faster the saturation regime is reached. **b**) At short times, the quadratic decay law is confirmed, showing excellent fit to Eq. 6.20, in the form $\log(1 - M_{LE}) = \delta \log(t) + \nu \log(J_{\mathcal{SE}}/(2\hbar))$. For (**a**) and (**b**) the coupling parameters $J_{\mathcal{SE}}$ are: 0.001, 0.01, 0.025, 0.05, 0.1, 0.25 and 0.5, in units of $J_{\mathcal{S}}$.

thus the polarization spreads uniformly along all the spins. At long times, each site is polarized by the amount $1/(2m)$ (1/10 for the particular case plotted). Different couplings $J_{\mathcal{SE}}$ produce a rescaling of the time in which the saturation is reached.

In order to asses the exponential regime, we plot the characteristic rate $1/\tau_\phi$ in Fig. 6.4-**a**, as a function of $J^2_{\mathcal{SE}}/\hbar J_{\mathcal{E}}$. This quantity is appropriate to verify the FGR validity (Eq. 6.19), as long as $J^2_{\mathcal{SE}}$ is the typical scale for the second moment of the $\mathcal{S}$-$\mathcal{E}$ interaction and $1/J_{\mathcal{E}}$ that of the density of directly connected states. Although several forms of the interchain Hamiltonians were considered by varying the parameter α in Eq. 6.3, we show only those more relevant to NMR experiments: XY ($\alpha = 0$), isotropic ($\alpha = -\frac{1}{2}$), and truncated dipolar interaction ($\alpha = 1$). We observe that the boundary conditions play a non-trivial role [Danieli *et al.*, 2004]. For the case of open boundary conditions (Figs. 6.1-**a**), some oscillations appear mounted on the decay which also depend on the parity of m, the number of spins in each chain. Below we present the results using closed boundary conditions (rings) where these effects are much weaker.

The linearity in Fig. 6.4-**a** evinces the validity of Eq. 6.19. The rates obtained from the different interactions are summarized in Fig. 6.4-**b**, where the rates derived from ME attenuation [Álvarez *et al.*, 2010a] are also included. The characteristic time $1/\tau_\phi$ (expressed in units of $J^2_{\mathcal{SE}}/\hbar J_{\mathcal{E}}$) is represented as a function of α^2. From the slopes of

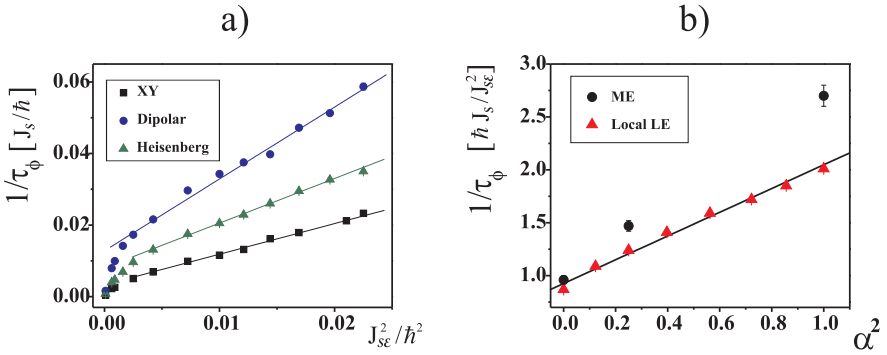

Figure 6.4: **a**) Decay rates for the interchain coupling given by the three most typical NMR interactions, in units of $J_{\mathcal{S}}/\hbar$. The slopes clearly depend on the value of α, i.e. on the relative weight between the Ising (dephasing) and XY (polarization transfer) contributions to the interchain coupling. The first data points were not considered in the fitting. **b**) Loschmidt Echo decay rate as a function of α^2 in units of $\hbar J_{\mathcal{E}}/J^2_{\mathcal{SE}}$. Varying α allows to cover the region of physical interest. For comparison, Mesoscopic Echo degradation data obtained in Ref. [Álvarez *et al.*, 2010a] are also plotted.

that plot we derive the contributions to the global decay rate $1/\tau_\phi$, arising from XY and Ising processes in the interchain interaction:

$$\frac{1}{\tau_\phi} = \frac{1}{\tau_\phi^{XY}} + \frac{1}{\tau_\phi^{ZZ}}. \tag{6.21}$$

This contributions, for the local Loschmidt Echo measure, are:

$$LE: \quad \frac{1}{\tau_\phi^{XY}} = (0.92 \pm 0.04)\frac{J^2_{\mathcal{SE}}}{\hbar J_{\mathcal{E}}}, \tag{6.22}$$

$$LE: \quad \frac{1}{\tau_\phi^{ZZ}} = (1.12 \pm 0.04)\alpha^2\frac{J^2_{\mathcal{SE}}}{\hbar J_{\mathcal{E}}}. \tag{6.23}$$

In order to compare with the numerical results of Ref. [Álvarez *et al.*, 2010a], we adapt their variables to our inner notation ($-a/b \equiv 2\alpha$) and write the rates contributing to the ME degradation:

$$ME: \quad \frac{1}{\tau_\phi^{XY}} = (1.00 \pm 0.06)\frac{J^2_{\mathcal{SE}}}{\hbar J_{\mathcal{E}}}, \tag{6.24}$$

$$ME: \quad \frac{1}{\tau_\phi^{ZZ}} = (2.0 \pm 0.3)\alpha^2\frac{J^2_{\mathcal{SE}}}{\hbar J_{\mathcal{E}}}. \tag{6.25}$$

The most striking effect evinced by the comparison is that while the XY contributions are essentially the same in both methods, the Ising contribution (i.e. pure dephasing) in the ME (Eq. 6.25) is almost twice the value obtained from the local LE. In the following section we analyze the possible origin of such result.

6.4 DECOHERENCE RATE ANALYSIS

The first non-trivial issue is that there is always an exponential regime in $M_{LE}(t)$, whose parametric dependence follows that of the FGR (Eq. 6.19), which also gives the correct order of magnitude. This is not obvious a priori since, within the model adopted for the $\mathcal{S}$ and $\mathcal{E}$ interaction $(\hat{V}_{\mathcal{S}\mathcal{E}})$, and having both equivalent internal time-scales ($J_{\mathcal{S}} = J_{\mathcal{E}}$), the physical situation is strictly non-Markovian. Thus, one should expect both memory effects and environment mediated interactions, i.e. the second chain behaves collectively as a "public" environment [Dente *et al.*, 2011], just like in Chap. 5.

As discussed in previous chapters, one can often approximate a many-body problem as a one-body system plus a decoherent process [Danieli *et al.*, 2002, Pastawski, 1991, Pastawski, 1992]. Therefore, it turns out that even when such one-body picture is not rigorously valid, some of its physical insights can be retained (e.g. memory effects). According to this argument, we interpret the equivalence of the XY rates for ME [Álvarez *et al.*, 2010a] and LE using the mapping into a one-body evolution either in $\mathcal{S}$ or $\mathcal{E}$. The dynamics along the chains is only weakly affected by the tunneling process, (i.e. in a single particle picture, the kinetic energy along X commutes with that along Y). Thus, the rate $1/\tau_{\phi}^{XY}$ should coincide with the tunneling rate and we expect that it should not be affected by a time-reversal procedure within $\mathcal{S}$.

Memory effects relying on the time scale relation ($J_{\mathcal{S}} \simeq J_{\mathcal{E}}$) inevitably appear in the simulations and they must be considered to achieve a satisfactory analytical description (see, for instance [Rufeil-Fiori & Pastawski, 2006]). Thus, we recall the discussion already presented in Ref. [Dente *et al.*, 2011] and in Chap. 5, where the degradation rates are determined within a self-consistent Fermi golden rule (SC-FGR), by the appropriate LDoS (i.e. the density of directly connected states) at the precise energy of the excitation. Hence, a reliable analytical prediction would require more sophistication than the energy-independent bath's spectral weight (LDoS) used for the FGR in a wide

Band Approximation (WBA). Specifically, in [Álvarez *et al.*, 2010a] a semi-infinite linear chain was used to describe the numerical data because the more appropriate infinite chain seems to lead to a divergent FGR. While this issue remains open, our recent work [Dente *et al.*, 2011] showed that corrections to the FGR rates depend on the convexity of the bath's spectral structure (LDoS). In the next chapter we will focus our attention on the appropriate LDoS for the evaluation of the FGR for this kind of system.

In contrast to the simple decay induced by the XY component of the $\mathcal{S}$-$\mathcal{E}$ interaction, the Ising part is expected to add a diffusion-like process within the system through the energy fluctuations it induces. This tends to blur out the dynamical recurrences (i.e. MEs). Thus, the smaller decoherence rate observed from the LE indicates that the time reversal procedure is at least partially effective to reverse such processes. In fact, the rates for the pure Ising interaction observed here from the LE are about half of those obtained from the ME [Álvarez *et al.*, 2010a]. This means that the ME attenuation overestimates the phase degradation induced by the environment. As stated before, the displacement of a spin excitation in presence of a quenched spin environment plays the role of an Anderson's disorder degrading the wave packet dynamics that produces the ME, and is computed as decoherence. The reversal of the internal XY interaction would not be able to reverse such disorder. However, if the environment has an inner dynamics there would be certain fluctuations that allow a perfect reversal of the system dynamics. i.e. both the hopping and the site energy signs are inverted. Such specific $\mathcal{E}$-fluctuations are those needed to unravel the phase shifts produced during the forward evolution (see Fig. 6.5). One may say that in the presence of a fluctuating environment, the LE is able to reconstruct the phases in some of the local configurations. Since such arguments rely on a single particle picture where local dynamics on short time steps is crucial, it is not clear whether it is enough to fully justify the striking factor of two observed numerically.

6.5 Conclusions

We presented an approach to characterize decoherence for a spin chain in realistic many-body scenarios. It consists of the evaluation of a Loschmidt Echo, i.e. the local polarization recovered after an imperfect time reversal procedure. The attenuation of such echoes yields a first hand estimate of the decoherence rate. As a specific

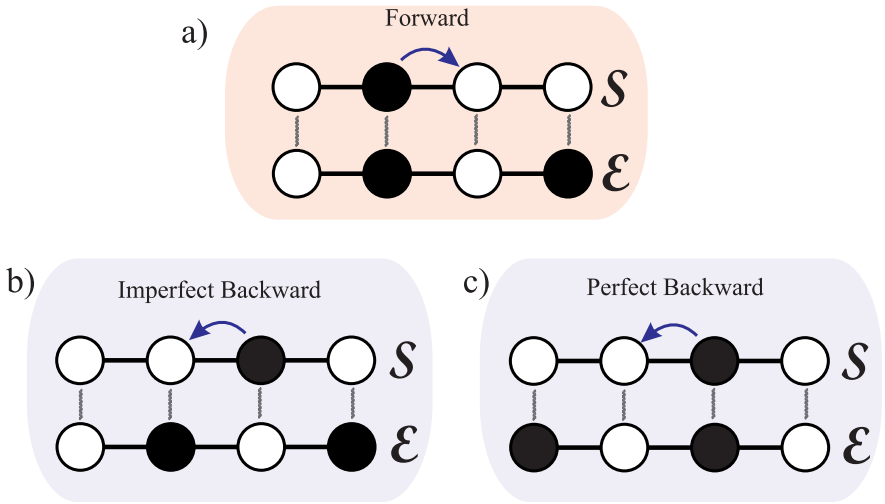

Figure 6.5: The Ising interchain interaction as a single particle in a binary alloy. A full circle is a spin up or a fermion, and an empty circle represents a spin down or a hole. All the processes are considered in the short time scale given by a single Trotter time step. **a**) Forward dynamics within $\mathcal{S}$, in presence of "random site energies". **b**) The backward evolution in $\mathcal{S}$ is imperfect because the environment $\mathcal{E}$ remains constant and "site energies" are not inverted. **c**) A particular evolution of $\mathcal{E}$ provides a perfectly reversed dynamics for $\mathcal{S}$. Here, all the "site energies" around the excitation that determined its forward evolution are reversed.

realization for a structured environment we used a second spin chain. This Hamiltonian for the bath leads to a non-Markovian scenario where the typical time scales are not well separated and $\mathcal{S}$-$\mathcal{E}$ interaction is *public* [Dente *et al.*, 2011], in the sense that it implies $\mathcal{E}$-mediated interactions. Thus, we obtain decoherence rates with no *ad-hoc* assumptions about spectral functions [Chakravarty & Leggett, 1984, Weiss, 2008] or stochastic noise operator [Blanchard *et al.*, 1994, Machida *et al.*, 1999].

Our computational technique involves a Trotter decomposition assisted by a recently developed algorithm that relies on quantum parallelism to evaluate local observables [Álvarez *et al.*, 2008]. The decoherence rates could be separated in two contributions. In spite of some subtleties that already appear in the corresponding single particle problem [Dente *et al.*, 2011], in this many-body context both contributions to decoherence are fairly well described by the Fermi golden rule.

The XY contribution to the decoherence rate coincides with that resulting from the ME attenuation. The reason is that the single particle picture for linear chains is approximately retained for weak interchain interactions. The Ising contribution to the rate obtained for the LE is about half that computed from the ME attenuation. Dynamics of the system in the presence of a random environment, produce phase shifts associated with the $\mathcal{S}$-$\mathcal{E}$ Ising interaction and contribute to the ME attenuation. However, when the imperfect LE procedure attempts to reverse dynamics inside $\mathcal{S}$, it may also benefit from some favorable fluctuations of the $\mathcal{S}$-$\mathcal{E}$ energy to fully reconstruct the phases in $\mathcal{S}$. The numerical simulation confirms that the Loschmidt Echo, is a better decoherence quantifier as it recovers information that escapes a standard analysis based on interference degradation. Also, by subtracting the intrinsic dynamical interferences of the system through time reversal, it gets rid of most of the trivial part in the $\mathcal{S}$ dynamics that conceals the decoherence effects. Thus the LE provides a smooth and continuous access to the decoherence processes that involve the environment.

Chapter 7

Effects of the Structured Spin Environment in Rabi Oscillators

7.1 Introduction

In this last chapter we will back to the problem of rabi oscillation in a two spin system, analyzing the decoherence process in the presence of a laterally couple spin chain (with XY interactions). The difference between the previous works and this one, is that here we focus in the analysis of Non-markovian dynamics produced by the Ising coupling and how the size of the environment affects the internal dynamics. We will use results from the non-equilibrium Keldysh formalism and compare with numerical simulations to understand the decoherence rates observed in equivalent systems like those treated in the previous chapter.

Along this thesis we have seen that the spin system $\mathcal{S}$ interacts with a spin environment $\mathcal{E}$, that perturbs it, smoothly degrading its quantum dynamics with a decoherence rate, $1/\tau_\phi$, proportional to the system-environment ($\mathcal{S}-\mathcal{E}$) interaction rate $1/\tau_{\mathcal{S}-\mathcal{E}}$. In fact, the inclusion of the $\mathcal{E}$ degrees of freedom may straightforwardly become an unsolvable problem and requires approximations usually not fully quantified.

A standard framework for dealing with open system dynamics is a Lindblad-type quantum master equation (QME), i.e. a generalized Liouville-von Neumann differential equation for the reduced density matrix [Abragam, 1986, Slichter, 1990]. In most of the cases, this approach is based on a fast fluctuation regime within E, i.e. a Markovian approximation. In addition, $S-E$ interactions occur at a rate given by the Fermi

Golden Rule (FGR), which is usually evaluated as an energy-independent variable. While these assumptions may be sufficient for most traditional applications, we have seen that they leave aside important memory effects and interferences in the time domain produced by a coherent $S-E$ interaction. An alternative to the previous QME approach is provided by the Keldysh non-equilibrium formalism [Keldysh, 1964], in the integral representation proposed by Danielewicz [Danielewicz, 1984]. The strategy uses perturbative expansions to infinite order in selected Feynman diagrams. Such integral representation also allows the manipulation of the energy-time domain in a similar way to the well known Wigner representation. In particular, for the fermionic case, the Danielewicz integral equation can be transformed into a generalized Landauer-Büttiker equation (GLBE) [Pastawski, 1991, Pastawski, 1992].

In this chapter we exhibit a systematic (both qualitative and quantitative) study of decoherence applied to a two-spin system $\mathcal{S}$, interacting with a one-dimensional spin set, which plays the role of the environment $\mathcal{E}$. This last is introduced by the specific XY (planar) Hamiltonian model (similar to the Public vs Private Chapter), which enables the access to its spectral structure or Local Density of States (LDoS). The many-body nature of the $\mathcal{S}-\mathcal{E}$ interactions yields a very rich behaviour in the decoherence rate $1/\tau_\phi$, that will be addressed with numerical methods and some analytical results.

A stricking point in the rate analysis relies on the effective LDoS or density of directly connected states (DDCS), when one tries to evaluate a FGR. In Chap. 5 we have seen that decoherence rates are evaluated from a self consistent (SC) FGR calculation [Rufeil-Fiori & Pastawski, 2006] in order to obtain a better approximation. Furthermore, if $\mathcal{S}$ and $\mathcal{E}$ are coupled by means of a public interaction, which enables possible $\mathcal{E}$-mediated interactions, then more quantitative and qualitative corrections to the FGR rate are expected [Dente *et al.*, 2011]. Additionally, the nature of the $\mathcal{S}-\mathcal{E}$ Hamiltonian (for example XY or Ising) could change radically the DDCS considered. Indeed, we will distinguish here two DDCSs that correspond to two different physical processes in the $\mathcal{S}-\mathcal{E}$ interaction.

It is important to notice that spectral correlations within $\mathcal{E}$, as described above, may become cumbersome to describe in statistical terms. However, realistic Hamiltonian models for the bath, as proposed here, should allow a natural description of such correlations. This is the main reason for choosing an XY Hamiltonian for $\mathcal{E}$, which

is not only understood by its single particle mapping [Lieb *et al.*, 1961], but also it is experimentally accessible [Mádi *et al.*, 1997].

Another important question in this context, is how to range from a Markovian description towards a non-Markovian scenario. In order to address such issue, we perform a numerical analysis, in which the non Markovian regime arises from many different contributions. These are: the time scale relation between $\mathcal{S}$ and $\mathcal{E}$, the public coupling between them, and the finite size of $\mathcal{E}$. Concerning to this last factor, we analyze how the degradation of $\mathcal{S}$ coherent evolution depends on the number of degrees of freedom in $\mathcal{E}$. A long-standing computational challenge shows up here: an efficient simulation of the evolution of N interacting spins. Thus, we employ both physical and numerical strategies to achieve such simulation. The first, relies on the use of the quantum parallelism for spin ensemble calculations [Álvarez *et al.*, 2008], while the second consists on the implementation of the Trotter-Suzuki algorithm in General Purpose Graphical Processing Units (GPGPU).

In the next section, we describe the spin system $\mathcal{S}$, the environment $\mathcal{E}$ (linear chains), and the way they interact. We also introduce the discussion on the time scales, Markovianity and how to quantify decoherence in many-spin systems. In Section 7.3, we deal with non Markovian cases by means of a numerical analysis. In Appendices C and D we present a description of the techniques involved in an efficient simulation of a many-spin evolution. In Section 7.4, the comparisons between the numerical and analytical rates (this analysis is not going to be developed in this thesis) will show the relevance of finite size and memory effects, environment-mediated interactions, the role of the bath spectral structure, among others. Finally, further discussions and conclusions are presented.

7.2 QUANTUM DYNAMICS OF SPIN-CHAIN SYSTEMS

7.2.1 THE MODEL

In Fig. 7.1 the spin model of interest is shown, i.e. a two-spin system $\mathcal{S}$ interacting with a ring-like environment $\mathcal{E}$. The number of spins within $\mathcal{E}$ is crucial to determine the dynamics and the approximations made to describe it. If that number is large enough, it can be thought as an infinite linear chain, enabling an attainable analytical treatment.

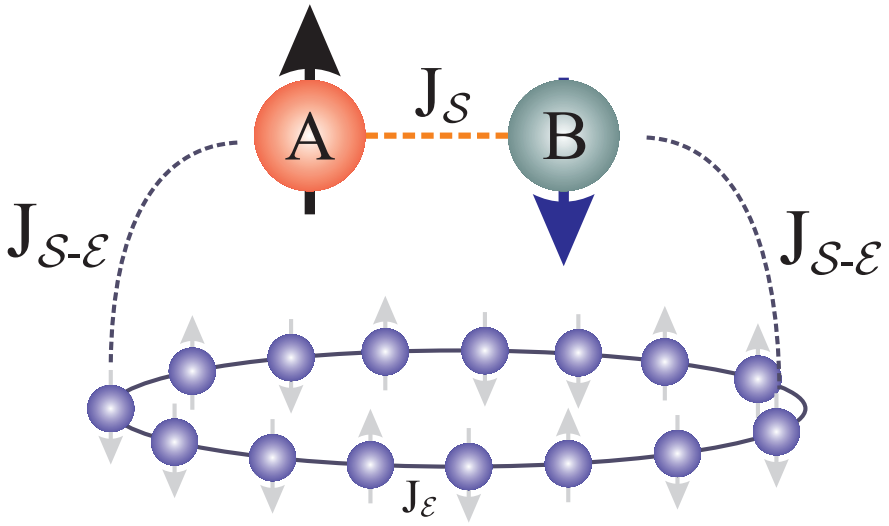

Figure 7.1: Two spin system couple to an environment of $m_{\mathcal{E}}$ spins. The rabi oscillations presented in $\mathcal{S}$ will decay at different rates depending on the number of spins of $\mathcal{E}$ and the type of coupling between $\mathcal{S}$ and $\mathcal{E}$.

The whole spin Hamiltonian is given by:

$$\hat{H}_{total} = \hat{H}_{\mathcal{S}} + \hat{H}_{\mathcal{E}} + \hat{H}_{\mathcal{S}-\mathcal{E}}, \tag{7.1}$$

where,

$$\hat{H}_{\mathcal{S}} = J_{\mathcal{S}}(\hat{S}_A^x \hat{S}_B^x + \hat{S}_A^y \hat{S}_B^y), \tag{7.2}$$

$$\hat{H}_{\mathcal{S}} = \frac{J_{\mathcal{S}}}{2}(\hat{S}_A^+ \hat{S}_B^- + \hat{S}_A^- \hat{S}_B^+), \tag{7.3}$$

represents the Hamiltonian for $\mathcal{S}$, typically understood as a Rabi oscillator between the $\uparrow\downarrow$ and $\downarrow\uparrow$ configurations. Also,

$$\hat{H}_{\mathcal{E}} = \sum_{n=1}^{m_{\mathcal{E}}-1} J_{\mathcal{E}}(\hat{S}_{n+1}^x \hat{S}_n^x + \hat{S}_{n+1}^y \hat{S}_n^y), \tag{7.4}$$

represents the Hamiltonian in $\mathcal{E}$, that describes the homogenous XY interaction between first neighbors spins within a linear chain of $m_{\mathcal{E}}$ spins. Notice that the closed boundary condition implies an extra XY coupling between spins 1 and $m_{\mathcal{E}}$. One should be aware that the typical energy scales for $\mathcal{S}$ and $\mathcal{E}$ are given by $J_{\mathcal{S}}$ and $J_{\mathcal{E}}$, respectively.

The $\mathcal{S} - \mathcal{E}$ Hamiltonian is:

$$\hat{H}_{\mathcal{S}-\mathcal{E}} = \sum_{i=A,B} J_{\mathcal{S}\mathcal{E}}[2\alpha \hat{S}_i^{(\mathcal{S})z}\hat{S}_{n_i}^{(\mathcal{E})z} - (\hat{S}_n^{(\mathcal{S})x}\hat{S}_{n_i}^{(\mathcal{E})x} + \hat{S}_n^{(\mathcal{S})y}\hat{S}_{n_i}^{(\mathcal{E})y})] \tag{7.5}$$

$$= \sum_{i=A,B} J_{\mathcal{S}\mathcal{E}}[2\alpha \hat{S}_i^{(\mathcal{S})z}\hat{S}_{n_i}^{(\mathcal{E})z} - \frac{1}{2}(\hat{S}_i^{(\mathcal{S})+}\hat{S}_{n_i}^{(\mathcal{E})-} + \hat{S}_i^{(\mathcal{S})-}\hat{S}_{n_i}^{(\mathcal{E})+})]. \tag{7.6}$$

Where n_i indexes the spin in $\mathcal{E}$ coupled to the i spin in $\mathcal{S}$. The parameter α (see Ref. [Pastawski *et al.*, 1995]) determines the nature of the interaction. For the ordinary NMR experiments: XY interaction is represented by $\alpha = 0$, isotropic -Heisenberg- by $\alpha = -\frac{1}{2}$, and $\alpha = 1$ for the truncated dipolar. In order to systematize our results, we will range the values for α from 0 to 1. Thus, the $\mathcal{S} - \mathcal{E}$ interaction has always a "single-particle" component (XY process), i.e. polarization interchange, and the two-body Ising interaction is progressively turned on by increasing α.

It is crucial to stress that $J_{\mathcal{S}}$, $J_{\mathcal{E}}$ and $J_{\mathcal{S}\mathcal{E}}$ determine the relevant time scales of the whole problem. As introduced above, the first two give the homogenous XY coupling within the system and the environment, respectively, while $J_{\mathcal{S}\mathcal{E}}$ stands for the transversal coupling "constant" between $\mathcal{S}$ and $\mathcal{E}$. With the purpose of a smooth degradation of the $\mathcal{S}$ coherent dynamics, we set $J_{\mathcal{S}\mathcal{E}}$ in a weak coupling regime, i.e. $J_{\mathcal{S}\mathcal{E}} \ll J_{\mathcal{S}}$, $J_{\mathcal{E}}$. Such an irreversible degradation or decay to the environment, and hence the FGR, implies that the unperturbed isolated system state has zero overlap with the eigenstates of $\mathcal{S} + \mathcal{E}$. This breakdown of the time independent perturbation theory occurs when the interaction with each environment eigenstate, $J_{\mathcal{S}\mathcal{E}}/\sqrt{m_{\mathcal{E}}}$, is much greater than the spacing between adjacent levels, of about $J_{\mathcal{E}}/m_{\mathcal{E}}$. In summary, the interaction time scale $\hbar/J_{\mathcal{S}\mathcal{E}}$ must be shorter than the bath's Heisenberg time $\hbar m_{\mathcal{E}}/J_{\mathcal{E}}$. Additionally, memory effects modifying appreciably the FGR rates are expected when both $\mathcal{S}$ and $\mathcal{E}$ have the same time scales. Thus $J_{\mathcal{S}} \simeq J_{\mathcal{E}}$, leads to a non-Markovian scenario. On the other hand, for the fast fluctuation regime, $J_{\mathcal{S}} \ll J_{\mathcal{E}}$, the Markovian approximation becomes satisfactory [Dente *et al.*, 2011].

7.2.2 MEASURING DECOHERENCE: MESOSCOPIC AND LOSCHMIDT ECHOES

A natural question that arises for the spin model introduced above, is how to quantify the destruction of the $\mathcal{S}$ coherent evolution in the presence of $\mathcal{E}$.In chapters 5

and 6 we started solving this question analytically and numerically. In particular, in Chap. 6, we compared the attenuation Mesoscopic Echoes (ME)[Pastawski *et al.*, 1995, Álvarez *et al.*, 2010a] and the Loschmidt Echo [Jalabert & Pastawski, 2001], [Levstein *et al.*, 1998] as two possible decoherence quantifiers.

For completeness we will write down the Loschmidt echo measure,

$$M(2t_R) = \frac{\left\langle \Psi_{eq} \right| \hat{S}_1^{(\mathcal{S})z}(2t_R)\hat{S}_1^{(\mathcal{S})z}(0) \left| \Psi_{eq} \right\rangle}{\left\langle \Psi_{eq} \right| \hat{S}_1^{(\mathcal{S})z}(0)\hat{S}_1^{(\mathcal{S})z}(0) \left| \Psi_{eq} \right\rangle}. \tag{7.7}$$

with the spin operators expressed in the Heisenberg representation:

$$\hat{S}_1^{(\nu)z}(2t_R) = e^{\mathrm{i}(\hat{H}_{\mathcal{S}}+\hat{\Sigma})\frac{t_R}{\hbar}} e^{\mathrm{i}(-\hat{H}_{\mathcal{S}}+\hat{\Sigma})\frac{t_R}{\hbar}} \hat{S}_1^{(\nu)z} e^{-\mathrm{i}(-\hat{H}_{\mathcal{S}}+\hat{\Sigma})\frac{t_R}{\hbar}} e^{-\mathrm{i}(\hat{H}_{\mathcal{S}}+\hat{\Sigma})\frac{t_R}{\hbar}}.$$

Here, $\hat{\Sigma} = \hat{H}_{\mathcal{E}} + \hat{H}_{\mathcal{S}-\mathcal{E}}$, is the perturbation which acts in both periods and t_R is the time for the forward and backward evolution time. The system Hamiltonian $\hat{H}_{\mathcal{S}}$ can we switched into $-\hat{H}_{\mathcal{S}}$ in backward evolution.

The computation of the Loschmidt echo in Eq. 7.7 for a spin system with arbitrary interactions, requires a full many-body evolution. We discuss the details on how to perform such a numerical evolution in Appendices C and D.

It is important to remember that the LE procedure have intrinsic advantage over the ME counterpart, since as discussed in previous chapters, it filters the relevant dynamics [Dente *et al.*, 2011, Zangara *et al.*, 2011].

Clearly, in the case where $\mathcal{S}$ is isolated, the local LE will have a steady value of 1. This means that the system is fully reversible. On the other hand, if the system is coupled to $\mathcal{E}$, the local LE should decay, i.e. our reversal procedure fails to recover the excitation spread to the environment. The LE decay rate is directly identified as the decoherence rate $1/\tau_\phi$ [Petitjean & Jacquod, 2006]. Naturally, this rate is a function of the $\mathcal{S}-\mathcal{E}$ coupling parameter $J_{\mathcal{S}\mathcal{E}}$ (from Hamiltonian of Eq. 7.6). Since we are interested in the regime of weak coupling with the fluctuating environment, we analyze the conditions of validity of a FGR [Rufeil-Fiori & Pastawski, 2006, Jacquod *et al.*, 2001, Cucchietti *et al.*, 2006]:

$$\frac{1}{\tau_\phi} \simeq \frac{2\pi}{\hbar}\left(\hat{H}_{\mathcal{S}-\mathcal{E}}\right)^2 N_0, \tag{7.8}$$

where $\left(\hat{H}_{\mathcal{S}-\mathcal{E}}\right)^2$ is a representative value of the $\mathcal{S}-\mathcal{E}$ coupling, and N_0 represents an appropriate density of directly connected states [Rufeil-Fiori & Pastawski, 2009].

7.3 NON-MARKOVIAN EVOLUTION OF SPIN SYSTEMS

In order to address the non-Markovian regime for the model introduced in Section 7.2.1, we perform a numerical approach for the spin dynamics. Here, the decoherence rate $1/\tau_\phi$ is obtained by both decoherence-) quantifiers previously introduced, i.e. the ME attenuation and the LE decay. As we mentioned before, every decay rate will be understood as function of $J^2_{\mathcal{SE}}/\hbar J_{\mathcal{E}}$. This quantity is indeed appropriate to verify the FGR validity (Eq. 7.8), as soon as $J^2_{\mathcal{SE}}$ is the typical scale for the $\mathcal{S}-\mathcal{E}$ interaction's second moment, and $1/\hbar J_{\mathcal{E}}$ has the units of a DDCS.

It is interesting to note that, in most of the cases, the equivalence of time scales between $\mathcal{S}$ and $\mathcal{E}$ (setting $J_{\mathcal{E}} = J_{\mathcal{S}}$), forbids the assumption of a fast fluctuation regime. Thus, in principle there should not be expected a smooth monotonous decay FGR-like. However, it turns out that the exponential regime is still present, but the rates are corrected by memory effects (typically understood as feedback from $\mathcal{E}$ to $\mathcal{S}$).

As in any other many-body quantum evolution, the computational time scales exponentially in the total number of spins N. Hence, one has to define an upper limit for N and a temporal window or evolution time. In our case, the maximum $N_{\max}$ is 20, and the evolution time depends on whether the observable is the ME or the LE. The numerical solution includes the use of the quantum parallelism and the Trotter-Suzuki algorithm implemented on Graphical Processing Units. Details on such physical and technical issues are presented in Appendix C.

7.3.1 NUMERICAL RESULTS

The spin system we analyze is schematized in Fig. 7.1. Here we deal with the non-Markovian version where the environment $\mathcal{E}$ is strictly finite. Additionally, we stress that for the spin model, $\mathcal{S}$ and $\mathcal{E}$ have the same time scale ($J_{\mathcal{E}} = J_{\mathcal{S}}$). The type of interaction between $\mathcal{S}$ and $\mathcal{E}$ presented in Fig. 7.1 made the system to have a "public interaction": both spins are coupled to the same reservoir (see Chap. 5).

We start analyzing the simplest case, which corresponds to a XY ($\alpha = 0$) $\mathcal{S}-\mathcal{E}$ Hamiltonian. Each spin in $\mathcal{S}$ is coupled to non-consecutive spins within the ring $\mathcal{E}$ (indeed, they are coupled to opposite spins in the ring). In Fig. 7.2, the Rabi oscillations (the most simplified version of a ME) and the LE are plotted. When the coupling is only

with an XY interaction, its dynamics keeps the essential physics discussed in Chap. 5 and in Ref. [Dente *et al.*, 2011], as long as the single-particle picture underlies its dynamical behavior (even though an exact mapping does not hold). Thus, one could perform the an equivalent analysis on time scales, Markovianity and public-private reservoirs as be made in that chapter.

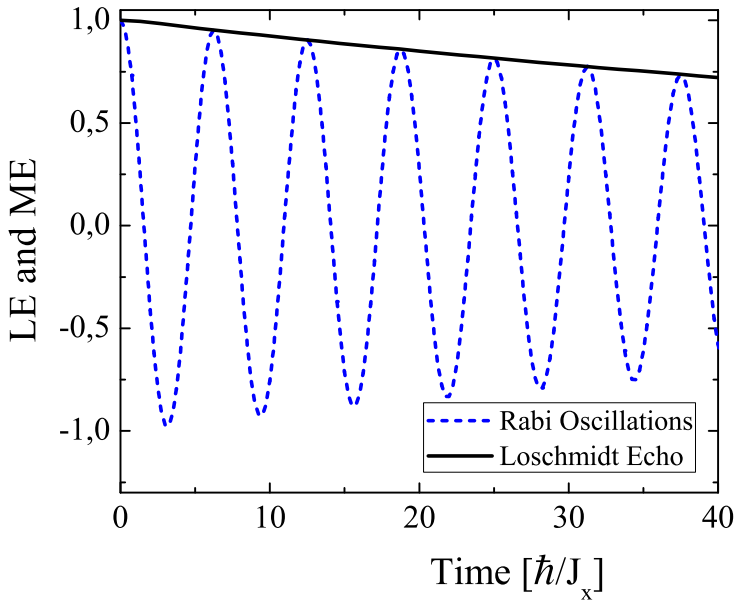

Figure 7.2: Rabi oscillations and Loschmidt Echo for the two spin system $\mathcal{S}$ coupled to the spin ring $\mathcal{E}$ (Fig. 7.1) by means of a pure XY Hamiltonian.

In Fig. 7.3 we used the LE quantifier to measure the total decoherence rate $1/\tau_\phi$ as a function of α^2. This was obtained by using the same methods of Chap. 6, but we now applied it to the Rabi system of Fig. 7.1.

The XY decoherence rate obtained (from the interception of the linear equation of Fig. 7.3 and its abscissa), $1/\tau_\phi^{XY} \simeq 0.68 \left[J_{\mathcal{SE}}^2/\hbar J_{\mathcal{E}}\right]$, is almost in agreement with the case analyzed in Chap. 5. Remember that there we only used a fermionic (tight binding) model to evaluate the decoherence. The hypothetical rates derived in that chapter in spin units, are $1/\tau_\phi^{XY} \simeq 0.58 \left[J_{\mathcal{SE}}^2/\hbar J_{\mathcal{E}}\right]$ for private environments, and $1/\tau_\phi^{XY} \simeq (0.60 \sim 0.85) \left[J_{\mathcal{SE}}^2/\hbar J_{\mathcal{E}}\right]$ for a public one (depending on the quantifier we use: ME or LE). Notice that the non-consecutive coupling to the ring bath may attenuate the correlations in

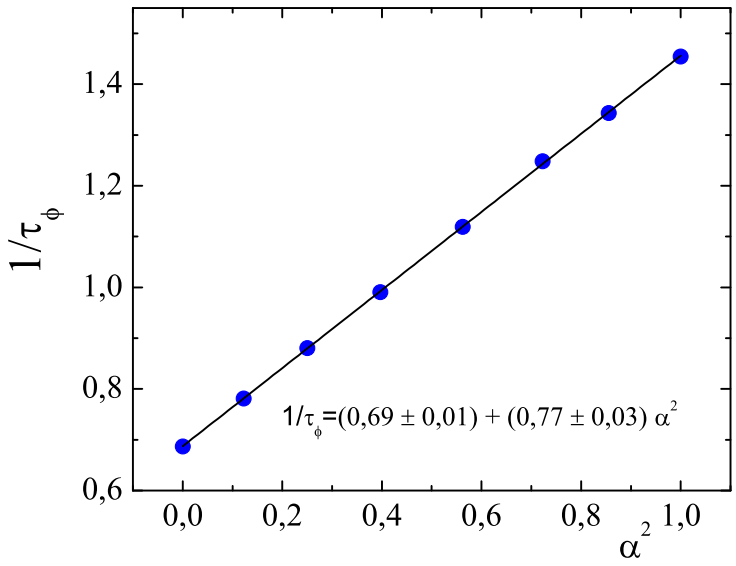

Figure 7.3: Total decoherence rate $1/\tau_\phi$ as a function of α^2 evaluated from the LE. Each point correspond to a particular α-election in Hamiltonian 7.5, and in expressed in units of $J_{s\mathcal{E}}^2/\hbar J_{\mathcal{E}}$.

the environment or any $\mathcal{E}$-mediated interaction, thus the rates becomes in the range of the expected for the tight-binding case, but not equal.

We stress here the role of the LE as a filter for relevant dynamical processes, as previously pointed in Ref. [Dente *et al.*, 2011]. In fact, it can be seen from Fig. 7.2 how the reversal procedure within the $\mathcal{S}$-degrees of freedom may reveal directly the smooth degradation due to the environmental degrees of freedom.

In order to study the role of a genuine many-body $\mathcal{S}-\mathcal{E}$ interaction, we coupled $\mathcal{S}$ and $\mathcal{E}$ by means of a pure Ising Hamiltonian. In principle, a Rabi oscillation perturbed by a phase fluctuation does not decay in amplitude unless several "decoherent" stories or trajectories are averaged (this is a well known fact from the quantum jump theory [Plenio & Knight, 1998]). However (and quite surprisingly), even though we are using few entangled states to represent the whole ensemble evolution (see Appendix C), the dynamics is self-averaging and the Rabi oscillations indeed attenuate. Such degradation is shown in Fig. 7.4, where the attenuation of the typical oscillations in the two-spin $\mathcal{S}$ are plotted for different $m_{\mathcal{E}}$ (spins within the bath). The strong influence of $m_{\mathcal{E}}$ in the decoherence process, can be interpreted as a direct consequence of a finite (discrete) spectrum within $\mathcal{E}$. These relevant non-Markovian effects evidenced in Fig. 7.4 justify our initial premise: every $\mathcal{S}-\mathcal{E}$ interaction must be built up from a single-particle base (XY) plus a gradually increased two-body interaction (Ising). The anisotropy (α) is increased from zero (XY, i.e. pure polarization transfer) up to one (Dipolar truncated Hamiltonian), with the purpose of smoothly mount the many-body physics over a one-body dynamics. Additionally, Fig. 7.4 allows to determine a suitable temporal window for analyzing the LE decay, in general situations. Therefore, we choose $m_{\mathcal{E}} = 18$, and a maximum reversal time t_R of approximately $30\hbar/J_{\mathcal{E}}$, to obtain the decoherence rate for as a function of $J^2_{\mathcal{SE}}/\hbar J_{\mathcal{E}}$. Then, we range over the anisotropy α and summarize the obtained rates in Fig. 7.3**.**

It is important to remark that the dependence of the dynamics as a function of $m_{\mathcal{E}}$, as in Fig. 7.4, tell us how far are we from simulating an infinite environment. This kind of example pushes us to search efficient numerical methods capable of compute bigger spin systems.

Summarizing this section, have found that the whole analysis (fitting of Fig. 7.3)

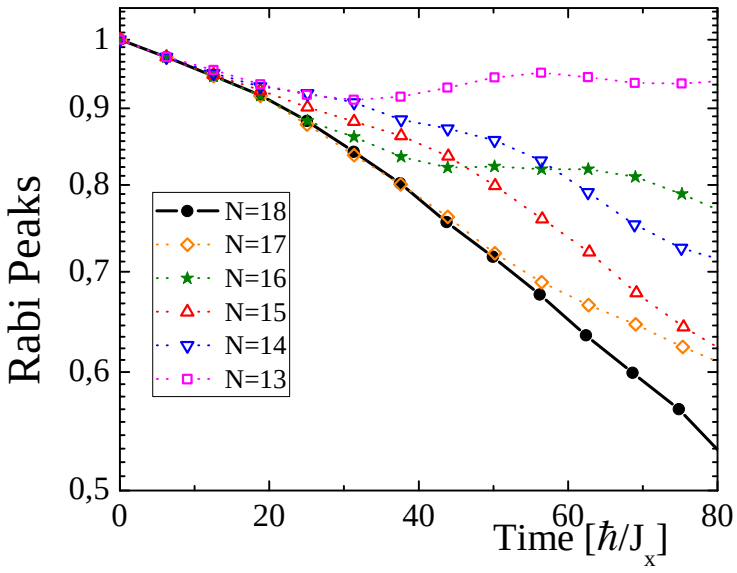

Figure 7.4: Peaks in the Rabi oscillation for site A, from a two spin system coupled to a XY ring (Fig. 7.1). Finite size effects (and discretness) in the ring spectrum is evidenced varying the number $m_{\mathcal{E}}$.

yields that the total decoherence rate $1/\tau_\phi$ can be written as:

$$1/\tau_\phi = 1/\tau_\phi^{XY} + 1/\tau_\phi^{ZZ}. \tag{7.9}$$

Hence:

$$1/\tau_\phi^{XY} \simeq 0.68 \left[J_{\mathcal{SE}}^2/\hbar J_\mathcal{E}\right], \tag{7.10}$$

and

$$1/\tau_\phi^{ZZ} \simeq 0.77 \left[J_{\mathcal{SE}}^2/\hbar J_\mathcal{E}\right]. \tag{7.11}$$

We again observe that this rate has the contribution of two different process, one corresponding to the flip-flop interactions and the other to the Ising couplings.

7.4 DECOHERENCE RATE ANALYSIS

By numerically studying the Non-Markovian dynamics over the Rabi system, we were capable of subtract the contributions to the decoherence rate. The XY contribution (see Eq. 7.10) obtained could be understood by the one body problem of the Chap. 5. Even though our spin problem cannot be mapped directly into a one-body problem (not even for a pure XY $\mathcal{S}-\mathcal{E}$ interaction), one has the confidence that the XY contribution may have many dynamical effects retained from the single particle picture [Dente *et al.*, 2011]. The reason relies on an usual strategy: a many-body evolution understood as a one-body evolution plus a decoherent process. Thus, it shows up here the question on understanding this decoherence rate $1/\tau_\phi$ properly. At this respect we recall that in Ref. [Álvarez *et al.*, 2010a] (and in Ref. [Alvarez, 2007]), the authors propose a model to analytically obtain this decoherence rate. There, they used an environment modeled by a semi-infinite tight binding chain (accordingly, a surface LDoS), which is connected to every site of the system. Although they could solve it, this model departs from the actual spin environment: a finite chain with periodic boundary conditions.

In this work we used similar analytical approach to that made in Ref. [Alvarez, 2007], but we now consider infinite chains (bulk LDoS) as a more realistic model for the environment. This model hamiltonian is presented in Fig. 7.5.

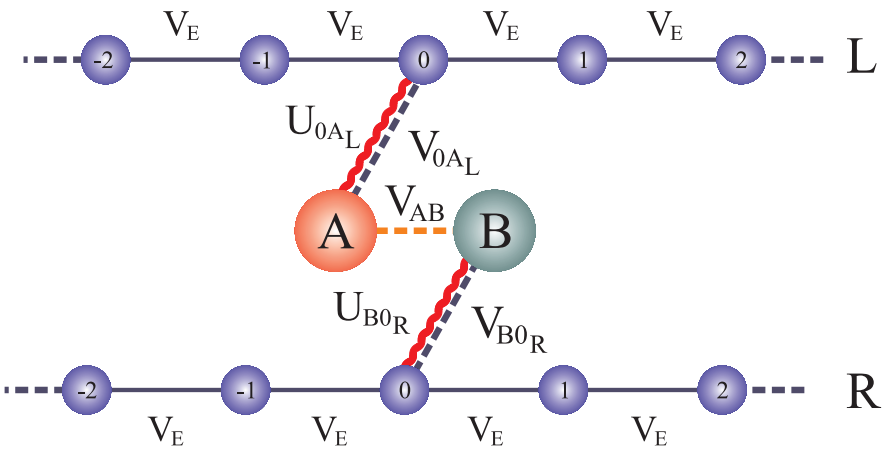

Figure 7.5: Fermionic model. Two sites coupled to two independent -private- infinite chains (Bulk LDoS must be employed).

With the use of the non-equilibrium Keldysh formalism [Keldysh, 1964, Pastawski, 1991] and similar methods to that included in Refs. [Álvarez *et al.*, 2010a] and [Alvarez, 2007], we obtained that the decay rate is,

$$\begin{aligned}\frac{1}{\tau_{SE}} &= \frac{1}{\tau_V} + \frac{1}{\tau_U} \\ &= |V|^2 \frac{1}{\hbar^2}\left[\int_{-\infty}^{\infty} J_0(\frac{2V_E\delta t_i}{\hbar})\mathrm{d}\delta t_i\right] \\ &+ |U|^2 f_s\left[1-f_s\right]\frac{1}{\hbar^2}\left[\int_{-\infty}^{\infty}[J_0(\frac{2V_E\delta t_i}{\hbar})]^2\mathrm{d}\delta t_i\right],\end{aligned} \tag{7.12}$$

where $J_0(t)$ denotes the Bessel function of first kind and zeroth order and f_s is the occupation factor, which at infinite temperature is $1/2$.

Remember that J_0 is the solution obtained from the Fourier transform of,

$$\int N_0(\varepsilon)\exp\{-\mathrm{i}\varepsilon\delta t_i\}\frac{\mathrm{d}\varepsilon}{2\pi\hbar} = \frac{1}{2\pi\hbar}J_0(\frac{2V_E\delta t_i}{\hbar}), \tag{7.13}$$

where $N_0(\varepsilon)$ is the bulk LDoS of a linear tight binding chain,

$$N_0(\varepsilon) = \frac{1}{2\pi V_E}\frac{1}{\sqrt{1-(\frac{\varepsilon}{2V_E})^2}}. \tag{7.14}$$

It is important to remark that $J_0(t)$ is just the survival probability for an state in the bulk of a tight binding chain. Thus the intrinsic dynamics of the environment appear in the solutions for the decoherence rates. In addition, we can observe that in Eq. 7.12 the total decay rate is separated into two contributions, $1/\tau_U$ and $1/\tau_V$, which stand for the Coulomb and Hopping decay rates, respectively.

The condition to solve Eq. 7.12 with the inclusion of the Ising interaction required a self-consistent self-energy calculation, which we will be left aside of this thesis. From such self-consistent condition, we can computed an analytical $\mathcal{S}-\mathcal{E}$ interaction rate which otherwise would diverge (because the integral of $[J_0(\frac{2V_E\delta t_i}{\hbar})]^2$ diverges).

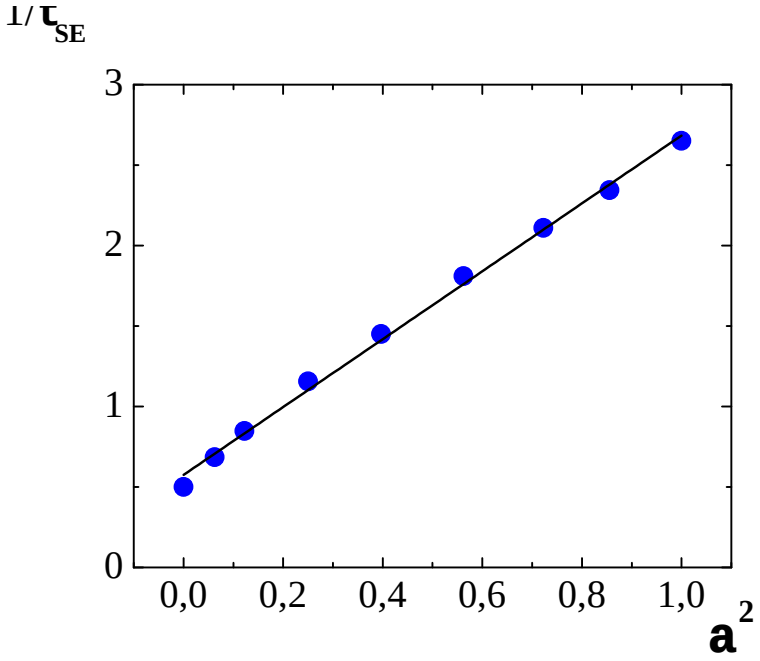

Figure 7.6: Characteristic rate as a function of α^2, in units of $\hbar J_{\mathcal{E}}/J^2_{\mathcal{S}\mathcal{E}}$, obtained by the Σ^{SC} calculation.

In Fig. 7.6 have plotted the equivalent analysis to that presented in Fig. 7.3, but in this case the points becomes from the analytical solutions of the problem presented in Fig. 7.5. By fitting the linearly dependence on α^2, we obtain:

$$\begin{aligned} 1/\tau_V &= 1/\tau_{SE}^{XY} \\ &= 0.5 \times \frac{(J_{\mathcal{S}\mathcal{E}})^2}{\hbar J_{\mathcal{E}}} \end{aligned}$$

and

$$1/\tau_U = \frac{1}{\tau_\phi^{ZZ}} \tag{7.15}$$

$$= (1.06 \pm 0.03)\alpha^2 \frac{(J_{s\varepsilon})^2}{\hbar J_\varepsilon}. \tag{7.16}$$

If we compare these rates with those presented in Eqs. 7.10 and 7.11, we observe that they are similar but not equals. These differences are mainly due to the presence of Non-Markovian elements in the system evolution.

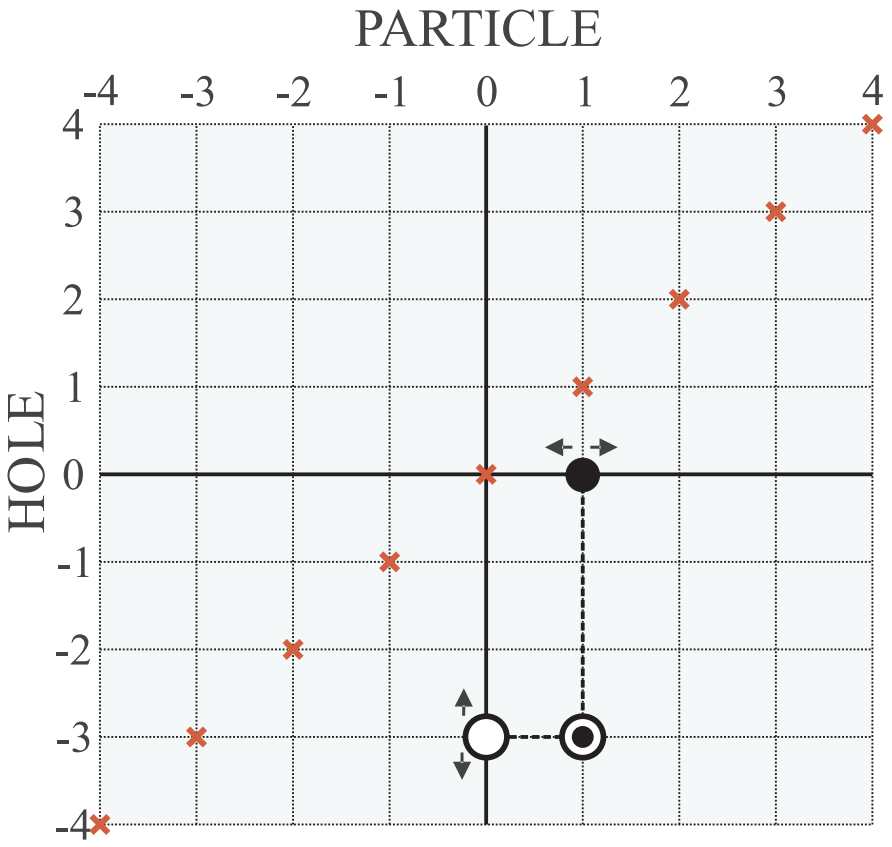

Figure 7.7: Horizontal dimension stands for *particle* coordinates in the 1-D system, and vertical for *hole* coordinates. A pair *particle-hole* is created and propagates (black and blue circles), thus the excitation moves through the 2-D lattice (green circle). In order to be mutually annihilated, the pair must be in the same site, i.e. the excitation must start and finish at the same site the diagonal (red crosses).

In what follows, let us make a discussion about the decay mechanism for the Ising

process. In our interpretation, this is formed by terms where a particle-hole excitation is created at the contact site in the reservoir, and then it propagates to finally mutually annihilate upon returning to the original site. In the Fock space representation, the independent propagation of a particle and a hole, each along a 1-D lattice, can be thought as a single particle excitation that returns to the original site in a 2-D lattice (see Fig. 7.7). In fact, we stress that Eq. 7.16 is indeed a convolution of two $1D$ LDoS, which must yield a $2D$ LDoS [Pastawski & Wiecko, 1987]. Such a convolution can be explicitly performed as follows:

$$N_{\square}(\varepsilon) = \frac{1}{4\pi^2 V_E^2} \int \frac{\theta(2V_E - |\varepsilon^{'}|)}{\sqrt{1-\left(\frac{\varepsilon^{'}}{2V_E}\right)^2}} \frac{\theta(2V_E - |\varepsilon - \varepsilon^{'}|)}{\sqrt{1-\left(\frac{\varepsilon - \varepsilon^{'}}{2V_E}\right)^2}} \mathrm{d}\varepsilon^{'}$$
$$= \frac{1}{2\pi^2 V_E} \int_{-1+x_0}^{1} \frac{\mathrm{d}x}{\sqrt{1-x^2}\sqrt{1-(x_0-x)^2}},$$

with $x_0 = \varepsilon/(2V_E)$. After some manipulation [Abramowitz & Stegun, 1964], [Gradshteyn & Ryzhik, 2007], the last expression can be written in the form:

$$N_{\square}(\varepsilon) = \frac{1}{2\pi^2 V_E} K\left(\sqrt{1-\left(\frac{\varepsilon}{4V_E}\right)^2}\right), \tag{7.17}$$

which is exactly the $2D$ square LDoS in the Tight Binding approximation [Economou, 2006]. Note also that the quantity $N_{\square}(\varepsilon)$ has a logarithmic divergence in $\varepsilon = 0$, due to the divergence of the Elliptic Integral $K(\xi)$ at $\xi = 1$. Therefore, the origin of the singularity in the FGR calculation is directly associated with the bath spectral structure; i.e. a $2D$ square lattice LDoS should stand for the corresponding DDCS (See Fig. 7.8).

The usual procedure in a FGR estimation is evaluation of the energy independent rate WBA, also understood as a first pole approximation:

$$\varepsilon - E_0 - \Sigma(E_0) = 0, \tag{7.18}$$

where $\Sigma(E_0)$ is the self-energy evaluated at the center of the band. Concerning to our problem, that approximation is equivalent to take the limit of $V_E \to \infty$ in Fig. 7.5. By taking this limit we found that the rate $1/\tau_U$ can be casted in such a standard FGR

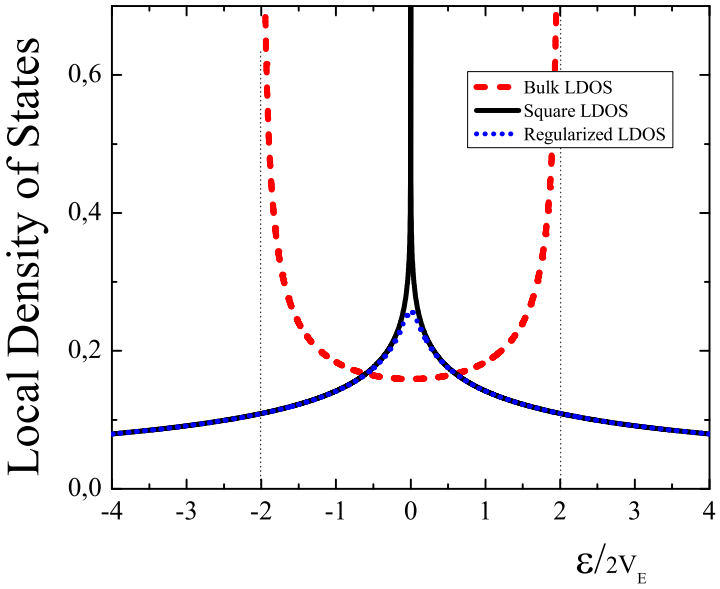

Figure 7.8: Local Density of States for an infinite linear tight binding chain (red dashed) and for a square lattice (blue dotted). The first plays the role of the DDCS for the XY contribution in the FGR, while the second is the DDCS for the Ising process. For this last DDCS, the regularization procedure would remove the singularity as it is shown (straight black line).

form by writing:

$$1/\tau_U = (2\pi/\hbar)\left|\bar{U}\right|^2 N_\square(\varepsilon = 0) \quad \text{with} \quad \left|\bar{U}\right|^2 = |U|^2 \times f_s(1-f_s)$$

where $N_\square(\varepsilon = 0)$ is the DDCS and $\left|\bar{U}\right|^2$is the effective second moment for the Ising interaction. In this sense, as we mention before, the evaluation of $N_\square(\varepsilon)$ at $\varepsilon = 0$ diverges, thus to perform an correct evaluation, we have to renormalize $N_\square(\varepsilon)$ in such a way that it becomes finite in $\varepsilon = 0$ (see Fig. 7.8). The method used for this regularization consist on the introduction of an extra exponential decay in the integrals of Eq. 7.12. This ansatz implies an exponential decay within the bath correlation function, whose characteristic time is the same as the system's. This the procedure leads to a slight shift in the complex plane that moves the singularity away and let us evaluate the Ising contribution with a self consistent calculation. This method is what we call the self-consistent evaluation of the self-energy (Σ^{SC}).

In order to connect the Markovian discussion with the non-Markovian situations, the results from the numerical simulations deserve a careful attention. The explanation of how the rates are corrected by memory effects relies mostly on the time scale relation imposed by such simulation of the many-spin dynamics. As before, the XY contribution appears to have an easier interpretation, since it is naturally linked to one-body physics. Thus, we recall the discussion already presented in the Chap. 5 (also found in Ref. [Dente *et al.*, 2011]). First, we stress that the $\mathcal{S}-\mathcal{E}$ interaction is collective, or public, due to the double connection between $\mathcal{S}$ and $\mathcal{E}$. In such a situation, memory effects grow up considerably, and the analytical prediction should be more sophisticated than an energy-independent rate model (WBA). Indeed, as claimed in Ref. [Dente *et al.*, 2011], a self-consistent Fermi Golden Rule (SC-FGR) would yield satisfactory predictions (not possible to compute here because it would involve the whole solution of the many-body problem). The bath's LDoS plays here a crucial role, since the SC-FGR involves its evaluation in the exact $\mathcal{S}-\mathcal{E}$ poles. For a convex LDoS (Eq. 7.14), the WBA value in a first pole approximation lies at the bottom of its valley. The evaluation of the LDoS at the exact poles (SC-FGR) moves the rate away from this first estimation, thus yielding a greater rate. As pointed in Ref. [Dente *et al.*, 2011], this shift is enhanced if the environment is "public" as it introduces $\mathcal{E}$-mediated interactions.

The obtained results point to verify the previous statements for the XY contribution. The associated rate $1/\tau_\phi^{XY} \simeq 0.68\left[J_{\mathcal{SE}}^2/\hbar J_{\mathcal{E}}\right]$ for the simulated pair of spins

(Fig. 7.1), evidences the overestimation of the WBA approach. As discussed in [Dente *et al.*, 2011], we expect to recover the (Markovian) rate $1/\tau_\phi^{XY} \simeq 0.50 \left[J_{\mathcal{SE}}^2/\hbar J_{\mathcal{E}}\right]$ in a fast fluctuating environment. However, accelerating the bath's dynamics will directly enhance finite-size signatures within $\mathcal{E}$. In Ref. [Dente *et al.*, 2011], due to the low computational complexity of that single-particle physics, such acceleration was able to be performed, explicitly showing the appearance of the Markovian decay.

On the other hand, the numerical results obtained for the Ising contribution deserves again carefull attention. The first striking point on the Ising component is influence of the number of degrees of freedom in $\mathcal{E}$, i.e. the number of spins $m_{\mathcal{E}}$. Obviously, it is not possible to perform a simulation which includes a thermodynamical limit in such number of spins, as soon as the computational capabilities are limited. Thus, one should be aware of the dependence on $m_{\mathcal{E}}$, and find an appropriate temporal window in order to reveal an exponential decay (Fig. 7.4). Moreover, our strategy relies on mounting the Ising process over the well-understood XY component. Hence, the Ising $1/\tau_\phi^{ZZ}$ contribution is computed systematically as a correction to the first $1/\tau_\phi^{XY}$ contribution, by smoothly increasing the α parameter.

The non-trivial DDCS identified for the Ising component implies that the comparison between the WBA (regularized) rate and the numerical one cannot be straightforward performed. The regularization procedure (Σ^{SC}) for the WBA rate, precludes a similar analysis on the DDCS convexity and the location of the exact eigen-energies (as in Ref. [Dente *et al.*, 2011]). However, if the shift from the singularity is small enough, one expects that the evaluation in the middle of a band spectrum yields a rate greater than the exact energy-dependent rate (Fig. 7.8). Thus, the decoherence contribution $1/\tau_\phi^{ZZ} \simeq 0.77 \left[\alpha^2 J_{\mathcal{SE}}^2/\hbar J_{\mathcal{E}}\right]$ appears to be in well agreement with the analytical value $1/\tau_\phi^{ZZ} \simeq 1.06 \left[\alpha^2 J_{\mathcal{SE}}^2/\hbar J_{\mathcal{E}}\right]$.

7.5 Conclusions

We have studied the decoherence introduced in a quantum spin system ($\mathcal{S}$) by an environment of interacting spins ($\mathcal{E}$) in different scenarios, both Markovian and non-Markovian. With this purpose we employed numerical evolutions with up to 20 spins and many-body analytical techniques. The first involves a Trotter decomposition assisted by a recently developed algorithm that relies on quantum parallelism [Álvarez *et al.*, 2008]

to evaluate local observables, implemented on GPGPU. In this case the measurable observable is the local polarization which is evaluated at the specific times when Mesoscopic Echoes, i.e. finite size recurrences, show up. Alternatively, this local polarization is evaluated after a time reversal procedure that produces Loschmidt Echoes. In both cases, the attenuation of the echoes yields an estimate of the decoherence rate. The analytical approach (not shown in this thesis) involves the evaluation in a self-consistent calculation where the environment suffers as much decoherence as the system itself. The self-energies are calculated within a Markovian approximation (WBA), which relies on a fast fluctuation regime for environment, as a Fermi Golden Rule. The Keldysh calculation of the dynamics in a Rabi oscillator let us obtain the decoherence rates: $1/\tau_\phi^{ZZ}$ and $1/\tau_\phi^{XY}$.

The analytical rates and those obtained by numerical evolution of finite spin sets reveal a well defined exponential decay (FGR), where the corresponding rates differ by the presence of memory effects. These become important when the time scales between $\mathcal{S}$ and $\mathcal{E}$ are naturally similar, and they are further enhanced when the $\mathcal{S}-\mathcal{E}$ coupling structure induces a form of "public" $\mathcal{E}$. A striking point shown by the calculation is that the same environment behaves very differently depending on the specific interaction. For example, it can provide a finite DDCS (Eq. 7.14) for the XY interaction while for the Ising interaction it results in a divergent one (Eq. 7.17). The many-body nature of the interaction is the origin of this wealth of possibilities. In the case of the XY contribution, the shape and convexity of the DDCS justifies the why the WBA rate is greater than the numerically computed. On the other hand, for the Ising contribution, the regularized WBA rate has given a well estimation for the general (non Markovian) situation.

Chapter 8

Conclusions

In this thesis we were interested on the quantum dynamical effects produced by the presence of a surrounding environment. In particular we were interested in the those effects which are beyond the perturbation theory and those where the memory (non-Markovian) effects in the bath play a significant role.

In Chap. 2 we begin analyzing the simplest dynamics possible in spin systems: Rabi oscillations. There, we showed how the presence of an semi-infinite array of spins, as the environment, produce several types of phase transitions in the quantum dynamics. One of the first observed transitions (which also correspond to that observed in Ref. [Álvarez *et al.*, 2006]) is the collapse of two resonances into a single one (actually two overlaping resonances of different widths). There we observe that the effective energies of the system have a non-analytical behavior a point in the complex plane called exceptional point [Rotter, 2009]. In this sense, the observed frequency shows a dynamical phase transition which makes that the previously oscillating survival probability to become an overdamped decay.

Another important result of that chapter was the discovery of new regime in this kind of problems: *The virtual states*. In the literature it is common to find that the localized states transforms into a resonant states without any surprises. However in this work, we have found that appear a very rich dynamical behavior just at this transition. The virtual states, which are poles of the non-physical Green functions, can be seen as precursors of the localized states. In this region, we found that the states associated with the out-of-band poles maintains a finite weight in the edge of the Local Density of states, while the poles themselves are outside this limit. Remember that these poles,

which represent effective energies with complex values, served to deduce the dynamical behavior in the short, medium, and long time dynamics. In addition, our analysis also showed that the LDoS could be written as a product of three functions: one is the LDoS of the semi-infinite chain and the other two are Lorentzian functions whose positions and widths are defined by the GF poles. This separation, not previously reported, allowed us to show that the virtual states still have weight over the LDoS, and this weight defines the behavior of the survival probability for long times. Indeed, we showed how the power law regime [Khalfin, 1958] is obtained from the evaluation of the LDoS at their band edges. The deep analysis of this regime jointly with the numerical simulations allowed us to evaluate the exact way in which the resonances are transformed into a localized state, and how the power law is converted in a constant oscillation without decay.

The full understanding of the *Exceptional Points* and the *Virtual States* in this kind of systems, enabled the consideration of new kind of problems. Indeed it was our *"leitmotiv"* for the rest of the thesis. In Chapters 3 and 4, we present two of those problems, where we exploit what we learned about phase transitions in the quantum dynamics.

In the first of those chapters (Chap. 3) we applied the *Green function formalism* and its relation with the *Local Density of States* to explain the molecular bond-breaking in the catalysis process. There, we found that the dissociation process occurs as different types of quantum phase transitions. In particular we analyzed two different forms in which a molecule can approach to the metal surface: the perpendicular on-top and the parallel on-top configurations. In the first one, we found that the bond-breaking is determined by a form of "resonance collapse" transition. There, the internal atoms of the metals produce bonding and antibonding states with the farthest atom, that collapse at a given value of the distance between the molecule and the metal forming an almost isolated atomic state and a fully metallic state. In the other case, where the molecule approach in parallel to the metal surface, we observe that the virtual states are the prelude for the molecular dissociation which occurs when a localized state favoring the occupation of the molecular antibonding states occur. These interpretations were corroborated with the analysis of the LDoS as a function of the distance to the transition metal (i.e. with variation of the coupling between the molecule and the first atom of the metal surface).

In the other work (see Chap. 4), we used the analysis of the behavior at the Exceptional Point to determine the dynamics of surface-plasmon polariton excitations in nano-particle arrays. In this work, we started looking for a phase transition that clearly defines the separation between the synchronized plasmonic oscillations from the non-synchronized ones. However, after the analysis of several types of realistic models we finish finding that the relative phase between the oscillations of the surface plasmons become fixed despite the fact that it does not occur as the phase transition but as a smooth crossover. Indeed, we show that in arrays of two and three nano-particles, their size (directly related to the damping rate) defines if they synchronize in phase or in anti-phase. The changing of the damping of one of the particles also allowed us to control the final phase. In addition we found that embedding the nano-particles in a active media could improve the survival of the oscillations. With the analysis of the GF poles and the numerical simulations we were able to obtain the critical value for the active media that maintains the surface plasmons oscillating forever. It is important to remark that all the parameters used in this chapter are derived from experimental data. Thus, the experimental observation of this phenomena could be possible provided that one has devices capable of measure such oscillating frequencies.

In the second part of this thesis we focused on the study of how the type of coupling between the system and the environment affects the decoherence of the dynamics of finite spin systems. Particularly, we analyzed the effects of coupling the system through multiple connections and the influence of the Ising interaction in the decay rate. The analysis of several non-Markovian environments enabled us to find how the environmental correlations modify the rates evaluated from the Fermi Golden Rule.

One of the first approaches to evaluate the effects of the environment is the Fermi Golden Rule. There, the environment is thought as a "reservoir" with has so fast dynamics that it is capable of absorb any amount of energy that it receives from the system. This approach is not realistic if the environment and the system have similar time scales. Then, the quantum system could sense the discrete structure of the environment, and then, the memory effects and the correlations created within the environment could interfere with its inner dynamics. This yields decay rates (dubbed as Self-Consistent Fermi Golden Rule) that differ from those evaluated in the standard FGR. In Chap. 5 we have focused on this topic and analyzed several types of

coupling between the system (Rabi oscillator) and the environment (infinite or semi-infinite tight-binding chains). There, we found that the convexity of the Density of Directly Connected States determines the correction to the FGR decoherence rate: it will be lower when the DDCS is convex or higher otherwise. Another important result in that chapter is that in the public environment (i.e. where the system has multiple connections with the environment that provide new interaction channels), the evaluated decoherence rate is conformed from the two different FGR rates evaluated from the Hamiltonian acting during the forward evolution and that manifesting in the backwards one. Each of this dynamics have different decay rates. In the case where the environment is Non-Markovian we demonstrated that the forward and backward decoherence rates have to be evaluated from different LDoS. For all the cases treated in this chapter, including the private environments (i.e. system states can not be connected through the environment) checked that in the Wide Band Limit, the decoherence rates tends to those predicted by the FGR.

In last part of this thesis (chapters 6 and 7) we considered the incorporation of an Ising coupling between $\mathcal{S}$ and $\mathcal{E}$. There we have shown that the combination of small system and Ising interactions could lead to surprises in the dynamical behavior. Once we systematized our analysis, and realized the importance of the Non-Markovian dynamics in this kind of systems, we began to understand its effects. The combination of analytical results with the use of advance simulations in spin systems let us made a deep analysis of the decoherence rates in this type of systems.

In Chap. 6 we increased the complexity of the problem and introduced the Ising interaction. Our first approach was the numerical study of this problem and the careful analysis of their decoherence rates. In this chapter we started testing the Loschmidt Echo (LE) as a decoherence quantifier in spin systems. We take advantage of previous works [Álvarez *et al.*, 2008] and develop new algorithms using of General-Purpose Computing on Graphics Processing Units (GPGPU) that allowed us to improve the computational time of the numerical simulations. To give and idea, a typical simulation of the Loschmidt echo in a 18-spin system, using the common Trotter-Suzuki algorithm and only one computer, could take more than three months to obtain the results. However, with the new algorithms based on the GPGPU we can evaluate them in less than 4-days (see appendixes C and D). This improvements allowed us to simulate much bigger systems in reasonable times.

In what concerns to the physics of results, we were able to compare the LE with the Mesoscopic Echo [Álvarez *et al.*, 2010a], as decoherence quantifiers. We showed that the LE is capable of recovers information that escapes a standard analysis based on interference degradation. With the use of this quantifier we found that the decoherence rate is formed by two contributions: $1/\tau_\phi = 1/\tau_\phi^{ZZ} + 1/\tau_\phi^{XY}$ (at least in the parametric regimes where we worked). By the moment that we were analyzing these rates, we found unusual results coming from the combination of Ising interactions and small systems. With the advances of the numerical algorithms, we were able to study how the Ising interaction modifies the system evolution in the presence of finite environments.

This study prompted us to analyze how the decoherence rates depart from the WBA approximation in the presence of small environments (see Chap. 7). We have showed that for the case where there is only XY interactions, the rates evaluated from the FGR approach to the numerical rates if we consider that the non-Markovian effects produce shifts equivalent to those analyzed in chapters 5. In cases where we consider the Ising coupling between the system and the environment we have shown that the effective DDCS is equivalent to the local density of state for a bulk square tight-binding chain. Then, the correction to the decoherence rate due to the convexity of this function (see Chap. 5) makes that the numerical rates were in agreement with the analytic ones.

In summary, through these years of work, we have found several examples of non-Markovian models that we solved analytically and which serve to test for new numerical tools. We were able to understand almost every dynamical behavior and put them in terms of simple physical situations. The incorporation of specifically structured environments in our analysis may also serve as a testground the decoherence theories that model the environments through their correlation functions. In turn our models are susceptible to be applied to many physical systems, both classical and quantum.

Appendix A

Excitation dynamics in 1-d systems and the Spin-Fermion mapping

In this thesis we developed a scheme that could be used to treat spin polarization dynamics [Mádi *et al.*, 1997, Pastawski *et al.*, 1995], under certain assumptions. In that sense, the well-known mapping between spins and fermions [Lieb *et al.*, 1961] has been used for formulating the spin problems in terms of the non-equilibrium Keldysh formalism [Keldysh, 1964, Danieli *et al.*, 2004, Danieli *et al.*, 2005]. We briefly present here the Spin-Fermion mapping, and how the tight binding models discussed along this thesis arise.

A simple case that can be treated in this context is a linear chain of M spins in an external magnetic field. They interact with their nearest neighbors through XY coupling:

$$\hat{H} = \sum_{n=0}^{M-1} \hbar\Omega_n \hat{S}_n^z - \sum_{n=0}^{M-2} J_{n+1,n}[\hat{S}_{n+1}^x \hat{S}_n^x + \hat{S}_{n+1}^y \hat{S}_n^y] \tag{A.1}$$

$$= \sum_{n=0}^{M-1} \hbar\Omega_n \hat{S}_n^z - \sum_{n=0}^{M-2} \frac{1}{2} J_{n+1,n}[\hat{S}_{n+1}^+ \hat{S}_n^- + \hat{S}_{n+1}^- \hat{S}_n^+], \tag{A.2}$$

where $\hat{S}_n^{\pm}$ are the rising and lowering operators $\hat{S}_n^{\pm} = \hat{S}_n^x \pm \mathrm{i}\hat{S}_n^y$. The dynamics of the M-spin system, evolving under the Hamiltonian $\hat{H}$, is usually described by means

of the two site spin correlation function,

$$P_{f,i}(t) = \frac{\langle \Psi_{eq} | \, \hat{S}_f^z(t) \hat{S}_i^z(t_0) \, | \Psi_{eq} \rangle}{\langle \Psi_{eq} | \, \hat{S}_f^z(t_0) \hat{S}_i^z(t_0) \, | \Psi_{eq} \rangle}. \tag{A.3}$$

The quantity of Eq. A.3 gives the amount of local polarization in the z component at time t on the fth site, provided that the system was, at time t_0, in its equilibrium state with a spin *up* ($\uparrow$) added at ith site. Also, $\hat{S}_f^z(t) = e^{\mathrm{i}\hat{H}t} \hat{S}_f^z e^{-\mathrm{i}\hat{H}t}$ is the spin operator in the Heisenberg representation and $|\Psi_{eq}\rangle = \sum_N a_N \left| \Psi_{eq}^{(N)} \right\rangle$ is the thermodynamical many-body equilibrium function constructed by states with different number N of spins *up* with the appropriate statistical weights and random phases.

The Jordan-Wigner transformation (JWT) links spin and fermion operators at each site [Lieb *et al.*, 1961], by the following relation :

$$\hat{S}_n^+ = \hat{c}_n^\dagger \exp\left[\mathrm{i}\pi \sum_{m=1}^{n-1} \hat{c}_m^\dagger \hat{c}_m \right] \tag{A.4}$$

where $\hat{c}_m^\dagger$, $\hat{c}_m$ are the canonical fermionic operators. The use of the JWT on the Hamiltonian A.2 yields:

$$\hat{H} = \sum_{n=0}^{M-1} \varepsilon_n (\hat{c}_n^\dagger \hat{c}_n - \frac{1}{2}) - \sum_{n=0}^{M-2} V_{n+1,n} [\hat{c}_{n+1}^\dagger \hat{c}_n + \hat{c}_n^\dagger \hat{c}_{n+1}], \tag{A.5}$$

where $\varepsilon_n \equiv \hbar\Omega_n$ are the site energies and $V_{n+1,n} \equiv \frac{1}{2} J_{n+1,n}$ are the hoppings. Due to the short range interaction (first neighbors), the application of the JWT only leads to non-zero coupling terms between spins which are proportional to $\hat{c}_{n+1}^\dagger \hat{c}_n = \hat{S}_{n+1}^+ \hat{S}_n^-$. Each subspace with $\binom{M}{N}$ states of spin projection $\left\langle \sum_{n=1}^M \hat{S}_n^z \right\rangle = N - M/2$ is now a subspace with N non-interacting fermions. The eigenfunctions $\left| \Psi_\gamma^{(N)} \right\rangle$ are expressed as a single Slater determinant built up with the single particle wave functions φ_α of energy ε_α. Under these circumstances, and setting $|i\rangle \equiv \hat{c}_i^\dagger \, |\emptyset\rangle$ (with $|\emptyset\rangle$ the fermion vacuum), Eq. A.3 reduces to:

$$\begin{aligned} P_{f,i}(t) &= \left| \langle f | \exp\left[-\mathrm{i}\hat{H}t/\hbar \right] |i\rangle \, \Theta(t) \right|^2 \\ &= \hbar^2 \left| G_{f,i}^R(t) \right|^2, \end{aligned} \tag{A.6}$$

where $G^R_{f,i}(t)$ is the retarded Green's function for a single fermion that connects sites f and i.

While similar steps lead to description of excitations in Double Quantum (DQ) Hamiltonian [Fel'dman & Lacelle, 1997, Doronin *et al.*, 2000, Cappellaro *et al.*, 2007, Rufeil-Fiori *et al.*, 2009]:

$$\hat{H}_{DQ} = \sum_{n=0}^{M-2} \frac{J_{n+1,n}}{2} [\hat{S}^+_{n+1}\hat{S}^+_n + \hat{S}^-_{n+1}\hat{S}^-_n], \tag{A.7}$$

those will not be detailed here. The fundamental issue is the underlying one-body dynamics, which for the DQ Hamiltonian is revealed by a unitary transformation $\hat{H}_{DQ} = U^\dagger \hat{H}_{XY} U$ [Doronin *et al.*, 2000, Rufeil-Fiori *et al.*, 2009] that links it to an XY Hamiltonian.

Hence, for one dimensional ($1D$) chains of spins with first neighbors XY or DQ interactions, and in the high temperature regime, the dynamics of an excitation (either an injected local polarization or multiple quantum coherence) is completely equivalent to the evolution of a single particle wave function, ruled by a tight-binding Hamiltonian (this also was corroborated in the Chap. 2). Therefore, it turns out that the analysis of Hamiltonians like the one in Eq. A.5, can be casted for treating and studying several effects in spin chains [Cappellaro *et al.*, 2011] (a typical scenario in quantum information processing).

A. EXCITATION DYNAMICS IN 1-D SYSTEMS AND THE SPIN-FERMION MAPPING

Appendix B

Green's Function Poles.

Here we present the detailed analytical derivation of the GF poles and further approximations for the cases presented in Chap. 5. The results from this appendix have been summarized in the Table 5.1 showed in Sec. 5.4.

The first model under consideration (see Fig. 5.2-**I**) is given by one site coupled to a semi-infinite chain. In this case the GF pole results purely imaginary,

$$\varepsilon_{pole} = -\mathrm{i}\frac{V_0^2}{\sqrt{V^2 - V_0^2}}. \tag{B.1}$$

Even though this is indeed the exact solution, we span it for $V_0^2/V \ll 1$ and obtain:

$$\varepsilon_{pole} \simeq \frac{V_0^2}{V} \ . \tag{B.2}$$

Thus the theoretical decay rate for this model can be expressed as:

$$\frac{1}{\tau} = \frac{2}{\hbar}\Gamma_0 = \frac{2}{\hbar}\,\mathrm{Im}(\varepsilon_{pole}) \simeq \frac{2}{\hbar}\frac{V_0^2}{V}. \tag{B.3}$$

If we change the environment to an infinite chain (Fig. 5.2-**II**) the pole is,

$$\varepsilon_{pole} = -\mathrm{i}\left(2V^2(1 - \sqrt{\frac{V_0^4}{4V^4} + 1})\right)^{1/2} \simeq -\mathrm{i}\frac{V_0^2}{2V} \tag{B.4}$$

The case **III,** which corresponds to two sites coupled to a semi-infinite chain, has been solved previously in Ref. [Dente *et al.*, 2008] and in the Chap. 2,

$$\varepsilon_{pole}^2 = \frac{V_{AB}^2\left(2V^2 - V_0^2\right) - V_0^4 \pm V_0^2\sqrt{\left(V_{AB}^2 + V_0^2\right)^2 - 4V_{AB}^2V^2}}{2\left(V^2 - V_0^2\right)}. \tag{B.5}$$

Using the solutions of Eq. (26) and (27) in Ref. [Dente *et al.*, 2008], we can directly evaluate the real and imaginary parts of the poles,

$$\begin{aligned}\Delta_0 &= \pm\left(\frac{V_{AB}^2\left(2V^2-V_0^2\right)-V_0^4}{2\left(V^2-V_0^2\right)}+\Gamma_0^2\right)^{1/2}\\ &\simeq \pm V_{AB}\left(1-\frac{1}{4V}\frac{V_0^2}{V}\right) \qquad \text{(B.6)}\\ \Gamma_0 &= \left(\frac{V_0^4-V_{AB}^2(2V^2-V_0^2)}{4(V^2-V_0^2)}+\sqrt{\frac{V^2V_{AB}^4}{4(V^2-V_0^2)}}\right)^{1/2}\\ &\simeq -\frac{1}{4}\frac{\sqrt{4V^2-V_{AB}^2}}{V}\frac{V_0^2}{V}. \qquad \text{(B.7)}\end{aligned}$$

Now, we change slightly the geometry of these systems and consider again an infinite chain as environment instead the semi-infinite. For these cases we will write only the first non trivial terms of their Taylor expansion instead of the full solution. For the model of Fig. 5.2-**IV,** the solution is:

$$\Delta_0 \simeq \pm V_{AB} + O(\frac{V_0^4}{V^4}) \qquad \text{(B.8)}$$

$$\Gamma_0 \simeq -\frac{1}{2}\frac{V}{\sqrt{4V^2-V_{AB}^2}}\frac{V_0^2}{V} + O(\frac{V_0^4}{V^4}). \qquad \text{(B.9)}$$

The next case (Fig. 5.2-**V)** is a two-site system coupled to two private baths. In this case, the solution is,

$$\Delta_0 \simeq \pm V_{AB} + O(\frac{V_0^4}{V^4}) \qquad \text{(B.10)}$$

$$\Gamma_0 \simeq -\frac{V}{\sqrt{4V^2-V_{AB}^2}}\frac{V_0^2}{V} + O(\frac{V_0^4}{V^4}). \qquad \text{(B.11)}$$

At this point we observe that the imaginary part for the case **V** is twice of the system **IV**. This behavior is consistent with the count of the "number" of private baths connected to the system, and the proportion affected by those private baths.

Finally, for the case of Fig. 5.2-**VI**, the model involves a two-site system coupled to a common bath. For this case the solution is expressed in the following form,

$$\Delta_0 \simeq \pm\left(V_{AB} - \frac{1}{2}\frac{V_0^2}{V}\right) + O(\frac{V_0^4}{V^4}) \tag{B.12}$$

$$\Gamma_0 \simeq -\frac{\sqrt{4V^2 - V_{AB}^2}}{4V - 2V_{AB}}\frac{V_0^2}{V} + O(\frac{V_0^4}{V^4}). \tag{B.13}$$

At a first glance of the last equation, it is possible to notice that the imaginary part of the pole is linear on V_{AB} (in the sense of sign dependence, which is not present in the previous cases). This linearity translate into a different value for Γ_0 depending on the sign of V_{AB}. As a matter of fact, the local LE indeed relies on the change of sign to revert the dynamics. To understand the physics below this difference we have to identify the LDoS involved in the decay process. Accordingly, we symmetrize the basis, as shown in Fig. 5.6, so dimmerizing the system, and build a new basis. We take pairs of site states and map them into symmetric and anti symmetric states. Therefore the tight binding Hamiltonian for this case changes in the form of Eq. B.14.

$$
\begin{array}{c}
\\
\hat{H} = \\
\\
\\
\\
\\
\\
\\
\\
\\
\longrightarrow \hat{H}' = \\
\\
\\
\\
\\
\\
\\
\\
\\
\end{array}
\begin{array}{c}
\begin{array}{cccccccc} |A\rangle & |B\rangle & |1\rangle & |-1\rangle & |2\rangle & |-2\rangle & \cdots & \cdots \end{array} \\
\begin{pmatrix}
 & V_{AB} & & V_0 & & & & \\
V_{AB} & & V_0 & & & & & \\
 & V_0 & & V & V & & & \\
V_0 & & V & & & V & & \\
 & & V & & & & \ddots & \\
 & & & V & & & & \ddots \\
 & & & & \ddots & & & \\
 & & & & & \ddots & &
\end{pmatrix} \\
\begin{array}{cccccccc} \cdots & |2_S\rangle & |1_S\rangle & |AB_S\rangle & |AB_A\rangle & |1_A\rangle & |2_A\rangle & \cdots \end{array} \\
\begin{pmatrix}
 & \ddots & & & & & & \\
\ddots & & V & & & & & \\
 & V & V & V_0 & & & & \\
 & & V_0 & V_{AB} & & & & \\
 & & & & -V_{AB} & V_0 & & \\
 & & & & V_0 & -V & V & \\
 & & & & & V & & \ddots \\
 & & & & & & \ddots &
\end{pmatrix}
\end{array}
\tag{B.14}
$$

where $|n_S\rangle = (|n\rangle + |-n\rangle)/\sqrt{2}$, $|n_A\rangle = (|n\rangle - |-n\rangle)/\sqrt{2}$, $n = 1, 2, 3..$and $|AB_S\rangle = (|A\rangle + |B\rangle)/\sqrt{2}$, $|AB_A\rangle = (|A\rangle - |B\rangle)/\sqrt{2}$. From the Hamiltonian $\hat{H}'$ (Eq. B.14) it is easy to identify the splitting of the original problem into two semi infinite tight binding chains, with only the first two site energies non zero. This problem has been previously addressed in Refs. [Rufeil-Fiori & Pastawski, 2006] and [Rufeil-Fiori & Pastawski, 2009] and we recall the LDoS computed there. Thus in Fig. 5.7 we identify the energy excitation on the spectral structure of the environment, which is relevant during the decay process.

Appendix C

MANY-SPIN DYNAMICS: AN EFFICIENT SIMULATION ON GPGPUs.

In this appendix we specify several details on the numerical methods employed to simulate de spin dynamics introduced in chapters 6 and 7. Let us first assume we deal with a general system of N spins, which we want to evolve. The first approach to solve this evolution is the use of exact diagonalization methods. However their are not suitable for two reasons. First this methods require enough memory to store the full density matrix (which scale as 2^{2N}). Due to the memory capability of computers today, this issue could becomes a problem if the system has $N > 20$. The other, and more important, issue is the computational time spent to diagonalize the full Hamiltonian. Typical methods scale as m^3 where $m \times m$ is the size of the matrix. This makes that the computational time for evolving a general Hamiltonian, scales as 2^{3N}, implying that usual computers will take months to solve a system of $N = 20$. Generally speaking, the evolution N interacting quantum spins, is classified as a NP (non polynomial) problem, which scale with an exponential factor. Thus, it is necessary to implement other methods which take advantage of some particular symmetries (like the Wigner-Jordan mapping does) or make use of approximations which reduce the number of numerical operations.

In order to perform a reasonable fast algorithm, we employed the 4^{th} order Trotter-Suzuki decomposition [Rieth & Schommers, 2006]. This approximated method reduces

the computational efforts in the dynamics calculation, while at the same time it ensures unitarity. According to section 7.2.2, an initial equilibrium state $\left|\Psi_{eq}\right\rangle$ in the high temperature regime implies that one has to evolve the whole basis of pure states satisfying certain initial conditions. For example, in most of the cases presented in this thesis, we set the A-spin in the up state. In our numerical simulations we found that, it is only necessary to evolve *few* pure entangled states, to obtain a self-averaging evolution equivalent to the ensemble evolution [Álvarez *et al.*, 2008]. A typical initial state can now be written as:

$$|\Psi_{initial}\rangle = |\uparrow\rangle_A \otimes \left\{ \sum_{j=1}^{2^{\mathtt{N}-1}} \frac{1}{\sqrt{2^{\mathtt{N}-1}}} e^{\mathrm{i}\varphi_j} \ |\beta_j\rangle \right\}, \quad \varphi_j = \text{aleatory phase}, \tag{C.1}$$

where $|\beta_j\rangle$ is a state of the product base. In this from, the computation a time dependent observable now requires an evolution of few states which exploits the quantum entanglement over the whole spin set. Notice that the efficiency in this physical strategy depends strongly on the kind of observables we are interested in. This method can be implemented if we use only local observables, i.e. restricted to a set of spins. Then, global or non-local magnitudes should not be straightforward computed by this parallelism-based technique.

Beyond this, its implementation for large systems, soon becomes quite expensive in computational resources. Thus, we decided to boost this method with the use of a recent technology of massive parallel computing: the General Purpose Graphical Processing Units (GPGPU). This advanced tool can enhance the efficiency in the computational times provided that the algorithm does not require huge amount of memory, e.g. the whole density matrix (we believe that this restriction will be lifted soon). The main requirement relies on an accurate manipulation of the information to perform the parallel task distribution (physical parallelization), in order to avoid possible lost of coherences.

The Trotter Suzuki algorithm has already been implemented by us in problems of one-body dynamics in discrete lattices [Bederián & Dente, 2011]. In comparison with such implementation, the present algorithm has to cope with the many-body nature of multi-spin systems. This implies that in each time step of the evolution, a fully set of

correllations appear bewteen almost every state of the product base. The skecht of the algorithm is presented in Appendix D.

An evolution Trotter-Suzuki algorithms implemented on GPGPUs has allowed us to deal with sets of up to 20 spins, in reasonable computational times. In Fig. C.1 we show the comparison between the computational times for the CPU and the GPU algorithms, as a function of the size of the system. The GPU implementation results approximately 22 times faster than the CPU when the number of spins is near 20. However if the number of spins is lower than 10, the CPU is faster because the massive parallel computation of the GPU is not fully employed. Indeed, if we observe in detail, the GPU performance scale linearly up to 14 spins. This indicates that there are processors not yet occupied. This effect is only due to form of parallelizing the program.

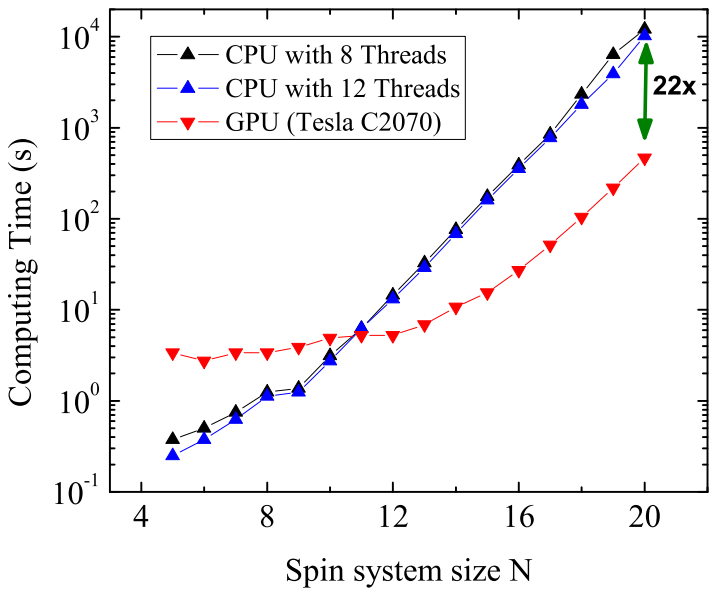

Figure C.1: Computational time for the CPU (black circles) and GPU (blue triangles) implementation of the Trotter Suzuki Algorithm for a system of N spins. The continuous line is the extrapolation for the CPU computational time. For a system of $\mathtt{N} = 20$ the GPU performance is greater than the CPU in at least 20x.

C. MANY-SPIN DYNAMICS: AN EFFICIENT SIMULATION ON GPGPUS.

Appendix D

The Trotter-Suzuki Algorithm implemented on GPGPUs

In this appendix we will present an sketch of the algorithm used to implement the Trotter-Suzuky dynamics on GPGPU. We will start following the numerical method detailed in Ref. [De Raedt & Michielsen, 2004] (see Sec. Suzuki-Trotter Product-Formula Algorithms). There they consider the general evolution operator,

$$\mathbf{U}(t) = e^{-\mathrm{i}tH} = e^{-\mathrm{i}t(H_1+...+H_K)} = \lim_{m\to\infty}\left(\prod_{k=1}^{K} e^{-\frac{\mathrm{i}tH_k}{m}}\right)^m.$$

This last equation suggest that $\mathbf{U}(t)$ can be approximated by,

$$\tilde{\mathbf{U}}_{\mathbf{1}}(t) = e^{-\mathrm{i}tH} = e^{-\frac{\mathrm{i}tH_1}{m}}...e^{-\frac{\mathrm{i}tH_K}{m}},$$

if t is sufficiently small. This approximation is called the first-order approximation. From the analysis of the following approximations, it is possible to observe that $\tilde{\mathbf{U}}_{\mathbf{2}}(t)$ and $\tilde{\mathbf{U}}_{\mathbf{4}}(t)$, corresponding to the second and fourth orders, can be written in terms of $\tilde{\mathbf{U}}_{\mathbf{1}}(t)$:

$$\tilde{\mathbf{U}}_{\mathbf{2}}(t) = \tilde{\mathbf{U}}_{\mathbf{1}}^{\dagger}(-t/2)\tilde{\mathbf{U}}_{\mathbf{1}}(t/2),$$

$$\tilde{\mathbf{U}}_{\mathbf{4}}(t) = \tilde{\mathbf{U}}_{\mathbf{2}}(at)\tilde{\mathbf{U}}_{\mathbf{2}}(at)\tilde{\mathbf{U}}_{\mathbf{2}}((1-4a)t)\tilde{\mathbf{U}}_{\mathbf{2}}(at)\tilde{\mathbf{U}}_{\mathbf{2}}(at),$$

where $a = 1/(4-4^{1/3})$. In this form, by only implementing $\tilde{\mathbf{U}}_{\mathbf{1}}(t)$ we can easily obtain the fourth order.

D. THE TROTTER-SUZUKI ALGORITHM IMPLEMENTED ON GPGPUS

In our algorithms we have separate of the total evolution time t into small Δt steps, and then we use $\tilde{\mathbf{U}}_{\mathbf{4}}(\Delta t)$ to complete the full evolution. The crucial issue that we have to consider now is how to choose the Hermitian H_n such that the matrix exponentials e^{-itH_1}, ..., e^{-itH_K} can be calculated efficiently.

If there are external time-dependent fields, it is expedient to decompose the Hamiltonian into single-spin and two-spin contributions. Suppose we consider a Hamiltonian of the form,

$$H = \sum_{j=1}^{N} \sum_{\alpha=x,y,z} h_j^\alpha \ S_j^\alpha + \sum_{j,k=1}^{N} \sum_{\alpha=x,y,z} J_{j,k}^\alpha S_j^\alpha S_k^\alpha.$$

Then, the single-spin evolution operator can be written as follows,

$$\exp\left(-\mathrm{i}t\left[\sum_{j=1}^{N}\sum_{\alpha=x,y,z} h_j^\alpha \ S_j^\alpha\right]\right) = \prod_{j=1}^{N} \exp\left(-\mathrm{i}t \sum_{\alpha=x,y,z} h_j^\alpha \ S_j^\alpha\right). \tag{D.1}$$

The evolution determined by the jth factor of Eq. D.1, which rotates the spin j about the vector $\mathbf{h}_j = \left(h_j^x, h_j^y, h_j^z\right)$, can be easily deduced. Then to perform a full step evolution we have perform N spin rotations.

We now consider the XYZ decomposition of the two-spin terms [De Raedt *et al.*, 1999]. There we start considering the H^z evolution ($H^z = \sum_{j,k=1}^{N} J_{j,k}^z S_j^z S_k^z$). The evolution of this type of operators only chain the phases of each of the basis operators. As H^z is a sum of pair interactions, it is trivial to implement this operation as a sequence "phase operators". Now we still have to solve the H^x and H^y Hamiltonians. The strategy consist now in perform single spin rotations (X_j or Y_j) to convert H^x (or H^y) into H^z. Writing $X = \prod_{j=1}^{N} X_j$ and $Y = \prod_{j=1}^{N} Y_j$ we have,

$$\begin{aligned} e^{-\mathrm{i}tH^x} &= \bar{Y} Y e^{-\mathrm{i}tH^x} \bar{Y} Y = \bar{Y} \exp\left(-\mathrm{i}t\left[\sum_{j,k=1}^{N} J_{j,k}^x S_j^z S_k^z\right]\right) Y, \\ e^{-\mathrm{i}tH^y} &= X \bar{X} e^{-\mathrm{i}tH^y} X \bar{X} = X \exp\left(-\mathrm{i}t\left[\sum_{j,k=1}^{N} J_{j,k}^y S_j^z S_k^z\right]\right) \bar{X}. \end{aligned} \tag{D.2}$$

From this equations. it is easy observed that the evolution of H^x and H^y can be wrote in term of H^z evolution which we have already decomposed.

Then all the operations can be reduced to single spin rotations and phase shift. In what follows we will describe how the algorithms works. Due to technical applications we decided to implement directly the second order evolution operator $\tilde{\mathbf{U}}_{\mathbf{2}}(t)$.

This is implemented by performing the following evolutions: $H_y/2 \rightarrow H_x/2 \rightarrow H_z \rightarrow H_x/2 \rightarrow H_y/2$.

We will show only the $H_y/2$, because the other operations are similar. This consist in three steps:

$$\text{Rotation } X90 \ \rightarrow \text{Phases in } Z \rightarrow \ \text{Rotation } X\text{-}90$$

Where $X90$ and X-90 are the rotations in 90 or -90 degrees (respectively), of each spin about the vector X and "Phases in Z" is the application of the H^z like evolution (see Eq. D.2) jointly with the single-spin evolutions of Eq. D.1. Thus, our program, essentially has two "building blocks": "Rotations" and "Phases corrections".

To understand their implementations let us first describe how we store the states. In our programs we use the product base to describe each state. Each of them is denoted by a binary number which represent the polarization of the spins. For example the state $\downarrow\uparrow\downarrow\uparrow\uparrow\downarrow\downarrow$ is written as: 0101100 (in binary notation) or 44 (in decimal notation). Then, with a single state of length 2^N we can define the state we are evolving.

In the "rotation blocks" we first start selecting spin by spin and performing the rotation $\exp\left(-\mathrm{i}tS_j^\alpha\right)$. Each individual rotation implies operations over pair of states that have the jth spin up ($\uparrow$) or down ($\downarrow$). Here we perform our first parallelization. Each pair of states (one which the jth spin up and the other with the spin down) are completely independent. Thus, we can send each of these "pair-rotations" to each core we have available.

Let us make an example of this with a four spin system. Suppose we want to rotate the second spin. Thus the "pair-rotations" we have to made are the following,

$$\begin{matrix}\downarrow\downarrow\downarrow\downarrow \\ \downarrow\uparrow\downarrow\downarrow\end{matrix}\ ,\ \begin{matrix}\downarrow\downarrow\downarrow\uparrow \\ \downarrow\uparrow\downarrow\uparrow\end{matrix}\ ,\ \begin{matrix}\downarrow\downarrow\uparrow\downarrow \\ \downarrow\uparrow\uparrow\downarrow\end{matrix}\ ,\ \begin{matrix}\downarrow\downarrow\uparrow\uparrow \\ \downarrow\uparrow\uparrow\uparrow\end{matrix}\ ,\ \begin{matrix}\uparrow\downarrow\downarrow\downarrow \\ \uparrow\uparrow\downarrow\downarrow\end{matrix}\ ,\ \begin{matrix}\uparrow\downarrow\downarrow\uparrow \\ \uparrow\uparrow\downarrow\uparrow\end{matrix}\ ,\ \begin{matrix}\uparrow\downarrow\uparrow\downarrow \\ \uparrow\uparrow\uparrow\downarrow\end{matrix}\ \text{and}\ \begin{matrix}\uparrow\downarrow\uparrow\uparrow \\ \uparrow\uparrow\uparrow\uparrow\end{matrix}\ .$$

Where we can observe that there are no repetitions in any of the states. Thus, each operation is independent and the parallelization can be made without any problem.

Here, it is important to mention that we have implemented this algorithm on a GPGPU processor. This type of processors could handle more than 500 operations

at the same time (depending on the number of cores of the video card). The only restriction is the available memory, which nowadays is no more than few Mb per core. Therefore, our calculations, which only implies small 4x4 matrix operations, no require higher amounts of memory.

Turning back to the algorithm implementation, the next step is to applied the "Phases" operations. This operations is completely independent for each state of the product base. Thus it is fully parallelizable.

Now suppose we choice on state of the product base. Them we only have to correct the phases due to the single and the double-spin operations in the form of Eqs. D.1 and D.2.

In this form, combining all the building blocks we can obtain the evolution for a Δt period. The rest of the evolution only consist in the successive application of these steps.

References

[Abragam, 1986] Abragam, A. (1986). *The principles of nuclear magnetism.* The International Series on Monographs on physics. Oxford: Oxford University Press. 119, 131

[Abramowitz & Stegun, 1964] Abramowitz, M. & Stegun, I. (1964). *Handbook of mathematical functions with formulas, graphs, and mathematical tables.* Number v. 55,n.º 1972 in Applied mathematics series. U.S. Govt. Print. Off. 146

[Alvarez, 2007] Alvarez, G. A. (2007). *Decoherence of many-spin systems in NMR: From molecular characterization to an environmentally induced quantum dynamical phase transition.* PhD thesis Universidad Nacional de Cordoba - Argentina. ArXiv: 0705.2350. 142, 143

[Álvarez *et al.*, 2006] Álvarez, G. A., Danieli, E. P., Levstein, P. R., & Pastawski, H. M. (2006). *The Journal of Chemical Physics,* **124** (19), 194507. 14, 22, 23, 36, 38, 45, 90, 151

[Álvarez *et al.*, 2007] Álvarez, G. A., Danieli, E. P., Levstein, P. R., & Pastawski, H. M. (2007). *Phys. Rev. A,* **75** (6), 062116. 22, 24, 90

[Álvarez *et al.*, 2008] Álvarez, G. A., Danieli, E. P., Levstein, P. R., & Pastawski, H. M. (2008). *Phys. Rev. Lett.* **101** (12), 120503. 120, 130, 133, 149, 154, 166

[Álvarez *et al.*, 2010a] Álvarez, G. A., Danieli, E. P., Levstein, P. R., & Pastawski, H. M. (2010a). *Phys. Rev. A,* **82** (1), 012310. 11, 24, 90, 107, 111, 114, 115, 120, 125, 126, 127, 128, 136, 142, 143, 155

[Álvarez *et al.*, 2010b] Álvarez, G. A., Mishkovsky, M., Danieli, E. P., Levstein, P. R., Pastawski, H. M., & Frydman, L. (2010b). *Phys. Rev. A,* **81** (6), 060302. 114

[Andersen *et al.*, 2006] Andersen, M. F., Kaplan, A., Grünzweig, T., & Davidson, N. (2006). *Phys. Rev. Lett.* **97** (10), 104102. 90, 96, 114

[Anderson, 1954] Anderson, P. W. (1954). *Journal of the Physical Society of Japan,* **9** (3), 316–339. 18, 22, 33, 90

[Anderson, 1972] Anderson, P. W. (1972). *Science,* **177**, 393–396. 90

[Anderson, 1978] Anderson, P. W. (1978). *Rev. Mod. Phys.* **50**, 191–201. 48, 49

[Bartels, 2011] Bartels, B. (2011). *ArXiv: 1106.1371,* . 93

[Bederián & Dente, 2011] Bederián, C. S. & Dente, A. D. (2011). *Proceedings of HPC 2011: High-Performance Computing Symposium,* **40**, 63–75. 166

[Bennett & DiVincenzo, 2000] Bennett, C. H. & DiVincenzo, D. P. (2000). *Nature,* **404** (6775), 247–255. iv, 21

[Bergman & Stockman, 2003] Bergman, D. & Stockman, M. (2003). *Physical Review Letters,* **90** (2), 1–4. 70, 83

[Berry & Dennis, 2003] Berry, M. V. & Dennis, M. R. (2003). *Royal Society of London Proceedings Series A,* **459** (2033), 1261–1292. 23, 38

[Blanchard *et al.*, 1994] Blanchard, P., Bolz, G., Cini, M., de Angelis, G. F., & Serva, M. (1994). *J. Stat. Phys.* **75**, 749–755. 130

[Bloembergen *et al.*, 1948] Bloembergen, N., Purcell, E. M., & Pound, R. V. (1948). *Phys. Rev.* **73** (7), 679–712. 22

[Bose, 2003] Bose, S. (2003). *Phys. Rev. Lett.* **91** (20), 207901. 114

[Breuer & Petruccione, 2007] Breuer, H. & Petruccione, F. (2007). *The theory of open quantum systems.* Oxford University Press. 91

[Breuer *et al.*, 2009] Breuer, H.-P., Laine, E.-M., & Piilo, J. (2009). *Phys. Rev. Lett.* **103** (21), 210401. 110

[Brongersma *et al.*, 2000] Brongersma, M. L., Hartman, J. W., & Atwater, H. A. (2000). *Physical Review B,* **62** (24), 16356. 71, 72, 74

[Buchleitner *et al.*, 2007] Buchleitner, A., Carvalho, A. R. R., & Mintert, F. (2007). *Acta Phys. Pol. A,* **112**, 575. 92

[Buck, 1938] Buck, J. (1938). *Quarterly Review of Biology,* **13**, 301–304. 71

[Bustos-Marún *et al.*, 2010] Bustos-Marún, R. A., Coronado, E. A., & Pastawski, H. M. (2010). *Phys. Rev. B,* **82**, 035434. 44, 71, 72, 78, 93

[Calvo *et al.*, 2007] Calvo, H. L., Danieli, E. P., & Pastawski, H. M. (2007). *Physica B: Condensed Matter,* **398** (2), 317 – 320. 45

[Calvo & Pastawski, 2006] Calvo, H. L. & Pastawski, H. M. (2006). *Brazilian Journal of Physics,* **36**, 963 – 966. 23

[Calvo & Pastawski, 2010] Calvo, H. L. & Pastawski, H. M. (2010). *Europhys. Lett.* **89** (6), 60002. 93

[Calvo, 2007] Calvo, R. (2007). *Applied Magnetic Resonance,* **31**, 271–299. 23

[Cappellaro *et al.*, 2007] Cappellaro, P., Ramanathan, C., & Cory, D. G. (2007). *Phys. Rev. A,* **76** (3), 032317. iv, 92, 114, 159

[Cappellaro *et al.*, 2011] Cappellaro, P., Viola, L., & Ramanathan, C. (2011). *Phys. Rev. A,* **83** (3), 032304. 114, 159

[Cardamone *et al.*, 2002] Cardamone, D., Stafford, C., & Barrett, B. (2002). *physica status solidi (b),* **230** (2), 419–423. 23

[Carre're *et al.*, 2006] Carre're, H., Marie, X., Lombez, L., & Amand, T. (2006). *Applied Physics Letters,* **89** (18), 181115. 83

[Chakravarty & Leggett, 1984] Chakravarty, S. & Leggett, A. J. (1984). *Phys. Rev. Lett.* **52**, 5–8. 90, 130

REFERENCES

[Citrin, 2004] Citrin, D. S. (2004). *Nano Letters,* **4** (9), 1561–1565. 71

[Citrin, 2006] Citrin, D. S. (2006). *Optics Letters,* **31** (1), 98–100. 70, 80

[Cohen-Tannoudji *et al.*, 1998] Cohen-Tannoudji, C., Dupont-Roc, J., & Grynberg, G. (1998). *Atom-photon interactions: basic processes and applications.* Wiley science paperback series. 91

[Coronado *et al.*, 2011] Coronado, E. A., Encina, E. R., & Stefani, F. D. (2011). *Nanoscale,* **3** (10), 4042–59. 70

[Coronado & Schatz, 2003] Coronado, E. A. & Schatz, G. C. (2003). *The Journal of Chemical Physics,* **119** (7), 3926. 73

[Costa-Filho *et al.*, 1999] Costa-Filho, A. J., Munte, C. E., Barberato, C., Castellano, E. E., Mattioli, M. P. D., Calvo, R., & Nascimento, O. R. (1999). *Inorganic Chemistry,* **38** (20), 4413–4421. 23

[Cucchietti *et al.*, 2003] Cucchietti, F. M., Dalvit, D. A. R., Paz, J. P., & Zurek, W. H. (2003). *Phys. Rev. Lett.* **91** (21), 210403. 96

[Cucchietti *et al.*, 2006] Cucchietti, F. M., Lewenkopf, C. H., & Pastawski, H. M. (2006). *Phys. Rev. E,* **74**, 026207. 124, 136

[Danielewicz, 1984] Danielewicz, P. (1984). *Ann. Phys.* **152**, 239–304. 132

[Danieli *et al.*, 2007] Danieli, E., Álvarez, G., Levstein, P., & Pastawski, H. (2007). *Solid State Communications,* **141** (7), 422 – 426. 23, 90

[Danieli *et al.*, 2005] Danieli, E. P., Pastawski, H. M., & Álvarez, G. A. (2005). *Chemical Physics Letters,* **402** (1-3), 88 – 95. 22, 24, 90, 92, 119, 157

[Danieli *et al.*, 2002] Danieli, E. P., Pastawski, H. M., & Levstein, P. R. (2002). *Physica B,* **320**, 351–353. 127

[Danieli *et al.*, 2004] Danieli, E. P., Pastawski, H. M., & Levstein, P. R. (2004). *Chem. Phys. Lett.* **384** (4-6), 306 – 311. 24, 92, 118, 119, 125, 157

[De Raedt *et al.*, 1999] De Raedt, H., Hams, A., Michielsen, K., & De Raedt, K. (1999). *Computer Physics Communications,* **132** (1-2), 28. 170

[De Raedt & Michielsen, 2004] De Raedt, H. & Michielsen, K. (2004). *arXiv:quant-ph/0406210,* . 169

[Dembowski *et al.*, 2003] Dembowski, C., Dietz, B., Gräf, H.-D., Harney, H. L., Heine, A., Heiss, W. D., & Richter, A. (2003). *Phys. Rev. Lett.* **90** (3), 034101. 23, 38

[Dembowski *et al.*, 2004] Dembowski, C., Dietz, B., Gräf, H.-D., Harney, H. L., Heine, A., Heiss, W. D., & Richter, A. (2004). *Phys. Rev. E,* **69** (5), 056216. 23, 38

[Dembowski *et al.*, 2001] Dembowski, C., Gräf, H.-D., Harney, H. L., Heine, A., Heiss, W. D., Rehfeld, H., & Richter, A. (2001). *Phys. Rev. Lett.* **86** (5), 787–790. 23, 38

[Dente *et al.*, 2008] Dente, A. D., Bustos-Marún, R. A., & Pastawski, H. M. (2008). *Phys. Rev. A,* **78** (6), 062116. iv, 91, 97, 98, 102, 103, 161, 162

[Dente *et al.*, 2011] Dente, A. D., Zangara, P. R., & Pastawski, H. M. (2011). *Phys. Rev. A,* **84**, 042104. iv, v, 115, 118, 121, 127, 128, 130, 132, 135, 136, 138, 140, 142, 148, 149

[Dietz *et al.*, 2007] Dietz, B., Friedrich, T., Metz, J., Miski-Oglu, M., Richter, A., Schäfer, F., & Stafford, C. A. (2007). *Phys. Rev. E,* **75** (2), 027201. 23, 38

[DiVincenzo, 1995] DiVincenzo, D. P. (1995). *Science,* **270** (5234), 255–261. 7

[Doronin *et al.*, 2000] Doronin, S., Maksimov, I., & Fel'dman, E. (2000). *J. Experiment. Theoret. Phys.* **91**, 597–609. 92, 114, 159

[Doronin & Fel'dman, 2005] Doronin, S. I. & Fel'dman, E. B. (2005). *Solid State Nucl. Mag.* **28** (2-4), 111 – 116. 114

[Ebbesen *et al.*, 2008] Ebbesen, T. W., Genet, C., & Bozhevolnyi, S. I. (2008). *Physics Today,* **61** (5), 44. 70

[Economou, 2006] Economou, E. (2006). *Green's functions in quantum physics.* Springer series in solid-state sciences. 29, 30, 42, 44, 93, 146

[Einstein, 1905] Einstein, A. (1905). *Annalen der Physik,* **322**, 132–148. 1

[Ernst *et al.*, 2004] Ernst, R., Bodenhausen, G., & Wokaun, A. (2004). *Principles of nuclear magnetic resonance in one and two dimensions.* Oxford: Clarendon Press. 119

[Facchi & Pascazio, 1999] Facchi, P. & Pascazio, S. (1999). *La regola d'oro di Fermi.* Saggi scienze filos. natur-Quad.fis.teor. Bibliopolis. 9, 29, 103

[Fel'dman & Lacelle, 1997] Fel'dman, E. B. & Lacelle, S. (1997). *J. Chem. Phys.* **107** (18), 7067–7084. 92, 114, 159

[Fonda *et al.*, 1978] Fonda, L., Ghirardi, G. C., & Rimini, A. (1978). *Reports on Progress in Physics,* **41**, 587–631. 30, 103

[Gamow, 1971] Gamow, G. (1971). *Treinta años que conmovieron la física: la historia de la teoría cuántica.* Lectores de Eudeba. Buenos Aires: Editorial Universitaria de Buenos Aires. 9

[García-Calderón *et al.*, 1995] García-Calderón, G., Mateos, J. L., & Moshinsky, M. (1995). *Phys. Rev. Lett.* **74** (3), 337–340. 30, 103

[García de Abajo, 2007] García de Abajo, F. J. (2007). *Rev. Mod. Phys.* **79**, 1267–1290. 71

[Giannoni *et al.*, 1991] Giannoni, M., Voros, A., & Zinn-Justin, J. (1991). *Chaos and quantum physics.* Ecole d'ete de physique theoretique les Houches, Proceedings. North-Holland. 29

[Goldstein *et al.*, 2011] Goldstein, R. E., Polin, M., & Tuval, I. (2011). *Phys. Rev. Lett.* **107**, 148103. 71

[Gorin *et al.*, 2006] Gorin, T., Prosen, T., Seligman, T. H., & Znidaric, M. (2006). *Phys. Rep.* **435** (2-5), 33 – 156. 90, 96, 115

[Gradshteyn & Ryzhik, 2007] Gradshteyn, I. S. & Ryzhik, I. M. (2007). *Table of Integrals, Series, and Products*. Academic Press, 7 edition. 146

[Gutiérrez *et al.*, 2006] Gutiérrez, L., Díaz-de Anda, A., Flores, J., Méndez-Sánchez, R. A., Monsivais, G., & Morales, A. (2006). *Phys. Rev. Lett.* **97** (11), 114301. 45

[Halas *et al.*, 2011] Halas, N. J., Lal, S., Chang, W.-S., Link, S., & Nordlander, P. (2011). *Chemical Reviews,* **111** (6), 3913–3961. 70

[Haydock *et al.*, 1972] Haydock, R., Heine, V., & Kelly, M. J. (1972). *Journal of Physics C Solid State Physics,* **5** (20), 2845–2858. 52

[Heiss, 2000] Heiss, W. D. (2000). *Phys. Rev. E,* **61** (1), 929–932. 23

[Heiss & Sannino, 1991] Heiss, W. D. & Sannino, A. L. (1991). *Phys. Rev. A,* **43** (8), 4159–4166. 23

[Hernández *et al.*, 2005] Hernández, J. V., Noordam, L. D., & Robicheaux, F. (2005). *The Journal of Physical Chemistry B,* **109** (33), 15808–15811. 71, 74

[Hoffmann, 1988] Hoffmann, R. (1988). *Rev. Mod. Phys.* **60**, 601–628. 48

[Hogreve, 1995] Hogreve, H. (1995). *Physics Letters A,* **201** (2-3), 111 – 118. 23, 34, 42

[Hor-Meyll *et al.*, 2009] Hor-Meyll, M., Auyuanet, A., Borges, C. V. S., Aragão, A., Huguenin, J. A. O., Khoury, A. Z., & Davidovich, L. (2009). *Phys. Rev. A,* **80** (4), 042327. 92

[Hu *et al.*, 1992] Hu, B. L., Paz, J. P., & Zhang, Y. (1992). *Phys. Rev. D,* **45** (8), 2843–2861. 93

[Hush, 1958] Hush, N. S. (1958). *The Journal of Chemical Physics,* **28** (5), 962–972. 48

[Huygens, 1673] Huygens, C. (1673). *Horologium oscillatorium: sive, De motu pendulorum ad horologia aptato demostrationes geometricae*. F. Muguet. 13, 39, 71

[Ingold, 2002] Ingold, G.-L. (2002). In: *Coherent Evolution in Noisy Environments*, (Buchleitner, A. & Hornberger, K., eds) volume 611 of *Lecture Notes in Physics* pp. 1–53. Springer Berlin / Heidelberg. 100

[Inoue & Ohtaka, 2004] Inoue, J. & Ohtaka, K. (2004). *Journal of Luminescence,* **108** (1-4), 251 – 254. Proceedings of the Fourteenth International Conference on Dynamical Processes in Excited States of Solids. 23

[Jacquod & Petitjean, 2009] Jacquod, P. & Petitjean, C. (2009). *Adv. Phys,* **58** (6), 67–196. 90, 115

[Jacquod *et al.*, 2001] Jacquod, P., Silvestrov, P., & Beenakker, C. (2001). *Phys. Rev. E,* **64**, 055203. 124, 136

[Jalabert & Pastawski, 2001] Jalabert, R. A. & Pastawski, H. M. (2001). *Phys. Rev. Lett.* **86** (12), 2490–2493. 90, 96, 114, 123, 136

[Jones, 1945] Jones, R. C. (1945). *Phys. Rev.* **68**, 93–96. 71

[Keck *et al.*, 2003] Keck, F., Korsch, H. J., & Mossmann, S. (2003). *Journal of Physics A: Mathematical and General,* **36** (8), 2125. 23

[Keldysh, 1964] Keldysh, L. V. (1964). *Zh. Eksp. Teor. Fiz.* **47**, 1515–1527. Sov. Phys. JEPT **20**, 1018 (1965). 132, 143, 157

[Kelly *et al.*, 2003] Kelly, K. L., Coronado, E., Zhao, L. L., & Schatz, G. C. (2003). *Journal of Physical Chemistry B,* **107** (3), 668–677. 71, 73

[Khalfin, 1958] Khalfin, S. A. (1958). *Soviet Journal of Experimental and Theoretical Physics,* **6**, 1053. 30, 103, 152

[Khitrova *et al.*, 2006] Khitrova, G., Gibbs, H. M., Kira, M., Koch, S. W., & Scherer, A. (2006). *Nat Phys,* **2** (2), 81–90. 23, 38

[Kottos, 2010] Kottos, T. (2010). *Nature Physics,* **6** (3), 166–167. 70, 80

[Krasavin *et al.*, 2011] Krasavin, A. V., Vo, T. P., Dickson, W., Bolger, P. M., & Zayats, A. V. (2011). *Nano Letters,* **11** (6), 2231–2235. 70, 80

[Kuznetsov, 1995] Kuznetsov, A. (1995). *Charge Transfer in Physics, Chemistry and Biology: Physical Mechanisms of Elementary Processes and an Introduction to the Theory*. Gordon and Breach Publishers. 48

[Lai *et al.*, 2011] Lai, Y. M., Newby, J., & Bressloff, P. C. (2011). *Phys. Rev. Lett.* **107**, 118102. 71

[Lanczos, 1950] Lanczos, C. (1950). *Journal Of Research Of The National Bureau Of Standards,* **45** (4), 255–282. 52, 98

[Levich, 1970] Levich, V. G. (1970). In: *Physical Chemistry and Advanced Treatise, vol. Xb*, (H. Eyring, D. H. & Jost, W., eds). Academic Press New York. 48

[Levstein *et al.*, 1998] Levstein, P. R., Usaj, G., & Pastawski, H. M. (1998). *J. Chem. Phys.* **108** (7), 2718–2724. 90, 96, 114, 121, 136

[Li & Xia, 2010] Li, Z.-Y. & Xia, Y. (2010). *Nano Letters,* **10** (1), 243–249. 70, 80, 83

[Lieb *et al.*, 1961] Lieb, E., Schultz, T., & Mattis, D. (1961). *Ann. Phys. (N.Y.),* **16** (3), 407 – 466. 10, 24, 92, 133, 157, 158

[Longhi, 2006a] Longhi, S. (2006a). *Phys. Rev. A,* **74** (6), 063826. 23

[Longhi, 2006b] Longhi, S. (2006b). *Phys. Rev. Lett.* **97** (11), 110402. 45

[Luke A. Sweatlock & Atwater, 2003] Luke A. Sweatlock, S. A. M. & Atwater, H. A. (2003). *Proceedings of Electronic Components and Technology Conference,* , 1648 – 1651. 45

[Machida *et al.*, 1999] Machida, K., Nakazato, H., Pascazio, S., Rauch, H., & Yu, S. (1999). *Phys. Rev. A,* **60**, 3448–3460. 130

[Mádi *et al.*, 1997] Mádi, Z. L., Brutscher, B., Schulte-Herbrüggen, T., Brüschweiler, R., & Ernst, R. R. (1997). *Chem. Phys. Lett.* **268** (3-4), 300 – 305. 157

REFERENCES

[Maier, 2007] Maier, S. (2007). *Plasmonics: fundamentals and applications.* New York: Springer. 70

[Malyshev *et al.*, 2008] Malyshev, A. V., Malyshev, V. A., & Knoester, J. (2008). *Nano Letters,* **8** (8), 2369–2372. 71

[Marcelis *et al.*, 2004] Marcelis, B., van Kempen, E. G. M., Verhaar, B. J., & Kokkelmans, S. J. J. M. F. (2004). *Phys. Rev. A,* **70** (1), 012701. 23, 42

[Marcus, 1956] Marcus, R. A. (1956). *The Journal of Chemical Physics,* **24** (5), 979–989. 48

[Markel & Sarychev, 2007] Markel, V. A. & Sarychev, A. K. (2007). *Phys. Rev. B,* **75**, 085426. 71

[Mádi *et al.*, 1997] Mádi, Z. L., Brutscher, B., Schulte-Herbrüggen, T., Brüschweiler, R., & Ernst, R. R. (1997). *Chemical Physics Letters,* **268** (3-4), 300 – 305. iv, 6, 8, 24, 26, 90, 92, 114, 117, 120, 133

[Mertens & Weaver, 2011] Mertens, D. & Weaver, R. (2011). *Phys. Rev. E,* **83**, 046221. 71

[Misra & Sudarshan, 1977] Misra, B. & Sudarshan, E. C. G. (1977). *Journal of Mathematical Physics,* **18** (4), 756–763. 22

[Müller *et al.*, 1974] Müller, L., Kumar, A., Baumann, T., & Ernst, R. R. (1974). *Phys. Rev. Lett.* **32** (25), 1402–1406. 90

[Müller *et al.*, 1995] Müller, M., Dittes, F.-M., Iskra, W., & Rotter, I. (1995). *Phys. Rev. E,* **52** (6), 5961–5973. 22, 38

[Myatt *et al.*, 2000] Myatt, C. J., King, B. E., Turchette, Q. A., Sackett, C. A., Kielpinski, D., Itano, W. M., Monroe, C., & Wineland, D. J. (2000). *Nature,* **403** (6767), 269–273. 21

[Napolitano *et al.*, 2008] Napolitano, L. M. B., Nascimento, O. R., Cabaleiro, S., Castro, J., & Calvo, R. (2008). *Phys. Rev. B,* **77** (21), 214423. 23

[Narevicius *et al.*, 2003] Narevicius, E., Serra, P., & Moiseyev, N. (2003). *EPL (Europhysics Letters),* **62** (6), 789. 31

[Newns, 1969] Newns, D. M. (1969). *Phys. Rev.* **178**, 1123–1135. 49, 51

[Noginov *et al.*, 2009] Noginov, M. A., Zhu, G., Belgrave, A. M., Bakker, R., Shalaev, V. M., Narimanov, E. E., Stout, S., Herz, E., Suteewong, T., & Wiesner, U. (2009). *Nature,* **460** (7259), 1110–2. 70, 80, 83

[Noginov *et al.*, 2008] Noginov, M. A., Zhu, G., Mayy, M., Ritzo, B. A., Noginova, N., & Podolskiy, V. A. (2008). *Phys. Rev. Lett.* **101**, 226806. 83

[Novotny & Hecht, 2006] Novotny, L. & Hecht, B. (2006). *Principles of nano-optics.* Cambridge: Cambridge University Press. 70

[Oberthaler *et al.*, 1996] Oberthaler, M. K., Abfalterer, R., Bernet, S., Schmiedmayer, J., & Zeilinger, A. (1996). *Phys. Rev. Lett.* **77** (25), 4980–4983. 23, 38

[Palma *et al.*, 1996] Palma, G. M., Suominen, K.-A., & Ekert, A. K. (1996). *Proc. R. Soc. A,* **452** (1946), 567–584. 91

[Park & Stroud, 2004] Park, S. Y. & Stroud, D. (2004). *Phys. Rev. B,* **69**, 125418. 71

[Pascazio & Namiki, 1994] Pascazio, S. & Namiki, M. (1994). *Phys. Rev. A,* **50** (6), 4582–4592. 22

[Pastawski, 1996] Pastawski, H. (1996). *Chem. Phys. Lett.* **261**, 329–334. 114, 119, 120

[Pastawski, 1991] Pastawski, H. M. (1991). *Phys. Rev. B,* **44**, 6329–6339. 127, 132, 143

[Pastawski, 1992] Pastawski, H. M. (1992). *Phys. Rev. B,* **46** (7), 4053–4070. 127, 132

[Pastawski, 2007] Pastawski, H. M. (2007). *Physica B: Condensed Matter,* **398** (2), 278 – 286. 30, 31, 90

[Pastawski *et al.*, 1995] Pastawski, H. M., Levstein, P. R., & Usaj, G. (1995). *Phys. Rev. Lett.* **75** (23), 4310–4313. 24, 90, 92, 100, 114, 117, 120, 123, 135, 136, 157

[Pastawski *et al.*, 2000] Pastawski, H. M., Levstein, P. R., Usaj, G., Raya, J., & Hirschinger, J. (2000). *Physica A,* **283** (1-2), 166 – 170. 90, 96, 114

[Pastawski & Medina, 2001] Pastawski, H. M. & Medina, E. (2001). *Revista Mexicana de Fisica,* **47**, 1 – 23. 23, 30, 57, 58, 102

[Pastawski & Usaj, 1998] Pastawski, H. M. & Usaj, G. (1998). *Phys. Rev. B,* **57** (9), 5017–5020. 22

[Pastawski *et al.*, 1996] Pastawski, H. M., Usaj, G., & Levstein, P. R. (1996). *Chem. Phys. Lett.* **261** (3), 329 – 334. 90, 92

[Pastawski & Wiecko, 1987] Pastawski, H. M. & Wiecko, C. (1987). *Phys. Rev. A,* **36** (12), 5854–5857. 146

[Paz & Roncaglia, 2009] Paz, J. P. & Roncaglia, A. J. (2009). *Phys. Rev. A,* **79** (3), 032102. 92

[Petitjean & Jacquod, 2006] Petitjean, C. & Jacquod, P. (2006). *Phys. Rev. Lett.* **97** (12), 124103. 121, 122, 124, 136

[Pikovsky *et al.*, 2003] Pikovsky, A., Rosenblum, M., & Kurths, J. (2003). *Synchronization: a universal concept in nonlinear sciences.* nonlinear science series. Cambridge University Press. 69, 70

[Pisignano *et al.*, 2002] Pisignano, D., Anni, M., Gigli, G., Cingolani, R., Zavelani-Rossi, M., Lanzani, G., Barbarella, G., & Favaretto, L. (2002). *Applied Physics Letters,* **81** (19), 3534. 83

[Plenio & Knight, 1998] Plenio, M. B. & Knight, P. L. (1998). *Rev. Mod. Phys.* **70**, 101–144. 140

[Press, 1992] Press, W. (1992). *Numerical recipes in FORTRAN: the art of scientific computing.* FORTRAN Numerical Recipes. Cambridge University Press. 74

[Prigodin *et al.*, 1994] Prigodin, V. N., Altshuler, B. L., Efetov, K. B., & Iida, S. (1994). *Phys. Rev. Lett.* **72**, 546–549. 4, 114, 120

[Pupasov *et al.*, 2008] Pupasov, A. M., Samsonov, B. F., & Sparenberg, J.-M. (2008). *Phys. Rev. A,* **77** (1), 012724. 23

[Rieth & Schommers, 2006] Rieth, M. & Schommers, W. (2006). *Handbook of Theoretical and Computational Nanotechnology: Quantum and molecular computing, quantum simulations.* Nanotechnology book series. American Scientific Publishers. 120, 165

[Rotter, 2009] Rotter, I. (2009). *Journal of Physics A: Mathematical and Theoretical,* **42** (15), 153001. 22, 45, 90, 151

[Rotter, 2010] Rotter, I. (2010). *10110645,* , 27. 22

[Ruderman, 2011] Ruderman, A. (2011). *Disociación molecular, en catálisis heterogénea, como una transición de fase cuántica.* Degree thesis Universidad Nacional de Córdoba. 48

[Rufeil-Fiori & Pastawski, 2006] Rufeil-Fiori, E. & Pastawski, H. (2006). *Chemical Physics Letters,* **420** (1-3), 35 – 41. 17, 31, 36, 38, 64, 90, 92, 98, 102, 103, 107, 118, 120, 124, 127, 132, 136, 164

[Rufeil-Fiori & Pastawski, 2009] Rufeil-Fiori, E. & Pastawski, H. (2009). *Physica B,* **404** (18), 2812 – 2815. 107, 124, 136, 164

[Rufeil-Fiori & Pastawski, 2006] Rufeil-Fiori, E. & Pastawski, H. M. (2006). *Braz. J. Phys.* **36**, 844–847. 98

[Rufeil-Fiori *et al.*, 2009] Rufeil-Fiori, E., Sánchez, C. M., Oliva, F. Y., Pastawski, H. M., & Levstein, P. R. (2009). *Phys. Rev. A,* **79** (3), 032324. 92, 114, 159

[Sachdev, 2011] Sachdev, S. (2011). *Quantum Phase Transitions.* Cambridge University Press. 13

[Sánchez *et al.*, 2009] Sánchez, C. M., Levstein, P. R., Acosta, R. H., & Chattah, A. K. (2009). *Phys. Rev. A,* **80** (1), 012328. 114

[Santos *et al.*, 2011] Santos, E., Bartenschlager, S., & Schmickler, W. (2011). *Journal of Electroanalytical Chemistry,* **660** (2), 314 – 319. 49

[Santos *et al.*, 2006] Santos, E., Koper, M., & Schmickler, W. (2006). *Chemical Physics Letters,* **419** (4-6), 421 – 425. 49

[Santos *et al.*, 2008] Santos, E., Koper, M., & Schmickler, W. (2008). *Chemical Physics,* **344** (1-2), 195 – 201. 49

[Santos *et al.*, 2009] Santos, E., Lundin, A., Pötting, K., Quaino, P., & Schmickler, W. (2009). *Phys. Rev. B,* **79**, 235436. 49

[Santos & Schmickler, 2007a] Santos, E. & Schmickler, W. (2007a). *Chemical Physics,* **332** (1), 39 – 47. 49

[Santos & Schmickler, 2007b] Santos, E. & Schmickler, W. (2007b). *Angewandte Chemie International Edition,* **46** (43), 8262–8265. 49

[Schäfer *et al.*, 2005] Schäfer, R., Stöckmann, H.-J., Gorin, T., & Seligman, T. H. (2005). *Phys. Rev. Lett.* **95** (18), 184102. 90, 96, 114

[Seidel *et al.*, 2005] Seidel, J., Grafström, S., & Eng, L. (2005). *Phys. Rev. Lett.* **94**, 177401. 83

[Serra *et al.*, 2001] Serra, P., Kais, S., & Moiseyev, N. (2001). *Phys. Rev. A,* **64** (6), 062502. 23

[Shuvalov & Scott, 2000] Shuvalov, A. & Scott, N. (2000). *Acta Mechanica,* **140**, 1–15. 10.1007/BF01175976. 23, 38

[Slichter, 1990] Slichter, C. (1990). *Principles of magnetic resonance.* Springer series in solid-state sciences. 131

[Stafford & Barrett, 1999] Stafford, C. A. & Barrett, B. R. (1999). *Phys. Rev. C,* **60** (5), 051305. 23

[Stefani & Gerbeth, 2005] Stefani, F. & Gerbeth, G. (2005). *Phys. Rev. Lett.* **94** (18), 184506. 23

[Stehmann *et al.*, 2004] Stehmann, T., Heiss, W. D., & Scholtz, F. G. (2004). *Journal of Physics A: Mathematical and General,* **37** (31), 7813. 23, 38

[Stein *et al.*, 2011] Stein, K., Timmermann, A., & Schneider, N. (2011). *Phys. Rev. Lett.* **107**, 128501. 71

[Stockman, 2008] Stockman, M. I. (2008). *Nature Photonics,* **2** (6), 327–329. 70, 80

[Stockman, 2009] Stockman, M. I. (2009). *Journal of Optics,* **12** (2), 024004. 70, 80, 83, 84

[Stockman, 2010] Stockman, M. I. (2010). *Physical Review Letters,* **106** (15), 156802. 70, 83, 84

[Taylor, 2006] Taylor, J. (2006). *Scattering Theory: The Quantum Theory of Nonrelativistic Collisions.* Dover Books on Engineering Series. Dover Publications. 23

[Taylor *et al.*, 2003] Taylor, J. M., Imamoglu, A., & Lukin, M. D. (2003). *Phys. Rev. Lett.* **91** (24), 246802. 90

[Van Vleck, 1948] Van Vleck, J. H. (1948). *Phys. Rev.* **74** (9), 1168–1183. 22

[Weidenmüller, 2003] Weidenmüller, H. A. (2003). *Phys. Rev. B,* **68** (12), 125326. 23

[Weinreich, 1979] Weinreich, G. (1979). *j-SCI-AMER,* **240** (1), 94–102. 15, 16, 77

[Weiss, 2008] Weiss, U. (2008). *Quantum dissipative systems.* Series in modern condensed matter physics. Singapore: World Scientific. 130

[Wójcik *et al.*, 2011] Wójcik, A. K., Yu, N., Diehl, L., Capasso, F., & Belyanin, A. (2011). *Phys. Rev. Lett.* **106**, 133902. 71

[Wuestner *et al.*, 2010] Wuestner, S., Pusch, A., Tsakmakidis, K., Hamm, J., & Hess, O. (2010). *Physical Review Letters,* **105** (12), 1–4. 70, 80

[Yamashita *et al.*, 2002] Yamashita, M. T., Frederico, T., Delfino, A., & Tomio, L. (2002). *Phys. Rev. A,* **66** (5), 052702. 23

[Zanardi & Rasetti, 1997] Zanardi, P. & Rasetti, M. (1997). *Phys. Rev. Lett.* **79** (17), 3306–3309. 91

[Zangara *et al.*, 2011] Zangara, P. R., Dente, A. D., Levstein, P. R., & Pastawski, H. M. (2011). *ArXiv: 1111.2004,* . 136

REFERENCES

[Zhang *et al.*, 2011] Zhang, J., Wei, T.-C., & Laflamme, R. (2011). *Phys. Rev. Lett.* **107**, 010501. iv

[Zhang *et al.*, 2009] Zhang, W., Cappellaro, P., Antler, N., Pepper, B., Cory, D. G., Dobrovitski, V. V., Ramanathan, C., & Viola, L. (2009). *Phys. Rev. A,* **80** (5), 052323–+. 114

[Zou & Schatz, 2004] Zou, S. & Schatz, G. C. (2004). *The Journal of chemical physics,* **121** (24), 12606–12612. 71

[Zurek, 2003] Zurek, W. H. (2003). *Rev. Mod. Phys.* **75** (3), 715–775. 21

[Zurek *et al.*, 2007] Zurek, W. H., Cucchietti, F. M., & Paz, J. P. (2007). *Acta Physica Polonica B,* **38**, 1685–+. 21